Searches for heavy vector-like quarks decaying to high transverse momentum W bosons and top- or bottom-quarks and weak mode identification with the ATLAS detector

by

Steffen Henkelmann

B.Sc., The University of Göttingen, 2011
M.Sc., The University of Göttingen, 2013

A THESIS SUBMITTED IN PARTIAL FULFILLMENT OF
THE REQUIREMENTS FOR THE DEGREE OF

DOCTOR OF PHILOSOPHY

in

The Faculty of Graduate and Postdoctoral Studies

(Physics)

THE UNIVERSITY OF BRITISH COLUMBIA

(Vancouver)

August 2018

CERN-THESIS-2018-212
29/06/2018

The following individuals certify that they have read, and recommend to the Faculty of Graduate and Postdoctoral Studies for acceptance, the dissertation entitled:

Searches for heavy vector-like quarks decaying to high transverse momentum W bosons and top- or bottom-quarks and weak mode identification with the ATLAS detector

submitted by **Steffen Henkelmann** in partial fulfillment of the requirements for
the degree of **Doctor of Philosophy**
in **Physics**

Examining committee:

Alison Lister, Physics & Astronomy
Supervisor

Colin Gay, Physics & Astronomy
Supervisory Committee Member

Gary Hinshaw, Physics & Astronomy
Supervisory Committee Member

David Morrissey, TRIUMF
Supervisory Committee Member

Janis McKenna, Physics & Astronomy
University Examiner

Donald Fleming, Chemistry
University Examiner

Abstract

The precise understanding of elementary particle properties and theory parameters predicted by the Standard Model of Particle Physics (SM) as well as the revelation of new physics phenomena beyond the scope of that successful theory are at the heart of modern fundamental particle physics research. The Large Hadron Collider (LHC) and modern particle detectors provide the key to probing nature at energy scales never achieved in an experimental controlled setup before. The assumption that the SM describes nature only up to a certain energy scale Λ can be relaxed if new particles are present. This helps in particular with the so called "fine-tuning" problem which requires large corrections – in the SM – to the bare mass of the Higgs boson in order to be consistent with the observed mass. A possible solution to this problem is the existence of partner particles of the heaviest known fundamental particle, the top-quark. The new partner particles are expected to be up to ten times heavier. Popular examples of theories predicting heavier top-quark partners are supersymmetric theories and theories that add an additional quark sector to the SM which might be a result of an additional spontaneously broken global symmetry. This dissertation documents two searches for heavy top-quark partners, namely vector-like quarks (VLQs), based on the proton proton (pp) collision data collected in 2015 and 2016, corresponding to an integrated luminosity of $\mathscr{L} = 36.1$ fb^{-1} at a center of mass energy of 13 TeV. It also elaborates on the work that contributed to a successful data taking campaign related to the alignment of the inner most part of the ATLAS detector with emphasis on the identification and mitigation of track parameter biases.

No signs for VLQs were found. The strongest lower mass limits on the pair-produced VLQs decaying into W bosons and top- or bottom-quarks are set to 1.35 TeV at the 95% Confidence Interval exceeding the one TeV scale for the first time. In addition, the analyses were re-interpreted for other expected VLQ decay signatures.

Lay Summary

The fundamental building blocks of matter and their interactions are described in the Standard Model of Particle Physics (SM). The theory has its limitations and is expected to describe nature only up to a certain energy and is assumed to be embedded in a more fundamental theory. Various theories that go beyond the SM predict the existence of new heavy particles. This dissertation presents searches for heavier partners to the heaviest known fundamental particle, the top-quark. Therefore, data recorded by the ATLAS detector, at the most powerful particle accelerator called the Large Hadron Collider at CERN, is analysed to search for these particles. Contributions to the determination of the relative spatial position of the inner most measurement devices of ATLAS, allowing for a successful data taking campaign, are also presented alongside. No new particles were found, but we are able to provide restrictions to their allowed mass range.

Preface

The presented research in this dissertation is based on the data collected by the ATLAS experiment and theory predictions from numerous authors. In order to become part of the ATLAS collaboration, every physicist is expected to fulfill a "qualification" task usually in the beginning of the PhD. The successful completion of this project entitles one to be an official author of the experiment. Every author is listed on each publication or public result that leaves the collaboration and the authorlist is always purely alphabetical. Final results are published in peer reviewed journals. Preliminary results can also be released for certain conferences in the form of conference notes (CONF notes) or made public in form of public documents (PUB notes) or public plots including short descriptions. The targeted journal as well as the type of public result is determined on mutual agreement between the collaborators and is evaluated on a case-by-case basis.

Individuals do not typically claim all public results by the collaboration but instead will highlight those in which they had major contributions. These are generally split into publications, conference and public notes. Most of the theoretical expectations are based on calculations and the simulation of physics processes that are mainly provided by authors not being part of the collaboration.

Simulated theory predictions rely on the preparation and validation which is handled by individuals chosen by each physics group of the collaboration. The shared collaborational effort with varying contributions of individual authors can not be fully disentangled. Individual ATLAS authors are contributing with a minimum of their qualification task during their PhD to the collaborational efforts and as such have the right to analyse the data. The author contributed to performance work of the ATLAS collaboration particularly in the context of the Tracking Combined Performance Group and the Top-quark Physics Group. The former resulted in support of the 2015 and 2016 data taking periods and the latter involved contributions to the generation and simulation of theoretical predictions associated with top-quarks. The qualification task was performed in a sub group of the Tracking group, the Inner Detector (ID) alignment team, and resulted in the update of the ID alignment performance monitoring package in preparation for Run II (the data taking period between 2015 and 2018). Additionally, the author updated and maintained the ID alignment monitoring exploiting the decay products of well known physics processes such as the Z and W boson, J/ψ and K_S^0 to determine the relative spatial position of measurement devices in the ID. This is done in real-time during online data taking. The author elongated his contribution to the Tracking group beyond the qualification task through the extension of a methodology to identify particular ID detector deformations (so called *weak modes*). This was achieved using dimuon decays of the Z boson employed to identify track parameter biases caused by such deformations. The author contributed to the extension of a dual-use tool released by the Tracking group to either assess systematic uncertainties on tracks or to calibrate tracks in situ. Through the usage of this tool, the mitigation of observed biases was made possible without relying on a reprocessing of the recorded data. The initial implementation was performed in collaboration with Paweł Brückman de Renstrom and continued with Michael Ryan Clark. In addition, the author performed measurements of the impact parameter resolution at medium to high transverse momenta employing Z boson decays. Consecutive contributions were performed on a consultative basis. The main contributions in the Top-quark Physics group were based on a one-year mandate overseeing and managing the Monte Carlo (MC) sample production for the group and working towards improvements in the assessment of theory predictions and associated uncertainties. In this role, the author provided support to $\sim$300 active physicists in the preparation and validation of samples entering the official ATLAS Monte Carlo event generation and simulation chain. Frequent liaising with group conveners of the Top-quark Physics Group and Physics Coordinators as well as the ATLAS central Monte Carlo (MC) production team was performed. Samples with top-quarks were tested and validated. A subset of these samples resulted in the updated top-quark sample baseline described in Chapter 10 and summarised in Section 12.1.

The dissertation text was written by the author and mostly not directly taken from previously published sources. Exceptions to this are parts of Sections 8.1, 8.2.1 and 12.1.2, Chapter 12.2, Chapter 13 and Chapter 14 that have appeared in internal (unpublished and non-public) documentations. Figures not including a reference or credit in the caption and not explicitly mentioned in this preface are produced by the author. Figures with the label **ATLAS**, **ATLAS** *Simulation* or **ATLAS** *Preliminary* reflect published and public results, and are officially approved by the ATLAS collaboration. The analyses presented in Chapters 13 and 14 have been published. Figures with no label or the label **ATLAS** *Internal* or **ATLAS** *Work In Progress* are results not approved by the ATLAS collaboration albeit depending on either ATLAS data or simulated samples using the ATLAS sample generation or simulation chain.

Information needed to support the general understanding of the results presented is summarised from sources indicated by the citations in the text. Parts I and II, Chapters 7 and 9 present material that serves as introduction for the reader. The author contributed to the data quality system described in Section 6.2.5 through the previously mentioned update, extension and consequent maintenance of the ID alignment performance monitoring package during 2015 and 2016 data taking. The primary work of the author is contained in Chapter 8, Chapter 10 and Part IV. The contributions of the author to published or public results emerged from the work presented in this dissertation is detailed below next to the respective references. Acknowledgement of the relative contributions is summarised in the following alongside with a list of publications as a result from the work presented.

The work presented in Chapter 8 was primarily performed by the author with contributions to the E/p studies by William Kennedy Di Clemente including the inputs for the bottom two figures in Figure 8.7 and work in collaboration with Oscar Estrada Pastor resulting in Figure 8.11. Public results that emerged from the work presented in Chapter 8 are contained in [7], [8] and [9] of the references below. Chapter 10 gives a brief summary of work related to the modelling of top-quarks at the LHC. The Rivet routines implemented by the author were based on a code skeleton by Lorenzo Massa and validated together with Federica Fabbri and Francesco La Ruffa for the respective analysis channels. Figures 10.2 and 10.3 used the developed routines and were prepared by Andrea Knue. The code to quantify the agreement between data and prediction was based on initial work by Riccardo Di Sipio. Public and published results based on work presented in Chapter 10 resulted in [3] and [6]. The author made primary contributions to the work described in Part IV. Chapter 13 presents an analysis performed in a research team with four members including the author, Alison Lister, Joseph Haley and Matthias Danninger. The main contributions by the author to this analysis were the development of the analysis framework based on a code skeleton with primary contributions from Danilo Ferreira de Lima. The author managed the production of the final samples used for the analysis and prepared the production of a subset of signal samples described in Section 12.1. The author made major contributions to the analysis design through optimisation of the event selection and object definition. The author evaluated the background and signal yields and assessed associated uncertainties with particular regard to the main background contributions. The author contributed to the documentation. The senior co-authors Alison Lister and Joe Haley contributed to the analysis structure and review. Alison Lister wrote the publication ([4]). Joe Haley in addition evaluated the data-driven background using a method developed by another analysis team, coordinated by Danilo Ferreira de Lima. Matthias Danninger was the main analyser performing the statistical analysis optimisation as well as writing the paper. Preliminary analysis results presented in form of the conference note [5] were prepared in collaboration with the additional authors Daniel Edison Marley, Allison McCarn and Thomas Andrew Schwarz.

Chapter 14 presents an analysis that built on the analysis infrastructure developed for the previous paper and was performed in a research team with three members including the author, Alison Lister, and Matthias Danninger. The author was the primary analyser performing all aspects of the analysis including the statistical analysis and design. The author was solely responsible for the detailed internal documentation of the analysis. Alison Lister and Matthias Danninger wrote the paper ([2]).

A combination of the VLQ searches is provided in [1] to which the author contributed crucial inputs from the analysis described in Chapter 14.

A commonly employed tool within the Top-quark, Higgs, and Exotics Physics Group was used for the statistical analysis of both searches. This code is developed and maintained mainly by Loïc Valéry and Michele Pinamonti.

The provision of the data through particle acceleration and collision by the LHC at CERN is a collaborational effort as well as the detector operation, data collection, subsequent processing, calibration, and selection of physics objects. Support is acknowledged to ANPCyT, Argentina; YerPhI, Armenia; ARC, Australia; BMWFW and FWF, Austria; ANAS, Azerbaijan; SSTC, Belarus; CNPq and FAPESP, Brazil; NSERC, NRC and CFI, Canada; CERN; CONICYT, Chile; CAS, MOST and NSFC, China; COLCIENCIAS, Colombia; MSMT CR, MPO CR and VSC CR, Czech Republic; DNRF and DNSRC, Denmark; IN2P3-CNRS, CEA-DRF/IRFU, France; SRNSFG, Georgia; BMBF, HGF, and MPG, Germany; GSRT, Greece; RGC, Hong Kong SAR, China; ISF, I-CORE and Benoziyo Center, Israel; INFN, Italy; MEXT and JSPS, Japan; CNRST, Morocco; NWO, Netherlands; RCN, Norway; MNiSW and NCN, Poland; FCT, Portugal; MNE/IFA, Romania; MES of Russia and NRC KI, Russian Federation; JINR; MESTD, Serbia; MSSR, Slovakia; ARRS and MIZŠ, Slovenia; DST/NRF, South Africa; MINECO, Spain; SRC and Wallenberg Foundation, Sweden; SERI, SNSF and Cantons of Bern and Geneva, Switzerland; MOST, Taiwan; TAEK, Turkey; STFC, United Kingdom; DOE and NSF, United States of America. In addition, individual groups and members have received support from BCKDF, the Canada Council, CANARIE, CRC, Compute Canada, FQRNT, and the Ontario Innovation Trust, Canada; EPLANET, ERC, ERDF, FP7, Horizon 2020 and Marie Skłodowska-Curie Actions, European Union; Investissements d'Avenir Labex and Idex, ANR, Région Auvergne and Fondation Partager le Savoir, France; DFG and AvH Foundation, Germany; Herakleitos, Thales and Aristeia programmes co-financed by EU-ESF and the Greek NSRF; BSF, GIF and Minerva, Israel; BRF, Norway; CERCA Programme Generalitat de Catalunya, Generalitat Valenciana, Spain; the Royal Society and Leverhulme Trust, United Kingdom. The crucial computing support from all WLCG partners is acknowledged gratefully, in particular from CERN, the ATLAS Tier-1 facilities at TRIUMF (Canada), NDGF (Denmark, Norway, Sweden), CC-IN2P3 (France), KIT/GridKA (Germany), INFN-CNAF (Italy), NL-T1 (Netherlands), PIC (Spain), ASGC (Taiwan), RAL (UK) and BNL (USA), the Tier-2 facilities worldwide and large non-WLCG resource providers. Major contributors of computing resources are listed in Ref. [1].

The results presented in this dissertation led to the following **publications** by the ATLAS collaboration. The individual contributions by the author are summarised for each one.

[1] *Combination of the searches for pair-produced vector-like partners of the third-generation quarks at $\sqrt{s}$=13 TeV with the ATLAS detector*, ARXIV:1808.02343 (submitted to Phys. Rev. Lett.), *Aug 2018*

- Vector-like quark combination liason: Production of samples for overlap checks and input preparation for analyses combination on behalf of the analysis team that prepared the publication [2]

⟩ Chapters 13 and 14

[2] *Search for pair production of heavy vector-like quarks decaying to high-p_{T} W bosons and top quarks in the lepton-plus-jets final state in pp collisions at $\sqrt{s}$=13 TeV with the ATLAS detector*, J. HIGH ENERG. PHYS. 08 (2018) 048, *Aug 2018*

- Primary analyser
- Analysis design
- Designed BDT classifier and $B\bar{B}$ system reconstruction
- Statistical analysis and limit setting

- Sole responsible for internal documentation
- All contributions mentioned in [4]

⟩ Chapter 14

[3] *Measurements of top-quark pair differential cross-sections in the lepton+jets channel in pp collisions at $\sqrt{s}$=13 TeV using the ATLAS detector*, J. HIGH ENERG. PHYS. 10 (2017) 141, *Nov 2017*

- Development of RIVET routine for the boosted and resolved channel
- Provision of χ^2/p-value machinery used to quantify differential top-quark measurements (widely used by differential top-analyses and distributed as an official RIVET release in order to improve future data to theory comparisons)

⟩ Chapter 10

[4] *Search for pair production of heavy vector-like quarks decaying to high-p_{T} W bosons and b-quarks in the lepton-plus-jets final state in pp collisions at $\sqrt{s}$=13 TeV with the ATLAS detector*. J. HIGH ENERG. PHYS. (2017) 2017: 141., *Oct 2017*

- Development of VLQ single lepton software framework
- Preparation of high mass signal predictions for central sample production
- Management of sample production
- Major contribution to analysis strategy design
- Evaluation of background and signal yields, and systematic uncertainties
- Evaluation of different top-quark MC predictions and uncertainties
- Optimisation of event selection and object definitions
- Internal analysis documentation

⟩ Chapter 13

The author contributed to the following preliminary **public results** released by the ATLAS collaboration:

[5] *Search for pair production of heavy vector-like quarks decaying to high-p_T W bosons and b-quarks in the lepton-plus-jets final state in pp collisions at $\sqrt{s}$=13 TeV with the ATLAS detector*, ATLAS-CONF-2016-102, *Sep 2016*

– See [4]

– Design of resolved analysis channel event selection and discriminant determination

⟩ Chapter 14

[6] *Studies on top-quark Monte Carlo modelling for Top2016*, ATL-PHYS-PUB-TOPQ-2016-02, *Sep 2016*

– Development of first RIVET routines for differential top-quark measurements at 13 TeV serving as basis to evaluate the updated top-quark MC baseline employed by all ATLAS analyses relying on top-quark pair background or signal prediction

⟩ Chapter 10

[7] *Early Inner Detector Tracking Performance in the 2015 data at $\sqrt{s}$=13 TeV*, ATL-PHYS-PUB-2015-051, *Jul 2015*

– Residual ID mis-alignment corrections using resonant $Z \to \mu^+\mu^-$ decays

– First impact parameter resolution measurements at moderate to high transverse momenta using resonant $Z \to \mu^+\mu^-$ decays

⟩ Chapter 8

[8] *Alignment of the ATLAS Inner Detector with the initial LHC data at $\sqrt{s}$=13 TeV*, ATL-PHYS-PUB-2015-031, *Jul 2015*

– Alignment Performance Monitoring and ID mis-aligned geometry preparation

⟩ Chapter 8

[9] *Study of the mechanical stability of the ATLAS Insertable B-Layer*, ATL-INDET-PUB-2015-001, *Jun 2015*

– Quantification of impact of the observed bowing of the IBL on track parameters

⟩ Chapter 8

[10] *Evidence for the associated production of a vector boson (W, Z) and top-quark pair in the dilepton and trilepton channels in pp collision data at $\sqrt{s}$=8 TeV collected by the ATLAS detector at the LHC*, ATLAS-CONF-2014-03, *Jul 2014*

- Estimation and evaluation of signal models and corresponding systematic modelling uncertainties

The author contributed to a number of internal ATLAS documentations. One that isn't part of a publicly available document is:

[11] *Top-quark physics with 100 fb^{-1}: Summary of the 2017 ATLAS top-quark workshop*, ATL-COM-PHYS-2017-1055, *Jul 2017*

- Main editor for future plans on studies and measurements to improve top-quark modelling and the associated theoretical assessment

⟩ Chapter 10

Table of Contents

List of Tables

List of Figures

Glossary

ATLAS A Toroidal LHC ApparatuS.

BCID Bunch Crossing ID.

BDT Boosted Decision Tree.

BL Beam line.

BS Beam spot.

BSM Beyond the Standard Model of Particle Physics.

CERN European Organization for Nuclear Research.

CKM Cabibbo-Kobayashi-Maskawa.

CL Confidence Interval.

CMB Cosmic Microwave Background.

CMS Compact Muon Solenoid.

CR Control Region.

CSC Cathode Strips Chamber.

DAQ Data Acquisition System.

DGLAP Dokshitzer-Gribov-Lipatov-Altarelli-Parisi.

DIS Deep-inelastic scattering.

dof Degrees of freedom.

DR Diagram removal.

DS Diagram subtraction.

DT Decision Tree.

EC End cap.

ECAL Electromagnetic Calorimeter.

EM electromagnetic.

EW Electro-weak.

EWSB Electro-weak Symmetry Breaking.

FastSim Fast Simulation.

FCCC Flavour Changing Charged Current.

FCNC Flavor changing neutral currents.

FSR Final State Radiation.

FullSim Full Simulation.

FWHM Full Width Half Maximum.

GI Gini Index.

GR General Relativity.

GRL Good runs list.

HCAL Hadronic Calorimeter.

HEP High Energy Physics.

HLT High Level Trigger.

IBL Insertable B layer.

ID Inner Detector.

IP Impact parameter.

IR Infrared.

ISR Initial State Radiation.

JER Jet energy resolution.

JES Jet energy scale.

JVT Jet Vertex Tagger.

KK Kaluza-Klein.

L1 Level 1.

LCW Local cluster weighting.

LEP Large Electron Positron Collider.

LH Likelihood.

LHC Large Hadron Collider.

LLR Log-Likelihood Ratio.

LO leading-order.

LumiBlock Luminosity Block.

MC Monte Carlo.

MCS Multiple Coulomb Scattering.

MDT Monitored Drift Tube.

ME Matrix Element.

MIP Minimum ionising particle.

MLE Maximum Likelihood Estimator.

MM Matrix Method.

MPI Multi Parton Interaction.

MS Muon Spectrometer.

MVA Multivariate Analysis.

NLO next-to-leading-order.

NNLL next-to-next-to-leading logarithmic.

NNLO next-to-next-to-leading-order.

NP Nuisance Parameter.

PDF Parton Distribution Function.

pdf probability density function.

PMNS Pontecorvo-Maki-Nakagawa-Sakata.

PMT Photo Multiplier Tube.

POI Parameter of Interest.

pQCD perturbative QCD.

PS Parton Shower.

PV Primary vertex.

QCD Quantum Chromo Dynamics.

Rivet Robust Independent Validation of Experiment and Theory.

RoI Region of Interest.

RPC Resistive Plate Chamber.

SCT Semiconductor Tracker.

SLC SLAC Linear Collider.

SM Standard Model of Particle Physics.

SR Signal Region.

SUSY Supersymmetry.

TGC Thin Gap Chamber.

TMVA Toolkit for Multivariate Data Analysis.

TRT Transition Radiation Tracker.

TST Track soft term.

TTVA Track-to-vertex association.

UE Underlying event.

vev Vacuum expectation value.

VLB Vector-like B quark.

VLQ Vector-like quark.

VLT Vector-like T quark.

VLX Vector-like X quark.

VLY Vector-like Y quark.

WP Working Point.

Dedication

I dedicate this work to all positive humans I deem friends.

Chapter 1

Introduction

> Wir fühlen, dass selbst, wenn alle möglichen wissenschaftlichen Fragen beantwortet sind, unsere Lebensprobleme noch gar nicht berührt sind. Freilich bleibt dann eben keine Frage mehr; und eben dies ist die Antwort.
>
> *—Ludwig Wittgenstein: Logisch-Philosophische Abhandlung. Tractatus Logico Philosophicus. Frankfurt a.M.: Suhrkamp 1963*

The Standard Model of Particle Physics (SM) forms the basis of modern elementary particle physics. It incorporates the known elementary particles and describes their respective interactions. It is a very successful theory, in accurate agreement with the bulk of collected particle physics data and provides precise predictions. The last missing building block of the model was discovered in 2012, a boson referred to as the Higgs boson. The observed mass value of the Higgs boson, on the order of the electroweak scale, leads to questions that are unanswered by the SM. Radiative corrections to the bare mass of the Higgs boson result in an expected mass value consistent with the Planck scale, which is sixteen orders of magnitude higher than the electroweak scale. The dominant contributions to the radiative corrections stem from its coupling to the heaviest known elementary particle, the top-quark. The effect of the radiative corrections is mitigated by highly fine-tuned theory parameters in the SM. This provides consistency with the observed Higgs mass value. The necessity for the large fine-tuning contrasts a natural theory that exhibits parameters that are of the same order of magnitude and thus demand only little to no fine-tuning. The magnitude of necessary fine-tuning in the SM is seen as a hint to unknown principles potentially covered by more general theories that go beyond the SM. These are referred to as Beyond the Standard Model of Particle Physics (BSM) theories. Some of these theories predict the existence of heavy partners of the top-quark. The new particles provide a possible way to cancel the dominant contributions to those radiative corrections.

Some of these theories foresee extensions of the quark sector of the SM with heavy top-quark partners referred to as Vector-like quarks (VLQs). The SM can be extended simply by additional mass terms that, unlike the SM quarks, do not break local gauge invariance. This is due to the non-chiral nature of these particles. Both the mixing of these new particles with the SM particles and their coupling to the SM Higgs yield cancelations of the radiative corrections to the Higgs mass.

VLQs could be within the reach of the Large Hadron Collider (LHC). They provide a rich decay phenomenology resulting from their decay to SM particles such as the W, Z, or Higgs boson accompanied by a top- or bottom-quark. The predicted mass range of VLQs as well as their rich decay phenomenology provides the opportunity to probe a wide phase space and to search for abnormalities with regard to the SM expectations.

This dissertation summarises two searches for pair-produced VLQs with expected decays into W bosons and top- or bottom-quarks. The searches are based on a data set collected in 2015 and 2016 by the A Toroidal LHC ApparatuS (ATLAS) detector with particle collisions provided by the LHC. In addition, this dissertation provides an overview of work contributed by the author to support a successful data taking campaign and to provide a reliable description as well as uncertainty assessment of pair-produced top-quarks.

The dissertation is organised as follows: Part I introduces the theoretical framework necessary to provide background on the theoretical expectations forming the basis of the presented searches. It provides a short summary of key aspects of the SM, including a description of both its successes and limitations as well as BSM theories. In addition, quark sector extensions of the SM are discussed with main focus on VLQs and the description of their phenomenology. Part II introduces the experimental facilities used in order to allow for analysis of the collected data. Both the European Organization for Nuclear Research (CERN) accelerator complex including the LHC and the ATLAS experiment with its respective sub detector components are portrayed. Part III presents the methodology and tools to reconstruct and simulate particle collisions. Two main aspects are discussed in that part. First, the alignment of the Inner Detector (ID) of the ATLAS detector in particular with regard to the identification and mitigation of residual detector deformations is outlined. Second, the generation and simulation of predicted events is summarised, with main focus on the $t\bar{t}$ modelling and uncertainty assessment. Part IV contains the two VLQ searches. In this part, the first chapter discusses general aspects and commonalities between the searches. Chapter 13 summarises the search for Vector-like T quarks (VLTs) decaying into a W boson and a bottom-quarks, whereas Chapter 14 describes the search for Vector-like B quarks (VLBs) decaying into a W boson and a top-quark.

Part I

Theoretical Motivation

Chapter 2

The Standard Model of Particle Physics

The SM [2–7] is a local gauge invariant quantum field theory, combining quantum mechanics with relativity encompassing all known elementary particles and respective interactions. The former are represented by quantum fields and the latter induced as a consequence of the gauge symmetry $SU(3)_C \otimes SU(2)_L \otimes U(1)_Y$ forming a matrix representation. The elementary particles carry either integer or half-integer spin and are denoted as bosons and fermions respectively. Three families or generations of fermions are observed and comprised by up- and down type reflecting their respective electric charge differences. Two classes of fermions exist, leptons and quarks. Each fermion has an associated oppositely charged anti-particle. Gauge bosons are the force carriers and mediate interactions between fermions and themselves. Each symmetry group is associated with a conserved quantum number indicated by the indices and is expressed by a (special) unitary ($SU(N)$) $U(N)$ Lie group with ($N^2 - 1$) N^2 generators. The *colour* unbroken symmetry group $SU(3)_C$ acts on the gluon fields G^i_μ with $i = 1, \ldots, 8$. The unified and broken *electro-weak* symmetry group $SU(2)_L \otimes U(1)_Y$ acts on the additional gauge fields W^a_μ with $a = 1, 2, 3$ and B_μ as well as the scalar Higgs field, ϕ. The conserved quantum numbers are carried by the elementary particles indicating their interaction with the quantum fields. The *colour charge* C is carried by particles that interact with the *strong* force described by the $SU(3)_C$ symmetry group. Quarks and gluons can carry three colour charges, namely "red" (r),

Table 2.1: The fundamental interactions, theoretical framework, and associated gauge fields.

interaction	theoretical framework	gauge field
strong	Quantum Chromo Dynamics (QCD)	G^i_μ (8 total)
electro-weak	Electro-weak Theory	B_μ, W^a_μ (4 total)
gravity	General Relativity (GR)	h_μ

"green" (g) and "blue" (b). The index L corresponds to the *weak isospin* of the $SU(2)_L$ group and indicates that only left-chiral fermions interact with the weak force due to the $V-A$ structure of the weak current. The *hypercharge* Y relates the electric charge Q with the third component of the weak isospin, T_3, by $Q = T_3 + Y$ (Gell-Mann-Nishijima relation) and is associated to the $U(1)_Y$ symmetry group. T_3 is 1/2 (-1/2) for left-chiral up-type (down-type) fermions.

The fourth fundamental force, gravity is not incorporated in the SM since its interaction strength has no impact on the elementary particles at the energy scales of importance for the validity of the SM. Table 2.1 provides a summary of the fundamental interactions, the respective theoretical framework, and associated gauge fields.

Field content of the SM [8] The gauge fields form the basis for interactions with fermions. The fermionic matter fields of the SM are quarks (Q_L^i, u_R^i or d_R^i) and leptons (L_L^i or ℓ_R^i) with $i = 1, 2, 3$ indicating the three families or generations. A summary of the SM fermion content including their respective quantum numbers are provided in Table 2.2. The number of fermions is equal to the number of anti-fermions that have the same mass but opposite charge and weak isospin values. The quark doublet Q_L^i comprises an up- (u, c, t) and a down-type (d, s, b) quark which have a charge of either $q = +2/3$ or $q = -1/3$ in units of the elementary charge e. Each quark is a colour triplet which means that each quark flavour exists in three colours (r, g or b). Leptons are colourless and thus do not interact strongly but they have electroweak charges. The lepton doublet L_L^i, contains an electrically neutral neutrino and a charged lepton $q = -e$. Assuming the neutrinos to be massless, their chirality is always left-chiral. This results in the existence of only left-chiral weak isospin doublets L_L^i and right-chiral singlets ℓ_R^i. The electromagnetic current couples to left-chiral and right-chiral types, whereas the weak currents only couple to left-chiral states.

2.1 The SM Lagrangian

The SM theory is specified with the previously discussed symmetry structure and the quantum numbers for the gauge fields therein. It can be expressed in the following Lagrangian:

$$\mathscr{L}_{\mathrm{SM}} = \mathscr{L}_{\mathrm{SU(3)}} + \mathscr{L}_{\mathrm{SU(2)\otimes U(1)}} = \mathscr{L}_{\mathrm{gauge}} + \mathscr{L}_{\mathrm{matter}} + \mathscr{L}_{\mathrm{Higgs}} + \mathscr{L}_{\mathrm{Yukawa}}. \tag{2.1}$$

Table 2.2: The fields of the SM with a selection of their quantum numbers, weak hypercharge Y, the third component of the weak isospin T_3, the electric charge Q, and the colour.

fermions	fields	generation i 1	2	3	Y	T_3	Q $[e]$	colour
leptons	L_L^i	$\begin{pmatrix} \nu_e \\ e \end{pmatrix}_L$	$\begin{pmatrix} \nu_\mu \\ \mu \end{pmatrix}_L$	$\begin{pmatrix} \nu_\tau \\ \tau \end{pmatrix}_L$	-1/2 -1/2	+1/2 -1/2	0 -1	- -
	ℓ_R^i	e_R	μ_R	τ_R	-1	0	-1	-
quarks	Q_L^i	$\begin{pmatrix} u \\ d \end{pmatrix}_L$	$\begin{pmatrix} c \\ s \end{pmatrix}_L$	$\begin{pmatrix} t \\ b \end{pmatrix}_L$	+1/6 +1/6	+1/2 -1/2	+2/3 -1/3	r,g,b r,g,b
	u_R^i	u_R	c_R	t_R	+2/3	0	+2/3	r,g,b
	d_R^i	d_R	s_R	b_R	-1/3	0	-1/3	r,g,b

The gauge Lagrangian incorporates all field strength tensors, $F^{\mu\nu} \in \{G^{\mu\nu}, W^{\mu\nu}, B^{\mu\nu}\}$, for the gluon, weak and hypercharge gauge fields respectively:

$$\begin{gathered} G^i_{\mu\nu} = \partial_\mu G^i_\nu - \partial_\nu G^i_\mu - g_S f_{ijk} G^j_\mu G^k_\nu \\ \text{with } [\lambda^i, \lambda^j] = 2i f_{ijk} \lambda^k \text{ and } \lambda^i \text{ the Gell-Mann matrices (defined later),} \end{gathered} \tag{2.2}$$

$$\begin{gathered} W^a_{\mu\nu} = \partial_\mu W^a_\nu - \partial_\nu W^a_\mu - g \epsilon_{abc} W^b_\mu W^c_\nu \\ \text{with } \epsilon_{abc} \text{ the Levi-Civita symbol,} \end{gathered} \tag{2.3}$$

$$B_{\mu\nu} = \partial_\mu B_\nu - \partial_\nu B_\mu. \tag{2.4}$$

These terms include the kinetic energy of the gauge fields and their self interactions. The matter Lagrangian:

$$\mathscr{L}_{\text{matter}} = i\bar{Q}^i_L D^\mu \gamma_\mu Q^i_L + i\bar{u}^i_R D^\mu \gamma_\mu u^i_R + i\bar{d}^i_R D^\mu \gamma_\mu d^i_R \text{ (quark fields)} \tag{2.5}$$

$$+ i\bar{L}^i_L D^\mu \gamma_\mu L^i_L + i\bar{e}^i_R D^\mu \gamma_\mu e^i_R \text{ (lepton fields)} \tag{2.6}$$

contains the kinetic energy of the fermions and their interactions with the gauge fields expressed in the covariant derivatives, D^μ. The fermion fields are summarised in Table 2.2. The $L(R)$ indicates the left- (right-) chiral projection under $SU(2)$ transformations of the field given by $\Psi_{L(R)} = 1/2(1 \mp \gamma^5)\Psi$. Two example covariant derivatives for left-chiral $SU(2)$ quark doublets

Q_L^i, chosen for illustrative purpose on the basis that quarks interact with all the three gauge fields, are expressed as:

$$D^{\alpha}_{\mu\beta} = \partial_\mu \delta_{\alpha\beta} + i g_s G^i_\mu L^i_{\alpha\beta}$$
$$\text{with } L^i = \lambda_i/2 \text{ and } \alpha, \beta \in \{r, g, b\}, \tag{2.7}$$

$$D^L_\mu = \partial_\mu + \tfrac{i}{2} g \tau^a \cdot W^a_\mu + \tfrac{i}{6} g' B_\mu$$
$$\text{with } \tau^a \text{ the Pauli matrices and } Y = 1/6 \text{ and } T_3 = 1/2 \text{ for } Q^i_L. \tag{2.8}$$

A full list of covariant derivatives for fermions is provided in Ref. [7]. The three gauge couplings g_S, g and g' correspond to $SU(3)$, $SU(2)$, and $U(1)$ respectively. The coupling values evaluated at M_Z are $g_s \simeq 1$, $g \simeq 2/3$, and $g' \simeq 2/(3\sqrt{3})$.

The strong interaction The strong force is described by QCD. It is a non-Abelian gauge theory with a $SU(3)$ gauge group. The eight gluon fields G^i_μ ($N^2 - 1 = 8$ with $N = 3$) are called *gluons* (see Equation 2.2). The latter are electrically neutral, massless spin 1 bosons carrying bi-colour combinations (simultaneously colour and anti-colour) and thus exist in eight states forming a *colour octet*. The Lagrangian describing the strong interaction is:

$$\mathscr{L}_{\mathrm{SU(3)}} = \mathscr{L}_{\mathrm{gauge}} + \mathscr{L}_{\mathrm{matter}} = -\frac{1}{4} G^i_{\mu\nu} G^{i,\mu\nu} + \sum_r \bar{q}_{r\alpha} i D^{\mu\alpha}_\beta \gamma_\mu q^\beta_r, \tag{2.9}$$

where r indicates the quark flavour $q \in \{u, c, t, d, s, b\}$ with the colour indices α, β, and $D^{\mu\alpha}_\beta$ the gauge covariant derivative introduced in Equation 2.7. The group of rotations in the colour space is induced by the $SU(3)_C$ group and allows for eight generators, the 3×3 Gell-Mann matrices, λ^i, that transform the three colour components without changing the quark flavour through $U_{\alpha\beta} = \exp(i\theta(x)_i L^i)$ with θ expressing real number rotation angles. Three and four-point self interactions are induced by the G^2 term. The eight gluon fields transform as $G^i_\mu \to (G^i_\mu)' = G^i_\mu - 1/g_s \partial_\mu \theta(x)_i$. The colour transformations transform with a vector coupling in contrast to the weak interaction and connect only to fermions with colour (quarks) or gluons. Fermion mass terms are allowed by the $SU(3)_C$ group but violate gauge invariance under the $SU(2)_L$ transformation of the electro-weak part of the SM. The running of g_S behaves such that at low energies or large distances ($Q^2 \gg \Lambda \sim$1 GeV) the coupling strength is strong, whereas as high energies or small distances ($Q^2 \lesssim \Lambda$) the coupling strength decreases. The former is referred to as *confinement* where quarks form quantum states with compensating colour charges resulting in a net colour charge of zero whereas the latter is dubbed *asymptotic freedom*. In the latter regime, quarks can be treated as free particles and can be described by perturbative QCD (pQCD) [9, 10]. At low energy scales, QCD is non-perturbative and thus analytical calculations are limited (see Chapter 9.1). Colour neutral bound states comprised of two (three) quarks are denoted as *mesons* (*baryons*). More generally, bound states composed of quarks are referred to as *hadrons*.

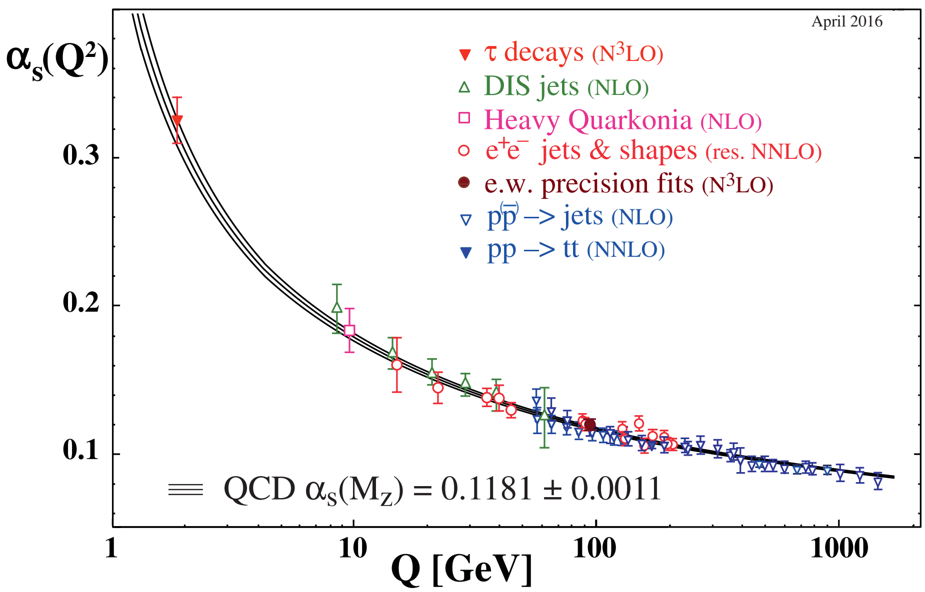

Figure 2.1: The running coupling $\alpha_S(Q) = {g_S(Q)^2}/{4\pi}$ theory prediction at a fixed probing scale $Q = M_Z$ and as a function of Q compared to precision measurements Q [11].

The weak interaction and spontaneous symmetry breaking The electro-weak force unifies the weak and electromagnetic interactions [2–4]. It is a non-Abelian gauge theory with gauge group $SU(2)_L \otimes U(1)_Y$. The four gauge fields W^a_μ and B_μ corresponding to the $SU(2)$ and $U(1)$ gauge group respectively, are massless. After Electro-weak Symmetry Breaking (EWSB), the latter fields mix into the mass eigenstates. The massive fields expressed as a linear combination of the four gauge fields are referred to as the massive $W^{\pm}$, Z^0 bosons and the massless γ (identified as the photon) which are the force carriers of the electro-weak force. The Lagrangian describing the electro-weak interaction is given by:

$$\mathscr{L}_{\mathrm{SU(2)\otimes U(1)}} = \mathscr{L}_{\mathrm{gauge}} + \mathscr{L}_{\mathrm{Higgs}} + \mathscr{L}_{\mathrm{matter}} + \mathscr{L}_{\mathrm{Yukawa}}. \tag{2.10}$$

The individual electro-weak Lagrangian parts will be discussed in the following. The gauge part is described by:

$$\mathscr{L}_{\mathrm{gauge}} = -\frac{1}{4} W^a_{\mu\nu} W^{a,\mu\nu} - \frac{1}{4} B_{\mu\nu} B^{\mu\nu}, \tag{2.11}$$

with the field strength tensors given in Equations (2.3) and (2.4). The W^2 terms impose three and four-point self-interactions due to the non-Abelian structure of $SU(2)$ whereas the B gauge field has no self interaction. The $SU(2)_L$ symmetry group constitutes a rotational symmetry group acting solely on left-chiral fermion fields due to the parity violating nature of the electro-weak interaction [12]. $U(1)$ transformations act on left- and right-chiral fermion fields and carry the previously discussed conserved quantum number hypercharge Y. Under $SU(2)\otimes U(1)$, each fermion field transforms as $U = \exp\left(i\Theta(x)_a T^a + iY\Phi(x)\right)$ with $T^a = {}^{\tau_a}/_2$ (0) for left-chiral (right-chiral) fermion fields with Θ and Φ expressing real number rotation angles. The three $SU(2)$ gauge fields transform as $W^a_\mu \to (W^a_\mu)' = W^a_\mu - {}^1/_g \partial_\mu \Theta(x)_a - \epsilon_{abc}\Theta(x)^b W^c_\mu$ (for $\Theta \ll 1$) and the $U(1)$ gauge field transforms as $B_\mu \to (B_\mu)' = B_\mu - {}^1/_{g'} \partial_\mu \Phi(x)$.

The next term is the scalar Higgs Lagrangian that depends on the Higgs potential $V(\phi^\dagger\phi)$ and provides the kinetic energy of the Higgs and its gauge interactions:

$$\mathscr{L}_{\mathrm{Higgs}} = (D^\mu\phi)^\dagger D_\mu\phi - V(\phi) \text{ with} \tag{2.12}$$

$$V(\phi) = \mu^2\phi^\dagger\phi + \lambda(\phi^\dagger\phi)^2 \text{ with } \phi = \begin{pmatrix} \phi^+ \\ \phi^0 \end{pmatrix} = \frac{1}{\sqrt{2}} \begin{pmatrix} \phi_1 - i\phi_2 \\ \phi_3 - i\phi_4 \end{pmatrix}. \tag{2.13}$$

The scalar Higgs field ϕ transforms as a $SU(2)$ doublet with the corresponding covariant derivative expressed in Equation 2.8 and carries $Y = {}^1/_2$. The Higgs field component ϕ^+ (ϕ^0) carries $Q = 1$ (0) and $T_3 = {}^1/_2$ ($-{}^1/_2$). The D^2 term leads to three and four-point interactions between the gauge and scalar fields.

The last term in the Lagrangian is the Yukawa term describing the interactions of the Higgs field with the fermions:

$$\mathscr{L}_{\mathrm{Yukawa}} = -\Gamma^{ij}_u \bar{Q}^i_L \tilde{\phi} u^j_R - \Gamma^{ij}_d \bar{Q}^i_L \phi d^j_R - \Gamma^{ij}_e \bar{L}^i_L \phi e^j_R + h.c. \tag{2.14}$$

with $\Gamma^{ij}_{u,d,e}$ matrices for different fermion generations that describe the Yukawa couplings between the Higgs doublet ϕ and different fermion flavours, and $\tilde{\phi} \equiv i\tau^2\phi^\dagger = \begin{pmatrix} \phi^{0\dagger} \\ -\phi^- \end{pmatrix}$. The latter choice is made to ensure that only one Higgs doublet is required in the SM in order to generate fermion masses for which $Y = \pm 1/2$ is needed.

Explicit mass terms for fermions of the form $-m_f \Psi\bar{\Psi}$ and gauge bosons are forbidden due to the imposed gauge invariance of the SM Lagrangian. Experimental observations showed that massive gauge bosons and fermions are realised in nature (see Section 2.2).

A mechanism is introduced that spontaneously breaks the $SU(2)_L \otimes U(1)_Y$ symmetry and results in mass terms while preserving gauge invariance. The structure of the Higgs potential given in Equation (2.13) is chosen on the basis of preserving both gauge and $SU(2) \otimes U(1)$ invariance. The form of the potential is given by the choices for μ^2 and λ which is the quartic coupling of the Higgs field. The case $\lambda < 0$ leads to an unstable vacuum which is considered unphysical. The idea behind the mechanism is that the lowest energy state, the vacuum state, does not respect the gauge symmetry which results in masses for particles that propagate through the vacuum. The Higgs potential can be rewritten as

$$V(\phi) = \frac{1}{2}\mu^2 \left(\sum_i^4 \phi_i^2 \right) + \frac{1}{4} \left(\sum_i^4 \phi_i^2 \right)^2 \tag{2.15}$$

in the Hermitian basis where $\phi = \phi^\dagger$ (see Equation 2.13) with $\mathbf{v} = \langle 0 \mid \phi \mid 0 \rangle$ a complex vector with Vacuum expectation values (vevs) of the complex scalar fields $\phi_i = 1, 2, 3, 4$. The basis of the four dimensional vector space can be chosen such that $\langle 0 \mid \phi_i \mid 0 \rangle = 0$ with $i = 1, 2, 4$ and $\langle 0 \mid \phi_3 \mid 0 \rangle \geq 0$ which results in:

$$V(\phi) \rightarrow V(v) = \frac{1}{2}\mu^2 v^2 + \frac{1}{4}\lambda v^4. \tag{2.16}$$

For $\lambda > 0$, two different potentials are established. In case $\mu^2 > 0$, the potential has a single minimum $V'(v) = 0$ at $v = 0$ with a vev of $\langle 0 \mid \phi_3 \mid 0 \rangle = 0$. This reflects the case at which $SU(2) \otimes U(1)$ is not broken. For $\mu^2 < 0$, the maximum at $v = 0$ is unstable and one additional solution to

$$V'(v) = v(\mu^2 + \lambda^2 v^2) = 0 \tag{2.17}$$

result in $|v| = (-\mu^2/\lambda)^{1/2}$ $(v \geq 0)$. The vev in the second case ($\mu^2 < 0$) replaces the Higgs doublet developed around its minimum ($\phi = v + \phi'$) such that $v \equiv \phi \simeq 1/\sqrt{2} \begin{pmatrix} 0 \\ v + H \end{pmatrix}$. No invariance is obtained applying $SU(2)$ transformations on v. Since the vev is electrical neutral ($Qv = 0$) $U(1)_Q$ is not broken. Thus, $SU(2) \otimes U(1)_Y \rightarrow U(1)_Q$ is spontaneously broken by choosing a particular form of the Higgs potential. In the unitary gauge, the kinetic term in Equation 2.12 after EWSB breaking can be written as:

$$(D^\mu \phi)^\dagger D_\mu \phi = \frac{1}{2}(0\ v)\left[\frac{g}{2}\tau^a W_\mu^a + \frac{g'}{2}B_\mu\right]^2 \begin{pmatrix} 0 \\ v \end{pmatrix} + H \text{ terms} \tag{2.18}$$

while omitting the kinetic energy and gauge interaction terms of the Higgs boson H. The Higgs self interaction terms are expressed in the Higgs potential term after EWSB in the unitary gauge. The previous Equation contains the following terms:

$$M_W^2 W^{+\mu} W_\mu^- + \frac{M_Z^2}{2} Z^\mu Z_\mu + H \text{ terms.} \tag{2.19}$$

The result of the spontaneous symmetry breaking are mass terms in the SM Lagrangian for the one (two) neutral (charged) gauge bosons Z^μ ($W^{\mu,\pm}$). The photon field A^μ is obtained through mixing with the four massless gauge bosons of the $SU(2) \otimes U(1)$ group:

$$W^{\mu,\pm} = \frac{1}{\sqrt{2}}\left(W_1^\mu \mp i W_2^\mu\right), \tag{2.20}$$

$$\begin{pmatrix} A^\mu \\ Z^\mu \end{pmatrix} = \begin{pmatrix} \cos\theta_W & \sin\theta_W \\ -\sin\theta_W & \cos\theta_W \end{pmatrix} \cdot \begin{pmatrix} B^\mu \\ W_3^\mu \end{pmatrix}, \tag{2.21}$$

where θ_W describes the Weinberg mixing angle ($\tan(\theta_W) \equiv g'/g$) that connects the masses of the weak gauge bosons. The coupling constants g and g' of the $SU(2)_L \times U(1)_Y$ define θ_W as follows:

$$\cos\theta_W = \frac{g}{\sqrt{g^2 + g'^2}}, \quad \sin\theta_W = \frac{g'}{\sqrt{g^2 + g'^2}}, \quad M_Z = \frac{M_W}{\cos\theta_W}. \tag{2.22}$$

The Weinberg angle θ_W has a measured value of $\sin^2\theta_W = 0.21316 \pm 0.00016$ [11]. The electric charge e can be expressed in terms of θ_W, $e = g\sin\theta_W = g'\cos\theta_W$. The vev can be expressed as $v \simeq (\sqrt{2}G_F)^{-1/2} \simeq 246$ GeV. The Fermi constant $G_F \sim g^2/8M_W^2 = 1/2v^2$ is obtained with its most precise experimental determination arising from the measurement of the muon lifetime [13]. The Higgs mass is obtained from the Higgs potential after EWSB. At leading order, it is given by $(m_H)_0 = (-\mu^2)^{1/2} = (2\lambda)^{1/2} v$ with the quartic coupling λ. Table 2.3 provides a summary of the fermion and boson masses and respective couplings to the Higgs potential after EWSB where applicable.

The photon is of neutral charge and couples only to charged fermions. The fields $W_{1,2}^\mu$ and thus the associated massive electromagnetically charged $W^\pm$ bosons couple only to left-chiral

Table 2.3: Fermion and boson masses and respective Higgs couplings, all in GeV [11].

			Quarks			
v coupling			$y_f \, v/\sqrt{2}$			
flavour	u	d	c	s	t	b
mass	0.0022	0.0047	1.28	0.96	173.1	4.18
			Leptons			
v coupling			$y_f \, v/\sqrt{2}$			
flavour	e	μ	τ		ν	
mass	$0.511 \cdot 10^{-3}$	0.106	1.777		0	
			Bosons			
	gluons	γ	$W^{\pm}$	Z^0	Higgs	
v coupling	0	0	$(g^2 v^2/4)^{1/2}$	$((g^2+g'^2)v^2/4)^{1/2}$	$(2\lambda)^{1/2} v$	
mass	0	0	80.39	91.19	125.09	

particles. The field B^μ couples to both left- and right-chiral fermions. Consequently, the same applies to the associated electromagnetically neutral Z^0 boson and photon γ, though with a different coupling strength for the Z^0. Due to the large mass of the electroweak gauge bosons, the weak force has only a limited range but is stronger than electromagnetism at high energies.

The weak charged current vertices are unique in the SM as they change the flavour of the left-chiral fermion fields. If an up-type quark u, defined in the mass eigenbasis, radiates a W^+, it turns into a down-type quark d' (the weak isospin partner of the up-type quark) in a weak eigenstate. The eigenstates of d'-type quarks are linear combinations of the mass eigenstates d. However, for the case of a non-vanishing rest mass of a particle, mass eigenstates and weak flavour eigenstates can be different. If the particles are not degenerate in mass, an allocation of different bases for the interaction and the mass is possible. This theoretical construct is called *mixing*. It is described by two unitary matrices. In the quark sector, it is known as the Cabibbo-Kobayashi-Maskawa (CKM) matrix V_{CKM} [14, 15]. The SM can be extended to incorporate massive neutrinos by adding an additional matrix referred to as the Pontecorvo-Maki-Nakagawa-Sakata (PMNS) matrix, U_{PMNS}, in the leptonic sector [16]. The CKM matrix generates a unitary transformation between different eigenstates. It satisfies $VV^\dagger = \mathbf{1}$ and is defined as follows:

$$\begin{pmatrix} d' \\ s' \\ b' \end{pmatrix} = \begin{pmatrix} V_{ud} & V_{cd} & V_{td} \\ V_{us} & V_{cs} & V_{ts} \\ V_{ub} & V_{cb} & V_{tb} \end{pmatrix} \cdot \begin{pmatrix} d \\ s \\ b \end{pmatrix} = V_{\text{CKM}} \cdot \begin{pmatrix} d \\ s \\ b \end{pmatrix}. \tag{2.23}$$

It acts on down-type quark mass-eigenstates by convention. It is constructed under the assumption that unitarity holds and only three quark generations exist in nature. The CKM matrix is determined by four parameters - three mixing angles and one complex CP-violating phase. This phase is the only known source for CP-violation in the SM [15]. Due to the fact that the mass eigenstates and the weak eigenstates do not coincide ($\mathbf{V} \neq \mathbf{1}$), transitions occur between the up- and down-type quarks within and across generations (Flavour Changing Charged Current (FCCC)). The neutral current couplings where the Z boson mediates the weak interaction are diagonal in both bases and no deviation in form of the observation of Flavor changing neutral currents (FCNC) has so far been observed [17].

Fermion mass terms As previously mentioned, $SU(2) \otimes U(1)$ acts only on left-chiral fermion fields. The Lagrangian term for the FCCC of a quark coupling to the W bosons is given by:

$$\mathscr{L}_{\text{CC}} = -\frac{g}{2\sqrt{2}} \left(J^{\mu-} W_{\mu}^{-} + J^{\mu+} W_{\mu}^{+} \right) \text{ with the weak-charge raising current} \tag{2.24}$$

$$J^{\mu+} = J_L^{+} + J_R^{+} \text{ with } \begin{cases} J_L^{+} = 2\bar{u}_L \gamma^{\mu} d_L = (\bar{u}\ \bar{c}\ \bar{t}) \gamma^{\mu} (1-\gamma^5) \begin{pmatrix} d \\ s \\ b \end{pmatrix} = \bar{u} \gamma^{\mu} (1-\gamma^5) d \\ J_R^{+} = \bar{u}_R \gamma^{\mu} d_R = 0 \end{cases} . \tag{2.25}$$

The weak-charge raising current has a pure $(V - A)$ structure which is maximally parity and charge violating but conserves CP. A fermion mass term in the Lagrangian would be of the form $-m_f \bar{\Psi}\Psi$ which, decomposed in its helicity states, can be written as:

$$-m_f \bar{\Psi}\Psi = -m_f \left(\bar{\Psi}_R + \bar{\Psi}_L \right) \left(\Psi_L + \Psi_R \right) \tag{2.26}$$

$$= -m_f \left(\bar{\Psi}_R \Psi_L + \bar{\Psi}_L \Psi_R \right), \text{ since } \bar{\Psi}_R \Psi_R = \bar{\Psi}_L \Psi_L = 0. \tag{2.27}$$

As previously mentioned, the left-chiral doublet $\Psi_L = L_L^i$ has $T_3 = 1/2$ and the right-chiral singlet $\Psi_R = \ell_R^i$ carries $T_3 = 0$ which breaks local gauge invariance under a $SU(2) \otimes U(1)$ transformation. A mass term for chiral fermions of the latter form is thus forbidden in the SM.

After EWSB Equation 2.14 results in the fermion masses obtained through coupling to the Higgs field:

$$\mathscr{L}_{\text{Yukawa}} = \bar{Q}_L^i (M_u^{ij} + h_u^{ij} H) u_R^j + (d, e) \text{ terms } + h.c., \tag{2.28}$$

with the fermion mass matrix $M_u^{ij} = \Gamma_u^{ij} v/\sqrt{2}$ and the Yukawa coupling matrix $h = M_u/v = gM^u/2M_W$ (only example terms are shown). The two terms in Equation 2.28 present the mass term for the up-type quarks and their coupling to the Higgs field. The corresponding fermion masses are $m_f = y_f/\sqrt{2}$. The higher the mass of a particle, the stronger it couples to the Higgs field through its respective Yukawa coupling, y_f.

2.2 Successes of the SM

The SM constitutes the most precise theory to date, accommodating experimental observations in elementary particle physics. Its predictive power is unparalleled and led to major discoveries throughout the late 20th and early 21st century. The discovery of the J/ψ [19, 20] was predicted by the SM in order to explain the absence of FCNC through the existence of the c quark. A third fermion generation was predicted and observed through the discovery of the b-quark [21], top-quark [22, 23], τ lepton [24] and ν_τ neutrino [25] allowing for a source of CP violation as a result of the CKM matrix [26]. The vector gauge bosons (W and Z) were discovered [27, 28] at the $Sp\bar{p}S$ collider and the accompanied properties precisely measured at the Large Electron Positron Collider (LEP), agreeing to a high precision with the SM predictions. Constraints from precision measurements led to predictions for particles discovered at a later stage. A particular example is the combined LEP and Tevatron Higgs boson mass limits [29] that restricted the allowed mass window for the Higgs boson, discovered independently by ATLAS and Compact Muon Solenoid (CMS) in 2012 [30, 31]. The SM has thus been and continues to be tested in a wide range of phase space and holds up to its high level of predictivity. Figure 2.2 provides a summary of representative SM total and fiducial production cross section measurements at $\sqrt{s} = 7,\ 8,$ and 13 TeV carried out by ATLAS.

2.3 SM Limitations

Not all physics phenomena can be explained within the SM despite it being remarkably successful in the precise description of the bulk of experimental particle physics data. The SM is

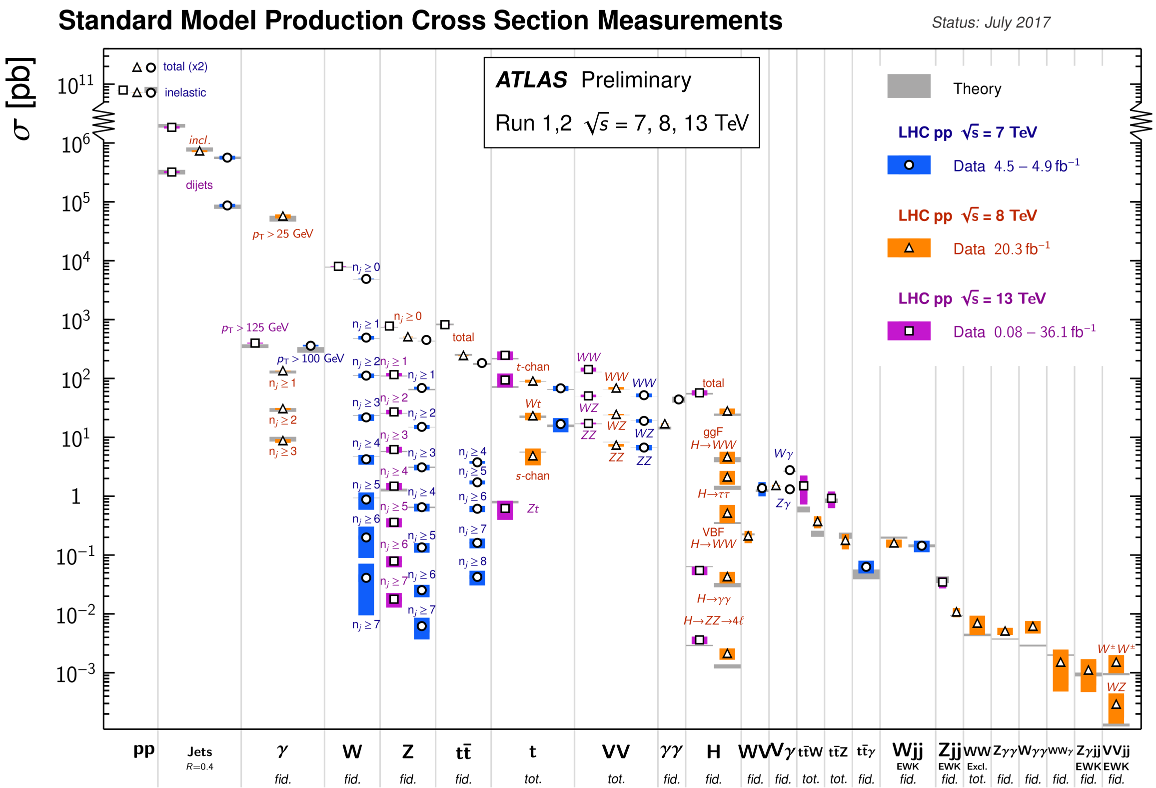

Figure 2.2: Summary of a representative set of total and fiducial production cross section measurements compared to the theory prediction at $\sqrt{s} = 7$, 8, and 13 TeV. All theoretical expectations were calculated at NLO or higher. Uncertainties for the theoretical predictions are quoted from the original ATLAS papers. They were not always evaluated using the same prescriptions for PDFs and scales. Not all measurements are statistically significant yet [18].

nowadays seen as an effective field theory valid at low energies, embedded in a generalised fundamental theory possibly explaining a wider spectrum of physics phenomena and observations. In order to obtain hints and constraints on the formulation of such a generalised theory, it is important to understand the successes as well as investigate the limitations of the SM.

One aspect that is not explained by the SM is the observed asymmetry between matter and antimatter. Although the CP violation in the SM is parametrised by one CP violating phase in the CKM matrix, its experimentally determined value it is not sufficiently large to account for the observed **baryon asymmetry** [32]. Rotational curve measurements [33] and gravitational lensing effects [34] are not explained by ordinary luminous matter alone. The elusive matter responsible for the observed deviations is called **dark matter**. This is also confirmed by large-scale structures and the Cosmic Microwave Background (CMB) [35, 36]. The new form of matter is expected to be weakly interacting and massive since it interacts gravitationally while withstanding direct detection. It constitutes ∼84% of the matter in the known universe according to the Standard Model of Cosmology [37, 38]. The SM does not predict the number of families of chiral fermions and the respective magnitude of the Yukawa couplings.

Neutrino masses are not directly measured but the observed neutrino oscillations [39] require a neutrino mass hierarchy. No mass term is present for neutrinos in the SM. However, the SM can be extended to account for their potential masses and mixing with other SM particles.

Without the inclusion of the free parameters needed to accommodate neutrinos, the SM exhibits 19 free parameters. These parameters are fitted to data from experimental measurements. Thirteen parameters comprise of the nine fermion Yukawa couplings (six quarks and three charged lepton couplings) and four parameters accompanied with the CKM matrix, namely three quark mixing angles and one phase. Three are the gauge group couplings of the strong, electromagnetic, and weak interaction. Two are related to the EWSB: the vev and the quartic coupling of the Higgs, λ. An additional free parameter, θ, scales with the amount of CP violation in QCD which is not observed yet (**the strong CP problem**). What is problematic with the parameter values is that they do not appear as *natural* and demand a high grade of *fine-tuning* in order to agree with observations. In particular, the wide spread of the fermion masses across $\mathcal{O}(\sim 10^5)$ leads to questions not answered by the SM. A *natural* theory exhibits parameters that are of the same order of magnitude and thus demand no to little fine-tuning to match the data. The amount of necessary fine-tuning in theories is seen as hinting at unknown principles covered by a more general and complete theory. The unification of the electroweak and strong interaction given by the SM gauge group (see Section 2) is foreseen to be unified in such a theory at higher energy scales since their respective gauge couplings scale as such. At energy scales on the order of the Planck scale, $M_P = (8\pi G)^{-1/2} \simeq 10^{18}$, quantum gravitational effects are expected to be not longer negligible and need to be accommodated within a generalised theory. In case of absence of observed new physics up to a certain scale, Λ, the SM has to be valid up to Λ, which introduces a problem referred to as the **hierarchy problem**.

Hierarchy problem In contrast to fermions and bosons that are protected against divergent mass corrections due to the chiral symmetry and gauge invariance respectively, scalar particles such as the Higgs boson are accompanied by unprotected radiative corrections to their mass. This in turn leads to the expectation of new physics phenomena close to the electro-weak scale if we want the assumption that the amount of necessary fine-tuning of the SM is small, $\mathscr{O}(\sim$few %) to be true. The larger Λ, the higher the amount of necessary fine-tuning. The Higgs mass squared is expressed as:

$$m_H^2 \sim (m_H)_0^2 + \Delta m_H^2 + \partial m_H^2 \tag{2.29}$$

with $(m_H)_0^2$ expressing the bare Higgs mass, Δm_H^2 the radiative corrections and ∂m_H^2 the mass counter term. The quadratically divergent radiative correction for a fermion loop is expressed as:

$$\Delta m_H^2 = -\frac{y_f^2}{16\pi^2}\left[2\Lambda^2 + \mathscr{O}\left(m_f^2 \ln\left(\Lambda/m_f\right)\right)\right], \tag{2.30}$$

with the fermion Yukawa coupling y_f, fermion flavour f and Λ the theory cut off scale parameter. At the scale of Λ, new physics phenomena enter and the effective SM is superseded by a more general theory. The top-quark loop corrections are the most significant contributions since $y_t = \sqrt{2}m_t/vev = 0.996 \pm 0.005$ for the world average top mass combination [40]. Thus the cancelation of the quadratic divergences stemming from y_t is of high importance to regulate the Higgs mass.

In case $\Lambda \simeq M_P$ and no cancellation due to new physics is present ($\partial m_H^2 = 0$) $m_H^2 \sim 10^{32}$. This disagrees by $\mathscr{O}(10^{30})$ with the measured Higgs mass and thus a hierarchy problem is introduced (denoted as the *big hierarchy problem*).

The dominant contributions to the radiative corrections of the Higgs mass stem from the top-quark ($-3/8\pi^2 y_t^2 \Lambda^2$), the $SU(2)$ gauge bosons ($9/64\pi^2 g^2 \Lambda^2$), and the Higgs boson ($1/16\pi^2 \lambda^2 \Lambda^2$) shown in Figure 2.3 at the one-loop level. All three diagrams are quadratically divergent. The

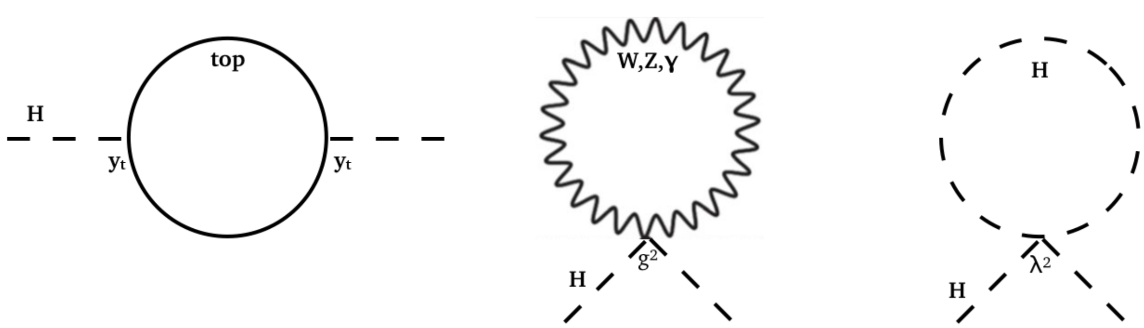

Figure 2.3: A subset of the dominant loop corrections to the Higgs mass from top-quarks (left), $SU(2)$ gauge bosons (middle), and the Higgs boson itself.

respective dominant contributions lead to radiative corrections of $-(2\text{ TeV})^2$, $(700\text{ GeV})^2$, and

(500 GeV)^2 for the top-quark, $SU(2)$ gauge boson, and Higgs loop, respectively assuming that the SM is valid up to Λ ∼10 TeV which roughly reflects the highest reach of the LHC (denoted as the *little hierarchy problem*). The amount of necessary fine-tuning needed in order to allow a theory to be natural can be used as a measure on when the loop corrections have to be cut off. Allowing a maximum fine-tuning of 10% yields a cut off at energy scales $\Lambda \lesssim 2, 5, 10$ TeV for the top-quark, $SU(2)$ gauge boson and Higgs boson loops, respectively. This led to the expectation for the discovery of new physics phenomena at the LHC since the SM is largely fine tuned at $\Lambda \sim 10$ TeV. New particles are thus expected to cancel the divergent loop corrections at the corresponding scales. If looking for cancellation, the top loop corrections suggest that new particles are expected with masses of up to 2 TeV. Such new particles need to couple to the Higgs in order to result in cancellation. For this cancellation to appear natural, the new particles need to have similar quantum properties as the top-quarks. This is realised by various theories suggesting new multiplets of coloured particles below 2 TeV in order to keep the Higgs mass at its measured value. Similar arguments apply for the $SU(2)$ gauge bosons and Higgs boson albeit with higher masses suggesting that additional hierarchy problems might occur [41].

Chapter 3

Theories beyond the SM

Theories attempting to address questions unanswered by the SM are plentiful. Of particular popularity are theories forecasting the existence of new particles within the energy reach of the LHC. This section gives a short overview of selected BSM theories.

Supersymmetry Supersymmetry (SUSY) [42] introduces an additional symmetry assigning to each fermion a bosonic partner. The additional bosonic states lead to a hierarchy problem solution through:

$$\partial m_H^2 = +\frac{y_S^2}{16\pi^2}\left[2\Lambda^2 + \mathcal{O}\left(m_S^2 \ln\left(\frac{\Lambda}{m_S}\right)\right)\right], \tag{3.1}$$

with m_S reflecting the mass of the bosonic partner S of the SM fermion leading to cancelation with Δm_H^2 as given in Equation 2.30. In case the Yukawa coupling of the bosonic partner, y_S, is of similar size to y_f, the Higgs mass is protected. If the bosonic partner is of similar mass SM fermion the logarithmic terms are small. However, the majority of SUSY mass limits disfavour small masses. The lightest supersymmetric particle is massive, stable, and weakly interacting, constituting a good candidate for dark matter.

Compositeness Historically, particles assumed previously to be elementary, i.e. to be point like, turned out to be composite, i.e. having some substructure that is connected by strongly bound constituents, as the experimental apparatus improved and higher energy scales were probed. Examples are the atom and hadrons. Some BSM theories build on this idea, postulating that elementary SM particles are actually composite states formed by bound constituents. The *composite Higgs model* assumes that the Higgs boson is a condensate of strongly interacting fermions accompanied by a mechanism referred to as *strong* EWSB through which a composite boson is produced, obtaining a vev at the TeV scale resulting in the observed SM Higgs at lower energy scales. Two particle sectors are described by the theory: The first is the SM and the second a composite sector encompassing the Higgs field and new heavy resonances above a composite scale. Mixing between the two sectors is imposed. The radiative corrections to the Higgs mass are only imposed up to the composite scale. *Composite top-quark models* assume that the top-quark is a condensate containing strongly coupled composite particles which mix with the SM sector [43–52]. The idea of compositeness was further developed in so called Little Higgs models [41, 53–55].

Extra dimensions The SM is embedded in a four dimensional space time. Extra dimensional models assume that our universe sits on a 4D-*brane* embedded in a multi dimensional space referred to as *bulk*. In some simple models, the only particle allowed to cross between the various spanned dimensions are *gravitons*, the hypothetical force mediators of gravity. The strength of gravity is diluted across the extra dimensions serving as an explanation why it is observed to be $\mathcal{O}(10^{32})$ weaker than the electro-weak force. Excitations of particles traveling through the extra dimensions manifest as Kaluza-Klein (KK) states in our brane. The latter are infinite modes referred to as *towers* which carry higher masses the farther they traverse through extra dimensions [56–58].

Chapter 4

Quark Sector Extensions to the SM

This chapter provides a motivation for quark sector extensions to the SM in order to account for new physics phenomena expected within the reach of the LHC. Particular focus is given to VLQs, particles that are good candidates to solve the hierarchy problem, canceling the most significant contributions stemming from top-quark loop corrections.

4.1 Motivation for Vector-like Quarks

The SM summarised in the previous chapter, incorporates three generations of chiral quarks and leptons. The extension of the SM by a fourth generation of chiral fermions (SM4) beyond the three SM generations is constrained by theory [59] to an upper mass bound of ∼600 GeV and excluded at the 5σ level by global fits to Higgs and electroweak precision data [60]. SM4 fermion masses are of non-decoupling nature[1] as they obtain their masses through Electroweak (EW) symmetry breaking and coupling to the evolved SM Higgs field. SM4 fermions would thus increase (decrease) the $gg \to H$ ($H \to \gamma\gamma$) production (decay) at leading-order (LO) by a factor of ∼9 (∼1/9) [61, 62] compared to SM fermion contributions alone which are ruled out by experiment [63]. Hence, we need to go beyond the SM4 fermions to extend the quark sector.

4.2 Vector-like Quarks

VLQs are hypothetical spin 1/2 fermions that transform as colour-triplets under $SU(3)_C$ to ensure a mixing with SM quarks. Their left- and right-handed components carry the same colour and transform the same under $SU(2)_L$ transformations [64] with several possibilities for their electro-weak quantum numbers as shown in Table 4.1. In Section 2.1, it was described that only the left-chiral fermionic matter fields interact through weak interactions since their right-chiral

[1]Decoupling results in vanishing loop contributions of particles with increasing masses.

Table 4.1: The fields of the SM with a selection of their quantum numbers, weak hypercharge Y, the third component of the weak isospin T_3, the electric charge Q and the colour [64, 65]. The L,R chirality subscripts are omitted.

Q [e]	SM quarks (generation i)	VLQs singlets		VLQs doublets			VLQs triplets	
$5/3$				X			X	
$2/3$	u c t	(T)		T	T		T	T
$-1/3$	d s b		(B)		B	B	B	B
$-4/3$						Y		Y
T_3	$u_L = 1/2$ $d_L = -1/2$ $u_R = d_R = 0$	0	0	$1/2$	$1/2$	$1/2$	1	1
$U(1)_Y$	$q_L = 1/6$ $u_R = 2/3$ $d_R = -1/3$	$2/3$	$-1/3$	$7/6$	$1/6$	$-5/6$	$2/3$	$-1/3$
$\mathscr{L}_Y$	$-\frac{y_u^i v}{\sqrt{2}}\bar{u}_L^i u_R^i$ $-\frac{y_d^i v}{\sqrt{2}}\bar{d}_L^i V_{\text{CKM}}^{i,j} d_R^j$	$-\frac{\lambda_u^i v}{\sqrt{2}}\bar{u}_L^i T_R$ $-\frac{\lambda_d^i v}{\sqrt{2}}\bar{d}_L^i B_R$		$-\frac{\lambda_u^i v}{\sqrt{2}}\bar{T}_L u_R^i$ $-\frac{\lambda_d^i v}{\sqrt{2}}\bar{B}_L d_R^i$			$-\frac{\lambda_i v}{\sqrt{2}}\bar{u}_L^i T_R$ $-\lambda_i v \bar{d}_L^i B_R$	
$\mathscr{L}_m$	forbidden	$-M\bar{\Psi}\Psi$						

counter parts carry no weak isospin ($T_3 = 0$) resulting in the V-A structure of the weak $SU(2)_L$ current described in Equation 2.25. VLQs in contrast are of non-chiral nature, which means that both the left- and right-chiral fields transform the same under $SU(2)_L$ transformations, allowing to add bare mass terms of the form $-M\bar{\Psi}\Psi$ (as described in Equation 2.27) to the SM Lagrangian, conserving local gauge invariance. Thus, the weak current in Equation 2.25 can be rewritten as:

$$J^{\mu,+} = J_L^+ + J_R^+ = \bar{u}_L\gamma^\mu d_L + \bar{u}_R\gamma^\mu d_R = \bar{u}\gamma^\mu d. \tag{4.1}$$

The weak current couples the VLQ fields via a vector coupling in contrast to the SM quark fields, hence the name. The coupling allows for FCNC, that change the flavour of the particle without altering its electric charge [66, 67], in addition to FCCCs. Decays of the VLQs into first and second quark generations are theoretically allowed but not favoured [68, 69] and suffer from far stronger constraints by experimental measurements than the decay into third generations [70]. The VLQ fields can manifest in different representations of $SU(2)_L$ and be assigned different hypercharge $U(1)_Y$ quantum numbers. The SM symmetry structure only allows for seven multiplets: two triplets, three doublets and two singlets [71]. As a result, the particle content of the extension of the SM contains only four additional species of quarks, T, B, and X, Y. The former two carry identical electric charges to their lighter SM partners, t and b (2/3 and −1/3, respectively), whereas the latter two exhibit exotic charges (5/3 and −4/3, respectively). The previously described mixing between SM and VLQs occurs for the left-handed SM quark sector with the singlet and triplet VLQ representations. For the doublet VLQ representation, mixing occurs with the right-handed SM quark sector (see Table 4.1). The mixing of VLQs and SM quarks to the SM Higgs will be denoted by the Yukawa coupling λ (see Equation 4.2) in contrast to the SM Yukawa couplings.

The VLQ states with more than one member share the same bare mass term. The mixing to SM quarks of the VLQs in the $SU(2)$ multiplets induces a mass splitting of the members in the same multiplet. This results in the following mass hierarchy $m_T \geq m_X, m_B \geq m_Y$ where m_T can either be larger or smaller than m_B. To be consistent with the results from precision electroweak measurements, a small mass splitting between VLQs belonging to the same $SU(2)$ multiplet is required. Cascade decays such as $T \to WB \to WWt$ are thus assumed to be kinematically forbidden. As a consequence, a VLQ will always be assumed in this dissertation to directly decay into a top or bottom-quark in addition to a Z, W, or SM Higgs boson. The VLQ models studied here are moreover restricted to obey $\mathscr{B}(T(B) \to Wb(t)) + \mathscr{B}(T(B) \to Ht(b)) + \mathscr{B}(T(B) \to Zt(b)) = 1$. The latter requirement can be extended for the presence of additional new particles by allowing VLQs mixing with additional new bosons that are too heavy to be directly produced at the LHC and could introduce additional interactions of the VLQs to SM particles [72].

Various BSM theories predict VLQs. An extended CKM matrix allows for extra phases and thus additional source of CP violation [73]. Little Higgs models predict a $SU(2)$ singlet coupling to the SM top-quark and thus lead to the regulation of the Higgs mass. $SU(2)$ singlet VLTs are predicted as KK excitations mixing to right handed top-quarks in the bulk. A $SU(2)$ VLB singlet is predicted in grand unification models incorporating an E_6 group [74]. The predicted VLQs in the grand unification and extra dimensional models are not expected to be observed within the reach of the LHC energy.

In addition, VLQs can be used to explain observed experimental deviations from SM expectations. An example is the observed A_{FB}^{b} [11] asymmetry at LEP. A possible explanation is obtained through mixing of the bottom-quarks to the $SU(2)$ $(B\ Y)$ doublet resulting in a modification of the $Zb\bar{b}$ coupling [75].

Higgs production and decay contributions Contributions to the leading SM Higgs production mode, $gg \to H$ fusion, do not necessarily emerge from new chiral particles with masses generated by the coupling to the SM Higgs field such as previously discussed SM4 fermions.

SM extensions with a new scalar field receiving a vev through the breaking of a new gauge symmetry can mix with the SM Higgs and lead to deviations of the expectations for the $gg \to H$ production of a SM Higgs boson. The latter can also be caused by new coloured VLQs that either mix or do not mix with SM fermions. In case mixing is imposed, modified SM calculations accommodate the mixing between VLQs and SM quarks through a Yukawa coupling to the SM Higgs which scales with the mixing angle, θ_L. The mass eigenstates will be a mixture of the VLQs and the SM quarks. In case no mixing is imposed, the SM calculations are unmodified and the VLQs do not contribute. A third case involves no mixing with SM fermions but VLQ mixing with a new scalar in which case the contributions arise from Yukawa coupling terms with the SM Higgs, the new scalar, or both [61].

The presented dissertation focuses on SM extensions of the quark sector with VLQs that preferentially mix with third generation SM quarks. This assumption becomes apparent by the mixing angle[2] that can be expressed as [72]

$$s_L \equiv \sin(\theta_L) \simeq \lambda_{3\Psi} \frac{v_H}{M_Q} \tag{4.2}$$

retaining only leading v_H/M_Q terms. The mixing angle, θ_L, between the SM and VLQ scales with the Yukawa coupling $\lambda_{3\Psi}$, the Higgs doublet $v_H = vev/\sqrt{2} \simeq 174$ GeV, and the VLQ mass, M_Q. The VLQ signal predictions in this dissertation assume $\cos(\theta_L) = 0.1$. The VLQ masses are not obtained by the EWSB and as a consequence, their impact on precision EW observables can decouple as their masses increase, particularly as their masses exceed the electroweak scale. This can directly be seen from Equation 4.2 in which s_L vanishes for $M_Q \to \infty$. The mixing angles are also constrained to be small by precision EW measurements performed at LEP and SLAC Linear Collider (SLC) constraining *oblique parameters* [64, 76]. These parameters are observables that combine electro-weak precision data in order to quantify deviations from the SM expectations. In addition, the mixing between the b-quark and a VLB modifies the $Zb\bar{b}$ coupling at tree-level [77].

[2] As example the mixing of a right-handed VLQ with the left-handed SM quark sector is illustrated.

The contributions of VLQs to the Higgs production and decay modes are suppressed by $\theta_{L,R}$ [78] if only one kind of VLQ exists. The largest expected deviations for VLQ models described in Section 4.2 stem from $H \to gg$ ($b\bar{b}$) with an expected deviation from SM predictions of about 5% (2.5%) [64]. Thus, in contrast to SM4 fermions, VLQs are still in agreement with the measured Higgs production and decay rates while regulating the quadratic divergences in m_H^2 (see Equation 2.29) arising from top-quark loop corrections as described in Section 2.3. Since no significant deviations from Higgs measurements with the current precision due to the existence of VLQs are expected, direct production is probed. A number of BSM theories predict the existence of VLQs which is further discussed in Section 4.2.

4.2.1 VLQ Production

In hadron collisions, the production of VLQs is predicted to occur either through their gauge couplings to gluons in the pair-production

$$gg, q\bar{q} \to Q\bar{Q} \text{ with } Q = T, B, X, Y, \tag{4.3}$$

or through weak-interaction in associated production with a weak boson or Higgs boson resulting in the production of a single VLQ in the final state. The latter is more model-dependent but can become the dominant production mechanism at high masses $m_Q = 1 - 1.5$ TeV [79].

Pair produced VLQs are the focus of this dissertation. For the pair production mode a narrow-width approximation is assumed resulting in dominant QCD production while suppressing electro-weak contributions. It is worth pointing out that a larger VLQ width impacts the coupling which might influence search results for $m_{\text{VLQ}} \gtrsim 1$ TeV as stated in Ref. [80]. A priori there is no prediction on the width of the VLQs.

To produce the $Q\bar{Q}$ pair at rest, the average momentum fraction, x, of the incoming protons is given by $x \sim {}^{2m_Q}/_{\sqrt{s}}$ which is 0.15 (0.25) for a center-of-mass energy of $\sqrt{s} = 13$ TeV ($\sqrt{s} = 8$ TeV) assuming $m_Q = 1$ TeV. The VLQs at $\sqrt{s} = 13$ TeV are produced at a sufficiently high x that the production is not dominated by the gluon PDFs, in contrast to $t\bar{t}$ pair production. For VLQ masses around 1 TeV, the leading contributions come from the up quark, gluon, and down quark with a relative contribution of ∼0.5, ∼0.32, and ∼0.22 respectively. Figure 4.1 illustrates the LO Feynman diagrams for the model-independent QCD pair production of VLQs.

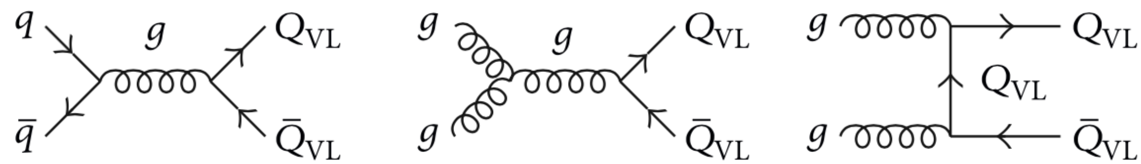

Figure 4.1: LO diagrams of the VLQ pair production for $q\bar{q}$ annihilation (first) and gg fusion (two to the right) [65].

4.2.2 VLQ Decay

The $SU(2)$ singlet up-type T quark with electric charge of 2/3 can not only decay into a W boson and b-quark but in addition to a Higgs or Z boson in association with a top-quark ($T \rightarrow Wb, Zt, Ht$).

Down-type B quarks of charge −1/3 can decay into a top-quark in associated production with a W boson and into a Higgs or Z boson with a b-quark ($B \rightarrow Wt, Zb, Hb$). The presented analyses are not sensitive to charge identification of the respective decay products and thus their charge indication is omitted for the remainder of the dissertation. The branching ratios to the different decay channels are dependent on the respective VLQ masses as well as the particular $SU(2)$ multiplet. A down-type B quark can decay to a Z or Higgs boson and a b-quark, in addition to decaying to a W boson and a top-quark ($B \rightarrow Wt$, Zb, and Hb). The branching ratio of a VLQ decay into a SM quark in the limit $m_{T(B)} \gg m_t + M_H$ is expressed as:

$$\mathscr{B}(T(B) \rightarrow Wb(t)) \simeq \frac{s_L^2 m_{T(B)}^3}{32\pi v_H^2} \text{ and} \tag{4.4}$$

$$\mathscr{B}(T(B) \rightarrow Zt(b)) = \mathscr{B}(T(B) \rightarrow Ht(b)) \simeq \frac{c_L^2}{2} \cdot \mathscr{B}(T(B) \rightarrow Wb(t)) \tag{4.5}$$

A more general description of the respective decay widths for all considered $SU(2)$ multiplets is given in Ref. [64]. In addition to the decay modes for the $SU(2)$ singlets described above, different decay modes apply for the $SU(2)$ doublets summarised in Table 4.2 and Figure 4.2. The different weak isospin properties of the $SU(2)$ doublets impose different couplings to the SM quarks. The $(T\ B)$ doublet is separated in three scenarios due to $m_T \simeq m_B$ characterised by their respective coupling strength to third generation quarks reflecting a matrix element in the extended 4×4 CKM matrix, V. Due to the measured mass hierarchy of SM quarks imposing $m_t \gg m_b$, the most natural assumption is $|V_{Tb}| \ll |V_{tB}|$ in which the VLB mixes more preferentially to the heavier SM quark leading to the decay modes summarised in Table 4.2. In

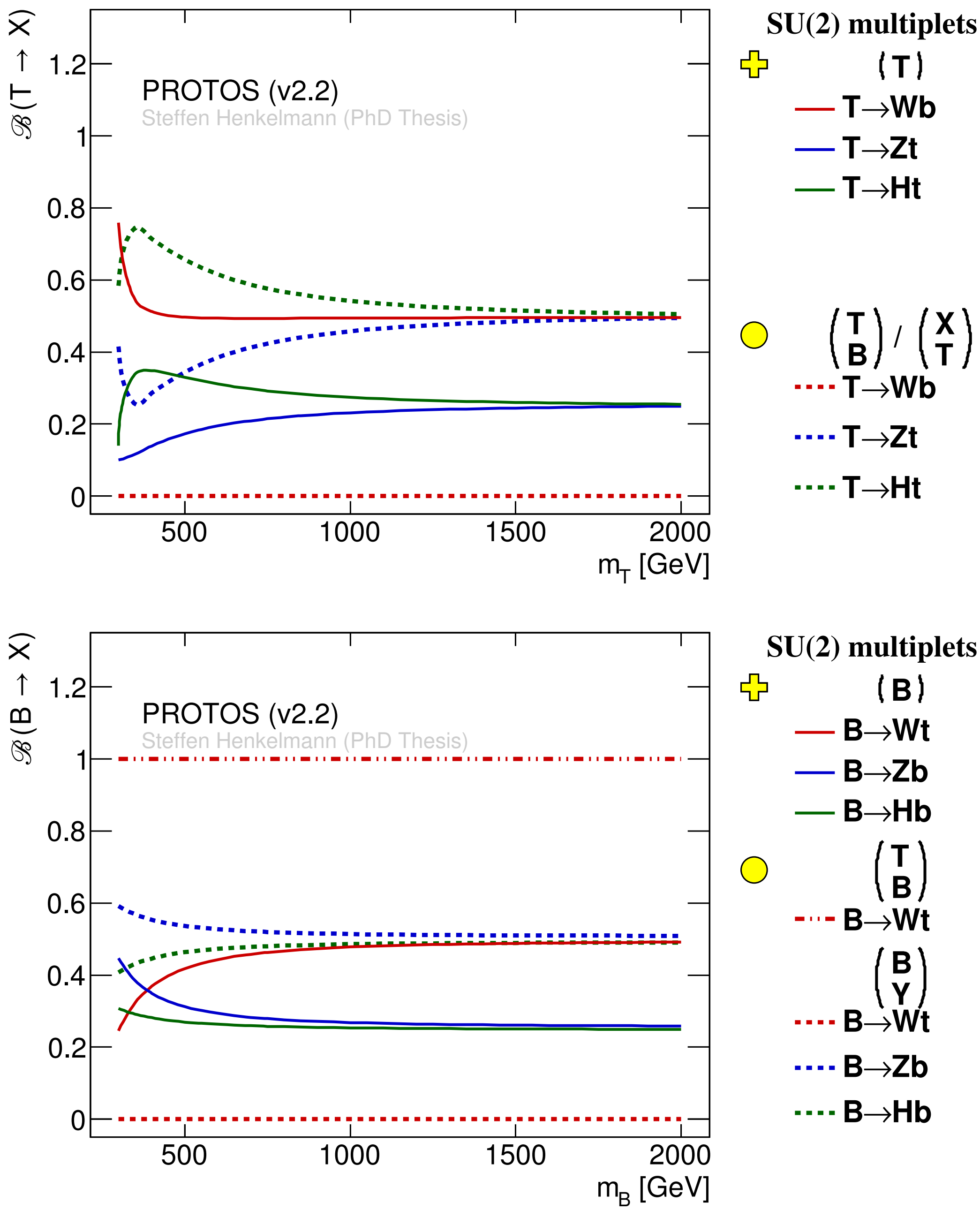

Figure 4.2: The expected branching ratios for the $SU(2)$ VLB and VLT singlet and doublet as function of mass. The yellow cross (dot) indicate the $SU(2)$ singlet (doublet) cases.

Table 4.2: The allowed decay modes for the members of the $SU(2)$ doublet and triplet. The subscripts L,R are omitted.

$SU(2)$ doublet	$\mathscr{B}$	$SU(2)$ triplet	$\mathscr{B}$
$\begin{pmatrix} X \\ T \end{pmatrix}$	Wt Ht, Zt	$\begin{pmatrix} X \\ T \\ B \end{pmatrix}$	Wt Wb, Ht, Zt Hb, Zb
$\begin{pmatrix} T \\ B \end{pmatrix}$	Ht, Zt Wt	$\begin{pmatrix} T \\ B \\ Y \end{pmatrix}$	Ht, Zt Wt, Hb, Zb Wb
$\begin{pmatrix} B \\ Y \end{pmatrix}$	Hb, Zb Wb		

case of $|V_{Tb}| \sim |V_{tB}|$, all three decay modes are allowed, whereas for $|V_{Tb}| \gg |V_{tB}|$, $T \to Wb$ and $B \to Z(H)b$ are possible. For the $(X\ T)$ doublet, the X with a charge of 5/3 can only decay to via FCCCs to up-type SM quarks, whereas the T decays to $H(Z)t$ assuming $m_X \simeq m_T$. For the $(B\ Y)$ doublet $(m_B \simeq m_Y)$, the Y with charge −4/3 can decay only to down-type SM quarks, with the B decaying to $Z(H)b$. The latter decay is similar to the scenario for the $(T\ B)$ doublet when assuming $|V_{Tb}| \gg |V_{tB}|$, which is not favoured though since this would imply $(m_b \gg m_t)$.

In summary, the $SU(2)$ singlet scenarios thus allow all three decays of the VLQs. For the $SU(2)$ $(T\ B)$ doublet in the natural case, assuming the observed SM quark mass hierarchy, the $T \to Wb$, $B \to Zb$, and $B \to Hb$ decays are not realised such that $\mathscr{B}(T \to Zt) \simeq \mathscr{B}(T \to Ht) \simeq 0.5$ and $\mathscr{B}(B \to Wt) = 1$. For both the T and B in the $(X\ T)$ and $(B\ Y)$ doublets, the FCCC are not realised leading to $\mathscr{B}(T \to Zt) \simeq \mathscr{B}(T \to Ht) \simeq 0.5$ and $\mathscr{B}(B \to Zb) \simeq \mathscr{B}(B \to Hb) \simeq 0.5$. The only allowed decays for the heavy quarks with anomalous charges 5/3 and −4/3 are $X \to W^+t$ and $Y \to W^-b$. For these anomalous charges, no explicit charge identification is imposed, the resulting experimental signatures are indistinguishable from FCCC decays $B \to Wt$ and $T \to Wb$, assuming $\mathscr{B}(B \to Wt) = 1$ and $\mathscr{B}(T \to Wb) = 1$, respectively [79]. Only minor kinematic differences of the decay products are expected as a result of the different weak isospin properties which are usually unresolvable given the precision of LHC analyses.

Part II

Experimental Facilities

This part describes the experimental facilities and apparatus used in order to provide and understand the collected collision data. Chapter 5 describes the most powerful particle accelerator constructed by human kind, the LHC. Chapter 6 summarises the ATLAS detector and its sub detector components used to collect the data analysed in preparation for this dissertation.

Chapter 5

The Large Hadron Collider

The LHC is part of a multi-purpose particle accelerator complex at CERN located near the city of Geneva in Switzerland. It is a 27 kilometre two-ring superconducting circular accelerator that collides proton or heavy-ion beams in opposing directions at previously unreached energies. With its pronounced circumference it crosses the border between two countries. After a planning and construction phase of around twenty years, the LHC began its operations in the Fall of 2009. The center-of-mass energy, initially at $\sqrt{s} = 7$ TeV during 2010-11, was increased in 2012 to $\sqrt{s} = 8$ TeV and to $\sqrt{s} = 13$ TeV in 2015. The data taking campaign between 2010 and 2012 is referred to as Run I. The LHC is designed for a center-of-mass energy of $\sqrt{s} = 14$ TeV and a luminosity of 10^{34} $\mathrm{cm}^{-2}\mathrm{s}^{-1}$, the latter of which was superseded during summer 2016. The data analysed in preparation for this dissertation was recorded at $\sqrt{s} = 13$ TeV during 2015 and 2016 as part of Run II of the LHC that will finish by the end of 2018.

5.1 The Accelerators and the Proton Beam

The protons are pre-accelerated before injection into the LHC. Figure 5.1 illustrates the accelerator complex at CERN. Hydrogen atoms are converted into protons by electron removal and are accelerated to an energy of 50 MeV in a linear collider (LINAC2). Afterwards, the Proton Synchrotron Booster accelerates the protons to an energy of 1.4 GeV. Up to 1.15×10^{11} protons are then grouped into proton bunches. The bunches are further accelerated in the Proton Synchrotron (PS) to an energy of up to 25 GeV. The PS can hold up to 72 bunches per fill. Either two, three, or four PS fills are injected in the Super Proton Synchrotron (SPS) where they are accelerated to the LHC injection energy of 450 GeV. Different filling schemes result in various proton bunch configurations. Twelve of the SPS fills are injected into each of the two beam pipes, most commonly resulting in a bunch separation of 50 ns or 25 ns. The latter beam configuration corresponds to 2808 bunches. After approximately 20 minutes of acceleration and beam optimisation the proton bunches are brought to collision at the center of each of the

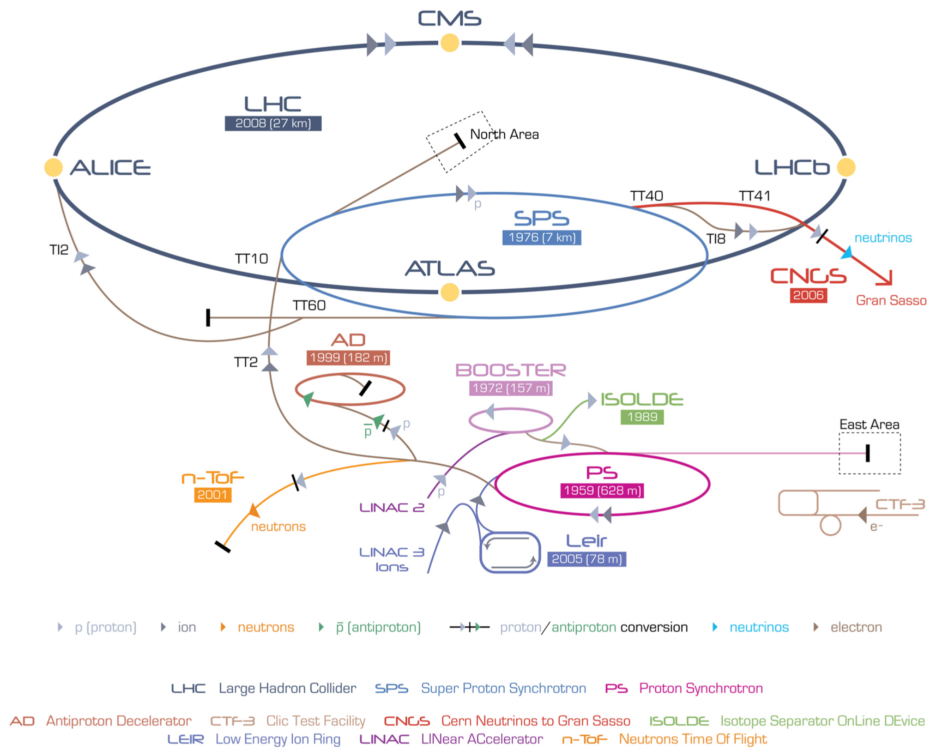

Figure 5.1: A sketch of the accelerator complex at CERN including the four experiments that are located at the LHC.

four experiments that are placed around the LHC accelerator ring, two of which are so-called multi purpose detectors – ATLAS and CMS. The ATLAS experiment collected the data analysed presented in this dissertation.

5.2 Luminosity and the LHC Run II Performance

The number of produced events is given by the time integrated product of the theoretical energy-dependent cross section (σ), and the instantaneous luminosity L, defined as:

$$L = f_{\text{rev}} n_B \frac{N_1 N_2}{4\pi\sigma_x\sigma_y}, \tag{5.1}$$

where n_B is the total number of injected bunches and $N_1(N_2)$ is the number of particles per bunch in ring 1(2). The revolution frequency is labeled as f_{rev} and σ_i is the so-called emittance that describes the beam spread defined in the position-momentum phase space in the horizontal and the vertical plane to the beam direction assuming Gaussian beam shapes. The time integrated luminosity is

$$\mathscr{L} = \int L \, \mathrm{dt} \tag{5.2}$$

and is generally defined in units of inverse *barns* (b) where $1b = 10^{-28}$ m^2. In addition to the proton-proton collision (pp) of interest, a number of other pp interactions occur during the recording of a single crossing of proton bunches that either originated from interacting neighbouring bunch crossings referred to as *out-of-time* pile-up or from multiple interactions within the same bunch crossing dubbed *in-time* pile-up. The former is present due to the read-out times of the sub-detector components which can be longer than the bunch spacing. The number of inelastic interactions of per bunch crossing follows a Poisson distribution with a mean value of μ, which is related to the instantaneous luminosity via

$$\mu = \frac{L\sigma_{\mathrm{inel}}}{n_b f_{\mathrm{rev}}}. \tag{5.3}$$

The value of μ decreases as a function of time while the beam intensity (emittance) decreases (increases) throughout a LHC run. The total inelastic pp cross section, σ_{inel}, increases with $\sqrt{s}$ and has a measured full phase space extrapolated value of 78.1 ± 2.9 mb at $\sqrt{s} = 13$ TeV [81] which is in agreement with theory predictions. The integrated luminosity as a function of the mean number of interactions per bunch crossings for the 2015 and 2016 data taking is illustrated in Figure 5.2.

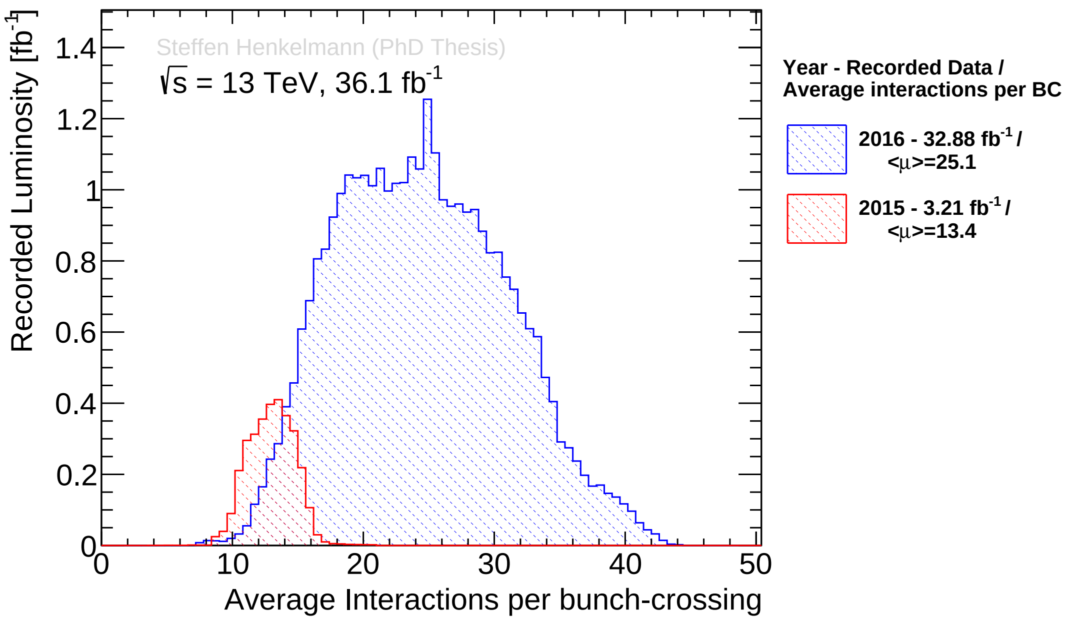

Figure 5.2: The integrated luminosity collected by ATLAS with all detector subsystems operational during stable beam conditions in 2015 and 2016 as function of the average interactions per bunch-crossing.

Chapter 6

The ATLAS Experiment

The ATLAS detector [82, 83] is one of the two multi-purpose detectors at the LHC. It has a cylindrical geometry which is forward-backward symmetric [84]. The design goal was to build a detector that covers a wide physics program with large coverage of the solid angle. Data at extremely high rates from pp and heavy ion collisions are recorded. The high LHC collision rates result in the need for radiation-hard electronics, as well as fast read-out systems including efficient trigger and Data Acquisition System (DAQ) systems. The high particle multiplicity requires a high-resolution particle identification and reconstruction system to enable searches for new physics while ensuring performance of precision measurements. It has a length of 44

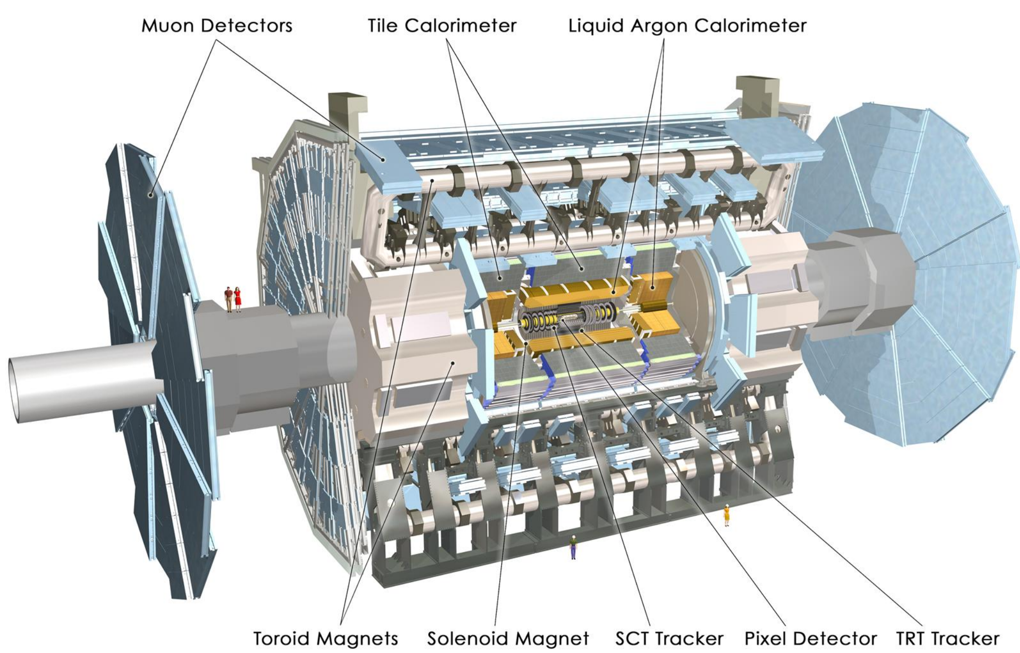

Figure 6.1: The profile of the ATLAS detector [85].

m, and a diameter of 25 m and a weight of ∼7000 t making it the largest detector at CERN. Figure 6.1 shows the ATLAS experiment with its solenoid and toroid magnets and the different sub detector systems that are arranged in an onion-shell-like structure surrounding the luminous beam interaction region. A brief summary of the main sub-detector systems – the ID, the calorimeters, the muon spectrometer, the magnet system, and the trigger and DAQ - is provided in Section 6.2. The global coordinate system and the definition of kinematic variables is given in Section 6.1.

6.1 The ATLAS Coordinate System and Kinematic Variables

The origin of the global coordinate system of the detector is set to its center. It is Cartesian and right-handed with its z-axis along the beam line. The x-axis points to the center of the LHC ring and the y-axis is aligned in the direction upward to the surface. The cylindrical coordinates (r, ϕ) are aligned in the transverse plane. The azimuthal angle $\phi \in [-\pi, \pi[$ is the angle around the beam pipe with $\tan(\phi) = y/x$. The pseudorapidity η is defined as $\eta \equiv -\ln[\tan(\theta/2)]$, where $\theta \in [0, \pi]$ is the polar angle. Distances between two objects are described by:

$$\Delta R = \sqrt{(\Delta\eta)^2 + (\Delta\phi)^2} \text{ or } \Delta R_y = \sqrt{(\Delta\eta)^2 + (\Delta y)^2}. \tag{6.1}$$

The rapidity y is defined as $y \equiv 1/2 \ln[\tan{(E+p_Z)}/{(E-p_Z)}]$, with y tending to η for vanishing particle masses. Differences in the rapidities are invariant under Lorentz transformations along the z-axis. The coverage of ATLAS goes up to $|\eta| < 4.9$. The z-component of the colliding parton's momenta is unknown which results in the definition of transverse kinematic variable properties. The transverse components are the projection of the kinematic properties onto the plane spanned by the x- and y-axis. The transverse kinematic variables associated with a reconstructed particle are defined as:

$$p_{\mathrm{T}} = \sqrt{p_x^2 + p_y^2} = p \cdot \sin(\theta) \text{ and } E_T = \sqrt{E_x^2 + E_y^2} = E \cdot \sin(\theta), \tag{6.2}$$

with the former (latter) describing the transverse momentum (energy). The transverse momentum and the transverse energy are identical in the relativistic limit. The missing transverse energy is defined as $E_{\mathrm{T}}^{\mathrm{miss}} = \sqrt{(E_x^{\mathrm{miss}})^2 + (E_y^{\mathrm{miss}})^2}$. $E_{\mathrm{T}}^{\mathrm{miss}}$ is the magnitude of the negative vector sum of the momenta of all particles present in an event (see Section 7.6).

Individual detector structures (components or modules) often use local right-handed Cartesian coordinate systems as reference frame with the origin defined at the center of the individual component (described in more detail in Section 6.2.1).

6.2 The Sub Detector Systems

The different sub detector systems are arranged within different layers as sketched in Figure 6.1 and detect interactions of different particle types. The performance requirements with regard to the energy and momentum resolution for the individual detector components as well as the η coverage of the respective components is shown in Table 6.1.

Detector components	Required resolution	η coverage Measurement	η coverage Trigger
Tracker	$\sigma_{p_T}/p_T = 0.05\%\ p_T \oplus 1\%$	± 2.5	
Electromagnetic Calorimeter (ECAL)	$\sigma_E/E = 10\%/\sqrt{E} \oplus 0.7\%$	± 3.2	± 2.5
Hadronic Calorimeter (HCAL):			
– barrel/End cap (EC)	$\sigma_E/E = 50\%/\sqrt{E} \oplus 3\%$	± 3.2	± 3.2
– forward	$\sigma_E/E = 100\%/\sqrt{E} \oplus 10\%$	$3.1 < \lvert\eta\rvert < 4.9$	$3.1 < \lvert\eta\rvert < 4.9$
Muon Spectrometer (MS)	$\sigma_{p_T}/p_T = 10\%$ at $p_T = 1$ TeV	± 2.7	± 2.4

Table 6.1: The general performance goals of the ATLAS detector. E and p_T are in GeV [86].

6.2.1 Inner Detector and Solenoid Magnet

The ID [87–89] consists of a silicon pixel detector, a silicon micro strip detector (SCT), and a Transition Radiation Tracker (TRT). The ID covers the region $|\eta| < 2.5$ and determines the charge and the momentum of the interacting particles. It is also used to perform vertex reconstruction for both primary collisions as well as reconstructing decays of heavy hadrons such as B and D hadrons. Charged particles are traced via the creation of electron-hole pairs in semiconductors or by ionising gas in the TRT. Fast response electronics, high radiation damage resistance with a minimal amount of material in order to reduce the degradation of energy measurements performed in the calorimeters were the primary design goals. All three subsystems are divided into one barrel and two ECs. A schematic visualisation of the barrel part of the ID is depicted in Figure 6.2. The barrel consists of several cylindrical layers of sensors while the ECs are composed of several discs or wheels of sensors. The next layer, at higher radius, is a thin superconducting **solenoid magnet** [90–92] with an axial magnetic field. It enables the measurement of charged particle momenta in the ID by curving their trajectories while passing through the detector. The axial magnetic field is parallel to the z-axis and bends particles in

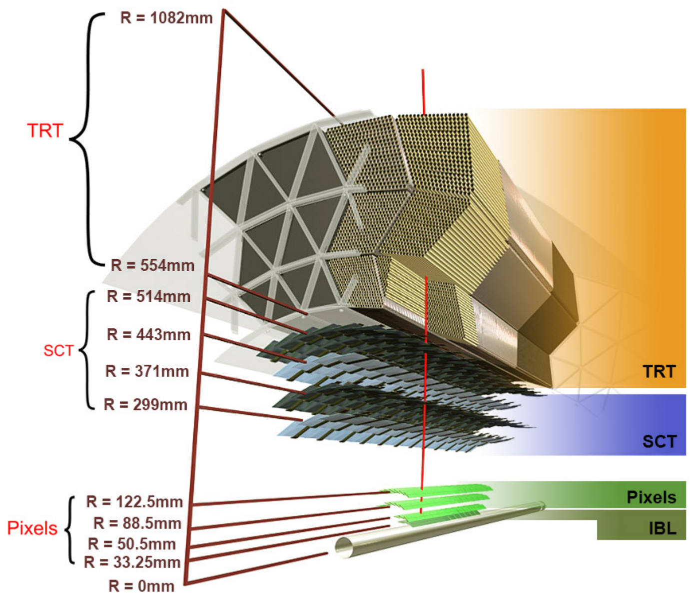

Figure 6.2: A schematic view of the ID barrel. The beam pipe, IBL, Pixel layers, the four cylindrical layers of the SCT, and the 72 straw layers of the TRT are shown [85].

the ϕ-direction. The magnetic field strength is 2 Tesla (T) at the center of the detector and remains constant towards the outer extent of the ID. The field strength is reduced towards the outer extent in the z-direction due to the finite size of the solenoid magnet in that direction. The long shutdown (LS1) that took place between 2013 and 2015 was used to replace the original beam-pipe with a new one with a reduced diameter allowing the insertion of an additional layer of pixel detectors in the barrel region, dubbed IBL [93]. It consists of 280 silicon pixel modules which are arranged on 14 carbon fibre staves arranged around the beam-pipe. Each stave is instrumented with 12 two chip planar modules ($|\eta| < 2.7$) and 4 single chip modules with 3D sensor technology at each end of the stave ($2.7 < |\eta| < 3.0$). The length of the IBL along the global z coordinate is 664 mm. The insertion of the IBL resulted in an improvement of the identification and reconstruction of secondary vertices such as expected from particles with a relatively long lifetime such as B-hadrons, that stem from the fragmentation of b-quarks.

The four pixel layers with a total coverage of $|\eta| < 2.5$ are located at the radii 33.2, 50.5, 88.5 and 122.5 mm, while the new beam pipe is located approximately at a radius of 24.3 mm. In the original pixel detector, the typical sensor dimensions in the pixel detector are 50 μm in the transverse direction and 400 μm in the longitudinal direction with a total number of 1744 pixel silicon modules arranged in three barrel layers and two ECs with three disks each. The pixels of the IBL have the same transverse dimension and a smaller longitudinal dimension of 250 μm. The expected hit resolution is 14 (8) μm in $r\phi$ and 115 (40) μm in z for the original pixel detector (IBL).

The SCT with a coverage of $|\eta| < 2.5$ consists of 4088 silicon strip modules arranged in four barrel layers and two ECs each encompassing nine wheels. Each strip module contains 768 micro strips that are mounted back-to-back, tilted by a stereo-angle of 40 mrad. As such, the crossing point of a traversing particles at both sides can be used to determine the 3D space point position at that measuring device unit. The channel size is 80 μm in transverse and 120 mm in longitudinal direction. The intrinsic resolution is $\sim$23 μm in $r\phi$ and $\sim$580 μm in z. The outermost sub-system of the ID is the TRT which is made of 350 848 gas-filled straw

Sub detector	Element size [μm]	Hits/track (barrel)	Intrinsic resolution [μm]	Radius barrel layers [mm]
IBL	50 ×250	1	8×40	33.2
Pixel	50 ×400	3	14×115	50.5, 88.5, 122.5
SCT	80 ×120 mm	4	23	299, 371, 443, 514
TRTs	4 mm	$\sim$ 30	170	from 554 to 1082

Table 6.2: The intrinsic resolution of the IBL and the Pixel is reported along $r\phi$ and z, while for SCT and TRT is only along $r\phi$. For SCT and TRT the element size refers to the spacing of the readout strips and the diameter of the straw tube, respectively.

tubes and has a channel size of 4 mm in transverse and 740 mm in longitudinal direction. The TRT enables tracking within $|\eta| < 2$. The transition radiation for traversing particles depends on the Lorentz factor $\gamma = E/m$ and is induced by polyethylene materials. The threshold of the TRT hit-signal amplitude depends on the amount of transition radiation induced. As such, particles with a higher γ have a higher number of high threshold hits. This probability is used to mainly distinguish electron (high threshold probability) and pions (low threshold probability) traversing the detector material. The single hit resolution along $r\phi$ is $\sim$170 μm.

The ID sub detector components, element dimensions, intrinsic resolution, and their respective radial distance from the ATLAS center are provided in Table 6.2. The precision of the three sub-detector components of the ID is comparable. The relatively lower intrinsic resolution of the TRT is recovered by both the high number of hits per track and the possibility of a longer track segment. A track with p_{T} =1 GeV (1 TeV) has a resolution of $\sim$1% ($\sim$50%).

Local Coordinate System The local coordinate system for individual detector modules of the ID is illustrated in Figure 6.3. The right-handed Cartesian coordinate system (x', y', z') is defined with respect to the center of the respective module. In the pixel and the SCT, the x' and

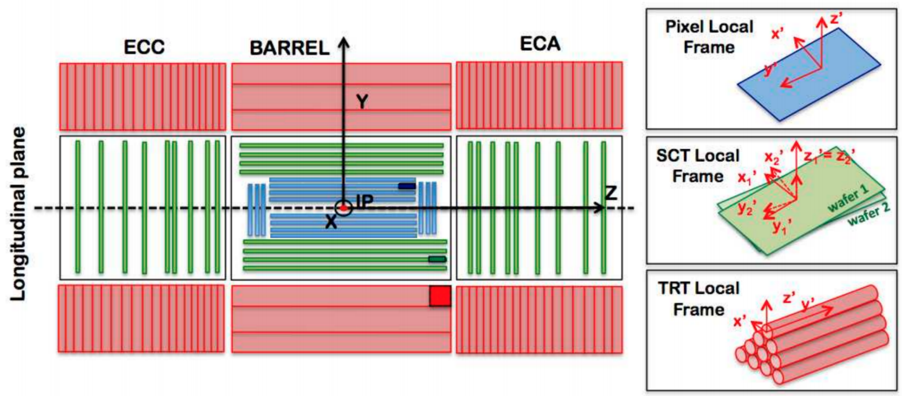

Figure 6.3: A schematic representation with the global ATLAS coordinate system of the longitudinal plane of the inner detector showing the Pixel layers and IBL (four innermost layers in blue), the SCT (green layers), and the TRT (red layers) on the left. The local system of coordinates on the corresponding sub detector components is shown on the right [94].

y' axes coincide with the module plane. The x'-axis points along the direction to which the module is performing the most precise measurements. For the pixel detectors this direction corresponds to the shorter pitch sides. It is perpendicular to the strip-orientation for the SCT modules. In the TRT modules and wires the z'-axis points along the wire. The x'-axis is perpendicular to both the wire direction and the radial direction. The latter is defined from the center of the global frame to the straw center. For all silicon detectors the y'-axis points along the long side of the module and the z'-axis is perpendicular to the local spanned (x'-y') plane. Hits are reconstructed in the local frame. For the SCT, the hit position needs to be extracted by combining two local coordinates since the SCT consists of double sided modules, each having an associated local frame. The radial distance of the tracks from the wire in the TRT is defined as $r = \sqrt{x'^2 + y'^2}$.

6.2.2 Calorimeters

The ID and solenoid magnet are surrounded by two types of calorimeters, namely the ECAL and the HCAL, covering the full range in ϕ and up to $|\eta| < 4.9$. Their purpose is to measure the energy and position of particles interacting with the detector material through full containment of their decay products within the volume of the respective calorimeter. The calorimeter has at least $22X_0(Z,A)^3$ ($24X_0$) radiation lengths of material in the barrel (EC). In addition, particle identification resulting in the discrimination between electrons, photons, and hadrons is performed. The detector material is comprised of alternating absorber and active materials. The former cause a high interaction rate of particles continuously losing energy while traversing through the calorimeter whereas the latter collect the charge of the induced particle spray (shower) that is proportional to the total energy deposited by the incident particle. Calorimeters of that kind are referred to as *sampling* calorimeters. The shower evolution is either of hadronic or electromagnetic nature. The average ratio of the respective shower components is a typical measure for sampling calorimeters. The central region has a high granularity resulting in precision measurements for electrons and photons. The forward and hadronic calorimeters have a coarser segmentation sufficient for precise determination of jet kinematics. The wide coverage of the solid angle ensures a good reconstruction of the missing transverse momentum in the event. The ECALs and the forward HCALs employ liquid argon as active material whereas the barrel and extended-barrel HCAL uses scintillating tiles. The liquid argon is cooled to a temperature of 88 K using two cryostats. The barrel ECAL shares a cryostat with the solenoid magnet. In the forward region another cryostat is shared between the EC and forward ECAL and the HCAL EC.

The energy resolution of the calorimeters follows Poisson statistics and is parametrised by:

$$\frac{\sigma_E}{E} = \frac{a}{\sqrt{E}} \oplus \frac{b}{E} \oplus c. \tag{6.3}$$

The first term covers basic phenomena in the shower evolution of the sampling calorimeter. Since those processes follow statistical fluctuations, the intrinsic limiting accuracy improves with increasing energy. The second component describes further effects that are due to instrumental effects such as noise and pile-up energy fluctuations. Its relative contribution to the energy resolution decreases with increasing energy. This term limits the low-energy performance of the detector. The last contribution, c, accounts for calibration errors, non-uniformities such as dead material in the detector, and limits the detector performance at high energies. The number of particles that are produced in the shower is proportional to the energy of the incoming particles. Thus, the energy resolution increases if the number of particles entering the

[3] The radiation length, X_0, is defined as mean distance that corresponds to the energy loss through Bremsstrahlung (pair creation) of a high energetic, electromagnetically interacting particle to $1/e$ ($7/9$) of its original energy. It is a function of the atomic number Z and the mass number A.

detector increases.

Electromagnetic calorimeter Photons and electrons form electromagnetic showers by interacting with the detector material via alternating pair creation and Bremsstrahlung effects (dominant for energies $\gtrsim 100$ MeV). The ECAL is a high-granularity lead/liquid Argon (LAr) sampling calorimeter [95, 96]. It measures the energy and the direction of electromagnetic showers with a pseudorapidity coverage of $|\eta| < 3.2$. The barrel coverage goes up to $|\eta| < 1.475$ and is separated by a 4 mm gap at $z = 0$. The ECs extend to $1.375 < |\eta| < 3.2$. The latter are divided into two coaxial wheels. A pre-sampler ($|\eta| < 1.8$) placed in front of the barrel ECAL determines the energy lost by the particle in the material before the calorimeter and has no absorber material. The lead plates serving as absorber material follow an accordion shape and extend towards the outer part of the calorimeter. The latter shape results in full symmetric ϕ coverage without any holes. The lead plates are connected to high voltage which results in charge collection of the ionisation electrons in the active detector material. The depth of the absorber material is a function of the pseudorapidity, so as to ensure that propagating particles with varying incident angles traverse the same amount of material. In addition to the variation of absorber material in the barrel, the depth of the liquid argon is varied in the radial position in the ECs. The ECAL barrel is divided into three longitudinal segments that differ in depth and cell structure defined in the plane spanned by η and ϕ. The first segment ($4.3X_0$) has a high granularity with $\Delta\eta \times \Delta\phi = 0.0031 \times 0.098$ readout strips resulting in a precise measurement of the pseudorapidity to ensure direction determination. A good discrimination between photons and pions is obtained. The second layer ($16X_0$) contains the bulk of the photon and electron shower products. A granularity unit is referred to as *tower* and is of size $\Delta\eta \times \Delta\phi = 0.025 \times 0.025$. The tower direction determination is used in the electromagnetic (EM) cluster formation (see Section 7.3). The majority of the EM shower is contained in 3×7 towers. The combination of the information of the first and second layer is used for the photon production vertex determination. The third layer ($2X_0$) has a coarser granularity with $\Delta\eta \times \Delta\phi = 0.05 \times 0.025$ towers. This layer provides additional information on *punch through* jets (see Section 7.5). Three different layers are also employed in the ECAL ECs. Figure 6.4(a) provides a schematic overview of the different ECAL layers for the barrel.

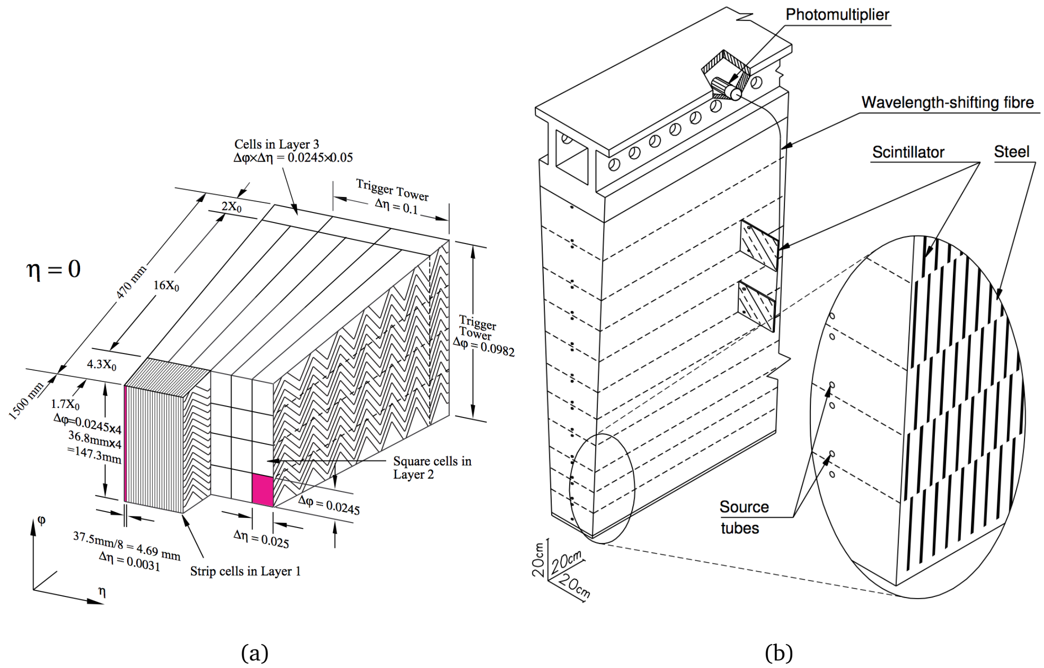

Figure 6.4: A schematic view of an ECAL barrel module in $\eta \times \phi$ showing cells in three different layers (left) and the mechanical assembly and optical readout of the tile calorimeter (right) [82].

Hadronic calorimeter The HCAL, located outside the radius of the ECAL, measures showers formed by hadrons. Different detector materials and technologies are used in different parts of the detector. Hadronic showers tend to have an extended shower profile in comparison to showers caused by electromagnetically interacting particles. Although hadrons will leave energy deposits already in the ECAL, the majority of energy is contained in the HCAL. Hadronic showers are the result of various interactions of the hadrons with the detector material. Hadrons either ionise the traversed matter or undergo nuclear interactions. The energy deposit by nuclear interactions, such as nuclear breakup or excitation, is not directly detectable. Such undetectable energy deposits are referred to as *invisible energy*. Hadronic showers have an electromagnetic shower component as a result of secondary hadron interactions, e.g. $\pi^0 \rightarrow \gamma\gamma$. The barrel and extended-barrel HCAL in the region $|\eta| < 1.7$ is referred to as the tile calorimeter. Figure 6.4(b) shows one tile calorimeter module. Instead of liquid argon, plastic scintillators are used as active material. The ultraviolet light emitted is collected by wavelength shifting fibre optics coupled to the steel tiles (absorber) and are read out by two Photo Multiplier Tubes (PMTs). The tile calorimeter measures the energy and direction of jets and isolated hadrons. It is segmented in three parts in the radial direction with varying hadronic interaction length,

λ. The latter defines the material length needed in order to fully absorb a strongly interacting particle and increases logarithmically with the particle's energy. The three components from nearest to farthest radial extent is 1.5, 4.1 and 1.8λ for the barrel ($|\eta| < 1.$) and 1.5, 2.6 and 3.3λ for the extended barrel ($0.8 < |\eta| < 1.7$). The barrel has 64 modules segmented in $\Delta\phi = 0.1$ rad. The $\Delta\eta$ separation is 0.1, 0.1 and 0.2 in the three components. The ECs of the HCAL ($1.5 < |\eta| < 3.2$) use copper as absorbing material and liquid argon as active material chosen due to its radiation resistance. Both ECs are comprised of two independent wheels. The respective granularity varied as a function of η. In the region $1.5 < |\eta| < 2.5$, the first two layers have segments of the size $\Delta\eta \times \Delta\phi = 0.1 \times 0.1$ and the third $\Delta\eta \times \Delta\phi = 0.2 \times 0.1$. For the region $2.5 < |\eta| < 3.2$ all layers have segments of size $\Delta\eta \times \Delta\phi = 0.2 \times 0.2$. The forward HCAL covers the forward region $3.1 < |\eta| < 4.9$ ensuring the good η coverage of the ATLAS detector to minimise unrecorded energy deposits and improve the $E_{\mathrm{T}}^{\mathrm{miss}}$ determination. It uses copper (tungsten) for EM (hadronic) shower sensitivity as absorber while employing liquid argon as active material.

6.2.3 Muon Spectrometer

The MS [97] surrounds the calorimeters and consists of three large superconducting air-core toroids [90, 98, 99], each with eight coils, a system of precision tracking chambers determining the muon momentum and position ($|\eta| < 2.7$) and fast tracking chambers for triggering (see Section 6.2.4). The toroid magnet system results in deflection of charged particles in the η direction. The three toroids are located in the central and two EC regions. The former (latter) produces a magnetic field of 3.9 (4.1) T in $|\eta| < 1.4$ ($1.6 < |\eta| < 2.7$). The magnetic field in the transition region ($1.4 < |\eta| < 1.6$) is a combination of the produced magnetic fields in the central and EC regions. Regions in which the magnetic fields cancel induce a poorer muon momentum resolution. The chosen toroid system configuration results in the provision of a magnetic field over a large volume, while maintaining only small material consumption. Since muons are Minimum ionising particles (MIPs), they are the only electrically charged particles that can pass through the calorimeters and reach the MS. The momentum resolution suffers from degradation if multiple scattering processes occur and improves when the applied magnet field is high. The muon chambers comprise four different sub-detector systems employed due to different needs with regard to position and momentum measurement on the one hand and triggering and timing measurements on the other. The four sub-detectors are: Monitored Drift

Tubes (MDTs), Cathode Strips Chambers (CSCs), Resistive Plate Chambers (RPCs), and Thin Gap Chambers (TGCs). In the barrel region three chambers are present with the first layer in front of the barrel toroid. Three layers are also present in the ECs.

Detection chambers MDTs (covering $|\eta| < 2.7$, with the exception of the innermost EC layer covering $|\eta| < 2.0$) are precision tracking chambers with thin aluminium drift tubes (400 μm) with a diameter of 3 cm and varying length between 0.9 and 6.2 m. A radial electric field is induced inside the tube by a 50 μm anode made of a tungsten-rhenium wire. The gas mixture is argon and carbon dioxide (93% and 7% respectively). Each chamber has a group of six or eight associated tubes. The high number of hits results in a reduction of mis-identified tracks. The momentum resolution achieved corresponds to 80 μm, 40 μm, and 30 μm for the individual tube, chamber, and three MDT layers of tubes, respectively. The precision coordinate η in the bending plane is determined. The maximum drift time is $\sim$700 ns.

At higher η, CSCs are used. They replace MDTs in the first layer of the MS EC region ($2.0 < |\eta| < 2.7$). Relative to the MDTs, the CSCs can cope with hit rates up to seven times higher. CSCs have the same gas mixture as the MDTs. They consist of two discs with eight chambers per disc. The multi-wire chambers have wires with a diameter of 30 μm which are oriented along the radial direction with a separation of 2.5 mm. Copper strips run perpendicular to the wires on one side of the cathode measuring the precision coordinate η (in the bending direction). Parallel oriented copper strips on the other side of the cathode provide the measurement of the transverse coordinate ϕ (in the non-bending direction). The resolution in the (non-) bending plane is (5 mm) 40 μm. The maximum drift time is 40 ns which is higher than the time between individual LHC bunch crossings.

Triggering chambers The drift times in the MDTs and CSCs are too long to resolve individual bunch crossings. Therefore, they are supplemented with trigger chambers. In the barrel (EC) region, parts of the MDT layers are supplemented by RPCs (TGCs) in $|\eta| < 1.05$ ($1.05 < |\eta| < 2.4$). RPCs perform a measurement of the ϕ coordinate with a 1 cm spatial resolution in addition to the MDT measurement of the η coordinate. The time resolution is 1 ns. TGCs also provide a measurement of the ϕ coordinate and provide a timing resolution of 5 ns with a spatial resolution of 1 mm. The timing resolution for the two trigger chamber technologies is sufficient to resolve individual bunch crossings and to provide the Level 1 (L1) trigger decision (see Section 6.2.4).

6.2.4 Trigger and Data Acquisition Systems

A multi-level trigger [100] and DAQ system is employed to perform real-time decision-making triggering on interesting event characteristics to keep or to discard an event. This is needed as the detector read out, information processing and storage is limited. The detector was designed to deal with high event rates of up to 40 million events per second which was exceeded for peak luminosities already in summer 2016. In Run II, a two level trigger system was added with increasing selection criteria imposed. The first level, L1, is hardware based and triggers on calorimeter and MS information. The latter are fast enough to be in sync with the Bunch Crossing ID (BCID) identifying uniquely each occurred bunch crossing. If an event passes L1, one or several Region of Interests (RoIs) are defined in η and ϕ indicating the presence of interesting event features. The High Level Trigger (HLT) is software based and incorporates all relevant sub-detector information to refine the measurement of the trigger candidate defined in the RoIs. The maximum frequency data can be recorded is limited by the bandwidth of writing to storage corresponding to 1 kHz. A trigger chain is defined as the sequence of selection criteria imposed on the different trigger levels. Pre-scales (P) are imposed in order to reduce the number of selected events for certain trigger chains. A pre-scaled trigger only fires $1/P$ times with P defined in advance based on the physics needs. Pre-scaled triggers are applied generally if the number of events expected exceeds the available bandwidth, or if the trigger is mostly used for calibration or other purposes not necessarily relying on a high statistics. The primary triggers used in most data analyses are not pre-scaled. The DAQ is configured for each run with a pre-defined trigger menu that constitutes a list of trigger chains and associated pre-scale values. Each run is divided into smaller time intervals denoted as Luminosity Blocks (LumiBlocks). The latter are generally on the order of one to two minutes and constitute the shortest time interval of data taking. During that defined time period, respective detector conditions are expected to be stable such that the DAQ can monitor the conditions without the necessity of a restart.

6.2.5 Data Quality

The recorded events are required to meet additional data quality requirements. The DAQ maintains a record of performance during a LumiBlock. The data quality procedure can be categorised into two stages. The first stage is the *online monitoring* in which online shifters decide in close to real-time if a subset of recorded and reconstructed events in a dedicated data stream, referred to as *express stream*, are in agreement with pre-defined reference data. This ensures an early alert system in case any detector related problems occur. This monitoring system consists of a set of histograms related to a variety of global event characteristics and physics object properties. The author provided the tools to perform the real time reconstruction of W, Z, and K_S^0 resonances with regard to the identification of potential ID movements to mitigate problems occurring during data taking as fast as possible and to reduce potential data losses in Run II. The online reconstruction of such *standard candles* is of particular interest since they depend on physics objects such as electrons and muons with their reconstruction relying on a good performance of many detector sub-systems. The second stage is denoted as *offline monitoring* in which additional data quality requirements are imposed on fully reconstructed events and detector and physics object calibrations relying on higher event statistics. The author contributed to the latter through monitoring of the ID alignment performance, offline Z boson reconstruction, and associated identification and mitigation of observed track parameter biases in the recorded data set. The reader is referred to Section 8.2.2 for details.

Different so called Good runs lists (GRLs) are defined which ensure that a combination of sub-detector components were fully or partially operational during the data taking period. Different analyses needs result in different GRL choices. The specific data quality requirements imposed for the two analyses presented in this dissertation are specified in Section 7.7.

Part III

Event Reconstruction and Modelling

The ATLAS detector introduced in the previous chapter is designed to collect maximal information about the high energy particle interactions. With the exception of the weakly interacting neutrinos, (quasi-) stable particles interact with the different detector parts. These are charged leptons, photons, and light hadrons (p, n, π, and K) and are directly detected.

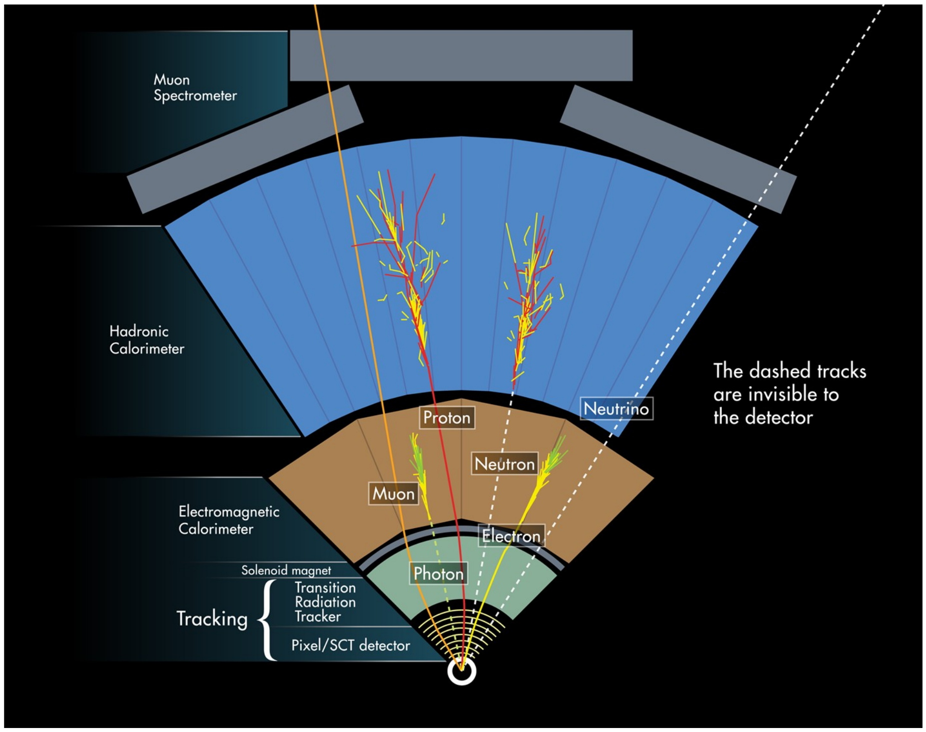

Figure 6.5: An illustration of different particles interactions with the detector material resulting in topologies that lead to particle identification [101].

Electrons, photons, and hadrons are detected in the calorimeters through energy deposition. Charged particles in addition leave curved traces while propagating through the detector components. They leave ionisation deposits detectable by active position-sensitive devices embedded in a magnetic field. The deposit detection along the particle's trajectory allows for its precise determination and hence the deduction of its momentum and sign of charge.

The output of the registered information constitutes electronic signals that demand correct interpretation, forming the first step of a staged offline reconstruction and identification of physics objects. The combination of these measurements form the second stage of the object reconstruction, resulting in constituents of these physics objects such as a reconstructed particle trajectory or energy cluster. In a third stage, the constituents are combined, exploiting the full detector response in order to identify a specific physics object.

This part of the dissertation describes in general terms both the reconstruction and identification of physics objects in Chapter 7 that are later used in the presented data analyses. Chapter 8 provides an insight into the alignment problem of the ID stemming from the determination of the actual position of detector elements. A particular focus is given to the identification and mitigation of associated track parameter biases. Chapter 9 gives an overview of the event modelling and the detector simulation of ATLAS. Chapter 10 summarises the Monte Carlo (MC) sample production providing an overview of event generators used in the presented analyses with a focus on the MC tuning and the modelling of top-quarks.

Chapter 7

Standard Object Reconstruction

This chapter describes reconstruction algorithms and methods used for the identification and uncertainty assessment of different physics objects using the collected information provided by the detector described in Chapter 6. Section 7.1 describes how the trajectory of charged particles traversing the ID are reconstructed as tracks. Section 7.2 provides an overview of the reconstruction and identification of interaction vertices. Both tracks and vertices are used for the reconstruction of electrons and muons that are discussed in Section 7.4. The reconstruction and identification of jets is discussed in Section 7.5. The reconstruction of the missing transverse energy related to the undetectable neutrinos is summarised in Section 7.6. Section 7.7 gives a list of data quality requirements that need to be fulfilled in order for an event to be considered in the presented analyses. The sections in this chapter focus on physics objects that are used in the analyses presented in Chapter 8 and in Part IV, namely electrons, muons and jets of varying sizes.

7.1 Tracks

A reconstructed charged particle trajectory is referred to as a "track". The track reconstruction is based on fitting a track model to a set of measurements following a sequential algorithm described in Ref. [102, 103]. The track model encompasses the parameters describing the track with respect to a global reference surface such as the perigee (distance of closest approach with respect to the origin of the detector or the primary vertex location). In the ATLAS software model, tracks are described by five parameters [104], namely

$$\tau = (d_0, z_0, \phi_0, \theta, q/p). \tag{7.1}$$

The first two represent the Impact parameter (IP) at the perigee, whereas the latter three are embedded in the global ATLAS frame and form a representation of the momentum. The impact parameter d_0 is the signed distance to the z-axis from the perigee. It is defined to be positive

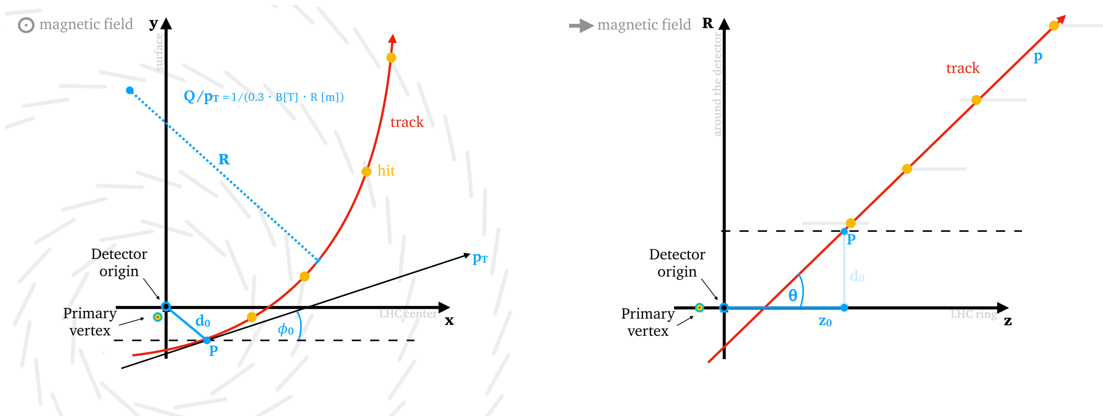

Figure 7.1: An illustration of the geometric definition of the track parameters in the $(x-y)$ plane (left) and the $(R-z)$ plane (right) with respect to different detector origin chosen as reference point. The track is shown by the red line and the detector hits are represented by yellow dots. The perigee is marked by the point P. The dimensions are arbitrary for illustration purposes.

in case the direction of the track is clockwise with respect to the origin. The impact parameter z_0 is the z coordinate of the perigee. The azimuthal angle ϕ_0 and θ of the track provide the momentum direction at the perigee. The ratio q/p is the inverse of the momentum of the particle multiplied by its charge. The projection of the momentum onto the $x-y$ plane is given by $p_{\mathrm{T}} = p \cdot \sin\theta$. Figure 7.1 illustrates the track parameters defined with respect to the perigee, using the detector origin as global reference point.

A brief overview of the iterative **track reconstruction** procedure is given in the following. Silicon detector hits are transformed into three-dimensional space points. Three of the space points at different layers are combined to form seeds for hit finding. This is performed in a defined window towards the outer radius of the SCT based on a simplified Kalman filtering approach [105] neglecting particle deflection effects caused by material interactions. This "*inside-out*" procedure defines a large track candidate collection including track candidates sharing hits and fake tracks.[4] The next sequence of the track reconstruction algorithm is the *Ambiguity solving* step which cleans the candidate track collection and resolves existent ambiguities (see later). As a first step, the track is iteratively refitted based on global minimisation of track-hit residuals incorporating material effects modelled by a set of scattering angles, θ, to account for Multiple Coulomb Scattering (MCS). The residual measurement vector of a track, $\mathbf{r}$ is given as

[4]Fake tracks are tracks for which the majority of associated measurements do not originate from a single particle.

$\mathbf{r} = \mathbf{m} - \mathbf{e}(\tau, \theta)$. The measurement vector $\mathbf{m}$ of the track is subtracted by the vector containing the expected track parameters and scattering angles at a measured surface, $\mathbf{e}$ according to the test track parameters τ. The track-fitting procedure yields the set of track parameters and scattering angles that minimise the following χ^2_{track}:

$$\chi^2_{\text{track}} = \mathbf{r}(\tau, \theta)^T V^{-1} \mathbf{r}(\tau, \theta). \tag{7.2}$$

The covariance matrix $V(\Omega, \Theta)$ is given by the uncertainty of the detector measurements, Ω and variance of the scattering expectation values $\hat{\theta}$, Θ that depends on particle momentum and the total material the particle propagated through [106]. In addition to the resulting χ^2_{track}, different quality criteria are used in order to rank each track based on a *reward-penalty* ranking [107]. The more hits associated to a single track, the higher the reward which ensures fully reconstructed tracks get selected preferentially over reconstructed tracks with short track segments. Precision hits such as pixel detector hits are assigned higher weight, penalising hits measured by less precise detection layers. Detection holes, that are defined as a track having no hit associated to a layer it traversed, result in penalisation. The $\ln(p_{\text{T}})$ of the track is used as a measure to reward high p_{T} tracks. The latter requirement helps to suppress tracks originating from incorrectly assigned combinations of layer measurements that tend to result in low p_{T} tracks. Hits that are shared between tracks are assigned to the track with a higher score. The remaining tracks are refitted with the previously shared hit removed. Through this iterative procedure, an updated track collection is formed. The next step is the TRT extension which extrapolates those tracks to the TRT and tests for compatibility with the observed hits. In order to collect tracks missed by the "*inside-out*" procedure, the final step of the track reconstruction is the "*outside-in*" procedure which is seeded in the TRT and extrapolated back ("back-tracking") to measured hits in the silicon detectors [103, 108–110].

The ATLAS *tight* track selection is defined as $p_{\text{T}} > 400$ MeV, $|\eta| < 2.5$, at least seven silicon hits, fewer than or equal to one shared module[5], fewer than or equal to two silicon holes, and in addition at least nine (eleven) silicon hits in $|\eta| \leq 1.65$ ($|\eta| > 1.65$), at least one hit on one of the two innermost pixel layers, and no pixel holes. The associated track reconstruction efficiency was assessed through matching simulated to detected information on the basis of the association of truth particle energy deposits to measured hits in bins of η and p_{T}. It is found to be ∼86% (∼63%) for $|\eta| \geq 0.1$ ($2.3 \leq |\eta| \leq 2.5$). An efficiency decrease is observed for $|\eta| >$

[5]A module hit represents at least two shared hits (one or more shared hits) in case of the SCT (pixel layer).

1.0 due to an increase of material that the particles traverse. An efficiency increase is observed for $|\eta| > 2.0$, which is due to the particle traversing more position-sensitive layers. The total uncertainty assessed through variations of the ID material composition in simulation is assessed and corresponds to ~0.5% (~2.7%) for $|\eta| \geq 0.1$ ($2.3 \leq |\eta| \leq 2.5$) [110]. Tracks are the basis for the following described physics objects, though slight variations on the track selection are used to ensure optimal performance.

The IP resolution is assessed and corrected for simulation in bins of η and p_{T}. For low p_{T} tracks, material effects are of higher importance for the efficiency, whereas for moderate to high-p_{T} tracks, residual mis-alignment of the ID position-sensitive devices is more important. For moderate to high p_{T}, the d_0(z_0) resolution varies from ~10 μm for 30 GeV tracks to ~8 μm for 100 GeV (~70 μm for 30 GeV and above) [109].

7.2 Vertices

Vertices denote the location of particle interactions during a bunch crossing in the detector. Tracks are associated to a given vertex. A collection of at least two reconstructed tracks serve as input for the **vertex reconstruction** which can be divided into two stages: the vertex finding and fitting [111, 112].

The vertex finding associates selected tracks (fulfilling a slightly looser selection compared to the previously introduced tight track selection) to a vertex candidate seeded by the beam spot. The beam spot is defined as the luminous region of hard interactions defined by a likelihood fit of a data sample with reconstructed Primary vertices (PVs) fulfilling the requirement of having with at least five associated tracks. If more than one such vertex exists, the one with the highest $\sum p_{\mathrm{T}}^2$ of associated tracks is used as the PV. The mean beam spot width was $\sigma_x = 15\ \mu m$ and $\sigma_y = 19\ \mu m$ ($\sigma_x = 9\ \mu m$ and $\sigma_y = 8\ \mu m$) in the transverse plane and $\sigma_z = 44$ mm ($\sigma_z = 34$ mm) in z-direction integrated for all data runs in 2015 (2016). The transverse width depends on the beam focus near the interaction region described by the minimum of the β function, $\beta^\star$, and the emittance (see Section 5.2). The beam spot width in the z-direction depends on the length of the bunches as well as the bunch crossing angle.

An iterative fitting procedure is used in order to determine the best fit to the vertex position. The fit procedure iteratively downgrades weights of associated tracks as a measure for their compatibility with a certain vertex. After fit convergence is controlled by an annealing procedure [113], tracks tagged as incompatible ($> 7\sigma$) with the located vertex are considered for the next vertex fit. This procedure is repeated until all tracks are associated or no additional vertex is found with the remaining tracks.

The vertex reconstruction efficiency as a function of the number of associated tracks steeply increases from two tracks with an vertex efficiency of ∼86% to ∼98% with four associated tracks. The vertex resolution depends on multiple scattering, energy losses due to ionisation of charge particles with detector material, and residual ID mis-alignments. The resolution in the transverse plane is ∼150 μm for two to four tracks and decreases to ∼20 μm above associated 25 tracks. The resolution in z is ∼330 μm for two to four tracks and decreases to ∼35 μ m above 25 tracks [114]. All other vertices are expected to originate from pile-up events or the decay of secondary particles.

7.3 Energy Clusters

Particles propagating through the calorimeter deposit fractions of their energy in a number of calorimeter cells. Energy clusters are the output of dedicated clustering algorithms [115] that group cells with energy deposits. The total collected energy in a cluster is calibrated depending on the incoming particle type to account for dead material and energy that is deposited outside the resulting cluster. The reconstruction of jets (electrons and photons) depends on topological clusters (EM clusters) whose measured calorimeter energy is calibrated to the EM scale [116] that correctly measures the energy deposited by electromagnetic showers (see later).

EM clusters ("towers") are the result of an algorithm denoted as *sliding-window* algorithm. Cells within a rectangular shaped window are summed and the window center position is iteratively adjusted until the contained deposited transverse energy, E_{T}, in all longitudinal layers is maximal. The starting point for the algorithm are 3×5 calorimeter segments out of an initial grid spanned by $N_\eta \times N_\phi = 200 \times 256$ segments of size $\Delta\eta \times \Delta\phi = 0.025 \times 0.025$. The chosen calorimeter segment matches the granularity of the second EM calorimeter layer and the resulting EM towers are dubbed as *pre-clusters*.

Topological clusters, *topoclusters*, are the output of a topological algorithm that is optimised with regard to suppressing noise in reconstructed clusters with a large number of cells. The idea is to iteratively group neighbouring cells in three dimensions with energy deposits exceeding the expected noise defined by the energy significance (signal-to-noise ratio). In contrast to the towers, the topoclusters can have a varying number of cells. The topological cluster algorithm is designed to follow the shower development of a single interacting particle [117].

7.4 Charged Leptons

This section describes the reconstruction and identification of charged leptons. Only electrons and muons will be discussed since both of the presented analyses do not explicitly select τ-leptons. However, the leptonic decay products of the latter can contribute to the reconstruction of isolated electrons or muons. The VLQ signal topologies considered mostly result in a single high-p_{T} charged lepton in each event.

7.4.1 Electrons

The **electron reconstruction** relies on the presence of an EM cluster that is topologically matched to a reconstructed ID track requiring the track to be compatible with the PV through Track-to-vertex association (TTVA) with the requirement $\left|\Delta z_0^{\mathrm{BL}} \sin\theta\right| < 0.5$ mm and $|d_0^{\mathrm{BL}}/\sigma(d_0^{\mathrm{BL}})| < 5$. The latter requirements decrease the contamination from secondary interactions. The IP parameters are defined with respect to the Beam line (BL) (defined by the Beam spot (BS)). The latter definition is chosen due to the smaller size of the transverse beam spot size with respect to the vertex position resolution obtained with track information. $\Delta z_0^{\mathrm{BL}} = z_0^{\mathrm{track}} + z^{\mathrm{BS}} - z^{\mathrm{vertex}}$ is used for compatibility of the track with a given vertex (the PV in this case) and the multiplication by $\sin\theta$ ensures acceptance for tracks in the forward region that have large expected uncertainties. $\sigma(d_0^{\mathrm{BL}})$ represents the estimated uncertainty of the d_0 parameter. The track association to the EM pre-cluster checks if a track, extrapolated from its last measurement in the ID volume to the second layer of the EM calorimeter, coincides with the pre-cluster seed position within $|\eta| < 0.05$ and $-0.05 < q\Delta\phi < 0.10$. This is dependent on the bending direction of the associated ID track in the solenoid field and is optimised for losses induced by Bremsstrahlung. An electron candidate is established when at least one ID track can be associated. In case multiple tracks are associated, the one with the minimum $\Delta R^2 = (\Delta\eta)^2 + (\Delta\phi)^2$ is chosen. Due to computational arguments, the EM clusters of the resulting electron candidates are recomputed by enlarging initial calorimeter segment sizes of the pre-clusters to 3×7 (5×5) in the barrel (ECs). The varying calorimeter segment sizes were optimised to take the detector-dependent energy distributions into consideration mostly with regard to suppressing pile-up and noise contributions [117].

The energy of the identified electron candidate is obtained after the application of correction factors derived via a calibration scheme. This scheme adds contributions from the following terms [118]: the estimated energy loss in the material in front of and energy deposit behind the EM calorimeter, the measured energy in the EM cluster, and the estimated energy deposit outside the cluster (lateral leakage). The corrections are derived using dedicated MC simulations, test-beam campaigns, and cosmic rays. These establish the so called EM scale [116]. This further is corrected and improved using $Z \to ee$, $J/\psi \to ee$ and $Z \to \ell\ell\gamma$ events ($\ell = e, \mu$) [118]. The four momentum of the electron candidate is reconstructed using the calibrated energy as well as directional information in (η,ϕ) of the associated ID track.

Additional **electron identification** criteria are defined and imposed on the reconstructed electron candidates in order to suppress backgrounds mis-identifying electrons, most originating from photon conversions or jets. The identification criteria are defined in three selection sets, Working Points (WPs), and are defined as: *loose*, *medium*, and *tight*, with decreasing (increasing) electron reconstruction efficiency (background rejection) [119]. The selected electrons for the different WPs are a subset of one another (*tight* $\subset$ *medium* $\subset$ *loose*). A set of discriminating variables reflecting properties of the electron candidate are used for the design of a final discriminant constructed from a Likelihood (LH)-based ratio. The resulting discriminant is the probability for the input electron candidate to be signal or background like. The cut value on the discriminant varies by WP. On top of the LH-based discriminant, cuts on variables not entering the constructed LH ratio are imposed. The discriminating variables relate to the electron candidate EM cluster and track measurements. Particularly, information related to the shower shapes, TRT responses, track to cluster matching, ID track properties, and Bremsstrahlung effects. A full list of discriminating variables is provided in Ref. [119]. The WPs are optimised as a function of E_{T} and η in order to cope with electron shower shape differences depending on the material through which they propagate and change in efficiency as a function of energy. In order to ensure a high reconstruction efficiency without drastic background increase in high pile-up environments, the cut on the LH discriminant is loosened as a function of the number of PVs. Electrons used in both of the presented analyses are required to pass the *tight* WP with additional requirements on the EM shower width and track-cluster matching quantities such as the E/p ratio. Electrons used to derive the multi-jet background described in Section 12.1.3 are required to pass the *medium* WP. The latter requirements are optimised in order to account for efficiency losses for electrons with $E_{\mathrm{T}} > 125$ GeV. High E_{T} electrons tend to deposit more of their energy in the EM calorimeter layers farther from the interaction point or even in the HCAL. Electrons considered in the presented analyses are selected if they satisfy $p_{\mathrm{T}} > 30$ GeV and $|\eta| < 2.47$. Electron candidates in the barrel to EC EM calorimeter transition region, $1.37 < |\eta| < 1.52$, are not considered. The identification signal (background) efficiency for selected electrons with $E_{\mathrm{T}} = 30$ GeV fulfilling the *tight* WP is 80% (0.2%) and increase (decrease) with increasing E_{T} [119]. Electrons fulfilling the *medium* WP have a signal (background) efficiency of 90% (0.35%) for $E_{\mathrm{T}} = 30$ GeV.

To further discriminate between signal and background, isolation requirements are imposed that help disentangling prompt leptons, originating from the decay of W and Z bosons from a "fake" lepton. The latter originate either from the mis-identification of a jet, a converted photon as a lepton candidate, or from non-prompt leptons that originate from semileptonic b- or c-hadron decays or muons produced from the in-flight decay of pions or kaons passing the imposed isolation requirements. In the presented analyses a track isolation requirement, defined as the sum of the p_{T} of all tracks fulfilling quality criteria [119], are used to calculate the quantity $I_R = I_R^{\mathrm{track}}/p_{\mathrm{T}}^l$, where p_{T}^l is the electron p_{T} and I_R^{track} is defined as follows:

$$I_R^{\mathrm{track}} = \sum_{i \in \Delta R(\mathrm{track},l) < R_{\mathrm{cut}}} p_{\mathrm{T}}^{\mathrm{track,i}}. \tag{7.3}$$

The sum excludes the track associated to the EM cluster of the electron candidate. $R_{\mathrm{cut}} = \min\left[{}^{10\ \mathrm{GeV}}/_{\mathrm{E_T}}, \mathrm{R_{max}}\right]$ with $R_{\max} = 0.2$ and the electron must satisfy $I_R^{\mathrm{track}} < 6\%$ of the p_{T}^l (denoted as `FixedCutTightTrackOnly` procedure), $R_{\mathrm{cut}} = 0.2$ for $E_{\mathrm{T}} > 50$ GeV. With increasing electron p_{T} the size of the cone shrinks which increases the real electron efficiency for electrons close to jets. A *fixed-cone* overlap-removal[6] procedure prevents double-counting of energy between an electron and a nearby small-R jet(see Section 7.5). Small-R jets are removed if the separation between the electron and small-R jet is within $\Delta R < 0.2$. Electrons are removed if the separation is within $0.2 < \Delta R_y < 0.4$. This procedure is denoted `Standard OR`.

Residual differences observed between data and simulation are corrected in simulation as function a of the electron p_{T} and η. They are implemented as scale factors, $\epsilon_{\mathrm{data}}/\epsilon_{MC}$. Uncertainties on those correction factors are taken into account as systematic uncertainties on the electron trigger (described in Section 12.3), reconstruction, identification, and isolation efficiencies. The latter are derived employing $Z, J/\psi \rightarrow ee$ events in order to be sensitive across

[6]For all overlap removal procedures $\Delta R_y^2 = (\Delta y)^2 + (\Delta\phi)^2$ is used.

a wide E_{T} range (7 to 200 GeV and $|\eta| < 2.47$). The scale factors are found to be close to unity. The observed deviations originate mostly from mismodelling of tracking properties or shower shapes in the calorimeters. The electron energy measured in data is corrected for both the scale and resolution with respect to simulation and is measured for central electrons ($|\eta| < 2.47$) using the Z boson resonance and the respective decay into electrons. The latter method is cross-checked with $J/\psi \to ee$ and $W \to e\nu$ events. This is done through the measurement of the E/p ratio which relies on the precise knowledge of the momentum scale obtained through a good alignment of the ID (see Chapter 8). The energy scale correction is ~2% with an uncertainty that varies between 0.3% and 1.6% for central electrons.

7.4.2 Muons

Muons propagate through all sub-detector components and leave tracks in the ID and MSs. Muons are MIPs for the calorimeter materials over the momentum range of interest. Hence, they only leave a small fraction of their energy in the calorimeter material. The **muon reconstruction** is independently performed for the ID, as described in Section 7.1, and the MS. In the MS, track segments are found after a hit pattern search in each muon chamber with a requirement of the segment to be compatible with the beam spot. The segments are combined for the different layers and are selected using information on their hit multiplicity and fit quality, and are matched by their relative positions and angles, resulting in MS track candidates. A track candidate is accepted when a global χ^2-fit, associating the measured hits with the track candidate, fulfils defined selection criteria. The presented analyses use the *combined* (CB) muons that are formed by association of ID and MS tracks through a global refit of the hits in the respective detector sub components. In order to improve the fit quality, MS hits are added or removed. The muon reconstruction performs an *outside-in* pattern recognition. In this approach, MS tracks are reconstructed first and then extrapolated to the ID track while correcting for energy loss in the calorimeter material. ID tracks considered for matching need to have more than zero (four) pixel hits and crossed dead pixel sensors (SCT hits and crossed dead SCT sensors), fewer than three pixel and SCT holes, and a successful TRT extension that requires at least 10% of the TRT hits to be included in the final track fit. In case more than one ID track fulfils the criteria, the one with the smallest χ^2 is chosen. Combined muons have a high p_{T} resolution and efficiency for suppressing "fake" muons. In order to reduce the background contributions from "fake muons", **muon identification** criteria are defined. The main background contributions originate from in-flight hadron decays, mostly pions and kaons. The decay of such light hadrons results in a distinct decay topology characterised by a "kink" impacting the compatibility of the combined track due to fit quality degradation. Similarly to the electrons, four different muon identification WPs are defined: *high-p_T* $\subset$ *tight* $\subset$ *medium* $\subset$ *loose*. The presented analyses use the *medium* WP that has the smallest associated uncertainties in both the muon reconstruction and calibration. The combined muon tracks are required to have ≥ 3 hits in at least two MDT layers excluding tracks within $|\eta| < 0.1$. In the latter region, combined tracks are required to have at least one MDT layer with a maximum of one MDT hole layer. In order to extend the acceptance outside of the ID, MS tracks are required to have at least three MDT/CSC layers for the region $2.5 <|\eta| < 2.7$. As a measure of the compatibility of the two associated tracks, the q/p significance is required to be < 7. The latter is defined as the absolute difference between q/p_{IDtrack} and q/p_{MStrack} divided by the combined error of the two. It is used as a measure to distinguish between prompt and non-isolated muons. The uncertainty division ensures the stabilisation against poor momentum resolution for certain detector regions. Muons are selected for the presented analyses if $p_{\text{T}} > 30$ GeV and $|\eta| < 2.5$. The signal (background) efficiency is 96.1% (0.17%) and is close to constant as a function of selected muon p_{T} and η [120]. For the *loose* WP which is used for the estimation of the multi-jet background described in Section 12.1.3, the signal (background) efficiency is 98.1% (0.76%).

In order to ensure PV compatibility, similar IP cuts are imposed on the selected muons as on electrons only differing by a tighter requirement on the d_0 significance, $|d_0^{\text{BL}}/\sigma(d_0^{\text{BL}})| < 3$. Muons are required to be isolated from calorimeter detector activity using the same criterion that is applied to electrons but with $R_{\text{max}} = 0.3$ (`FixedCutTightTrackOnly`). A *sliding-ΔR cone* overlap-removal procedure is imposed. The muon is removed if a muon and small-R jet with at least three tracks are within $\Delta R < \min(0.4, 0.04 + 10 \text{ GeV}/{p_{\text{T}}}^{\mu})$. If the small-$R$ jet has fewer than three tracks, the small-R jet is removed. The procedure is referred to as `Boosted OR` WP. The sliding-ΔR cone is smaller for larger muon p_{T}, $\Delta R = 0.4$ (0.2) for p_{T}^{μ} ~28(60) GeV. The requirement ensures a high signal efficiency for high-p_{T} muons.

Both the momentum scale and resolution for muons is derived from precise measurements of the di-muon J/ψ and Z resonance and corrected in simulation. The former correction is on the per-mille level for muons within $\eta < 2.5$, the latter varies from 1.7% in the central region to 2.9% in the ECs (considering both $J/\psi, Z \to \mu\mu$). For $Z \to \mu\mu$ decays, the uncertainty on the momentum scale is 0.05% (0.3%) for $|\eta| < 1$ ($|\eta| \sim 2.5$). The relative muon momentum resolution is up to 2.9% in the ECs. The agreement between data and prediction of the p_{T} resolution is on the order of 5% across η. Uncertainties on both the muon scale and resolution are determined separately for the ID and MS measurements.

Uncertainties on the derived scale factors (see Section 7.4.1) are considered as systematic uncertainties in the presented analyses and stem from the track-to-vertex association, trigger, reconstruction, identification, and isolation efficiencies. In contrast to the electrons, the uncertainties are separated into their statistical and systematic components. The latter are derived using $J/\psi, Z \to \mu\mu$ events to ensure sensitivity across a large p_{T} spectrum ($5 < p_{\mathrm{T}} < 100$ GeV and $|\eta| < 2.5$). They are on the order of unity and found to be stable against different pile-up scenarios.

7.5 Jets

Jets are the result of the decays, fragmentation, and hadronisation evolution of the produced partons in proton collisions and form a collimated spray of hadrons interacting with the detector components. The collimated hadron spray detected by the calorimeters and reconstructed as topoclusters (see Section 7.3) is grouped using the *anti-k_t clustering algorithm* [121, 122] with different radius parameter, R, values. This algorithm is the main choice for analyses performed in ATLAS. The anti-k_t algorithm starts to sum high momentum topoclusters and tends to combine soft emissions to harder emissions which helps suppress pile-up. The algorithm is designed to be infrared and collinear safe. The former requirement needs to be fulfilled since soft particles are emitted during the fragmentation process and the latter since hard partons evolve through a number of collinear splittings. The output of the algorithm are *jets* which tend to be of cone-like shape. For this thesis two types of jets are of particular interest which are denoted as small-R jet and large-R jet with $R = 0.4$ and $R = 1.0$, respectively. The two jet collections are clustered independently and no overlap removal is imposed between the two. Different calibration schemes are used to relate the total energy deposited by the jet in the calorimeter back to the expected energy deposits from simulated jets. Corrections to the jet energy stem from non-compensated energy which escapes detection, energy losses due to dead material, not fully contained energy deposits with particles leaking outside of the calorimeters ("punch through"), non-clustered energy deposits of jet fragments, and signal losses in the topocluster formation and jet reconstruction. The four momentum of the jet is reconstructed from the corrected energy and directional information extrapolated back to the PV.

Small-R jets are reconstructed from topoclusters, calibrated at the EM scale (`EMTopo`), and selected if they have $p_{\mathrm{T}} > 25$ GeV and $|\eta| < 2.5$. Large-R jets are reconstructed from topoclusters with the Local cluster weighting (LCW) calibration [123] (`LCTopo`). The latter calibration corrects the topoclusters following an either electromagnetic or hadronic classification depending on the energy density and depth. A weighting scheme is imposed to correct for the different electron and pion responses in the respective calorimeters. The calibrated topoclusters are the input for the jet reconstruction algorithm. In order to suppress contributions from pile-up jets, the large-R jet are trimmed [124]. The trimming algorithm reclusters the jet constituents into sub-jets with a fine-grained resolution (the R-parameter for sub-jets R_{sub} is set to 0.2). If the p_{T} of the sub-jet is less than 5% of the large-R jets p_{T}, the sub-jet is discarded ($f_{\mathrm{cut}} = 0.05$). Associated large-R jet kinematics such as p_{T} and the trimmed mass [125] are recalculated using only the constituents of the remaining sub-jets, $M^2 = (\sum_i E_i)^2 - (\sum_i p_i)^2$, with E_i and p_i defined as the energy and momentum of the jet constituents (topoclusters). The combined mass, m^{comb}, for the large-R jets [126] is the weighted linear combination of the trimmed mass using calorimeter information and the track assisted mass, $m_{\mathrm{TA}} = p_{\mathrm{T}}^{\mathrm{calo}}/p_{\mathrm{T}}^{\mathrm{track}} \times m^{\mathrm{track}}$, with $p_{\mathrm{T}}^{\mathrm{calo}}$ ($p_{\mathrm{T}}^{\mathrm{track}}$) the transverse momentum of the calorimeter jet (of the four vector sum of all calorimeter jet associated tracks) and m^{track} the invariant mass of the four vector sum of all calorimeter associated tracks. The respective weights depend on the calorimeter jet and track assisted jet masses obtained through dijet simulations [125].

The angular separation of the decay products of a boosted massive particle is proportional to $\sim 1/p_{\mathrm{T}}$ (see Section 14.1.1). Thus, the angular separation of the decay products can be on the order of the granularity of the calorimeter. The track assisted mass combines the calorimeter information with the tracking information to restore directional information which results in an improved mass resolution for boosted physics objects. Trimmed large-R jets are only considered if they have $p_{\mathrm{T}} > 200$ GeV and $|\eta| < 2.0$.

The directional information of the reconstructed jets and contained constituents is calculated with the global origin of the ATLAS detector as reference. The derived four momentum of each jet is corrected for the PV on an event-by-event basis. The correction of the jet origin improves the angular resolution. On top of the topocluster calibrations, the reconstructed jets are calibrated to account for residual detector effects using energy and pseudorapidity dependent calibration factors derived from in situ techniques and simulation variations. For the large-R jet a combined mass calibration is employed in addition.

For the small-R jet a number of systematic uncertainties are associated to the calculation of the Jet energy scale (JES) calibration of jets. The uncertainties are derived from the combination of in situ measurements of the calorimeter response to hadrons, pion test beam measurements, varying detector material descriptions in simulation, the description of electronic noise, and modelling uncertainties of the event generation. The uncertainties are η-sliced in eight detector regions, namely the central barrel, two barrel-EC transition, EC, two EC-forward transition, and forward region. The baseline uncertainties recommended for the two presented analyses are parametrised as 84 orthogonal sources of systematic uncertainties (see Section 12.5.1). Those are grouped into uncertainties from the in situ analyses (Z+jet, γ+jet, and multi-jet balance) [75 components], η inter-calibration (modelling, employed method, and calibration non-closure) [3 components], high-p_{T} jet behaviour [1 component], pile-up correction [4 components], and the non-closure of a calibration using Fast Simulation (FastSim) [1 component]. In addition to the baseline uncertainties, uncertainties related to different jet compositions are imposed. Two systematic components account for JES differences related to quark and gluon initiated jets (flavour and response): one component accounts for differences in b-quark jets, and one component accounts for punch-through jets. The total number of 88 systematic sources is reduced to 21 components under consideration of minimising correlation effects. The systematic uncertainties related to the in situ analyses are combined to 8 components. The resulting set of systematic uncertainties is used in the two presented analyses. The total relative JES uncertainty decreases from $\sim$6% at $p_{\mathrm{T}}^{\text{small-}R\text{ jet}} = 20$ GeV to $\sim$1.5% at $p_{\mathrm{T}}^{\text{small-}R\text{ jet}} = 200$ GeV and increases for small-R jets above 1 TeV to $\sim$3%. The latter is mostly driven by the punch through effect of high-p_{T} small-R jets. An additional uncertainty is imposed which stems from the derivation of the Jet energy resolution (JER) [127] using two different in situ methods. The agreement between simulation and data is found to be within 10% for central jets $|\eta| < 2.8$ and $30 < p_{\mathrm{T}} < 500$ GeV. In order to suppress the contribution from jets associated to pile-up events, a multivariate Jet Vertex Tagger (JVT) [128] selectively removes small-R jets that are identified as not originating from the PV. The latter discriminant ranks between 0 (pile-up like jet) and 1 (PV like jet). A small-R jet is removed if it fulfils $p_{\mathrm{T}} < 60$ GeV, $|\eta| < 2.4$, and has a JVT discriminant value of < 0.59. The average efficiency of the imposed cut value is 92% measured in $Z \rightarrow \mu\mu$ events with at least one additional jet. Residual differences between data and simulation are considered in the analyses as a scale factor and associated scale factor uncertainties.

b flavour tagged jets

Some collisions produce b-quarks which hadronise. Such hadrons have a lifetime of the order of $c\tau \sim 450\ \mu m$. The resulting mean flight length ($\langle l \rangle = \beta\gamma c\tau$) is of the order of 3 mm for a hadron containing a b-quark with p_{T} of 50 GeV. The distance traveled results in a secondary vertex that is displaced with respect to the PV, resulting in large IP values for the tracks originating from the secondary vertex. Information from the displaced vertex is combined with information on kinematic differences stemming from the high mass and decay multiplicity of hadrons containing b-quarks and is exploited via various multivariate techniques [129]. Each small-R jet is augmented with the value of the resulting final multivariate discriminant. A cut value on this discriminant is chosen reflecting a compromise between a high b-jet identification efficiency and a high light jet (u, d, s, and gluons) rejection. The latter is defined as the inverse of the number of light jets misidentified as a b-jet. The higher the efficiency, the smaller the rejection. The lower the efficiency, the higher the purity of selected b-jets. The cut value on the multivariate discriminant, $\texttt{mv2c10} > 0.646$, employed by the two presented analyses, corresponds to a 77% efficiency to tag a b-jet, a light jet rejection factor of $\sim$134, and a c-jet rejection factor of $\sim$6, as determined for jets with $p_{\mathrm{T}} > 20$ GeV and $|\eta| < 2.47$ in simulated $t\bar{t}$ events [130].

The tagging efficiencies are corrected in simulation for b, c and light flavours in the form of scale factors as a function of jet p_{T} and η. Associated uncertainties to light jet mistagging [14 components], b tagging [5 components], and c tagging [4 components] are used in the presented analyses. In order to extend the b and c tagging calibration beyond the calibrated p_{T} range, a MC based extrapolation uncertainty is considered [2 components].

W boson tagged jets

To identify large-R jets that are likely from the hadronic decay of a W boson, jet substructure variables are exploited using an upper cut on the ratio of the energy correlation functions $D_2^{\beta=1}$ [131, 132], and a cut on the combined large-R jet mass corresponding to a defined p_{T} dependent mass window cut around the W boson mass [133]. The former are optimised to identify the N prong structure of the large-R jet through exploitation of both the angular separation and p_{T} of combinations of the jet constituents [131, 132]. The cuts on the substructure variables are p_{T} dependent and are used to define different WPs with different W tagging efficiency and multi-jet background rejection across a large-R jet p_{T} range from 200 to 2500 GeV. Selected large-R jets must pass the 50% efficient W-tagging WP [134] with a multi-jet background rejection of $\sim$12.5.

Associated large-R jet scale uncertainties are considered for the substructure variables, p_{T}, m^{comb}, and $D_2^{(\beta=1)}$. The systematic uncertainties are assessed comparing the agreement between data and simulation, different simulations as well as considering the total statistical uncertainty and uncertainties on the tracking information. For the latter, the tracking efficiency and related uncertainties, tracking fake rate uncertainties and q/p uncertainties are considered. For the presented analyses, four scale systematic components are considered as a combination of large-R jet p_{T} and m^{comb} (treated as fully correlated) and four substructure systematic components are related to $D_2^{(\beta=1)}$. The total relative uncertainty on large-R jet p_{T} is 3% (4%), large-R jet m^{comb} 6% (4%), and large-R jet $D_2^{(\beta=1)}$ 2% (5.5%), all for p_{T} of 200 GeV (2 TeV).

7.6 Missing Transverse Momentum

Particles escaping detection leave an apparent imbalance in the measured momentum in the transverse plane due to momentum conservation. Such particles, either neutrinos or yet undiscovered weakly-interacting BSM particles, are indirectly reconstructed through the calculation of the kinematic variable missing transverse momentum, $E_{\mathrm{T}}^{\mathrm{miss}}$, which is defined as the magnitude of the negative vector sum, $\vec{p}_{\mathrm{T}}^{\;\mathrm{miss}}$, of all reconstructed and calibrated physics objects in an event. In practice, $E_{\mathrm{T}}^{\mathrm{miss}}$ is calculated as the square root of the quadratic sum of the two transverse components, $E_{\mathrm{x(y)}}^{\mathrm{miss}} = -\sum_{i\in\mathrm{PO}}\sum_{j\in\mathrm{PO_i}}\vec{p}_{\mathrm{T\,x(y)}}^{\;\mathrm{miss,j}}$ with i representing a physics object (PO $= \mathrm{e}, \gamma, \tau, \mathrm{jet}, \mu,$ and *soft-term*) and j the respective number of physics objects per event [135]. The soft-term accounts for additional tracks or energy clusters not associated to any other defined object class and can be calculated by various algorithms. Track-based algorithms show a better performance under varying pile-up conditions due to the association of the tracks to the PV but are limited to the ID volume and are not sensitive to neutral particles. Calorimeter-based algorithms are dependent on the number of pile-up since the calorimeter cluster information is not matched to the hard objects such that they are sensitive to underlying event activity as well as soft radiations from the hard scatter. The two presented analyses make use of an algorithm combining the Track soft term (TST) with additional calorimeter information that needs to fulfil JVT requirements. An overlap-removal procedure avoids double counting of tracks considered in the soft-term with other physics objects. Uncertainties are propagated to the $E_{\mathrm{x(y)}}^{\mathrm{miss}}$ from the hard physics objects. Both the scale and resolution of the remaining soft-term are estimated employing $Z \rightarrow \mu\mu$ events without additional jets. The former shows a bias of $\sim$5% due to the limited acceptance of the ID and omission of neutral particles and the latter is $\sim$15% as a function of the number of PV and $E_{\mathrm{x(y)}}^{\mathrm{miss}}$ [136]. The simulation is corrected for both scale and resolution. The uncertainties considered are mainly driven by modelling uncertainties stemming from different simulation comparisons, the simulation of varying detector materials, and bunch spacing scenarios.

7.7 Data Quality Requirements

Various data quality requirements are imposed on the collected data from 2015 and 2016.

GRL Events are only considered for analysis if all ATLAS detector subsystems were operational and stable beam conditions are met. These criteria are summarised in LumiBlocks specified in the GRL. Only 7.5% of the recorded luminosity does not fulfil this requirement.

Removal of corrupted data Events recorded during temporary detector problems, lasting less than a LumiBlock length are flagged and removed. Those events mostly suffer from data corruption in the Tile calorimeter or noise bursts observed in the LAr calorimeter.

PV selection Events are required to have at least one PV with at least two associated tracks with $p_{\mathrm{T}} > 400$ MeV which gives sufficient resolution in order to reduce non-collision backgrounds such as interactions of the protons with beam gas and cosmic muons. This requirement has a negligible impact on the analyses presented.

Event veto from Jet cleaning Events can contain fake jets that are not connected to the hard scatter. Non-collisional backgrounds are due to proton losses induced by muons from secondary cascade decays and cosmic-ray muons that fake a jet. In addition, induced calorimeter noise results in fake jets. For more details, the reader is referred to Ref. [137]. The jet cleaning is of particular importance for the correct $E_{\mathrm{T}}^{\mathrm{miss}}$ calculation. The event rejection resulting from jet cleaning is applied after the jet overlap removal.

Chapter 8

Inner Detector Alignment

"Do not go where the path may lead, go instead where there is no path and leave a trail."

—Ralph Waldo Emerson

This chapter gives an overview of the track-based ID alignment procedures, summarises detector deformations that can be insensitive to that procedure, and describes how to correct for such geometrical deformations using external constraints.

8.1 Track-based ID Alignment

The track-based ID alignment procedure employs tracks reconstructed by the detector in order to deduce on the actual position of the detector elements, referred to as "true" geometry which is time dependent. As outlined in Section 7.1, the measurements of the residuals, reflecting the distance between the true track trajectory and the hit measurement at a position-sensitive device with an intrinsic resolution of $\mathcal{O}(\sim 10-100\mu\text{m})$ ($\mathcal{O}(\sim 170\mu\text{m})$) for the silicon detectors (TRT), are performed. Their relative position in the ID volume referenced by the global coordinate system of ATLAS described in Section 6.1. The initial determination of the relative positions was performed based on construction and design information as well as survey measurements before the ID assembly [138]. The early data thus had large uncertainties, limiting the track reconstruction performance. In order to achieve the high precision requirements on the tracking performance forming the basis for almost all physics objects described in Part III, a high precision on the spatial position of detector elements in the ID and thus the actual geometry of the ATLAS detector exceeding the intrinsic resolution is crucial.

This goal is achieved by the track-based alignment procedure that can be seen as a generalisation of the track fit described in Section 7.1. The track fit minimises the χ^2_{track} iteratively with respect to the first and second derivative of a set of *local* parameters defined by the vector π given by the track parameters τ and track scattering angles θ (see Equation 7.2) encompassing two angles at the scattering center and the energy loss. However, the actual hit position is not constant in time which results in a dependency of the residual vector of a track $\mathbf{r}$ on *global* parameters. These are the alignment parameters, α, common to all reconstructed tracks. The track reconstruction assumes a "perfect" geometry provided in simulation. However, the perfect geometry of the ATLAS detector provided by simulations is not a "perfect" reflection of the actual "true" detector geometry due to construction and assembly imperfections and in situ detector deformations. A track reconstruction without considering the actual geometry of the detector

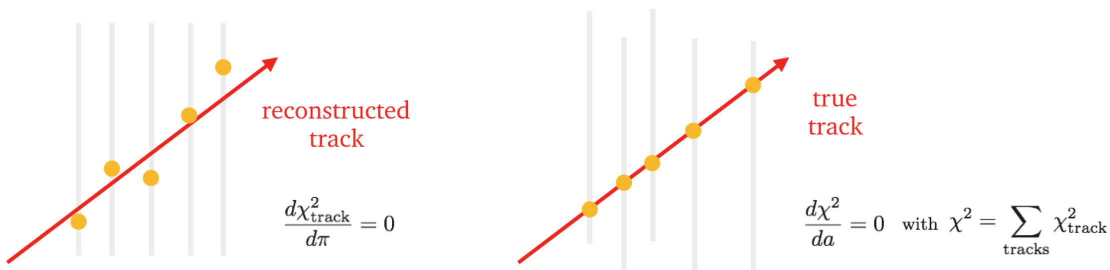

Figure 8.1: Track trajectories reconstruction assuming a "perfect" (left) and corrected, "true" detector geometry (right).

results in a poor fit quality as well as biased track parameters as displayed in Figure 8.1. The track-based alignment procedure minimises the following χ^2:

$$\chi^2 = \sum_{i \in \text{tracks}} \chi_i^2, \text{ with } \chi_i^2 = \mathbf{r_i}(\pi, \alpha)^T V_i^{-1} \mathbf{r_i}(\pi, \alpha), \tag{8.1}$$

of a certain number of tracks that ensures a sufficient hit statistic per position-sensitive device and a reduction of dependence on poor quality track fits. The resulting minimum reflects the spatial configuration of all considered *alignable structures* that corresponds to the true detector geometry. Throughout the alignment procedure, a set of alignment parameter corrections (*alignment constants*) is obtained reflecting the position and orientation of the aligned structure with respect to an initial position. Alignable structures are defined at different *Levels*, each Level consisting of a collection of grouped position-sensitive devices. Each defined structure gets six dof assigned, three translational, $\vec{T} = (T_x, T_y, T_z)$ and three rotational, $R = R_x(\alpha), R_y(\beta), R_z(\gamma)$, forming the alignment parameters α and uniquely defining the spatial configuration. The three rotational angles (α, β, γ) are defined as the three rotations around the local coordinate axes of a given structure. The local coordinate system is defined in Section 6.2.1. Each local spatial position of a structure, $\vec{P}$, is represented in the global reference frame as $\vec{T} + R \cdot \vec{P}$ with the rotation applied in the order $R_z(\gamma), R_y(\beta)$ and $R_x(\alpha)$ and $H = \vec{T} + R\cdot$. The alignment constants encode

Table 8.1: A general Run II definition of different alignment levels summarising the grouped alignable structures and respective detector description, associated dof and employed constraints. In case of movements that can only be constrained poorly, some dof are omitted.

Level	Description	Structures	dof	Employed constraints
1 (11)	IBL	1	All	
	Pixel detector	1	All	
	SCT end-caps (SCT barrel fixed)	2	All except T_z	
	TRT split into barrel and 2 end-caps	3	All except T_z	
2	Pixel barrel split into layers	4	All	Beam spot,
	Pixel end-caps split into discs	6	All	momentum bias, and
	SCT barrel split into layers	4	All	impact parameter bias
	SCT end-caps split into disks	18	All	
3	Pixel barrel modules	1736	All	Beam spot,
	Pixel end-caps modules	288	T_x, T_y, R_z	momentum bias,
	SCT barrel modules	2112	All	impact parameter bias, and
	SCT end-caps modules	1976	T_x, T_y, R_z	module placement accuracy
TRT 2	TRT barrel split into barrel modules	96	All except T_y	Momentum bias and
	TRT end-caps split into wheels	80	T_x, T_y, R_z	impact parameter bias
	Pixel and SCT detectors fixed			
TRT 3	TRT straws	351k	T_x, R_z	
	Pixel and SCT detectors fixed			

the corrections, ∂H, to the nominal assumed structure position H_0, resulting in the correction to the spatial configuration $H = H_0 \cdot \partial H$.

The ID was assembled independently for the three sub detector components [139]. The definition of alignment levels follows a hierarchical ordering starting from large alignable structures with a small number of dof successively increasing the number of alignable structures with a large number of dof. A general and simplified overview of different alignment levels used during Run II is shown in Table 8.1. The hierarchical ordering of alignment levels ensures that global movements of larger structures are corrected first while already reducing misalignment correlations of smaller structures. The first alignment level, *Level 11*, considers the IBL, and pixel detector, the SCT barrel (fixed) and ECs, and the TRT barrel and a group of two ECs separately as rigid bodies. The reference frame used by a Level 11 alignment is the same as the global ATLAS reference frame. For the following alignment levels, the local coordinate systems are used. *Level 2* corrects for relative movements of each layer and disc (modules and wheels) in the pixel detector and SCT barrel and ECs (TRT barrel and ECs). The third level, *Level 3*, considers each pixel detector and SCT module, and TRT straw as independent alignable structures.

The χ^2-minimisation with respect to the alignment parameters is given by:

$$\left.\frac{\mathrm{d}\chi^2}{\mathrm{d}\alpha}\right|_{\alpha=\hat{\alpha}} = 2\sum_{i\in\text{tracks}} \left(\frac{\mathrm{d}\mathbf{r}_i}{\mathrm{d}\alpha}\right)^T V^{-1}\mathbf{r}_i\bigg|_{\alpha=\hat{\alpha}} = 0, \tag{8.2}$$

with $\hat{\alpha}$ expressing the alignment parameters reflecting the actual position of the alignable structures. The alignment constants, $\Delta\alpha$ can be derived as corrections to an initial set of alignment parameters α_0. Under the assumption that the expected misalignments and $\Delta\alpha$ are small, Equation 8.2 can be linearly expanded around α_0, neglecting third and higher order derivatives, and has the following form:

$$\frac{\mathrm{d}\chi^2}{\mathrm{d}\alpha} \approx \left.\frac{\mathrm{d}\chi^2}{\mathrm{d}\alpha}\right|_{\alpha=\alpha_0} + \underbrace{\left.\frac{\mathrm{d}^2\chi^2}{\mathrm{d}\alpha^2}\right|_{\alpha=\alpha_0}}_{\mathscr{M}} \Delta\alpha. \tag{8.3}$$

The minimisation procedure is repeated iteratively until $\Delta\alpha$ is negligible (Newton-Raphson procedure). The total derivatives with respect to the alignment parameters are given by:

$$\frac{\mathrm{d}}{\mathrm{d}\alpha} = \frac{\partial}{\partial\alpha} + \frac{\mathrm{d}\pi}{\mathrm{d}\alpha}\frac{\partial}{\partial\pi}. \tag{8.4}$$

A system of N equations is defined by Equation 8.3 where N represents the total number of alignment parameters that is a product of all associated dof per considered alignable structure and the number of alignable structures with $\mathscr{M}$, a $N \times N$ matrix. An approach that solves the equations above under consideration of the correlations of all alignable structures given by simultaneous solution of the set of equations for the local track and global alignment parameters is generally referred to as the *global* χ^2-ansatz. However, for large N and large track statistics this approach results in numerical and computational limitations, particularly at Level 3 with $\mathscr{O}(\sim 700000)$ dof. For large N, a simplified approach is in place in order to ease the χ^2-minimisation. It assumes the track parameters to be constant and solves Equation 8.3 for the alignment parameters only. This ansatz simplifies Equation 8.4 to ${}^{\mathrm{d}}/_{\mathrm{d}\alpha} = {}^{\partial}/_{\partial\alpha}$ and thus relies only on the solution of a reduced independent set of equations with up to six individual dof describing individual alignable structures. The benefit of computational ease comes with the disadvantage of an increased number of iterations and loss of constraining power of true detector movements due to the information loss in the local χ^2-method [140, 141].

The alignment solution resulting in the set of alignment constants is obtained through the diagonalisation of the symmetric matrix $\mathscr{M}$. Thus, the system of equations can be transformed into its diagonal basis with its eigenspace spanned by the linearly independent eigenvectors composing the matrix U and the diagonalisation matrix D containing the eigenvalues λ_i:

$$\mathscr{M} = UDU^T. \tag{8.5}$$

The matrix elements of the resulting covariance matrix in this basis are $1/\lambda_i$. This shows that alignment corrections can be associated with large uncertainties for cases in which $\lambda \simeq 0$. Small eigenvalues are associated to eigenvector solutions corresponding to detector deformations to which the considered tracks have very low to no sensitivity. Such eigenvector solutions leave the χ^2 invariant up to the considered order in Equation 8.3 and introduce systematic biases generally referred to as *weak modes*. These are of particular importance as they cannot only form due to insensitivity of the track-based alignment to true detector deformations but also solely manifest as artefacts of the alignment procedure itself driven by statistical fluctuations [142].

The weak modes can result in track parameter biases directly impacting the calibration of physics objects relying on tracking information. Figure 8.2 shows potential weak mode deformations in the ID. Hence, the monitoring of the ID alignment performance and continuous corrections throughout data taking is crucial for a successful physics program and in order to avoid costly reprocessing campaigns of the collected data set which cost $\mathscr{O}$(millions) Swiss Francs of computing resources.

In order to improve the sensitivity of the alignment procedure to weakly constrained or unconstrained eigenvector solutions, one can either exploit tracks with different characteristics such as beam-halo muons or cosmic rays or by the introduction of additional constraints to the local or global parameters in the χ^2-minimisation [143]. The χ^2 expression given in Equation 8.1 can be extended by adding an additional term

$$\chi^2_{\text{constraint}} = \sum_{i \in \text{tracks}} (\rho - \mathbf{c})_i^T R_i^{-1} (\rho - \mathbf{c})_i \tag{8.6}$$

incorporating the additional constraints $\mathbf{c}$ on the global or local parameters ρ (either π or α), with R defined as the covariance matrix reflecting the constraint uncertainty. Additional constraints on track parameters adding constraining power and thus sensitivity to residual detector deformations can stem from universal measurements showing a dependency on track parameters such as the PV or beam spot position and the E/p ratio for reconstructed electrons using

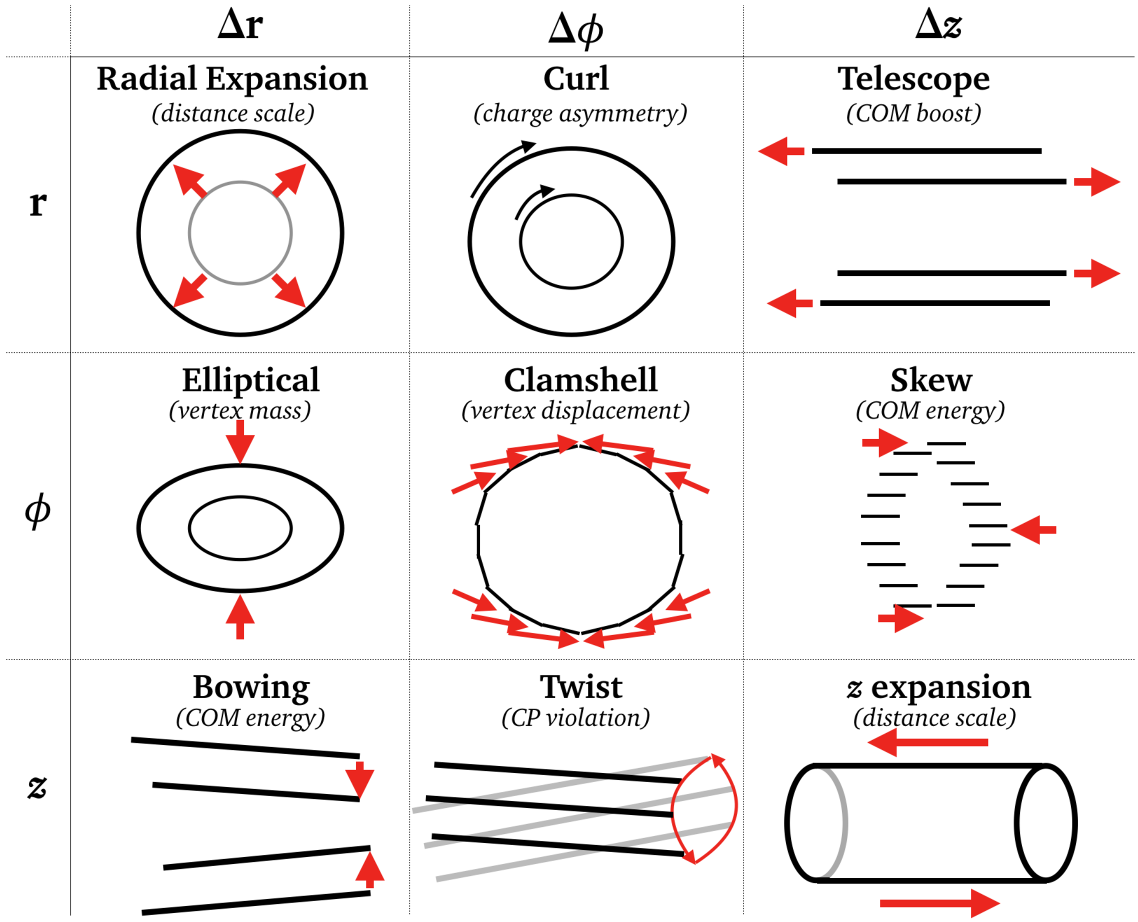

Figure 8.2: An illustration of potential classes of weak mode deformations in the ID.

calorimeter information. The additional constraint is implemented as an additional measurement (pseudo-measurement) on a track [104].

The invariant mass of a variety of neutral resonances such as $Z \to \mu^+\mu^-$, $J/\Psi \to \mu^+\mu^-$ and $K_S^0 \to \pi^+\pi^-$ that are sensitive to a wide track p_{T} range [144] can be used as additional constraint by adding the following term to the χ^2 expression given in Equation 8.1:

$$\chi^2_{\text{invariant mass}} = \sum_{i \in \text{tracks}} (\mathbf{m}_i - M)^T W_i^{-1} (\mathbf{m}_i - M), \tag{8.7}$$

where M is the known mass of the resonance and W the covariance matrix of the measured width of the resonance. Table 8.1 shows the employed additional constraints at the respective alignment level for Run II data taking.

8.2 Identification and Mitigation of Track Parameter Biases

As outlined in the previous section, weak modes can lead to systematic biases of track parameters that can stem from true detector deformations or systemic artefacts of the alignment procedure that leave the χ^2 invariant. For the resulting physics measurements the latter two cases are the same and as such, it is crucial to detect weak modes as they can bias fundamental physics measurements. Different additional constraints can improve the sensitivity and remove such residual misalignments. In this dissertation, the focus is on the external constraints originating from the well-known mass of the Z resonance and its respective decay into two muons. The latter "standard candle" provides tracks over a wide p_T range (15 GeV $< p_\mathrm{T} <$ 100 GeV) sensitive to certain classes of residual misalignments. In particular, the Z mass can be used to detect biases in the impact parameters and the track curvature reflected by its *sagitta*, S, as shown schematically in Figure 8.3.

8.2.1 Biased Sagitta and Impact Parameter Corrections

The transverse momentum of a highly relativistic particle with charge Q traversing a magnetic field, B, originating from the center of a cylindrically shaped detector is given by:

$$p_\mathrm{T} = 0.3 \cdot Q[\mathrm{e}]\, B[\mathrm{T}]\, R[\mathrm{m}], \tag{8.8}$$

with R expressing the track curvature that is approximated for medium to high p_T tracks ($S \ll L$) by $R = {}^{L^2}/_{8S}$. This then simplifies to:

$$p_\mathrm{T} = Q\kappa \frac{L^2}{S}, \tag{8.9}$$

with $\kappa = {}^{0.3B}/_{8}$. It is worth stressing that certain classes of detector deformations leave the sagitta of a track unaffected. An example for such a distortion, biasing oppositely charged particles in the same manner (*charge symmetric* deformations), is the radial distortion in which the radius of the detector layers is expanded and compressed, $\Delta x \sim r$.

However, the focus in this dissertation is on the set of detector distortions that impact the sagitta oppositely for oppositely charged particles. Such deformations are referred to as *charge anti-symmetric* deformations. An example detector distortion is the *curl* that reflects a transverse rotation of the detector layers proportional to their radius ($\Delta\phi \sim r$) as illustrated in Figure 8.4. As a result, the sagitta of the reconstructed track is biased due to the insensitivity of the χ^2-fit to such a detector deformation with respect to the true unbiased track. Assuming that the

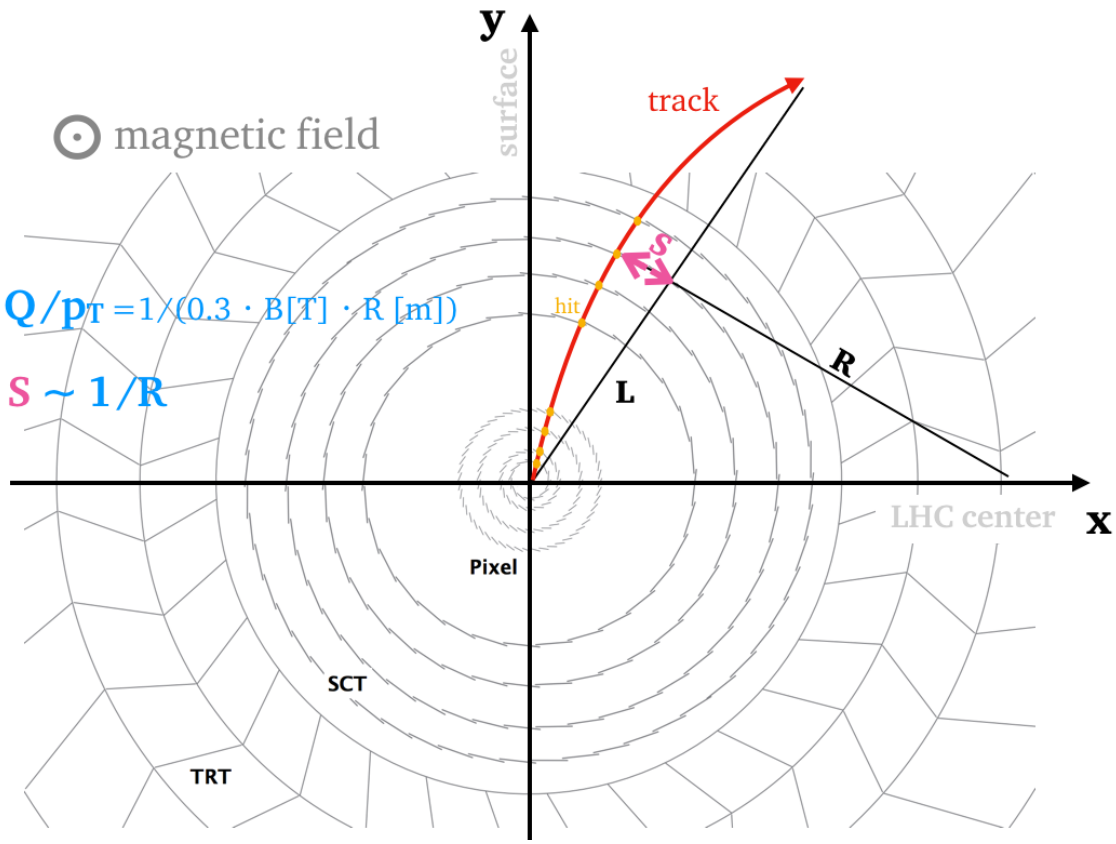

Figure 8.3: The track trajectory (red) with the hits (yellow) in the individual detector elements and the charge signed transverse momentum, sagitta and track curvature in an x-y transverse projection of the ID.

reconstructed track with $p_{\mathrm{T}}^{\mathrm{reco}}$ (with the distorted geometry) has a sagitta $S_{\mathrm{reco}} = S_0 + \Delta$ with respect to the unbiased track with $p_{\mathrm{T}}^{\mathrm{true}}$ with S_0, their p_{T} is related by:

$$\frac{Q}{p_{\mathrm{T}}^{\mathrm{reco}}} = \frac{Q}{p_{\mathrm{T}}^{\mathrm{true}}} + \partial_{\mathrm{sagitta}} \Leftrightarrow p_{\mathrm{T}}^{\mathrm{reco}} = p_{\mathrm{T}}^{\mathrm{true}} \cdot \left(1 + Qp_{\mathrm{T}}^{\mathrm{true}}\partial_{\mathrm{sagitta}}\right)^{-1}, \tag{8.10}$$

with $\partial_{\mathrm{sagitta}} = {}^{\Delta}/_{\kappa L^2}$ carrying units of eV^{-1}. No reconstruction bias is present if $\partial_{\mathrm{sagitta}} = 0$, e.g. when no geometric distortion is present, $\Delta = 0$. The sagitta bias is proportional to p_{T}^2 which motivates the usage of high p_{T} tracks for the detection of such weak modes. The longitudinal momentum component of the track is also affected by the sagitta bias as $p_z = p_{\mathrm{T}}\cot(\theta)$ and thus:

$$p^{\mathrm{reco}} = p^{\mathrm{true}} \cdot \left(1 + Qp^{\mathrm{true}}\partial_{\mathrm{sagitta}}\right)^{-1} \tag{8.11}$$

$$\Leftrightarrow p^{\mathrm{true}} = p^{\mathrm{reco}} \cdot \left(1 - Qp^{\mathrm{reco}}\partial_{\mathrm{sagitta}}\right)^{-1} \tag{8.12}$$

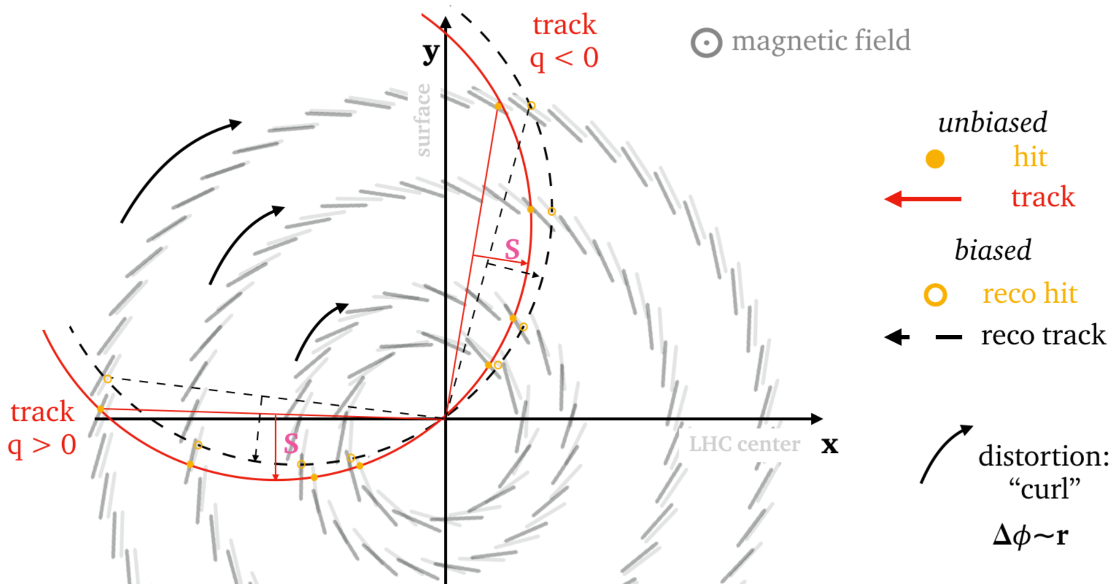

Figure 8.4: The figure illustrates the effect of a curl detector distortion on the p_T of a charged particle traversing the ID. True hits (orange dots) and the resulting unbiased particle tracks (red) as well as the hits (orange circles) corresponding to a distorted detector geometry resulting in a biased reconstructed track (dashed black lines) are shown. The detector distortion corresponds to a "curl" given by a rotation in $\Delta\phi$ which results in a distortion of the reconstructed track curvature R (sagitta S) impacting positively and negatively charged particles oppositely (charge anti-symmetric bias). The illustrated distortion biases the positively charged track ($q > 0$) such that the sagitta of the reconstructed track (with the distorted geometry) is larger than the unbiased track (without the distorted geometry). The reconstructed track p_T is therefore smaller compared to the unbiased track ($p_T^{\text{reco}} < p_T^{\text{true}}$). The contrary is the case for the negatively charged track ($q < 0$).

since $\theta^{\text{reco}} = \theta^{\text{true}}$ is not affected by a transverse detector distortion.

Identification of sagitta biases using the Z resonance In order to use the Z mass as external constraint to identify geometrical deformations biasing the sagitta and hence the momentum of a track, dimuon events are selected. The ID track component of the reconstructed muon is used in order to calculate $\partial_{\text{sagitta}}$. Muons originating from the Z resonance are particularly powerful as they populate various detector regions that enables the estimation of $\partial_{\text{sagitta}}(\eta, \phi)$ as a function of the detector region in (η, ϕ). The invariant mass of the two tracks originating from the Z will differ from its M_Z^{PDG} value in case the momentum measurement is biased. The invariant mass of the two muons is expressed as:

$$m_{\mu\bar{\mu}}^{2,\text{true}} = 2p_{\mu}^{\text{true}} p_{\bar{\mu}}^{\text{true}}(1-\cos\omega), \tag{8.13}$$

where the muon masses are neglected and ω represents the opening angle between the two muons. Using Equation 8.12 and $m_{\mu\bar{\mu}}^{2,\text{reco}}$ one obtains:

$$m_{\mu\bar{\mu}}^{2,\text{true}} = m_{\mu\bar{\mu}}^{2,\text{reco}} \left(1 + p_{\mu}^{\text{reco}} \partial_{\text{sagitta}}^{-}\right)^{-1} \left(1 - p_{\bar{\mu}}^{\text{reco}} \partial_{\text{sagitta}}^{+}\right)^{-1} \tag{8.14}$$

$$\simeq m_{\mu\bar{\mu}}^{2,\text{reco}} + m_{\mu\bar{\mu}}^{2,\text{reco}} \left(p_{\mu}^{\text{reco}} \partial_{\text{sagitta}}^{-} - p_{\bar{\mu}}^{\text{reco}} \partial_{\text{sagitta}}^{+}\right). \tag{8.15}$$

using the geometric series and neglecting terms of $\mathcal{O}(\partial^2)$ in the last step. The relative mass difference between the true unbiased mass and the biased reconstructed mass is expressed as:

$$\Delta m^2 = \frac{m_{\mu\bar{\mu}}^{2,\text{reco}} - m_{\mu\bar{\mu}}^{2,\text{true}}}{m_{\mu\bar{\mu}}^{2,\text{reco}}} \simeq \left(p_{\mu}^{\text{reco}} \partial_{\text{sagitta}}^{-} - p_{\bar{\mu}}^{\text{reco}} \partial_{\text{sagitta}}^{+}\right) \tag{8.16}$$

The two muon tracks are affected by the sagitta bias differently while only one constraint $m_{\mu\bar{\mu}}^{2,\text{true}} = M_Z^{\text{PDG}}$ is present. A priori it is ambiguous if one or the other or both muon tracks are affected. However, it is possible to solve for this ambiguity through an iterative procedure assuming that the bias originates 1/2 from either muon. The iterative process starts from the assumption that $\partial_{\text{sagitta}}^{i=0} = 0$ and iteratively calculates $\Delta m^{2,i}$ on an event-by-event basis while assigning:

$$\partial_{\text{sagitta,i}}^{+} = -\frac{\Delta m^{2,i}}{2p_{\bar{\mu}}^{\text{reco}}}, \tag{8.17}$$

$$\partial_{\text{sagitta,i}}^{-} = \frac{\Delta m^{2,i}}{2p_{\mu}^{\text{reco}}}. \tag{8.18}$$

In each iteration the muon momenta are updated and the computed $\partial_{\text{sagitta}}$ value is stored and used for the next iteration. As previously mentioned, the sagitta bias is evaluated as a function of (η, ϕ) in order to account for non-uniform geometrical deformations:

$$\partial_{\text{sagitta,i}}(\eta,\phi) = -Q\frac{\Delta m^{2,i}}{2p^{\text{reco}}} \cdot \left(1 + Qp^{\text{reco}} \partial_{\text{sagitta,i}-1}(\eta,\phi)\right) + \partial_{\text{sagitta,i}-1}(\eta,\phi), \tag{8.19}$$

where for each (η, ϕ) bin an iterative $\pm 1.5\sigma$-constrained Gaussian fit with mean μ_j and width σ_j is performed to the core of the $\partial_{\text{sagitta,i}}$ distribution per iteration j.

The fit is updated each time for events fulfilling the fit constrained until the fit is deemed stable and an abort condition kicks in which is a pre-set σ value. The fit is performed in an iterative and constrained manner in order to reduce the dependence of the $\partial_{\text{sagitta,i}}$ bias corrections on tails stemming from muon tracks with an invariant mass that is incompatible with the

Z mass (mostly from $\gamma^\star \to \mu\bar{\mu}$). The iterative process to calculate $\partial_{\text{sagitta,i=last}}(\eta,\phi)$ is repeated until convergence is reached and the $\Delta m^{2,i=\text{last}}$ agrees with the experimental uncertainties of M_Z^{PDG}.

Identification of impact parameter biases using the Z resonance The same Z events are used in order to derive constraints on the impact parameters. Since both tracks are expected to originate from the same production vertex, they should have the same longitudinal and opposite transverse impact parameters. Track parameter corrections are derived through the same iterative procedure and iterative core fit per (η,ϕ) as explained in the previous paragraph. Instead of an update of the muon momenta per iteration, the track parameter are corrected by:

$$\partial_{d_0}(\eta,\phi) = d_0^{\bar{\mu}} - d_0^{\mu} \tag{8.20}$$

$$\partial_{z_0}(\eta,\phi) = z_0^{\bar{\mu}} - z_0^{\mu}. \tag{8.21}$$

Identification of sagitta biases using the E/p ratio The calorimeter measurement of the energy of electrons and positrons can be related to the momentum measurement of their associated tracks through the ratio E/p. In the same way as the $Z \to \mu\mu$ method is insensitive to a potential radial expansion of the detector, so is the E/p method. Under the assumption that the mean $\langle E/p\rangle^+_{\text{true}} = \langle E/p\rangle^-_{\text{true}}$, potential momentum biases stemming from residual misalignments in the ID can be identified. A geometrical detector deformation will bias the momentum of the track according to Equation 8.10 such that:

$$\langle E/p\rangle^{\pm}_{\text{reco}} = \langle E/p\rangle^{\pm}_{\text{true}} \cdot \Big(1 + Q\langle p\rangle_{\text{true}}\partial_{\text{sagitta}}\Big). \tag{8.22}$$

Similar kinematic characteristics of the electrons and positrons ensures that no significant dependencies on the calorimeter energy scale induced on $\langle E_T\rangle$ is present. The sagitta corrections can be extracted through:

$$\partial_{\text{sagitta}} = \frac{\langle E/p\rangle^+_{\text{reco}} - \langle E/p\rangle^-_{\text{reco}}}{\langle E_T\rangle}. \tag{8.23}$$

Residual dependencies on the energy scale will change the normalisation of $\partial_{\text{sagitta}}$. In contrast to the $Z \to \mu\mu$ method described previously, the $\partial_{\text{sagitta}}$ of the E/p method accounts for the global sagitta bias that only enters at $\mathcal{O}(\partial^2_{\text{sagitta}})$ in Δm^2 that were neglected in Equation 8.15. The electron candidates are selected from W and Z events. Due to the larger statistics, the $Z \to \mu\mu$ method provides a much finer granularity in (η,ϕ) which makes a combination of the two methods desirable [144].

8.2.2 Identification and Mitigation of Track Parameter Biases

Baseline alignment constants are stored in a database [145] as reference. The database is accessed during on- and offline event reconstruction and contains information about the ATLAS geometry and conditions. The constants can be updated at any time. Time dependent alignment is necessary to cope with detector deformations occurring at different time intervals. The track-based alignment procedure depends on a sufficient amount of statistics in order to ensure sensitivity to certain geometrical deformations. However, the necessary statistics limits the sensitivity to geometrical deformations that might occur on short time scales and are averaged out. Different classes of deformations are captured in time intervals of differing lengths. Such deformations stem from environmental changes or changes to operational detector conditions. Examples are magnetic field changes, gas leakages, cooling, instantaneous luminosity changes, and technical stops with no detector operation. Originally, in Run I and early Run II, a Level 1 alignment was performed on an run-by-run basis in an automated manner during the ATLAS calibration loop in the offline reconstruction to correct for all observed coarse detector movements. The updated alignment constants are updated with respect to the baseline alignment constants. During Run II the necessity emerged to shorten the alignment time intervals to $\mathcal{O}$(LumiBlocks) in order to cope with IBL stave distortions caused by changes in the operating temperature, as well as instantaneous luminosity increases [146]. The observed bowing related to the luminosity increase led to individual IBL stave distortions of up to 30 μm in local x-direction between runs and 10 μm within a single run. Hence, an average shift of $\sim$0.5 μm/h was observed. The magnitude of the distortion was parametrised as a function of the IBL operation temperature. The latter parametrisation was derived through the performance of a track-based ID alignment procedure using cosmic ray data from 2015 and varying IBL operation temperatures $T^{\mathrm{op.}} = -20, -15, -10, 0, 7, 15$ °C fitted to a distortion model determined from a three-dimensional finite element analysis. The determined magnitude of the distortion M with respect to the temperature change is ${}^{\mathrm{d}M}/_{\mathrm{d}T} = -10.6 \pm 0.7$ ${}^{\mu\mathrm{m}}/_{\mathrm{K}}$. The latter is in agreement with the assumption that the distortion is closely related to the coupling of connected materials with differing thermal expansion coefficients.

The d_0 distribution (including the beam spot width) is expected to be most affected by the transverse distortion and shows a bias of $\sim$1 μm in comparison between the undistorted and distorted cases as shown in Figure 8.5. The resulting bias is small compared to the width of

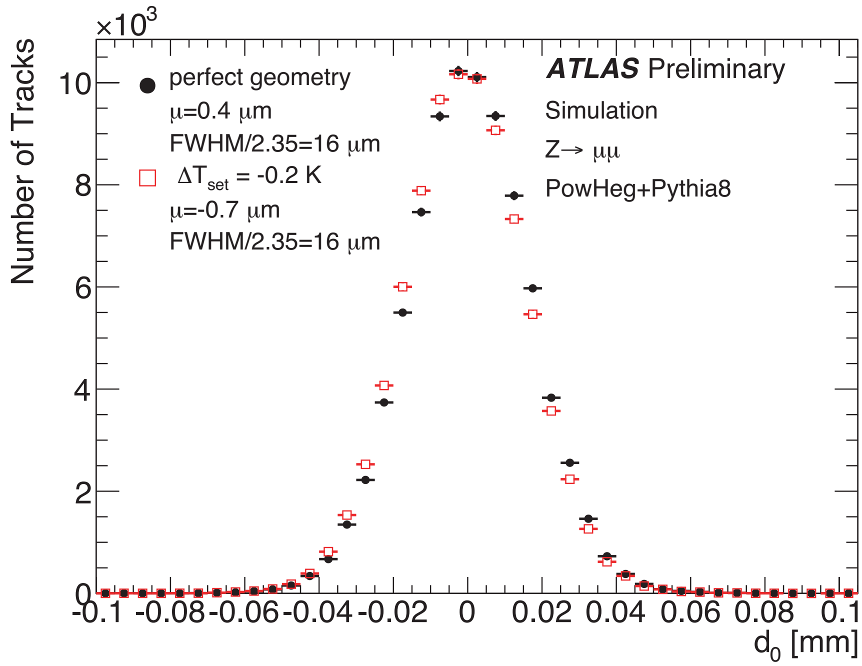

Figure 8.5: d_0^{BS} distribution of combined muon ID tracks with respect to the beam spot using $Z \rightarrow \mu\mu$ events. The black circles (red squares) show the nominal geometry (distorted geometry corresponding to $\Delta T_{set} = -0.2$K).

the distribution, $\mathcal{O}(10\ \mu\ \text{m})$. The preliminary studies were extended to assess the performance impact on other physics objects. It was inferred that sizeable effects start to be observed for distortions corresponding to $\Delta T_{set} >\ 0.2$K on the track parameter resolution and b-tagging performance. The multivariate discriminant, `mv2c10`, is used to assess the impact on the b-tagging performance which starts to be impacted for $\Delta T_{set} >\ 0.5$K. The nominal light jet rejection corresponding to the 70% efficiency b tag WP decreases by 10% (50%) for $\Delta T_{set} = 1$K (2K). As a result after that, the IBL distortions were closely monitored across and within runs and corrected in situ during the calibration loop.

In addition to the IBL distortions, kinematic distributions sensitive to charge anti-symmetric sagitta biases are monitored online during data taking. As discussed previously, deviations from the expected mass of e.g. the Z and J/ψ resonance indicate the presence of weak modes. Hence, the invariant mass of the Z and J/ψ, as reconstructed from ID tracks taken from combined muons, are monitored in different detector regions and as a function of weak mode sensitive kinematics on a run-by-run basis. Figure 8.6 shows the invariant mass of the J/ψ (Z) as reconstructed from two combined muon ID tracks recorded in the barrel and two ECs of the

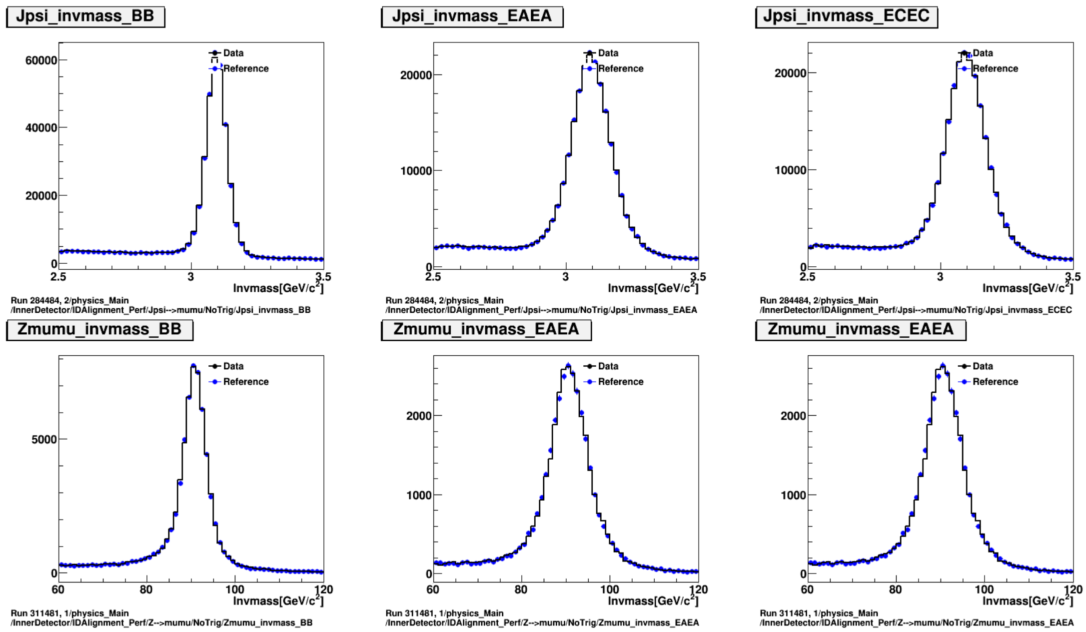

Figure 8.6: The invariant mass of the J/ψ (top) and Z (bottom) resonance reconstructed from stripped ID tracks of combined muons as detected in the barrel (left) and the two ECs (middle and right) illustrated for the last data run in 2015 (top) and 2016 (bottom).

ATLAS detector for the last run in 2015 (2016). These plots are part of the data quality system for the ID alignment performance monitoring (see also Section 6.2.5). The good agreement between the observed data in black and the reference data in blue indicates that no significant weak modes are present.

The baseline alignment constants described in Section 8.1 reflect the best knowledge of the spatial configuration of the position-sensitive devices in the ID that potentially suffer from weak modes. In addition to the online monitoring of the invariant mass and respective kinematics of different resonances serving as an alert system, the two methods sensitive to a potential sagitta bias, namely $Z \to \mu\mu$ and E/p are run on a collected data set with suffice statistics to populate sagitta bias correction maps in (η, ϕ) with a decent granularity. Sufficient statistics is collected after two to three runs for the $Z \to \mu\mu$ method depending on the instantaneous luminosity delivered by the LHC and corresponds to $\mathcal{O}(\sim 300000)$ events for the 2016 data set. Figure 8.7 illustrates the sagitta biases in an early subset of the 2015 data set with the initial alignment baseline constants as a function of the ID coordinates for the $Z \to \mu\mu$ and E/p methods. The methods are found to be in good agreement. Due to the larger size of the muon sample, the granularity is increased with respect to the electron sample. The two sagitta bias maps show

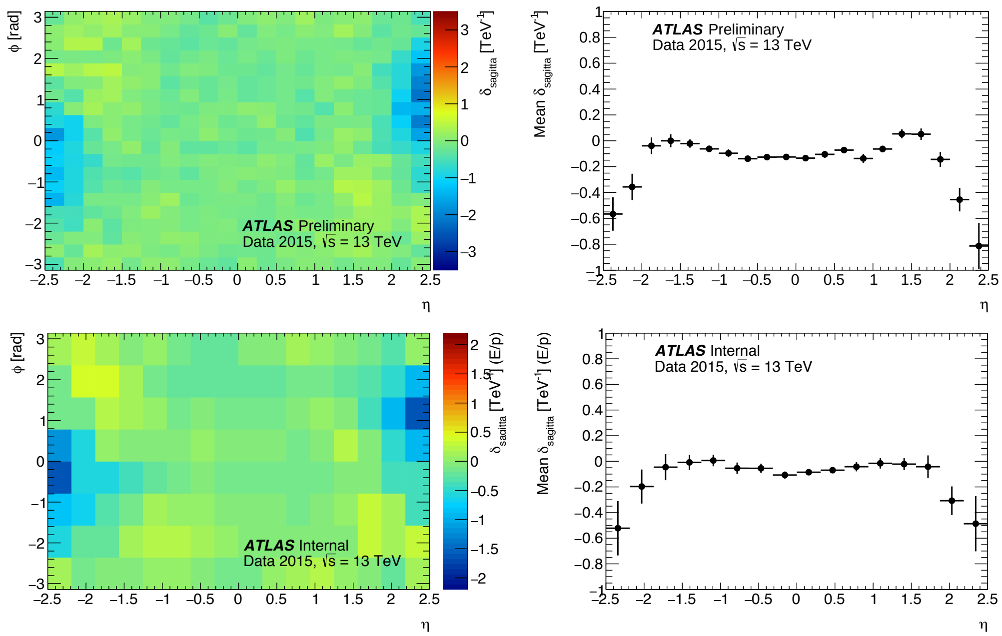

Figure 8.7: Derived sagitta bias corrections $\partial_{\text{sagitta}}$ as function of the ID detector acceptance in (η, ϕ) (left) and the profile with respect to η (right) in an early 2015 data set. The top (bottom) plots show the sagitta corrections derived by the $Z \to \mu\mu$ (E/p) method.

small biases that do not exceed 0.1 TeV^{-1} in the central detector region ($|\eta| < 2.0$). The mean sagitta bias is -0.17 TeV^{-1} integrated over the full acceptance which corresponds to a $\sim$1% ($\sim$8%) bias for $p_{\text{T}} = 50$ GeV (500 GeV). The bias can increase up to $\sim$4% ($\sim$30%) for $p_{\text{T}} = 50$ GeV (500 GeV) in the forward region ($|\eta| > 2.4$). Figure 8.8 shows the IP corrections derived with the $Z \to \mu\mu$ method based on the same early subset of the 2015 data set.

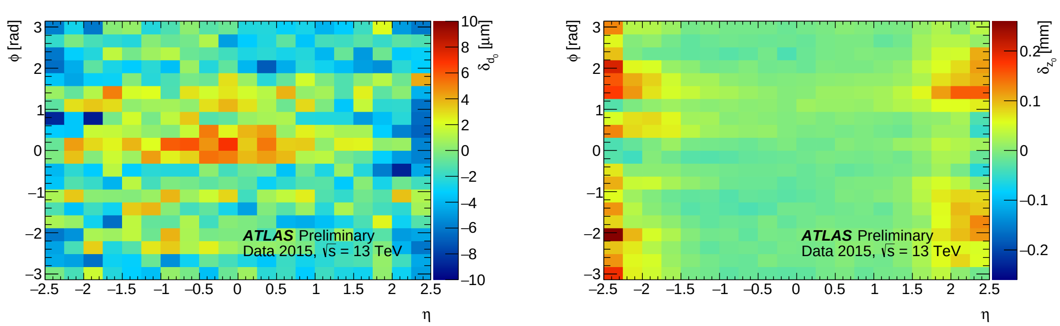

Figure 8.8: Derived IP corrections ∂_{d_0} (left) and ∂_{z_0} (right) as function of the ID detector acceptance in (η, ϕ) in an early 2015 data set as derived by the $Z \to \mu\mu$ method.

As previously mentioned, to avoid biased physics measurements it is of importance to either eliminate the present weak modes or to assess systematic uncertainties. During Run II data taking two different strategies were followed by the ATLAS Collaboration depending on the time line. The long term plan incorporates a "best" alignment baseline through improvements of the χ^2 of the alignment procedure with additional constraints using external information from either different track sources or universal measurements that depend on track parameters (see Equations (8.6) and (8.7)). In practice, (η, ϕ) dependent correction maps that were derived from the E/p and $Z \to \mu\mu$ method are used as additional constraints in the track-based alignment to provide new baseline alignment constants which reduced the track parameter biases in data. This plan relies on a reprocessing of the recorded data which is extremely CPU extensive, expensive and time consuming. Figure 8.9 shows the sagitta bias maps before and after an improved alignment baseline used for the reprocessing of the 2015 data set. After reprocessing, the mean sagitta bias is 0.004 TeV^{-1} integrated over the full acceptance which corresponds to a ~0.02% (~0.2%) bias for $p_{\mathrm{T}} = 50$ GeV (500 GeV). This is a significant improvement over the

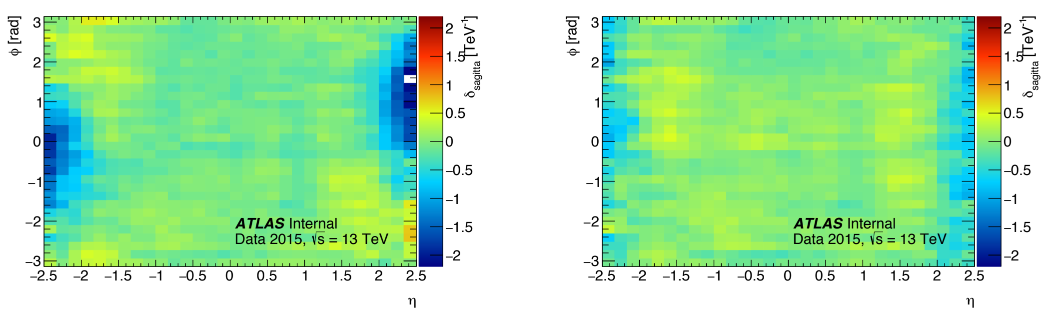

Figure 8.9: Derived sagitta bias corrections $\partial_{\mathrm{sagitta}}$ as function of the ID detector acceptance in (η, ϕ) before (left) and after (right) reprocessing of the 2015 data set based on improved baseline constants derived through iterative IP and sagitta correction map constraints and an updated IBL geometry.

initial baseline alignment and is of the order of the end of Run I alignment performance with a mean sagitta bias of 0.009 TeV^{-1} [147]. It is important to note that the derivation of baseline alignment constants relies on extended periods with stable detector condition. The updated alignment constants were derived with an updated IBL geometry description [148]. The biases for $|\eta| > 2.0$ relate to EC mis-alignments and were improved by a Level 2 alignment of the silicon detectors. The IP biases were improved through a Level 3 alignment.

The short term plan was and is still to provide tools that collaborators can use to either apply corrections to the track parameters as in situ calibration on the existing data or to mimic the biases in MC simulations to apply a systematic uncertainty on the track parameters before and also after alignment constant updates. Figure 8.10 shows the observed sagitta biases as a function of the ID acceptance in a subset of the 2016 data set before and after in situ correction of the q/p_{T} parameter. The bias is removed after application of the provided tool. Figure 8.11

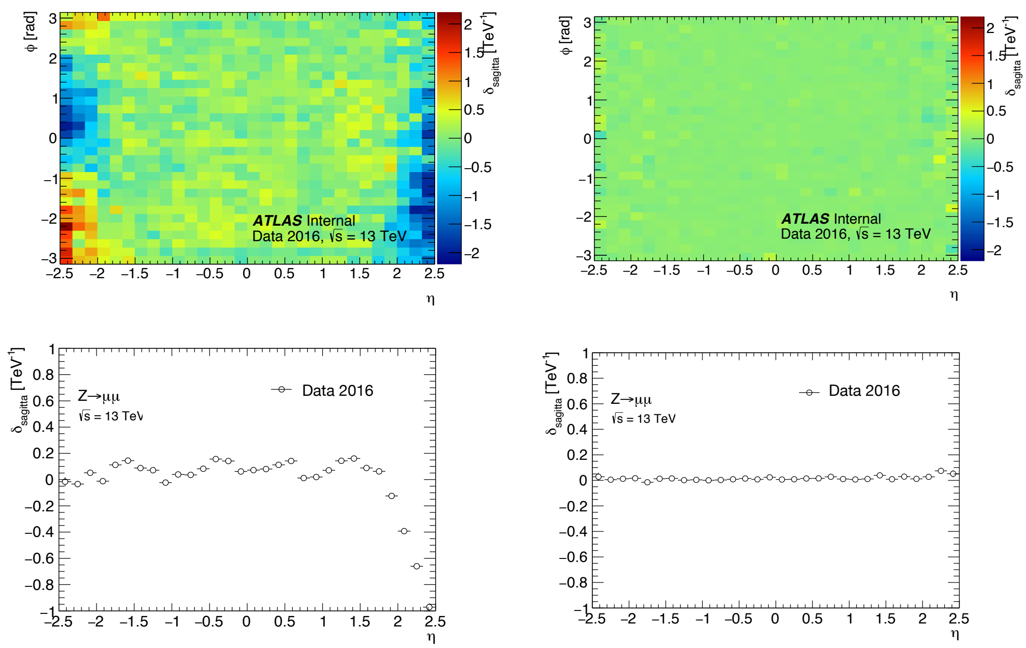

Figure 8.10: Derived sagitta bias corrections $\partial_{\mathrm{sagitta}}$ as function of the ID detector acceptance in (η, ϕ) before (left) and after (right) in situ correction of the q/p_{T} parameter per ID track on an event-by-event basis for an example run in 2016.

shows the η profile of the sagitta bias correction map for a subset of the 2016 data set. The uncertainty bands are calculated by adding in quadrature the statistical uncertainty with two systematic components. The first component accounts for the observed differences between the E/p method and the $Z \to \mu\mu$ method (due to neglection of second order terms in invariant $\Delta \mathrm{m}^2(Z)$ calculation) whereas the second component takes into consideration differences observed in subperiods of the studied data set. The nominal sagitta correction maps as well as the uncertainty maps are provided in order to estimate systematic uncertainties on the residual misalignment effects of the alignment procedure. A similar procedure is in place for the IP biases.

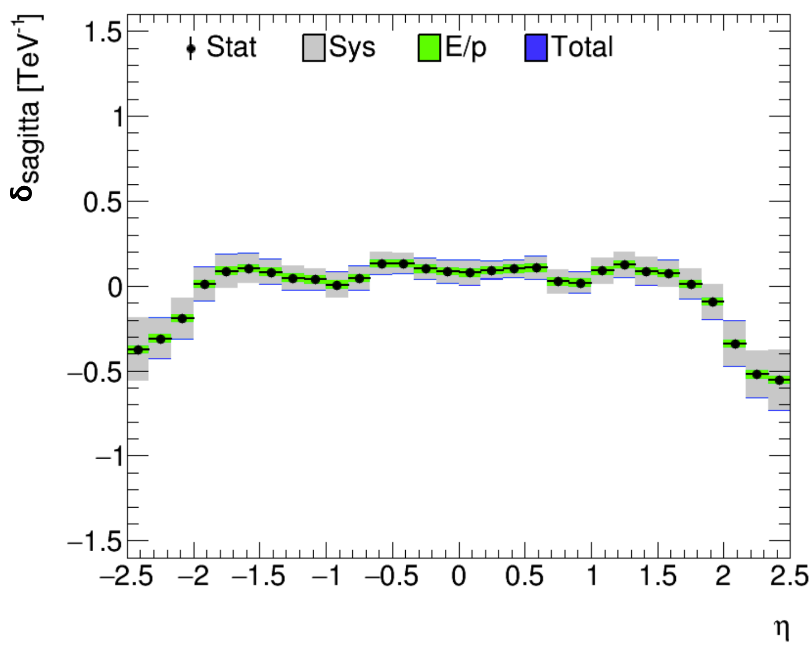

Figure 8.11: Derived sagitta bias corrections $\partial_{\text{sagitta}}$ as function of η for a subset of the data set recorded in 2016 including statistical and systematic uncertainties.

Chapter 9

Event Modelling and Simulation

This chapter of the thesis describes the physics process modelling and the simulation of events following theory predictions described in Part I. The collected data by ATLAS demands precise comparison to background and signal predictions that, unless they are fully derived from data-driven methods, stem from predictions of modern MC event generators. These are computer packages enabling the generation of events on the basis of pseudo-random number generation that converge towards the predicted kinematic distributions of the generated particles. MC methods are also employed to model the interactions of the generated particles with the detector material. A brief summary of state of the art MC for event generation is given in Section 10.1. Section 9.1 summarises the modelling of physics processes in pp collisions incorporating all necessary pieces from process event prediction to detector simulation and digitisation. Chapter 10 summarises studies performed to improve the $t\bar{t}$ MC modelling that led to the choice of the nominal sample and the assessment of the associated systematic uncertainties in the analyses presented in this dissertation as well as other ATLAS searches and measurements.

9.1 Particle Production at the LHC

The ATLAS simulation model [149] can be divided into four stages in its simplified form. The prediction of a hard physics process through generation of partons from the Matrix Element (ME) calculation in form of particle four vectors and evolution of their respective decay, fragmentation and hadronisation into colour neutral states is described by the first stage referred to as *Event generation*. The final state particles are then propagated through an ATLAS detector simulation and their interactions with the detector material is modelled; this is referred to as the *Detector simulation*. The resulting detector measurements (hits) are then digitised, denoted as *Digitisation*. The output format of this step is identical to the ATLAS DAQ output and is propagated through the same trigger and reconstruction chain as data in order to define and calibrate physics objects. The latter stage is called *Reconstruction* (see Part III). This section describes in broad terms the ATLAS simulation model.

9.1.1 Event Generation

The factorisation theorem

The particle collisions probed at the LHC demand the description of the hard partonic scattering process at high momentum transfers, Q^2, and the production of complex final states. The event generation spans a wide range of energy scales, forms the basis of inclusive and exclusive precision measurements, and allows to accurately probe complex final states in "extreme" regions of phase space such as these exploited in searches for new physics phenomena. The hard partonic cross section calculations can be described in pQCD due to asymptotic freedom in which α_S is small at large Q^2. Instead, analytical calculations in the low-energy regime, at which confined colourless states are formed are not feasible (non-pQCD regime). Moreover, strongly interacting particles at high energy scales emit gluons that in turn split into $q\bar{q}$ pairs until the partons reach the hadronisation scale Q_0 ∼1 GeV, at which point they combine and form colourless hadrons (see Section 9.1.1). The *factorisation theorem* [150] enables the factorisation of non-perturbative (long distance) from the perturbative (high energy) dynamics in QCD under the presence of a hard probing scale, Q^2, in the hadronic cross section calculation. The cross section for hadron A, h_A, interacting with hadron B, h_B, resulting in a partonic final state (N), $\sigma_{h_A h_B \to N}$ is given by:

$$\sigma_{h_A h_B \to N} = \sum_{i,j} \int \mathrm{d}x_A \mathrm{d}x_B \; f_{i/h_A}(x_A, \mu_F^2) f_{j/h_B}(x_B, \mu_F^2) \; \hat{\sigma}_{ij \to N}(x_i, x_j, \mu_F^2, \mu_R^2), \qquad (9.1)$$

in which indices i and j represent the partons within hadrons A and B, respectively. The different terms of the equation represent the parton level ME, the PDFs, and the integration over the corresponding phase space. The different terms factorise and are connected by different energy scales. A summary and description of the different terms is given in the following. The *hard process* is described by the hard partonic cross section, $\hat{\sigma}_{ij \to N}(x_i, x_j, \mu_F^2, \mu_R^2)$, which is the production cross section of final state N through the interacting partons i and j. It is described in more detail in one of the following paragraphs.

Parton distribution functions The PDFs, $f_{i(j)/h_A(h_B)}(x_A(x_B), \mu_F^2)$, describe the probabilities of finding a parton i (j) carrying a relative momentum fraction $x_A(x_B)$ of the total momentum of hadron $h_A(h_B)$. The PDFs depend on the momentum fractions as well as Q^2 of the hard process. Thus, the structure of the hadron is dependent on the energy scale at which it is being probed. The Q^2 dependence allows one to describe the evolution from a known scale Q_0^2 to a higher scale Q^2. This evolution is described by the so called Dokshitzer-Gribov-Lipatov-Altarelli-Parisi (DGLAP) equations [151–153]. A scale, μ_F^2, referred to as the *factorisation scale*, generally assumed to be the same for the two hadrons, is introduced to separate the low momentum regime that is governed by the PDFs from the short distance hard process regime. PDFs are universal measurements and extracted from global fits to data [154–157] mostly obtained in Deep-inelastic scattering (DIS) ep collisions at the HERA accelerator at DESY in Germany as well as hadron collider data.

The hard partonic cross section The hard scattering partonic cross section or hard process, $\hat{\sigma}_{ij\to N}$, provides information on a specific N-particle final state. At LO and for processes that do not have high final-state particle multiplicities, the number of MEs that need to be calculated is rather small whereas for increasing orders in perturbation theory or increasing particle multiplicities, the number of MEs that need to be taken into consideration significantly increases. The hard process calculation of $N + x$ at *all* orders with an inclusive arbitrary final state N is

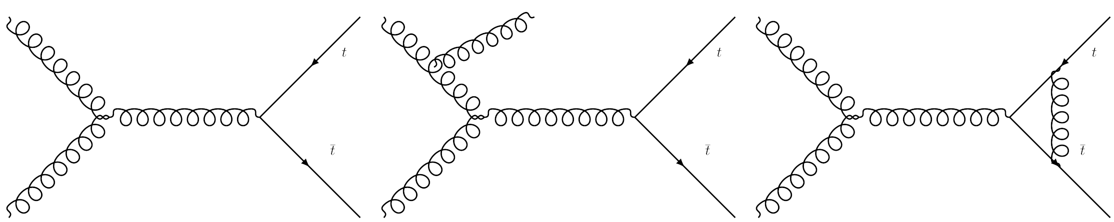

Figure 9.1: A subset of LO (left), first real emission (middle), and virtual correction (right) Feynman diagram for gluon initiated $t\bar{t}$ production.

schematically expressed as:

$$\hat{\sigma}_{ij\to N} \sim \underbrace{\sum_{x=0}^{\infty} \int d\Phi_{N+x}}_{\sum_{\text{legs}}} \underbrace{\left| \sum_{k}^{\infty} \mathcal{M}_{N+x}^{k} \right|^2}_{\sum_{\text{loops}}} . \tag{9.2}$$

The two sums run over both all "real emissions" x denoted as *legs* and overall "virtual corrections" k denoted as *loops*. The integrated full phase space with x additional legs is defined by Φ_{N+x}. The hard ME is a sum over the Feynman diagrams describing the process under investigation. Automated computer programs are needed to build and calculate a large number of Feynman diagrams. Figure 9.1 illustrates a subset of Feynman diagrams for gluon initiated $t\bar{t}$ production at LO ($x = 0, k = 0$), first real emission ($x = 1, k = 0$) and virtual correction ($x = 0, k = 1$). For higher-order processes the multidimensional phase space integration becomes inefficient due to its CPU time consumption [158]. The truncation of the infinite perturbative series calculation at a fixed order can be expressed by varying values of x and k. Inclusive production of N at LO corresponds to $x = 0, k = 0$. LO production for $N + q$ jets is expressed by $x = q, k = 0$. N^{q}LO for inclusive N production is achieved by $x + k \leq q$, which includes $\mathrm{N}^{\mathrm{q}-1}$LO for $N + 1$ jet, $\mathrm{N}^{\mathrm{q}-2}$LO for $N + 2$ jets, $\ldots$ to LO for N+q jets. Multi-leg LO production is realised by $x \geq 1, k = 0$. Calculating $\hat{\sigma}_{ij\to N}$ at a fixed order in pQCD introduces a dependence on the *renormalisation scale*, μ_R^2 (that is generally set to the same value as μ_F^2). This non-physical scale is introduced as a cut-off parameter in order to deal with Infrared (IR) divergences occurring at higher-orders in perturbation theory due to both real emissions and virtual corrections. Virtual corrections lead to divergent contributions to the calculated scattering amplitude. Real radiation of soft (divergence for $E \to 0$ with E the energy of the radiated parton relative to the parent) and collinear (divergence for $\theta \to 0$ and $\theta \to \pi$ with θ the opening angle of a parton emission) partons produce kinematic singularities that also lead to IR divergent contributions after integration over the phase space of the emitted partons. Although such divergences must cancel out for the calculation of inclusive cross sections following the KLN-theorem [159, 160], fixed order calculations suffer from divergences remaining at n orders in the perturbative expansion in form of terms including logarithms $\ln(Q^2/\mu_{F,R}^2)$ appearing in each order in the perturbation expansion and thus hinder the convergence of perturbation series, leading to singularities in the phase space integration. To guarantee convergence of the perturbation series, the logarithmic terms need to be resummed to all orders which is either done analytically or numerically. The former approach is carried out by different subtraction schemes, such as the FKS subtraction scheme [161], that are used to serve as a universal formalism for the analytic cancellation of IR singularities. The numerical method is performed by the so-called Parton Shower (PS) algorithms.

Parton showering

PS algorithms aim to capture the higher order contributions from QCD not covered by the hard process in an approximated manner and below the IR cut-off scale. The PS accounts only for the dominant contributions at each order, adding soft gluon emissions and nearly collinear parton splittings successively to initial and final state partons while omitting virtual corrections.

The cross section for a nearly collinear splitting of a parton i into partons $j+k$ for the differential cross section after the splitting $\mathrm{d}\sigma_{\mathrm{n+1}}$ is given by:

$$\mathrm{d}\sigma_{n+1} \approx \mathrm{d}\sigma_n \frac{\alpha_S}{2\pi}\frac{\mathrm{d}\theta^2}{\theta^2} P_{ji}(\mathrm{z},\phi)\,\mathrm{d}z\,\mathrm{d}\phi, \tag{9.3}$$

where θ and ϕ are the opening and azimuthal angle of the splitting and $P_{ji}(z,\phi)$ provides the probability of parton i splitting into two partons with j carrying a fractional momentum amount z of parton i. Three splittings are possible: $q \to qg$, $g \to gg$, and $g \to q\bar{q}$. The splittings are iteratively repeated using MC methods to generate values for z, θ, and ϕ until the virtual mass, q^2, of the two resulting partons drops below the hadronisation cut-off scale $Q_0^2 \sim$ 1 GeV^2.

The virtual corrections at each respective order in perturbation theory, that already evaluate the real parton emissions, are taken into account through Sudakov form factors, $\Delta_i(q_1^2, q_2^2)$. They describe the probability of a parton to *not* split during the evolution step from q_1^2 to q_2^2:

$$\Delta_i(q_1^2, q_2^2) = \exp\left(-\sum_j \int_{q_2^2}^{q_1^2} \int_{z_{\mathrm{min}}}^{z_{\mathrm{max}}} \mathrm{d}P_i\left(z, q^2\right)\right) \text{ with } \mathrm{d}P_i\left(z, q^2\right) = \frac{\alpha_S}{2\pi}\frac{\mathrm{d}q^2}{q^2} P_{ji}(z)\,\mathrm{d}z. \tag{9.4}$$

Final State Radiation (FSR) is generated through the procedure just described, whereas Initial State Radiation (ISR) depends on so called *backward evolution*. The momentum fractions of the incoming partons leading to the hard scatter are taken at the hard process scale and are evolved backwards towards the low scale of the incoming protons. The assumed virtual masses and momenta in the backward evolution follow momentum conservation at each successive splitting in the shower evolution [162]. In the described shower evolution the virtual mass of the two produced partons was used as *evolution variable*. However, different evolution variables are used in different PS shower algorithms.

Matching

The combination of fixed-order ME calculations with PS algorithms is not simply obtained by adding a parton shower to a generated event by the ME calculation. Matching schemes are used to match the fixed-order ME calculations to the PSs to avoid double counting of configurations that can be obtained from both or to miss configurations. A $N+1$ final state from the ME calculation and the first radiation from the PS algorithm that starts from $N+0$ will result in a double counting. An event-by-event assessment is used to decide which configuration should be described by which part (the ME or PS), with preference given to the one resulting in the best possible approximation of the underlying event kinematics controlled by a matching scale.

Fixed-order MEs provide a good description of well separated hard partons. Their description of collinear and soft parton emissions is not optimal as large logarithmic contributions occur at higher orders. Moreover, the description of MEs for high parton multiplicities is cumbersome. Soft, low-angle emissions and high particle multiplicities are often modelled more accurately by PS algorithms. Hadronisation models depend on a good description of soft- and collinear multi-parton states (see next section). Therefore, a combination of the ME calculation with the PS algorithm is desirable to provide a realistic model.

Matching prescriptions separate the phase-space into two distinct regions. The short distance region is described by the hard scattering partonic cross section that depends on the calculations of the MEs and the long distance region that is described by showers ensuring the evolution of the high energy particles to low energy hadrons as described previously.

In the long distance region, real-emission and virtual corrections are both generated by the shower and in the short distance region, the real corrections are generated by the MEs while the virtual corrections are still generated by the shower. The phase-space separation needs to be as smooth as possible between the two regions which is ensured by applying matching procedures [163]. Simply speaking, events are discarded if ME partons are too soft or if the PS generates radiation that is too hard. For the matching at tree-level, that involves the simultaneous treatment of final states with different multiplicities, several solutions are available such as CKKW [164, 165] and MLM [166]. At NLO, two methods namely MC@NLO [167] and POWHEG [168, 169], are used to match the hard ME calculations to PS algorithms. A detailed overview and a dedicated description of different matching schemes at LO and NLO is given in Ref. [170].

Hadronisation

The partons produced during a proton interaction shower and evolve from high energy scales down to energy scales at which the virtual masses of the partons are $\mathcal{O}(Q_0 \sim 1$ GeV). At this energy QCD confinement effects start to dominate, causing the recombination of partons into colourless final state hadrons. The QCD dynamics in that regime are of non-pQCD nature and hence rely on tuneable phenomenological models such as *string fragmentation* [171, 172] or *cluster hadronisation* models [173, 174].

The string fragmentation model is based on the idea that partons are connected by gluon strings as representation for the relative strength induced by the strong interaction between the partons. During the evolution, the strings can stretch proportionally to the distance between the partons. The farther apart the partons, the higher the potential energy. If the latter is $\mathcal{O}(\sim Q_0)$, it is energetically favourable to break the string which results in the creation of a new $q\bar{q}$ pair. The resulting string segments will undergo the same procedure until convergence is reached through conversion of all energy into $q\bar{q}$ pairs.

The cluster hadronisation model forces gluons in the shower evolution to undergo a $q\bar{q}$ splitting and to combine to colourless clusters at $\mathcal{O}(\sim Q_0)$. Based on the masses of the clusters, different sequential cluster decays are performed until all clusters are confined.

Underlying event

In addition to the partons taking part in the hard process, the other parton remnants of the colliding protons interact and form additional hadrons interacting with the detector. Any additional hadronic activity within a given pp collision not related to the hard scatter is referred to as Underlying event (UE). Since such interactions take place at low energy scales, phenomenological models are used and tuned to data [175, 176]. A general definition of UE is composed of Multi Parton Interaction (MPI) and beam remnants. ISR off the particles in the hard interactions is not considered as UE [177]. MPI are characterised by multiple hard parton scatterings per proton collision in addition to the hard scatter. Beam remnants are all parton interactions occurring during a pp collision that did not yield an inelastic scattering but are connected to the hard scatter through colour flow [178].

Hadron decays

After finalisation of the hadronisation process, unstable hadrons are decayed according to their measured branching modes and lifetimes, as summarised in Ref. [11]. A requirement during event generation is that the branching ratios for all decays of a given hadron need to yield unity. This leads to the necessity of assumptions on the modelling of decay modes that are not yet experimentally well determined such as some of the decay of hadrons constituted of heavy-flavour quarks. Kinematic information of multi particle decay signatures as well as spin correlations between the decay products need to be considered.

9.1.2 Detector Simulation and Digitisation

The output of the event generation is a set of stable[7] particles that were produced during the generated event and is denoted as *particle level*. However, in order to compare the predicted events with data, at the so called *reconstruction level*, the generated particles are propagated through an ATLAS detector simulation using GEANT 4 [179, 180]. This framework simulates the particle interactions occurring with the detector material. The material description is provided by the ATLAS geometry model and includes the detector conditions. Each generated particle traverses the detector elements resulting in information on the deposited energy, position, and time of the interaction. However, this Full Simulation (FullSim) is computationally expensive. Therefore a fast simulation, referred to as *ATLFAST II (AFII)* [181] or FastSim is employed in some cases. It is based on a simplified detector model and exploits parameterisations of the expected detector response. The fast simulation of the calorimeter [182] propagates a subset of particles per event through the calorimeters using a parametrisation of the longitudinal and lateral shower development.

The output of the detector simulation are hits in sensitive detector elements that are transformed into voltages or currents following a digitisation procedure. Hits are then overlaid with simulated pile up events, obtained from minimum bias measurements [183], and detector noise.

9.1.3 MC Prediction Corrections

The production rate of simulated MC events are corrected using so called k-factors that scale the inclusive cross section used to generate the events to the highest fixed order calculations available. The samples are scaled to the corresponding luminosity of the recorded data set and are weighted to match the pile up profile $\langle\mu\rangle$. In addition, scale factors and smearing are imposed to the simulation in order to correct for limitations in the simulation. More details on these corrections are given in Chapter 7 and Part IV.

[7]Particles are considered as stable at particle level if they have a minimum mean lifetime of $\tau = 30$ ps.

Chapter 10

MC Sample Production

This chapter gives a short summary and overview of MC event generators with a focus on those used in the analyses presented in Chapters 13 and 14. In addition, ATLAS wide MC tuning efforts are outlined. Specific "Top MC" tuning optimisations for event generators used for $t\bar{t}$ pair production is explained.

10.1 Event Generators

The accuracy of theoretical predictions in pp collisions has significantly increased in recent years in order to match the needs stemming from the capabilities of the LHC experiments. A brief description of a variety of physics processes beyond LO accuracy as well as an implementation of the full event generation chain is given here. Automated computations of fixed-order total and differential cross sections for various processes are available. This yields to predictions of the final products of hard process ME calculations, which are then matched to PS algorithms that describe the evolution of the final state particles at *parton level* to the final hadrons defining *particle level*, as described in the previous chapter. In principle, the development of the fully automated event generation chain of MC generators provides the opportunity to generate processes without restrictions on the complexity and particle multiplicities of the processes. In practice, the main restrictions of the event generation are related to accompanied computational costs with the increasing complexity or particle multiplicities. Thus, current tools are more limited when simulating the full production and decay chain at NLO in a reasonable amount of time. So far, only the generation of undecayed events at NLO accuracy is feasible. The enormous CPU time-consumption for NLO predictions still sometimes justifies the usage of LO generators. The predictions of the various MC generators available on the market need to be evaluated taking into account a variety of aspects both on the modelling side and on the side that deals with the evaluation of the theoretical uncertainties associated with the model. The following paragraphs provide a non-complete overview of commonly employed event generators in the High Energy

Physics (HEP) community.

PYTHIA [184, 185] Is a general purpose event generator that can describe the full ME and PS for e^+e^-, $p\bar{p}$ and pp collisions. Up to $\mathcal{O}(200)$ $2 \rightarrow n$ hard processes with $n < 4$ mostly at LO are available. It provides processes both for SM and BSM physics. PYTHIA 6 employs the mass virtuality or transverse momentum as evolution variable for the evolving partons in the PS whereas PYTHIA 8 in addition is capable of a so called dipole shower. PYTHIA has an exhaustive description for MPI modelling implemented. Both versions make use of the lund string model for hadronisation. PYTHIA 8 constitutes a complete stand-alone event generator and replaces the predecessor PYTHIA 6 whose further development is stopped.

HERWIG [186, 187] Is a general purpose event generator for $2 \rightarrow 2$ hard processes including the decays with full spin correlation considerations. It can model e^+e^-, ep, and hadron-hadron interactions. In addition to a wide vast of SM processes, it can be used for a variety of BSM models. It uses the emission opening angles as evolution variable for parton showering. The cluster model is employed for the hadronisation and UE description. An interface to JIMMY allows for the UE modelling. The C++ version of HERWIG is Herwig++. Herwig++ 3.0 is referred to as HERWIG 7. A recent development is the implementation of NLO hard process handling that can be matched to both PSs via the POWHEG or MC@NLO method. A second parton shower based on dipole showering is also implemented.

POWHEG [188–190] Is an event generator providing a set of hard processes at NLO accuracy with a single hard emission. In the experimental HEP community, POWHEG-BOX is commonly but mistakenly referred to as the POWHEG MC event generator. POWHEG-BOX [191] is a general framework that implements the set of processes and also serves as the interface between the NLO calculations and the PS programs such as PYTHIA 6/8 and Herwig++/HERWIG 7 by making use of the matching method POWHEG. PYTHIA or HERWIG are only employed for the modelling of subsequent parton showering, hadronisation, and UE.

MADGRAPH5_aMC@NLO [192–194] MADGRAPH5_aMC@NLO implements a fully automated approach to complete event generation at NLO accuracy and is based on the MADGRAPH 5 package. Automation refers to the ability of MADGRAPH5_aMC@NLO to calculate MEs that produce particle four vectors that can be matched to PS programs such as PYTHIA 6/8 and HERWIG.

Both multi-leg LO and single emission NLO calculations are implemented. Events produced at NLO are matched to the PS algorithms via the MC@NLO method. Spin correlation effects for both the decay and the production of generated particles in MadGraph5_aMC@NLO can be included using MadSpin.

Sherpa [195] Is a multi purpose event generator providing hard processes at LO and NLO. It models the parton shower, UE, hadronisation, and hadron decay of the produced events. Both multi-leg LO and single emission NLO calculations are implemented. The GoSAM package [196] is used to generate the virtual corrections and is linked to Sherpa that uses Amegic [197] as ME generator. The matching of NLO ME calculations with the PS part of Sherpa is implemented using the MC@NLO method.

Protos [198] Is an event generator implementing new physics processes, in particular those involving top-quarks and BSM top partner physics processes. The ME calculation is performed at LO. The generated events can be interfaced to PS programs.

10.2 MC Generator Tuning

The soft QCD processes, modelled phenomenologically, need to be tuned to data in order to yield a reliable prediction and to assess uncertainties on the predictions. MC generator models thus have free parameters that need to be adjusted such that they are in agreement with sensitive observables measured in data. The process of adjusting the free parameter set is denoted as *MC tuning*. A dedicated tune for the event generator Pythia 6 was established in 2012 and the set of tunes is referred to as Perugia2012 [199]. This set was employed to assess the baseline and systematic sample set for $t\bar{t}$ production for the initial phase of Run II. Systematic tune variations that were used for the assessment of systematic uncertainties corresponded to the RadLo and RadHi systematic sets. These varied the α_S values impacting the amount of ISR and FSR with sensitive MPI settings [199].

The MC tune currently used in Run II in ATLAS is the A14 tune [200] and is based on adjusting a set of the free parameters in Pythia 8. The A14 tune simultaneously tuned parameters within a pre-defined range. The tuned parameters are related to MPI, the interface between ME and PS, and colour flow between the beam remnants and the partons in the hard interaction. The observables were mostly based on Run I ATLAS results sensitive to the UE, structure of jets, and those sensitive to additional jet emissions. The main scope of the A14 tune is to tune ISR, FSR, and MPI. A set of tune variations was established, varying the parameter values from their nominal tuned values with regard to disentangling effects from UE, jet structure, and additional jet production. The tune variations provide maximal coverage of the observables used to tune in the respective categories. The employed tune variations for the assessment of systematic uncertainties with regard to the $t\bar{t}$ production are denoted as VAR3C. This set tunes the α_S value that is nominally set to $\alpha_S(M_Z^2)$ within $\Delta\alpha_S = \{0.115, 1.140\}$. The α_S value impacts the amount of ISR as can be seen in Equations (9.3) and (9.4).

10.3 Top MC Tuning and Systematic Uncertainty Assessment

Of particular interest for the two analyses presented in this dissertation is the nominal model (baseline) of the $t\bar{t}$ background and the assessment of associated uncertainties.

The uncertainty assessment strategy relies on the assumption that the performed variations are independent. Thus, the $t\bar{t}$ uncertainty assessment follows a factorisation approach. The idea of the approach is to disentangle different theoretical components contributing to the MC simulation and assess associated systematics with respect to a single baseline model. The baseline used for the $t\bar{t}$ production is the POWHEG MC generator that is widely used for top-quark event generation in ATLAS and CMS.

The modelling uncertainties can be either of *parametric* or *algorithmic* nature. Algorithmic uncertainties stem from the comparison of distinct methodologies used to model an underlying physics process, each employing a different algorithm. Algorithms are used to model the PS as well as the non-pQCD modelling of the hadronisation and UE. For example, comparing two distinct MC generators while using the same ME calculation assesses a systematic on differences between the algorithms used for PS and UE. Concretely, the events produced by POWHEG are interfaced to either PYTHIA or HERWIG to account for that systematic uncertainty. This difference between these predictions is denoted as the *fragmentation/hadronisation* uncertainty. Next, different matching scheme algorithms are used to match the NLO ME calculation to the PS algorithms. A comparison between the POWHEG method and MC@NLO method interfaced to the same PS algorithm are used to account for an uncertainty referred to as *hard scatter generation* uncertainty. A third $t\bar{t}$ uncertainty is of parametric nature and simultaneously varies parameters related to the ME calculation and those impacting the PS and hadronisation, resulting in more or less ISR and/or FSR. This uncertainty is referred to as the *additional radiation* uncertainty. The hadronic cross section defined in Equation 9.1 is fully specified only for a given

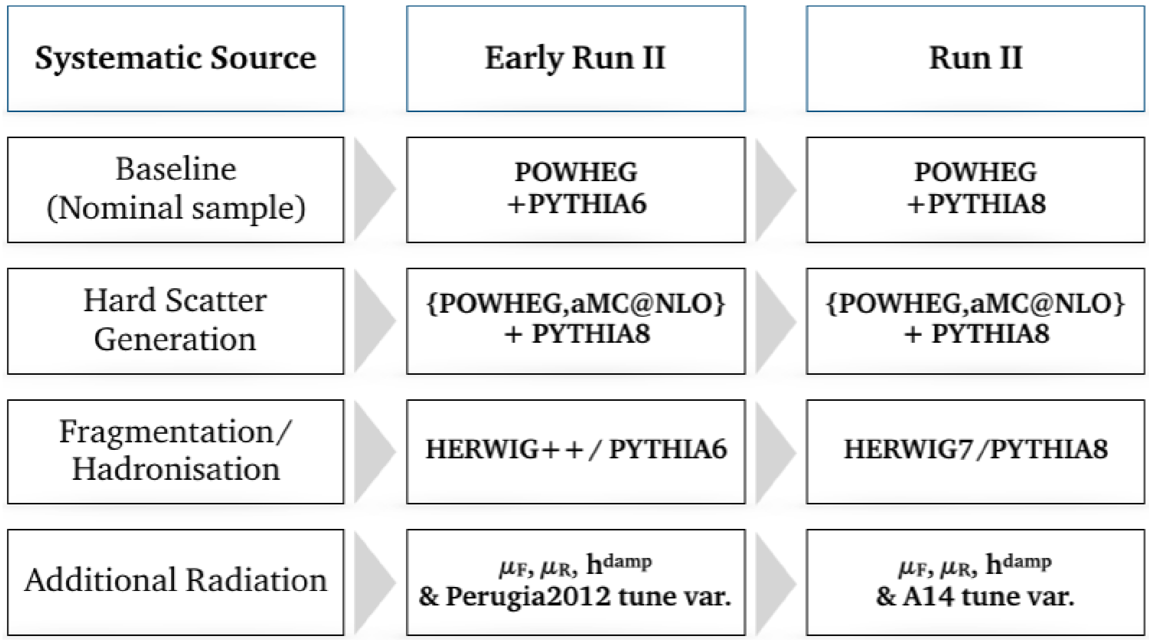

Figure 10.1: A schematic overview of samples constituting the modelling baseline for $t\bar{t}$ production and associated uncertainties in an early stage of Run II and subsequent Run II.

PDF set and a certain choice of the unphysical factorisation and renormalisation scale $\mu_{F,R}$. Both scales cannot be derived from first principles. The choice of their central value is arbitrary but guided by prior knowledge of different classes of hard scatter processes. A common choice is to equate both scales to the hard scale Q^2 of the process which also serves as the starting scale for the ISR and FSR evolution. The scale choice can either be static or dynamic. Static scales do not depend on individual event kinematics, whereas dynamic scales do. A static scale is often chosen for processes that are probed at their production threshold, whereas dynamic scales are used for the description in regimes with higher transverse momenta of the final state particles. The choice of the scale impacts both the overall normalisation as well as the underlying event kinematics. The order of the QCD calculation needs to match the order used to fit the PDF to allow for factorisation. A variation of the nominal scale choice represents an estimate for contributions from unpredicted higher order terms and results in an associated systematic uncertainty. A common choice is a variation of the nominal scale by a factor of two up and down. The hardest emission (leading p_{T}) in the POWHEG method is controlled by a so called resummation damping factor, h^{damp}. It effectively regulates the high p_{T} emission and thus its recoil against the $t\bar{t}$-system.

In order to both provide a reasonable baseline and to assess systematic uncertainties, a global tune such as PERUGIA or A14 is combined with additional specific "Top MC" tunes. This effort is necessary to improve the modelling between the MC generator prediction and measured spectra after unfolding for the detector response back to particle level or parton level [201, 202]. The Top MC tune optimises additional parameters related to the ME calculation, PS, or hadronisation, namely $\mu_{F,R}$, h^{damp}, and global tune variations. An overview of two $t\bar{t}$ baseline models and their associated uncertainties, based on the previously introduced factorisation approach, and employed in the two analyses presented in Chapters 13 and 14, is given in Figure 10.1. The baseline and systematic samples are detailed in the following paragraphs.

Initial Run II $t\bar{t}$ setup The $t\bar{t}$ baseline sample was generated with POWHEG-BOX V2 [188–190] interfaced with PYTHIA 6.428 [203, 204] using the CT10 NLO PDF set. PYTHIA 6 parameters are set to the PERUGIA2012 tune [199] prepared with the CTEQ6L1 LO [205] PDF set. The h^{damp} parameter was set to the mass of the top-quark, m_{top}. The nominal $\mu_{F,R}$ is set to the dynamic scale $\mu_{F,R} = (m^2_{\text{top}} + p^2_{\text{T,top}})^{1/2}$. The algorithmic and parametric uncertainties are evaluated with additional samples, namely using POWHEG-BOX V2 interfaced with Herwig++ 2.7.1 [186], POWHEG-BOX V2 interfaced with PYTHIA 8.186 and MADGRAPH5_aMC@NLO 2.2.1 interfaced with PYTHIA 8.186 [206]. All samples are generated with FullSim.

Further, samples with POWHEG-BOX V2 interfaced with PYTHIA 6.428 are generated with $\mu_{F,R}$ scales varied from their nominal value by a factor 2 and 0.5 as well as two h^{damp}variations between m_{top} and $2 \times m_{\text{top}}$. In addition, the PERUGIA2012 tune variations RADHI and RADLO are employed [199]. These samples are simulated with FastSim. A more detailed overview is given in Ref. [207]. These samples are used as $t\bar{t}$ baseline and associated systematic uncertainties in the analysis presented in Chapter 13.

Updated Run II $t\bar{t}$ setup The nominal $t\bar{t}$ sample uses the POWHEG-BOX V2 generator employing the NNPDF30 NLO PDF [208] set interfaced to the PYTHIA 8.2 [185] shower, fragmentation and hadronisation model. PYTHIA 8 parameters are set to the A14 tune with the NNPDF23 LO PDF set [209]. The nominal $\mu_{F,R}$ is set to dynamic scale $\mu_{F,R} = (m^2_{\text{top}} + p^2_{\text{T,top}})^{1/2}$. The h^{damp} parameter is set to $1.5 \times m_{\text{top}}$. The sample is simulated with FullSim.

Additional samples used to evaluate modelling uncertainties on the $t\bar{t}$ baseline use FastSim simulation and are generated using POWHEG-BOX V2 interfaced with HERWIG 7 [187], POWHEG-BOX V2 interfaced with PYTHIA 8.2 [185], and MADGRAPH5_aMC@NLO interfaced with PYTHIA 8.2 [206].

Additional $t\bar{t}$ samples with POWHEG-BOX V2 interfaced with PYTHIA 8.2 vary $\mu_{F,R}$ simultaneously by 1/2 (2), use the A14 Var3c Up (A14 Var3c Down) tune variation [200], as well as adjust h^{damp} to 3 (1.5) times m_{top}. A more detailed overview is provided in Ref. [207, 210]. These samples are used as $t\bar{t}$ baseline and associated systematic uncertainties in the analysis are presented in Chapter 14.

The initial Run II set of baseline and uncertainty samples is fully documented in Ref. [207, 211, 212], whereas the improvements for the updated $t\bar{t}$ setup are summarised in Ref. [210].

Top MC tuning With the abundance of top-quarks produced at the LHC a new era of precision measurements is accessible. This allowed, already in Run I, for the precise measurement of differential cross sections to probe and understand the kinematics of the top-quark. However, the combined ATLAS data set from 2015 and 2016 exceeded the number of recorded top-quark events in Run I by a factor of four. The constantly increasing amount of data allows to deepen the understanding of the top-quark modelling in a way never been possible before. The Top MC tuning efforts in the beginning of Run II were performed on a *qualitative basis* and were based on limited Run I information available at that time.

Tuning studies are preferentially performed at particle level in a well defined phase space in order to be independent of potential detector effects while also avoiding the expensive detector simulation step that is required for comparisons at reconstruction level. This makes a MC generator to MC generator comparison possible without relying on MC generator specific definitions that might be inconsistent. Parton level distributions on the other hand introduce large MC derived uncertainties during the unfolding step, needed to extrapolate to the full phase space (particularly low p_{T} and high η) and are thus not favourable either.

The strategy followed during the tuning campaign was that only one of the identified tuneable parameters was varied at a time and the impact of the variation on sensitive unfolded measured spectra was evaluated. The nominal setting of that parameter was chosen as the parameter value that yielded the best agreement between prediction and data. For the systematic assessment on the additional radiation, MC parameter and global tune variations were varied coherently in such a way that the nominal setting was bracketed by the systematic variations.

A new feature that was made possible already for the Run I differential $t\bar{t}$ cross section measurements is the computation of the full uncertainty correlation matrices for the measured spectra which allows then to assess the agreement with a particular generator setup through a quantitative χ^2 test and p-value extraction. This new tuning approach is now used in the current and future Top MC tuning efforts, thus superseding the qualitative approach. The latter approach is based on the availability of

- unfolded data of the measured spectra,
- full correlation model across bins of the measured spectra incorporating the statistical and the breakdown of systematic components.

In order to ease the concurrent evaluation of a new MC parameter set on a number of measurements, sensitive to various tuning parameters, it is desirable for analyses to provide tested and validated Robust Independent Validation of Experiment and Theory (Rivet) routines. Rivet [213] provides the infrastructure and tools for defining particle level analyses. Therefore, it becomes possible to compare new predictions to a large number of analyses across experiments and collision energies, allowing for a global validation. It is now possible to generate a new MC sample only up to particle level and assess the optimal parameter set in a quantitative manner before starting a computationally expensive large scale reconstruction level production of more than $\mathcal{O}(\sim 10^{10})$ events needed in order to populate "extreme" regions of phase space.

During early Run II data taking, new PS algorithms became available to use within the ATLAS MC generation infrastructure, in particular PYTHIA 8 and HERWIG 7. The initial Run II baseline and systematic assessment was established by tuning predictions to describe ATLAS data based on unfolded cross section and top property measurements at a center of mass energy of 7 and 8 TeV. The consecutive updated Run II Top MC tune included in addition the first unfolded spectra at 13 TeV.

The first unfolded differential $t\bar{t}$ cross section measurements with the complete 2015 data set collected at $\sqrt{s} = 13$ TeV were transformed into Rivet routines [214]. The unfolded spectra were then used to improve and validate the new Top MC tuning and modelling strategy [210]. The first differential $t\bar{t}$ cross sections in Run II were measured at particle level within a kinematic range closely matched to the detector acceptance both in the resolved and boosted analysis channels. Both analysis channels require exactly one lepton, ℓ, which is either an electron or a muon with $|\eta| < 2.5$ and $p_{\mathrm{T}} > 25$ GeV. A cut on $E_{\mathrm{T}}^{\mathrm{miss}} > 20$ GeV and $E_{\mathrm{T}}^{\mathrm{miss}} + M_{\mathrm{T}}^{W}$ [8] $>$ 60 GeV is imposed. In the resolved (boosted) channel at least four small-R jets (at least one large-R jet) are required in the event. The leptonic top-quark is reconstructed requiring at least one small-R jet with $\Delta R(\ell, \text{small-}R\text{ jet}) < 2.0$. The hadronically decaying top-quark is considered as the leading p_{T} large-R jet in the event with $|\eta| < 2.0$, $p_{\mathrm{T}} \in [300, 1500]$ GeV and mass above 100 GeV. A top-tagging requirement based on the N-subjettiness variable $\tau_{32} \equiv \tau_3/\tau_2 < 0.75$[9] [215] and the large-$R$ jet mass is imposed. In addition, the hadronic top needs to be well separated from the small-R jet associated with the lepton in the event (ΔR(large-R jet, small-R jet associated to lepton) > 1.5) and the lepton through $\phi(\ell, \text{large-}R\text{ jet}) >$ 1.0. In the resolved channel, the pseudo-top algorithm [216] is employed to reconstructs the top-quark four momenta from the final states of the top-quark decay products. For the reconstruction the kinematic information of the lepton, $E_{\mathrm{T}}^{\mathrm{miss}}$ and the at least four small-R jets out of which two are required to be b-tagged are used. For ≥ 3 b-tagged small-R jet events, the two with the highest p_{T} are considered as the b-jets.

To illustrate the tuning process, the impact of tuning parameters on the unfolded spectra of the resolved analysis channel is discussed. Figures 10.2 and 10.3 show the unfolded spectra of the resolved analysis for the transverse momentum of the hadronic top-quark ($p_{\mathrm{T}}^{\mathrm{t,had}}$), the $t\bar{t}$ system ($p_{\mathrm{T}}^{t\bar{t}}$), the absolute rapidity of the hadronic top ($|y_{\mathrm{t,had}}|$), and the mass of the $t\bar{t}$ system ($m_{t\bar{t}}$) for both the initial and the updated Run II baseline and associated systematic set. The resolved analysis channel is sensitive to top-quarks with p_{T} of up to 1 TeV in a rapidity range $|y| < 2.0$. Over the full p_{T} range the cross section falls off by $\mathcal{O}(10^3)$. The cross section decreases as a function of the rapidity with most of the top-quarks being produced centrally. The $t\bar{t}$ system is produced centrally with an invariant mass below 1.3 TeV and a transverse momentum typically below 200 GeV. The $p_{\mathrm{T}}^{t\bar{t}}$ and $m_{t\bar{t}}$ are sensitive up to 800 GeV and 3 TeV, respectively.

In Figures 10.2 and 10.3, a difference between data and simulation for the transverse momentum of the hadronic top-quark is noticeable and on the edge of the combined statistical and systematic uncertainty. This feature is a long standing observation present in various anal-

[8] The transverse mass of the leptonically decaying W boson, M_{T}^{W}, is defined as the projection of the W mass on the transverse plane through $M_{\mathrm{T}}^{W} = \sqrt{2 p_{\mathrm{T}}^{\ell} E_{\mathrm{T}}^{\mathrm{miss}} \cdot (1 - \cos(\phi^{\ell} - \phi^{\mathrm{miss}}))}$, with the lepton azimuthal angle ϕ^{ℓ} and $\phi^{\mathrm{miss}} = \arctan E_{\mathrm{y}}^{\mathrm{miss}}/E_{\mathrm{x}}^{\mathrm{miss}}$.

[9] The τ_{32} substructure variable is considered to separate between large-R jets with a sub-jet multiplicity of 3 and 2.

ysis channels, across varying center of mass energies and experiments. A slope was also observed in the unfolded $p_{\mathrm{T}}^{t\bar{t}}$ and $m_{t\bar{t}}$ spectrum in Run I measurements. The Top MC tuning effort started with an optimisation of the h^{damp} parameter [207]. The kinematic variables used for the tuning were chosen to be the ones that are sensitive to additional radiation in the $t\bar{t}$ system namely as $p_{\mathrm{T}}^{t\bar{t}}$, $m_{t\bar{t}}$ and $\mathrm{N_{jets}}$. The previously observed slope was reduced with a choice of $h^{\mathrm{damp}} = 1.0 \times m_{\mathrm{top}}$ and $h^{\mathrm{damp}} = 1.5 \times m_{\mathrm{top}}$ for the initial and updated baseline, respectively, as is shown in Figures 10.2(b), 10.2(d), 10.3(b) and 10.3(d). The observed $p_{\mathrm{T}}^{\mathrm{t,had}}$ slope is not significantly impacted by the choice of h^{damp}. An overall improvement is seen between the initial and updated $t\bar{t}$ baseline in the $p_{\mathrm{T}}^{\mathrm{top}}$, $p_{\mathrm{T}}^{t\bar{t}}$, $|y_{\mathrm{t,had}}|$ and $m_{t\bar{t}}$ spectrum. The latter kinematic variable shows an improved agreement for $m_{t\bar{t}} \gtrsim 350$ GeV, whereas the initial baseline shows a better agreement below that range.

The variations used for the uncertainty assessment are determined such that the systematic variations bracket the tuned baseline in a variety of sensitive unfolded spectra. Figure 10.2 shows the systematic up- and down variations accounting for changes to additional radiation obtained through simultaneous variation of $\mu_{F,R}$, h^{damp}, and the global tune variations for PERUGIA2012 and A14 for the initial and updated systematic set, respectively. The defined up- and down variations lead to the prediction of more and fewer top-quarks with high p_{T}, respectively. The same is observed for the $t\bar{t}$ system variables $p_{\mathrm{T}}^{t\bar{t}}$ and $m_{t\bar{t}}$. Figure 10.3 shows the variations used to assess the systematic uncertainty on the baseline accounting for the hard scatter generation and fragmentation/hadronisation model for the initial and updated systematic set. The fragmentation/hadronisation uncertainty is reduced for the measured spectra between the initial and updated systematic set with an overall improved description of the data by POWHEG +HERWIG 7.

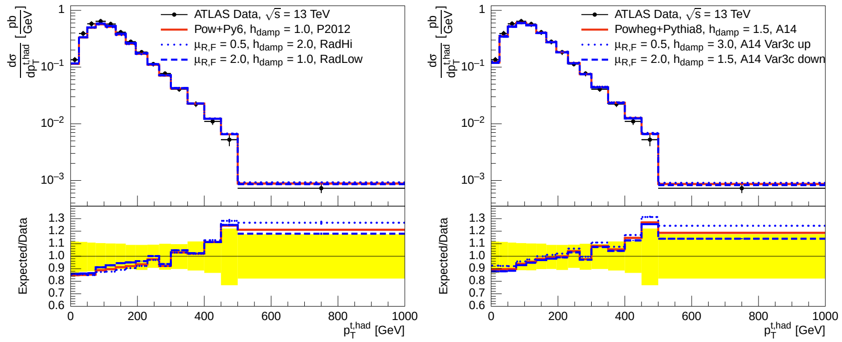

(a) $p_T^{t,\mathrm{had}}$

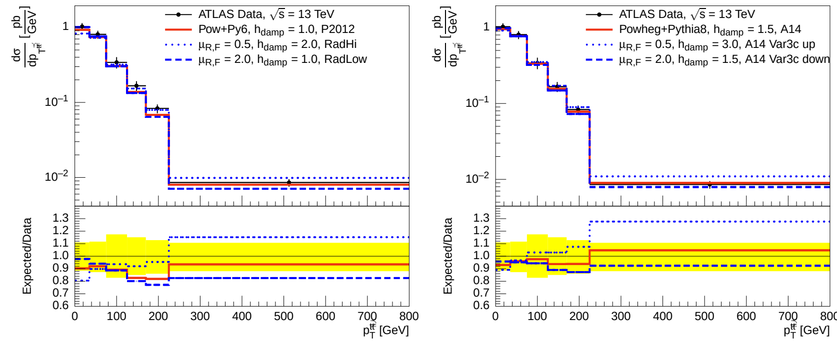

(b) $p_T^{t\bar{t}}$

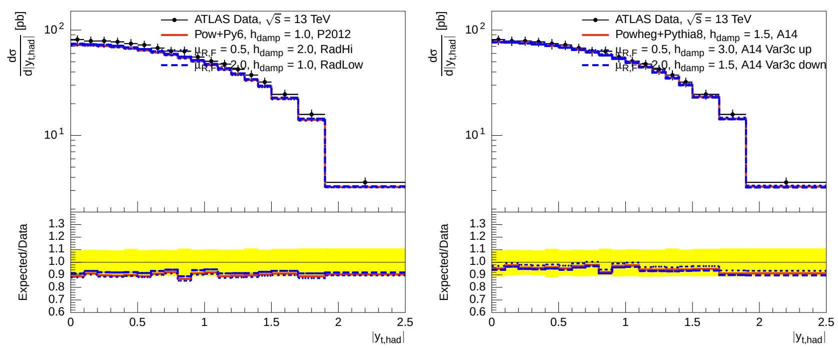

(c) $|y_{\mathrm{t,had}}|$

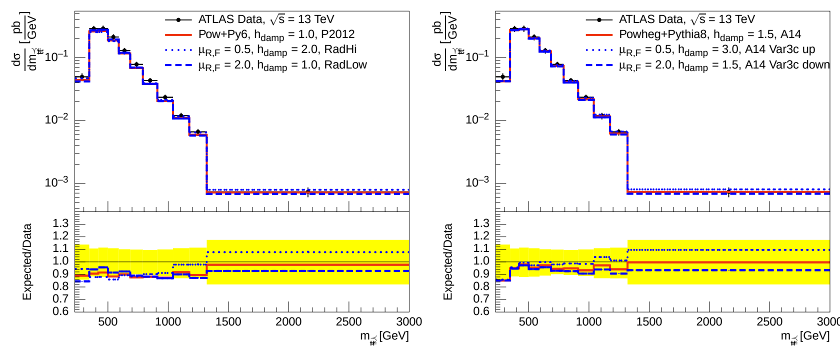

(d) $m_{t\bar{t}}$

Figure 10.2: Differential cross sections as a function of the transverse momentum of the hadronic top-quark (a) and $t\bar{t}$ system (b), the rapidity of the hadronic top-quark (c), and the invariant mass of the $t\bar{t}$ system (d) obtained from the resolved analysis channel in Ref [214]. The yellow bands indicate the total uncertainty in the data for each bin. The plots on the left (right) correspond to the initial (updated) Run II setup. The black curve corresponds to data. The red curve shows the nominal $t\bar{t}$ baseline. The dotted (dashed) curve corresponds to the prediction from POWHEG +PYTHIA with parameter variations corresponding to more (less) additional radiation.

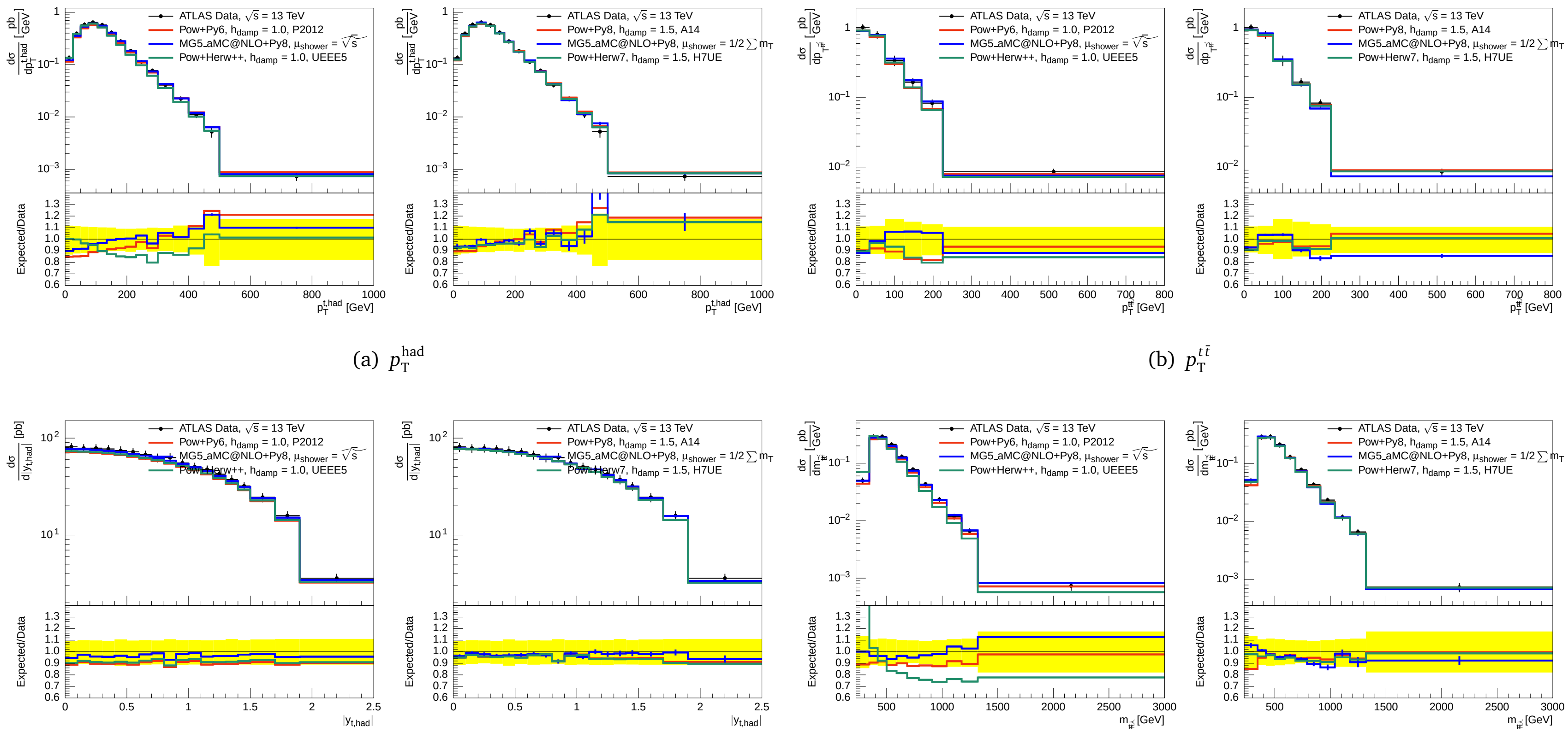

(a) $p_{\mathrm{T}}^{\mathrm{had}}$

(b) $p_{\mathrm{T}}^{t\bar{t}}$

(c) $|y_{\mathrm{t,had}}|$

(d) $m_{t\bar{t}}$

Figure 10.3: Differential cross sections as a function of the transverse momentum of the hadronic top-quark (a) and $t\bar{t}$ system (b), the rapidity of the hadronic top-quark (c), and the invariant mass of the $t\bar{t}$ system (d) obtained from the resolved analysis channel in Ref [214]. The yellow bands indicate the total uncertainty in the data for each bin. The plots on the left (right) correspond to the initial (updated) Run II setup. The black curve corresponds to data. The red curve shows the nominal $t\bar{t}$ baseline. The blue (green) curve corresponds to the prediction from MadGraph5_aMC@NLO +Pythia and Powheg +Herwig.

Part IV

Searches for Heavy Vector-like Quark Pairs in the One Lepton Final State

This part summarises two independent searches for pair produced VLQs in the one lepton final state. Chapter 11 describes the general strategy for such searches and gives a summary of the previous LHC results for VLT and VLB searches with targeted decays into Wb and Wt, respectively. Chapter 12 provides an overview of the commonalities between the two presented searches that are then described in Chapter 13 and Chapter 14. Both analyses are based on pp collision data collected at the LHC in 2015 and 2016 at a centre-of-mass energy of 13 TeV corresponding to an integrated luminosity of 36.1 fb^{-1} fulfilling the data quality criteria described in Chapter 7.7. All observed and expected exclusion limits are quoted at the 95% Confidence Interval (CL). Chapter 15 summarises the results of the two searches and provides an outlook.

Chapter 11

General Search Strategy

This chapter gives an overview of the general search strategy for VLQs based on the VLQ phenomenology that is summarised in Section 4.2. Possible decays of the VLT (VLB) are $\mathscr{B}(T \to Wb,\ Zt,\ Ht)$ ($\mathscr{B}(B \to Wt,\ Zb,\ Hb)$). Under the assumption that the three decays are the

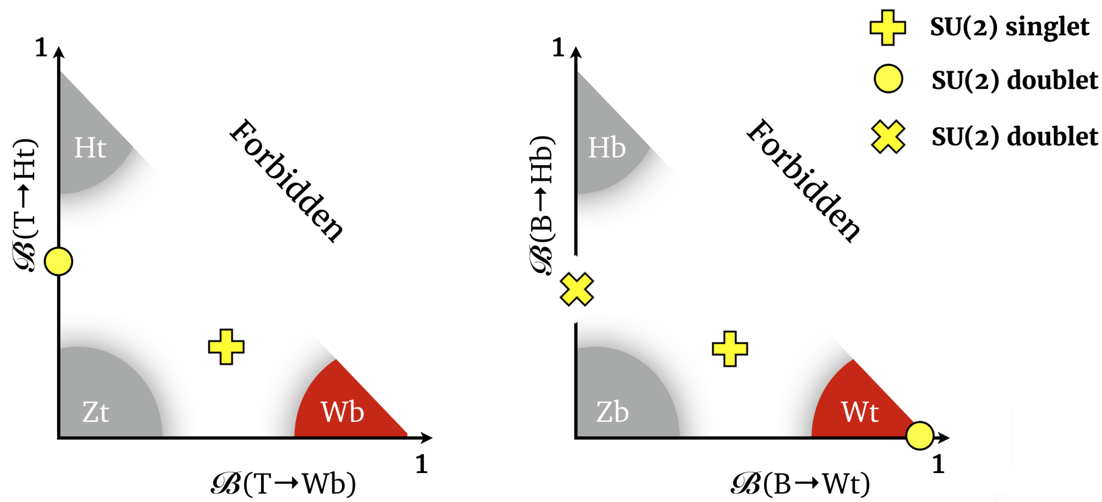

Figure 11.1: Illustration of the branching fractions plane for VLT (VLB) decays assuming $\mathscr{B}(T \to Wb)+\mathscr{B}(T \to Ht)+\mathscr{B}(T \to Zt) = 1$ ($\mathscr{B}(B \to Wt)+\mathscr{B}(B \to Hb)+\mathscr{B}(B \to Zb) = 1$).

only ones allowed, i.e. $\mathscr{B}(T(B) \to Wb(t)) + \mathscr{B}(T(B) \to Ht(b)) + \mathscr{B}(T(B) \to Zt(b)) = 1$, the branching planes illustrated in Figure 11.1 depict all possible decay mode combinations. Different benchmark models are indicated by yellow markers and illustrated in Figure 4.2 for the various $SU(2)$ multiplets. The x-axis shows the branching ratio of the VLT (VLB) decay into Wb (Wt), whereas y-axis shows the branching ratio of the VLT (VLB) decay into Ht (Hb). The bottom left corner thus corresponds to the 100% branching ratio of the VLT (VLB) decay into Zt (Zb).

The decay modes of the predicted VLQs within a given $SU(2)$ multiplet depend on their respective mass, though only a small dependence is predicted for masses $\mathscr{O}(> 1$ TeV$)$. Two VLT (VLB) benchmark signal models emphasised in the searches presented in this dissertation are the one with 100% branching ratio to $Wb(t)$ and the $SU(2)$ singlet hypothesis with branching ratios of ∼50%, ∼25%, ∼25% to $Wb(t)$, $Zt(b)$, and $Ht(b)$, respectively.

For the VLB production, the $SU(2)$ $(T\ B)$ doublet hypothesis coincides with the $\mathscr{B}(B \to Wt) = 1$ case and the $SU(2)$ $(B\ Y)$ doublet has a branching ratio of ∼0%, ∼51%, ∼49% to Wt, Zb and Hb, respectively. The $SU(2)$ doublet for the VLT production corresponds to the branching ratios of ∼0%, ∼45%, ∼55% to Wb, Zt and Ht, respectively. The presented searches are not sensitive to the charge of VLQs and hence the limits are equally applicable for $SU(2)$ doublet VLQs, and Vector-like Y quark (VLY) and Vector-like X quark (VLX) carrying exotic charges. The top-quark decays almost exclusively into a W-boson and a b-quark as $\mathscr{B}(t \to Wb) \simeq 1$. The W-boson decays either hadronically into two quarks or a lepton and a lepton-neutrino. The Z-boson decays either into two quarks or two leptons. In order to perform the general search for VLQs most efficiently, a full scan of the $\mathscr{B}$ plane assuming $\mathscr{B}(T(B) \to Wb(t)) + \mathscr{B}(T(B) \to Ht(b)) + \mathscr{B}(T(B) \to Zt(b)) = 1$ is performed which ensures the exploration of the rich decay phenomenology and broadens the sensitivity to a variety of VLQ models. It is not easy to explore the full VLQ model phase space within a single analysis due to the specific features and requirements of the various predicted decay modes. Thus, the general search strategy is that different analyses target different corners of the $\mathscr{B}$ plane with optimised analysis designs while attempting to maintain sensitivity to mixed decay modes. At a later stage the various analysis can be orthogonalised and combined to increase the sensitivity span. At the time of writing this dissertation, the combination between different analyses has not been completed. The two presented analyses can not be directly combined since they probe an overlapping phase space. However, depending on the model the presented analyses are optimised for, each can separately contribute to a combination targeting the individual models.

This dissertation summarises two searches that focus on pair produced VLTs (VLBs) decaying into $T \to Wb$ $(B \to Wt)$ indicated by the red corners in Figure 11.1.

11.1 Summary of LHC Results

A summary of the most recent results in searches for pair-produced VLQs expected to decay into $\mathscr{B}(T \to Wb) = 1$ or $\mathscr{B}(B \to Wt) = 1$ based on a center-of-mass energy of $\sqrt{s} = 13$ TeV is given in Table 11.1. A comparison of the final results of the two searches presented in this dissertation with the limits based on previous results at $\sqrt{s} = 8$ TeV are discussed in Chapter 15.

The results highlighted in blue are the results of the two analyses presented in this dissertation. The analysis published in Ref. [218] targeted the decay of VLT into $\mathscr{B}(T \to Wb) = 1$. However,

Table 11.1: Most recent public results on the BB (TT) production assuming $\mathscr{B}(B \to Wt) = 1$ ($\mathscr{B}(T \to Wb) = 1$) at $\sqrt{s} = 13$ TeV. The limits highlighted in blue correspond to the limits obtained by the two analyses presented in this dissertation.

	Observed (Expected) Mass Limits [GeV]		
	$\mathscr{B}(T \to Wb) = 1$	$\mathscr{B}(B \to Wt) = 1$	Data Set [fb^{-1}]
ATLAS [217]		1350 (1330)	36.1
ATLAS [218]	1350 (1310)	1250 (1150)	36.1
CMS [219]		1320 (1230)	35.9
CMS [220]	1295 (1275)		35.8

the analysis without any adjustments turned out to be also sensitive to a VLB signal decaying into $\mathscr{B}(B \to Wt) = 1$ which was tested through a simple signal injection. The analysis in preparation for publication (Ref. [217]) was optimised for a VLB signal decaying into $\mathscr{B}(B \to Wt) = 1$ and resulted in an expected mass limit improvement of ∼200 GeV. The results of ATLAS and CMS are of comparable size on the same data set with slightly stronger limits by ATLAS.

The CMS analysis in Ref. [219] targets the pure decay into Wt in the ℓ+jets channel. The pre-selection is based on the requirement of at least four small-R jets out of which at least one is required to be b-tagged. Additional requirements are applied on the angular separation between the selected lepton and the sub-leading small-R jet, $\Delta R(\ell$, sub-leading small-R jet$) > 1$, and the leading (sub-leading) small-R jet $p_{\mathrm{T}} > 450$ GeV (150 GeV). The analysis is based on a likelihood fit to data with min[$M(\ell, b$-jets)] as final discriminant in 16 categories defined by the number of b-jets, W-tagged and top-quark tagged anti-k_t jets with $R = 0.8$.

The CMS analysis in Ref. [220] targets the pure decay into Wb in the ℓ+jets channel. The pre-selection requires either at least four small-R jets or at least three small-R jets and at least one anti-k_t jet with $R = 0.8$. The minimum p_{T} requirement is 55 GeV, 30 GeV or 200 GeV for the selected lepton, small-R jet, or anti-k_t jet with $R = 0.8$, respectively. A minimum S_{T} requirement of 1000 GeV is applied. The final discriminant is constructed employing a kinematic fit. The fit is based on a χ^2 minimisation between the measured momentum components and their fitted true values divided by the corresponding uncertainties summed over all of the former selected reconstructed objects. The fit imposes a W mass constraint on the invariant mass of the lepton, neutrino and two quarks and that the reconstructed invariant mass of the two produced VLT quarks are equal. The reconstructed mass is used as final discriminant in the likelihood fit.

Chapter 12

Common Aspects of the Presented VLQ Searches

This chapter gives an overview of the commonalities between the two presented searches described in Chapter 13 and Chapter 14. It provides a summary of the signal and background estimates, systematic uncertainties, neutrino reconstruction, and a common event selection. Moreover, the employed analysis tools are introduced.

12.1 Data and Simulation

12.1.1 Selected Data Set

The VLT (VLB) search utilises a dataset corresponding to 36.1 ± 1.2 fb^{-1}(36.1 ± 0.8 fb^{-1}) of integrated luminosity from pp collisions at $\sqrt{s} = 13$ TeV collected by the ATLAS experiment, with 3.2 fb^{-1} collected in 2015 and 32.9 fb^{-1} in 2016. The reduction in the luminosity uncertainty between the two analyses is explained in Section 12.2.1.

12.1.2 Simulated Samples

This section contains an overview of simulated MC samples used to model both the signal and SM processes that produce final states similar to that of theses VLQs. All MC samples contain additional pp collisions generated with profiles that match the observed pile-up profile of the combined 2015 and 2016 data taking periods. Both in- and out-time pile-up events (see Section 5.2) were simulated. They are modelled as low p_{T} multi-jet production using the PYTHIA 8.186 generator and the A2 tune [221]. EVTGEN V1.2.0 [222] is used for the modelling of b-hadron decays in all simulated samples except for those using SHERPA. The samples are simulated either through a FullSim of ATLAS using GEANT 4 [149], or through a FastSim of the calorimeter response [181] and are reconstructed using the same analysis chain as the data (see

Section 9.1.2). Simulated MC events are corrected so that the object associated efficiencies, energy scales, and energy resolutions match those determined from data control samples. In all simulated samples, the top-quark and Higgs boson masses are set to 172.5 GeV and 125 GeV, respectively. All signal and background contributions are modelled using simulated samples with the exception of the multi-jet background that contributes in the single lepton channel via the misidentification of a jet or a photon as an electron or the presence of a non-prompt lepton. This background is assessed through a data-driven method described in Section 12.1.3.

Signal production

Signal samples for the pair-production of VLQs are generated with the LO generator PROTOS v2.2 [198] using the NNPDF2.3 LO PDF set and passed to PYTHIA 8.186 [223] for parton showering, fragmentation, and hadronisation. The A14 [200] set of optimised parameters for the UE

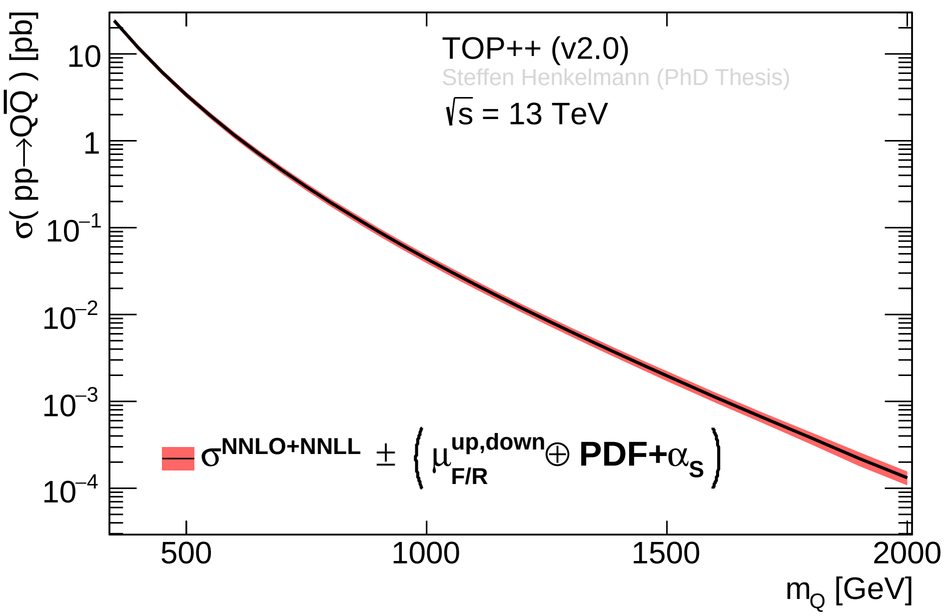

Figure 12.1: The VLQ pair production cross section at $\sqrt{s} = 13$ TeV as a function of the VLQ mass. Theoretical uncertainties are evaluated from variations of the factorisation and renormalisation scales, as well as from uncertainties in the PDFs and α_S. The computed values are extracted from Ref. [224].

description using the NNPDF2.3LO PDF set is used (denoted as A14 tune). VLQs are produced forcing an equal decay branching ratio of 1/3 to each of the three decay modes: $Wb(t)$, $Zt(b)$, and $H(t)b$. Re-weighting the samples using particle-level information enables for arbitrary sets of branching ratios consistent with the three branching fractions summing up to unity. This is accomplished by weighting events by $(\mathscr{B}(T(B) \to n)\times\ \mathscr{B}(\bar{T}(\bar{B}) \to m))/(1/3\times 1/3)$, where n,m = $Wb(t)$, $Zt(b)$, and $H(t)b$ and $\mathscr{B}(T(B) \to n)$, $\mathscr{B}(\bar{T}(\bar{B}) \to m)$ are the desired branching ratios.

VLQ samples are generated for masses of 700-1200 GeV in steps of 50 GeV, with additional samples produced at 500, 600, and 1300-2000 GeV in steps of 100 GeV. For these samples the pair production cross-sections vary from 3.38 ± 0.25 pb^{-1} ($m_Q = 500$ GeV) to 0.13 ± 0.02 fb^{-1} ($m_Q = 2000$ GeV) as illustrated in Figure 12.1. These values were computed using TOP++ v2.0 [225] at next-to-next-to-leading-order (NNLO) QCD accuracy, including resummation of next-to-next-to-leading logarithmic (NNLL) soft gluon terms, and using the MSTW 2008 NNLO set of PDFs [226]. Theoretical uncertainties result from variations on the factorisation and renormalisation scales, as well as from uncertainties on the PDF and α_S. The latter two represent the largest contribution to the overall theoretical uncertainty on the cross section and were calculated using the PDF4LHC [227] prescription with the MSTW 2008 68% CL NNLO, CT10 NNLO [228], and NNPDF2.3 [229] 5f FFN PDF sets. Figure 12.1 shows the pair production cross section for VLQ production at $\sqrt{s} = 13$ TeV as a function of the VLQ mass.

SM Background production

$t\bar{t}$ samples The $t\bar{t}$ baseline and uncertainty assessment recommendations were updated during Run II. While the initial Run II setup was used for the VLT search, the updated Run II setup was used for the presented VLB search. A detailed prescription on the respective nominal baseline and the associated systematic variations including a list of samples is given in Section 10.3.

Single-top samples Single-top production in the Wt- and s-channels is generated with POWHEG-BOX V2 interfaced with PYTHIA 6.428. The nominal Wt sample employs a Diagram removal (DR) scheme to handle overlaps with the $t\bar{t}$ production (see Section 12.2.4 for more details). The single-top production in the t-channel is generated with POWHEG-BOX V1 interfaced with PYTHIA 6.428. Single-top samples are generated using the PERUGIA2012 tune and the CT10 PDF set for the PS and hadronisation. The single-top cross sections for the t- and s-channels are normalised to their NLO predictions, while for the Wt-channel the cross section is normalised to its NLO+NNLL prediction [230].

V+jets, diboson and $t\bar{t}V$ samples For W+jets, Z+jets, and diboson (WW,WZ,ZZ) samples, the SHERPA 2.2.1 generator [195] is used with the CT10 PDF set. The W+jets and Z+jets production samples are normalised to the NNLO cross sections [231–233]. For diboson production, the generator cross sections (already at NLO) are used for sample normalisation. The $t\bar{t}V$ background is modelled using samples produced with MADGRAPH5_aMC@NLO 2.1.1 interfaced with PYTHIA 8.186. The $t\bar{t}V$ samples are normalised to their respective NLO cross sections [206].

12.1.3 Data-driven Multi-jet Background Estimate

The LHC produces a large amount of QCD multi-jet events, mostly with $2 \rightarrow 2$ processes resulting in dijet events. Also, higher order processes are very probable that provide higher jet multiplicities. For a multi-jet event to contribute as background to the searches, a lepton must be present and the energy balance of the event must have a non-negligible amount of $E_{\mathrm{T}}^{\mathrm{miss}}$. As such, multi-jet events contribute if either the lepton that originates from decays inside a jet passes the lepton identification criteria (non-prompt lepton) or if a jet or photon is mistakenly identified as an electron ("fake" lepton). The probability of the multi-jet event to meet these requirements is small but compared to the abundance of such events likely. The calculation of the higher order processes for multi-jet production is challenging since it is in the non-pQCD regime. Therefore, a data-driven method is employed to estimate the shape and normalisation of that background contribution to the presented searches. The method used in the two searches presented to extract the multi-jet background and associated uncertainties from data is called the Matrix Method (MM) method [234]. The method is based on populating two samples imposing different identification and isolation criteria on the leptons (as defined in Table 12.1) exploiting differences in the efficiencies between prompt leptons originating from W and Z decays and the previously introduced fake and non-prompt leptons. The first sample

Table 12.1: A summary of the imposed lepton identification and isolation requirements for the definition of "real" ("fake") leptons populating the "tight" ("loose") sample. A description of the respective quality requirements is described in Chapter 7.4.

	$e_{\text{"tight"}}$	$e_{\text{"loose"}}$	$\mu_{\text{"tight"}}$	$\mu_{\text{"loose"}}$
Identification:	`TightLH`	`MediumLH`	`Medium`	`Loose`
Isolation:	`FixedCutTightTrackOnly`	`None`	`FixedCutTightTrackOnly`	`None`

imposes the same lepton identification criteria as used in the analysis event selection and is denoted as "tight", while the second sample imposes less stringent criteria on the identification and isolation of the selected lepton candidates and is denoted as "loose". The "tight" sample is a subset of the "loose" sample.

The total number of selected events in the respective samples ($N^{\text{tight}}, N^{\text{loose}}$) is assumed to be represented as a linear combination of the number of events containing "real" leptons ($N_{\text{"real"}}$) and "fake" leptons ($N_{\text{"fake"}}$). The total number of events in each selection is thus:

$$N^{\text{loose}} = N^{\text{loose}}_{\text{"real"}} + N^{\text{loose}}_{\text{"fake"}} \tag{12.1}$$

$$N^{\text{tight}} = \epsilon_{\text{"real"}} N^{\text{loose}}_{\text{"real"}} + \epsilon_{\text{"fake"}} N^{\text{loose}}_{\text{"fake"}} \tag{12.2}$$

where $\epsilon_{\text{"real"}}$ ($\epsilon_{\text{"fake"}}$) is the efficiency for a "real" ("fake") lepton to satisfy the tight criteria if it already satisfies the loose criteria.

The contribution of fake leptons in the "tight" sample can then be estimated by:

$$N^{\text{tight}}_{\text{"fake"}} = \frac{\epsilon_{\text{"fake"}}}{\epsilon_{\text{"real"}} - \epsilon_{\text{"fake"}}} \left(\epsilon_{\text{"real"}} N^{\text{loose}} - N^{\text{tight}} \right). \tag{12.3}$$

The efficiencies are measured for each lepton flavour in dedicated control regions enriched with fake and real leptons. They are parametrised as a function of relevant kinematic variables. The parametrisation is a function on the lepton p_{T} and a calorimeter-based isolation for the electrons. In addition to the latter two-dimensional parametrisation, an additional dependency for the muons on min[$\Delta R(\mu$, small-R jet's)] is included. Good modelling is observed in dedicated control and validation regions between background prediction and data. In order to estimate the multi-jet background in the analysis regions of interest for the presented searches, each data event gets a weight assigned that is characterised by the efficiency parameterisations. The weight is assigned depending on if the electron or muon passes the tight or fails the tight but passes the loose lepton selection criteria. The parametrisation is extracted from the analysis in Ref. [235].

After final analysis selection, the multi-jet contribution is expected to be small. Thus, in order to validate the method, a dedicated validation region in which the contribution from the multi-jet events is still significant is defined and is described in Section 12.4.1.

The event selections used to define the Control Region (CR) and Signal Regions (SRs) in the presented searches reduces the contribution of the multi-jet background to the point at which the low statistical power makes the MM predictions unreliable. For both searches, looser region definitions were investigated and both the shape and normalisation were compared to other small background contributions, i.e. diboson, Z+jets, and $t\bar{t}V$. The shapes between multi-jet and the sum of these small backgrounds are found to be compatible in the looser regions. The ratio of the number of events between the multi-jet and other small backgrounds is obtained in the looser region and assumed to be the same in the tighter analysis regions. Finally, the template obtained from the other small backgrounds that does not suffer from large statistical fluctuations, is scaled by this ratio. The fractional contribution of the multi-jet background in the respective analysis regions is small (up to only 6%). The derived ratios and definition of the looser analysis regions are described in Sections 13.5 and 14.5 for the VLT and VLB analysis, respectively.

12.2 Systematic Uncertainties

This section provides a summary of the systematic uncertainties that can impact the normalisation of the total predicted event yield, the shape of the distributions, or both. Each systematic uncertainty described here is treated as a Nuisance Parameter (NP) in the statistical analysis of the final discriminant. Within an analysis, individual systematic sources are fully correlated across processes and analysis regions. They are derived such that they can be treated as individually uncorrelated. Shape effects are taken into account were relevant. The systematic uncertainties are organised in four categories: luminosity and cross section, detector-related experimental, data-driven background estimate, and signal and background modelling uncertainties. The dominant uncertainties in the respective categories are discussed in Sections 13.6.3 and 14.7 for the VLT and VLB analysis, respectively.

12.2.1 Luminosity and Cross Section Uncertainties

The uncertainty in the integrated luminosity in the combined 2015 and 2016 data set is 3.2% (2.1%) assuming partially correlated uncertainties in the two years for the VLT (VLB) search, respectively. It is derived following a methodology similar to that detailed in Ref. [236] from a calibration of the luminosity scale using x-y beam-separation scans performed in August 2015 and May 2016. The latter calibration was preliminary at the time of the VLT analysis and was revised, resulting in the uncertainty decrease at the time of the VLB analysis. This systematic uncertainty is applied to all backgrounds that are estimated using simulated samples and normalised to the measured integrated luminosity. This includes all backgrounds with the exception of the small contribution from the estimated multi-jet background. Theoretical cross section uncertainties have been used for the simulated samples considered in this thesis. The uncertainties for inclusive V+jets and diboson production is 5% and 6% as defined in Ref. [237]. The total uncertainty for the V+jets and diboson background is taken as 50%. This uncertainty is a conservative estimate that was cross checked against an uncertainty parametrisation based on the number of jets on an event-by-event basis assessed from an envelope constituted by variations of the factorisation and renormalisation scales, as well as PDFs and α_S variations from Ref. [238]. A 15% uncertainty on the $t\bar{t}V$ cross section is assumed following NNLO calculations [239]. For single-top production, the uncertainties are taken as 7% [240, 241]. The $t\bar{t}$ samples are normalised to the NNLO cross section using Top++2.0 [225], including NNLO QCD corrections and soft-gluon resummation to NNLL accuracy [242–247]. The normalisation of $t\bar{t}$ baseline is unconstrained in the fit.

12.2.2 Detector-related Experimental Uncertainties

The uncertainty sources summarised in this section are applied to both simulated signal and background samples. Both object reconstruction and calibration result in systematic sources that are related to leptons, small-R jets, large-R jets, $E_{\mathrm{T}}^{\mathrm{miss}}$, boson- and flavour tagging. These systematic uncertainties have already been described in Part III. An additional uncertainty in this category is the pile-up modelling uncertainty accounting for an uncertainty on the reweighting procedure of the simulation to a respective pile-up scenario matching the ones measured in the 2015 and 2016 data set.

12.2.3 Data-driven Background Estimate

For the assessment of the multi-jet background, a conservative uncertainty of 50% is imposed on the normalisation. This was found to cover observed differences between data and the estimate in the control and validation regions outlined in Section 12.1.3.

In the analysis regions where the multi-jet estimate from the MM method becomes unreliable, a 100% uncertainty on the multi-jet background normalisation is combined in quadrature with the uncertainty of the simulation derived "Others" background template.

12.2.4 Signal and top-quark modelling uncertainties

No theoretical signal uncertainty on the cross section is included for the final limit calculation. These uncertainties are only shown in the theoretical uncertainty band in the final results (see Figure 12.1).

For the top-quark background, either from $t\bar{t}$- or single-top production, the systematic uncertainties are imposed on shape and normalisation. The systematic samples are normalised to the same cross section as the nominal top-quark samples. For one-sided systematics the relative difference in the observable to the nominal prediction is computed. This relative difference is then applied as a symmetric uncertainty in the nominal prediction.

The additional $t\bar{t}$ modelling systematic samples are compared to assess uncertainties related to the hard scatter generation, fragmentation, and hadronisation as well as additional radiation as described in Section 10.3:

- **Hard scatter generation** The uncertainty on the hard scatter process is evaluated by the comparison of the MC generator MADGRAPH5_aMC@NLO and POWHEG both interfaced to PYTHIA for showering and hadronisation. The uncertainty then symmetrised around the nominal prediction.

- **Additional Radiation** To account for a systematic uncertainty on the amount of additional radiation in the event, the relative difference of two samples produced with POWHEG-BOX V2 interfaced with PYTHIA with a simultaneous up- and down variation of the parameters $\mu_{R,F}$ and h^{damp} and VAR3C is used. The relative difference is applied to the nominal $t\bar{t}$ sample.

- **Hadronisation and fragmentation model** The systematic accounting for the employed fragmentation and hadronisation model is assessed with the same ME generation given by POWHEG and different PS algorithms, namely PYTHIA and HERWIG. The uncertainty then symmetrised around the nominal prediction.

For the single-top production an additional systematic shape uncertainty is imposed assessing potential overlaps between NLO Wt and LO $t\bar{t}$ production as described in the next paragraph.

Wt and $t\bar{t}$ overlap systematic The single-top production in the Wt channel at NLO with additional b-quarks (Wtb) results in the generation of diagrams that interfere with $t\bar{t}$ pair production at LO. The cross section for inclusive Wtb production is proportional to the following

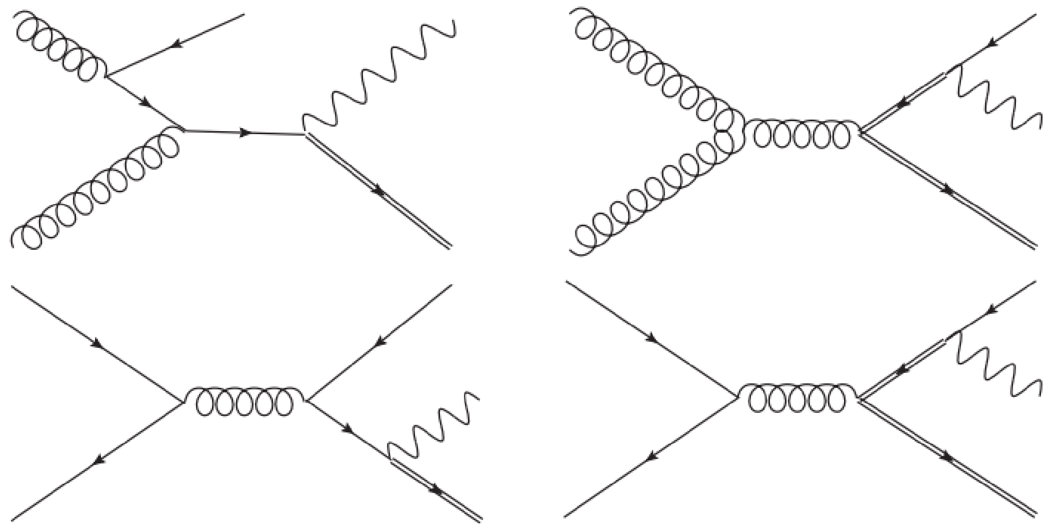

Figure 12.2: Representative Feynman diagrams for gluon (top) and quark (bottom) initiated Wtb production with single on-shell (left) and double on-shell top-quarks (right) [248].

amplitude:

$$\begin{aligned}\left|\mathcal{M}_{Wtb}\right|^2 &= \left|\mathcal{M}_{sr} + \mathcal{M}_{dr}\right|^2 \\ &= \left|\mathcal{M}_{sr}\right|^2 + \left|\mathcal{M}_{dr}\right|^2 + 2\mathrm{Re}\left(\mathcal{M}_{\mathrm{sr}} \cdot \mathcal{M}_{\mathrm{dr}}^{*}\right),\end{aligned}$$

with $\mathcal{M}_{sr}$ ($\mathcal{M}_{dr}$) representing the ME incorporating diagrams with single (double) resonant on-shell top-quarks as illustrated in Figure 12.2. Different procedures are in place to factorise out the $t\bar{t}$ and Wt contributions. The DR method removes the $t\bar{t}$ contribution as well as the interference between Wt and $t\bar{t}$ by setting $\mathcal{M}_{dr} = 0$ and is the nominal method employed in ATLAS for Wt production. The Diagram subtraction (DS) method removes the overlap while taking into account the interference term [210, 249]. One sample for each of the two overlap removal procedures for the Wt schemes are generated. Their relative difference is taken as a systematic uncertainty. The uncertainty is symmetrised.

12.2.5 Systematics Handling

Pruning The associated NPs to the systematic uncertainties listed in the previous sections and described in Part III are pruned in order to ease the fit performance. The latter procedure checks the impact of each systematic uncertainty with respect to the nominal sample on both normalisation and shape difference. Both analyses assume the shape and normalisation uncertainty of a given systematic source to be correlated. If the normalisation has an impact of more than 1% or the shape uncertainty varies by more than 1% between neighbouring bins, it is included in the fit as a NP, otherwise it is discarded. Statistical uncertainties on the signal and background predictions in each bin of the discriminant distributions are also taken into account in the fit.

Smoothing and symmetrisation Systematic variations can suffer from statistical fluctuations. The fluctuations can be misleading when the systematics get profiled. This can potentially lead to an over-constraint of the NPs. The individual systematic sources are checked on a case-by-case basis and modified were applicable before input into the fit framework. The applied procedure merges bins with statistically insignificant systematic variations and their average impact is used as a more reliable estimate. On top, a smoothing procedure is applied which is a combination of histogram re-binning and smoothing[10]. The latter is driven by a maximum number of allowed slope changes. For all affected systematic uncertainties a maximum of four slope changes is allowed. As long as less than four slope changes are present, no re-binning is performed. Otherwise, the bins are statistically combined until only a maximum of four slope changes is present.

Most one-sided uncertainties, corresponding to the uncertainty on JER, resolution on the $E_{\mathrm{T}}^{\mathrm{miss}}$ soft-term, and top modelling uncertainties (except for the additional radiation uncertainty), are smoothed before symmetrisation. An exception is that no smoothing is imposed on the top modelling systematics in one of the two analysis regions in the VLB analysis (BDTSR).

Two-sided systematics are symmetrised and smoothed in only one analysis region in the VLB analysis (RECOSR). The symmetrisation is performed on a bin-by-bin basis where the total difference of the up- and down variation is applied to the nominal sample. The latter procedure avoids the inclusion of systematic uncertainties in which case both the up and down variations are above or below the nominal sample.

[10]The TH1::Smooth implementation is based on algorithm '353QH twice', as it was presented by J. Friedman in Proc. of the 1974 CERN School of Computing, Norway, 11-24 August, 1974.

12.3 Common Event Pre-selection

This section summarises the PRE-selection common between the two searches presented in this thesis. The VLQ production cross section is several orders of magnitude lower compared to the main backgrounds which motivates additional kinematic cuts imposed on the PRE selected samples to increase signal purity, resulting in the two BASE selections described for the VLQ (VLB) search in Section 13.2.1 (Section 14.2.1).

Trigger selection To select events with one lepton over a wide p_{T} range with a maximum efficiency, electron (muon) triggers with varying E_{T} (p_{T}) thresholds are selected from the 2015 and 2016 trigger menu. A summary of the selected triggers is given in Table 12.2. Trigger object

Table 12.2: A summary of the lepton triggers used for this analysis.

	electron	muon
2015	HLT_e24_lhmedium_L1EM20VH HLT_e60_lhmedium, HLT_e120_lhloose	HLT_mu20_iloose_L1MU15 HLT_mu50
2016	HLT_e26_lhtight_nod0_ivarloose HLT_e60_lhmedium_nod0, HLT_e140_lhloose_nod0	HLT_mu26_ivarmedium HLT_mu50

isolation and quality requirements for the low threshold triggers result in inefficiencies at high lepton p_{T}. Therefore, high threshold triggers with looser quality and isolation requirements are selected and a logical OR between the triggers is imposed. All triggers used are un-prescaled. Each software-based HLT trigger is seeded by a hardware-based L1 trigger.

- **electron triggers**
  - **2015** For the HLT trigger, a medium and loose quality requirement to the likelihood-based electron identification (with slight differences to the one described in Section 7.4.1) is imposed. For the electron triggers in 2015 data, the highest E_{T} threshold trigger has a looser quality requirement on the trigger object compared to the ones at lower thresholds.

    The low threshold trigger in 2015 is seeded by a L1 trigger, L1_EM20VH, that requires an isolated EM cluster above a certain threshold ($E_{\mathrm{T}} > 20$ GeV) which varies slightly with η in order to compensate for passive material in front of the calorimeter. In addition, an E_{T} dependent veto is imposed against HCAL energy deposits behind the associated EM cluster of the selected electron candidate. The higher threshold triggers in 2015 are seeded by `L1_EM22VHI` which require $E_{\mathrm{T}} > 22$ GeV. In addition to the requirements for `L1_EM20VH`, an isolation requirement relative to the EM cluster is applied for $E_{\mathrm{T}} < 50$ GeV.

  - **2016** For the HLT trigger, a tight, medium, and loose quality requirement to the likelihood-based electron identification without applying the d_0 requirement for the electron candidate is imposed for the three electron triggers in 2016. The lowest threshold trigger has both stringent quality requirements and isolation requirements, whereas the higher threshold triggers have no isolation requirement. The isolation requirement for the low threshold trigger is passed when $\sum p_{\mathrm{T}}/E_{\mathrm{T}} < 0.1$, where the sum runs over all tracks within a p_{T} dependent *variable-sized cone*, $R(p_{\mathrm{T}})$, around the selected electron candidate excluding its own associated track.

    All 2016 electron triggers are seeded by `L1_EM22VHI`.

- **muon triggers**

  - **2015 and 2016** The HLT trigger requires for all muon triggers to pass a medium quality requirement for muon identification as described in Section 7.4.2. Low p_{T} threshold triggers with isolation requirements and high p_{T} threshold triggers with no isolation are used in 2015 and 2016. The low p_{T} threshold trigger in 2015 needs to fulfil a fixed cone ($R = 0.2$) requirement. The low p_{T} threshold triggers in 2016 is required to fulfil a p_{T} dependent variables-sized cone requirement.

    All selected muon triggers are seeded by `L1_MU20` except for the low threshold trigger in 2015 which is seeded by `L1_MU15`.

Data to MC scale factors are provided by dedicated performance groups, typically obtained through a tag-and-probe method using resonant $Z \to ee, \mu\mu$ decays, and cover the observed efficiency differences between data and MC for electrons and muons, respectively. The scale factors are applied to the MC prediction. The offline threshold on selected leptons is typically greater than the one used for the trigger selection to ensure a high efficiency reached on the trigger turn-on plateau. An offline cut according to the prescription from the respective performance groups is applied to the leptons as described in Section 7.4. Due to an instantaneous luminosity increase in 2016 that surpassed the expected design luminosity of the LHC as described in Section 5.2 and reflected in the peak in Figure 5.2, the p_{T} and E_{T} thresholds for the muon and electron triggers were increased to > 30 GeV as described in Sections 7.4.1 and 7.4.2.

Data quality Each event needs to meet the data quality criteria described in Section 7.7.

Lepton selection Events are discarded that do not contain either exactly one electron or one muon which is matched to the trigger object. This results in the suppression of processes with two isolated leptons such as Z+jets. The leptonically decaying W boson has a smaller branching ratio ($\mathscr{B}(W \to \ell\nu) \sim$ 20% with $\ell = e, \mu$) compared to the all hadronic decay mode ($\mathscr{B}(W \to qq) \sim 70\%$). Thus, this lepton selection results in a reduced number of expected signal events but is the key to reduce the overwhelming background contributions from multi-jet events.

Minimum jet multiplicity selection Events with fewer than three small-R jets are discarded due to the high number of expected jets in both signal topologies studied in this dissertation.

The main backgrounds passing this loose PRE-selection originate from $t\bar{t}$ in the semi-leptonic decay channel, W+jets where one of the W bosons decays leptonically. Smaller contributions originate from Z+jets (where one of the leptons is either mis-identified or outside of the acceptance with a remaining small fraction of events, where $Z \to bb$), single-top events (mostly from the Wt channel with a semi-leptonic W decay and jets from higher order contributions), diboson events, and $t\bar{t}V$ events. Moreover, multi-jet background events that contain one isolated fake lepton are present. The event PRE-selection is further tightened and optimised for the two presented searches in Sections 13.2.1 and 14.2.1.

12.4 Neutrino Reconstruction

In both analyses the leptonic W, W_{lep}, is reconstructed. This makes the reconstruction of the four-vector of the neutrino necessary. $E_{\mathrm{T}}^{\mathrm{miss}}$ is considered as the transverse momentum of the neutrino leaving the longitudinal z-component of the four-vector undefined. Under the assumption that the mass of the four-vector sum of the lepton and neutrino corresponds to the W boson mass, $m_W = 80.4$ GeV, an analytical approach results in two possible solutions for p_z^ν.

$$P_W^2 = \left(P^\ell + P^\nu\right)^2 = m_W^2$$

$$\rightarrow p_z^\nu = \frac{\mu^2 p_z^\ell}{(E^\ell)^2 - (p_z^\nu)^2} \pm \sqrt{\frac{\mu^4 (p_z^\ell)^2}{((E^\ell)^2 - (p_z^\nu)^2)^2} - \frac{(E^\ell)^2 (E_{\mathrm{T}}^{\mathrm{miss}})^2 - \mu^2}{(E^\ell)^2 - (p_z^\nu)^4}} \text{ ,with}$$

$$\mu^2 \equiv 1/2\ m_W^2 + p_x^\nu p_x^\ell + p_y^\nu p_y^\ell.$$

In case two real solutions are obtained, the one with a smaller absolute value is used. It is observed that in the kinematic regime of the analyses the majority of events provide two complex solutions. TMinuit [250] is employed to find the optimal solution to the neutrino four-vector components by finding p_x^ν and p_y^ν that result in a real solution to the m_W requirement with minimum change in p_T^ν. The latter assumption showed the best agreement for reproducing the p_z^ν and p_T^ν of the generated neutrinos in simulation.

12.4.1 Data to Expectation Comparison in an Inclusive $t\bar{t}$ Region

A $t\bar{t}$ validation region is defined in order to validate the SM predictions from both simulated and data-driven background predictions described in Section 12.1.3. In addition to the PRE-selection, at least four small-R jets and two b-jets (at the 77% efficiency WP) are required. Figure 12.3 shows a selection of kinematic distributions relevant for this analysis. Good agree-

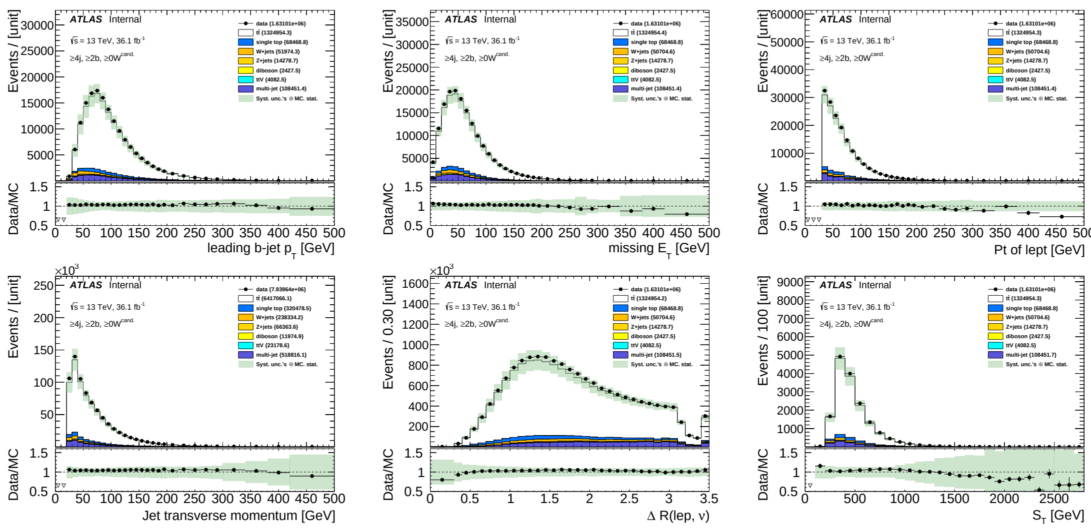

Figure 12.3: Data to prediction comparison of the leading b-jet p_{T}, $E_{\mathrm{T}}^{\mathrm{miss}}$, lepton p_{T}, the p_{T} of all small-R jet's, $\Delta R(\ell,\ \nu)$, and S_{T} in the combined e+jets and μ+jets channel in the inclusive $t\bar{t}$ region. The uncertainty bands includes MC statistics, $t\bar{t}$ modelling ("initial Run II setup"), and detector-related systematic uncertainties.

ment between data and SM background prediction is observed within the uncertainties. The scalar sum of $E_{\mathrm{T}}^{\mathrm{miss}}$, lepton p_{T}, and the sum of the p_{T} of all small-R jet's is defined as

$$S_{\mathrm{T}} = E_{\mathrm{T}}^{\mathrm{miss}} + p_{\mathrm{T}}^{\ell} + \sum_i p_{\mathrm{T,i}}^{\text{small-}R\text{ jet}}. \tag{12.4}$$

It provides a measure of the overall hardness of the decay products present in the event.

12.5 Statistical Analysis

This section provides an overview of statistical analysis tools employed in the analyses presented in this dissertation, describes the assessment of compatibility of the data with different predictions, and outlines the interpretation of search results. Frequentist likelihood-based statistical tests allowing for incorporation of systematic uncertainties on background and signal predictions are employed as implemented in the RooStats package [251] and steered by an analysis package denoted as TRexFitter [252]. Minimisation algorithms are used as implemented in MINUIT [250]. The objective of the searches performed in the context of this dissertation is to search for an expected signal process (signal), with varying signal hypotheses, above the expectations from SM predictions (background).

12.5.1 Profile Likelihood Construction and Test Statistic

Hypothesis testing The statistical significance or compatibility of observed data with a prediction can be assessed by computing the so called p-value which can be converted into an equivalent Gaussian significance. In addition, the *expected sensitivity* expressed by the median significance expected for different signal predictions is used to optimise an analysis.

Two statistical tests are distinguished. The first is a test performed in the so called *discovery mode* and the second is denoted as the *limit setting* mode. In discovery mode, the null hypothesis, H_0, corresponds to all known physics process predictions given by the total SM background (background-only, B) and is tested against the alternative (or test) hypothesis, H_1, defined as the sum of the background and signal prediction (signal-plus-background, $S+B$). In the limit setting mode, the test hypothesis is the B only hypothesis and is tested against the $S+B$ hypothesis. A *signal strength parameter*, μ, representing a multiplicative factor for the expected number of signal events for a given signal hypothesis $h_s \in \{H_s\}$ can be defined as $\mu = \sigma_x/\sigma_{\mathrm{h_s}}$. In case $\sigma_x = \sigma_{\mathrm{h_s}}$, the signal strength is one and corresponds to the specific $S+B$ hypothesis. In the absence of signal, μ is zero and corresponds to the B hypotheses. Specifying the value of μ fixes the defined hypothesis, H_μ. As such, the B only hypothesis is defined as H_0 with $\mu = 0$ and the $S+B$ hypothesis is defined as H_1 for a given signal hypothesis with $\mu = 1$. The expected sensitivity of an analysis is inferred from the discovery mode and can be tested for various signal hypothesis. The sensitivity to discovering a signal process described by h_s is inferred by quantification of the deviation of its median signal expectation from the B hypothesis.

The p-value quantifies the level of agreement of the observed data (or the median expectation of a given signal hypothesis h_s) with a defined hypothesis encoded in a test statistic, $t_\mu = -2\ln\lambda(H_0, H_1(\mu))$ (see Equation 12.14 for a definition of λ). The test statistic depends on μ. A p-value denoted as p_μ is computed from the *sampling distribution* of a test statistic obtained from a generated data set corresponding to a hypothesis $H_\mu(\mu)$. It corresponds to a probability, assuming the data originates from a model H_μ, of finding data (or a median signal expectation) that is of equal or greater incompatibility with H_μ. H_μ is regarded as excluded if p_μ is observed below a pre-defined threshold ($p_\mu \leq p^{\text{threshold}}$) chosen corresponding to a certain CL. It is common in the HEP community to express the computed p-value in units of the Gaussian significance, Z. As such the one sided probability given by the p-value corresponds to finding a Gaussian distributed variable Z standard deviations, σ, above its standard mean expectation, which is zero. The conversion is given by $Z = \Phi^{-1}(1-p)$, with Φ the cumulative distribution of the standard Gaussian distribution. Different thresholds are defined in the community as to when to consider a probability low enough to exclude a tested hypothesis. As an example, a $\geq 5\sigma$ deviation ($p \leq 2.9 \cdot 10^{-7}$ probability) from the B hypothesis ($\mu = 0$) is considered sufficiently large (low) enough to claim a discovery. A $\geq 1.96\sigma$ deviation ($p \leq 0.05$ probability) from the $S+B$ hypothesis ($\mu = 1$) is large (low) enough to exclude the predicted signal h_s at the 95% CL. For each $h_s \in \{H_s\}$ tested in this dissertation, the $S+B$ hypothesis exclusion threshold is defined as $\text{CL}_\text{s} < 0.05$, i.e. is quoted at the $\geq$ 95% CL. The CL_s [253] is defined as

$$\text{CL}_\text{s} = \frac{\text{CL}_\text{s+b}}{\text{CL}_\text{b}} = \frac{p_\mu}{1-p_0} \tag{12.5}$$

with $p_\mu(p_0)$ expressing the p-values for the $S+B$ (B) hypothesis. The CL_s ratio protects against artificial strong exclusion limits in case a downward fluctuation is observed in data. As an example, consider a downward fluctuation in data lower than the B hypothesis. This results in small $1-p_0$ and thus larger CL_s values. Therefore, signal predictions that would have led to exclusion with $\text{CL}_\text{s+b}$ only are not necessarily excluded. The signal strength μ can be evaluated at the 95% CL for a given signal hypothesis h_s. For the observed data $\mu^{\text{CL}_\text{s}}_{\text{obs}} = \sigma^{\text{CL}_\text{s}}_{\text{obs}}/\sigma_{h_s}$ and for the expected signal prediction $\mu^{\text{CL}_\text{s}}_{\text{exp}} = \sigma^{\text{CL}_\text{s}}_{\text{median exp}}/\sigma_{h_s}$ for a certain signal hypothesis h_s. If $\mu^{\text{CL}_\text{s}}_{\text{exp,obs}} \leq 1$, h_s is excluded at the 95% CL. The $\pm 1(2)\sigma$ uncertainty on $\mu^{\text{CL}_\text{s}}_{\text{exp}}$ is computed by $\mu^{\text{CL}_\text{s}}_{\text{exp},\pm 1(2)\sigma} = \sigma^{\text{CL}_\text{s}}_{\text{median exp},\pm 1(2)\sigma}/\sigma_{h_s}$ around the median significance.

Likelihood construction The Likelihood function, L_μ, provides the probability for an observation to originate from a model that depends on one or multiple Parameter of Interest (POI). The statistical analyses presented here are built starting from a binned likelihood function $L_\mu = L(\mu, \theta)$ constructed as a product of Poisson probability terms over all bins i of each of the considered distributions, r:

$$L(\mu,\theta) = \prod_{r}^{R\in SR,CR} \prod_{i}^{N_r} \frac{\left(\mu s_i + b_i\right)^{n_i}}{n_i!} e^{-(\mu s_i + b_i)} \tag{12.6}$$

with N_r being the number of bins in distribution r, s_i being the total number of signal events, e.g. given by h_s and $b_i(\theta_{\mathbf{b}}, \mu_{b,l}) = \sum_l \mu_{b,l} b_l(\theta_b)$, with l indicating all considered backgrounds. The total number of expected events $e_i = \mu s_i + b_i$ is compared to n_i which corresponds to the observed number of events in data or a toy data set drawn from a given probability density function (pdf) generated under a hypothesis, e.g. h_s with a given μ. The POI is defined as μ.

Equation 12.6 depends on the previously introduced signal strength parameter μ and $\theta = (\theta_{\mathbf{s}}, \theta_{\mathbf{b}})$, a set of NPs. These NPs are a set of uncertain parameters. They encode the effect of statistical and systematic uncertainties on the signal and background expectations affecting either all bins in the same way (normalisation) or with different impacts on different bins (shape). External inputs are used to provide an estimate of the NPs in the form of central value and width, generally encoded in the form of a Gaussian or log-Normal *constraint* on the likelihood. In most cases, the systematic uncertainties estimated from dedicated measurements, e.g. from a given physics object calibration, is provided only as a maximum likelihood estimate $\bar{\theta}$ and the associated standard error $\sigma_{\bar{\theta}}$. The former are implemented for statistical and systematic uncertainties of a given signal and background prediction, whereas the latter accounts for normalisation uncertainties. This results in the final form of the likelihood used in this thesis which is:

$$L(\mu,\theta) = \left[\prod_{r}^{R\in SR,CR} \prod_{i}^{N_r} \frac{\left(\mu s_i + b_i\right)^{n_i}}{n_i!} e^{-(\mu s_i + b_i)}\right] \times \prod_{u\in\mathcal{N}} \rho\left(\bar{\theta}_u, \sigma_{\bar{\theta}_u}\right) \tag{12.7}$$

where $\mathcal{N}$ is the full set of constrained NPs. The constraint term $\rho\left(\theta, \sigma_\theta\right)$ is either given by:

$$\rho(\theta) = \frac{1}{\sqrt{2\pi}\sigma_{\bar{\theta}}} \exp\left(-\frac{(\theta-\bar{\theta})^2}{2\sigma_{\bar{\theta}}}\right) \text{ (Gaussian)} \tag{12.8}$$

$$\text{or} \tag{12.9}$$

$$\rho(\theta) = \frac{1}{\sqrt{2\pi}\ln(\sigma_{\bar{\theta}})} \frac{1}{\theta} \exp\left(-\frac{(\ln(\theta/\bar{\theta})^2)}{2\ln(\sigma_{\bar{\theta}})^2}\right) \text{ (log-Normal).} \tag{12.10}$$

As a convention, all NPs are redefined such that they are centered at zero with a width of one σ which ensures consistency between all NP values. For small uncertainties, the redefined NP is given by the Gaussian residual:

$$\theta' \equiv \frac{\theta - \bar{\theta}}{\sigma_{\bar{\theta}}}. \tag{12.11}$$

A continuous description of the systematic sources by the NPs is approximated given the limited information (binned distributions) and applied as *up*- and *down* variation to the nominal process expectation. The expected number of events per bin, N^p, where p denotes either the signal prediction or a particular background prediction, depends on a certain systematic source following:

$$N^p = N^p_{\text{nom}} \cdot \left(1 \pm \sum_j \Delta^p_j \theta_j\right) \tag{12.12}$$

with $\Delta^p_j \theta_j$ the absolute systematic variation from the nominal expectation induced by a systematic source j encoded in θ_j.

The POI μ is an unconstrained normalisation parameter accounting for the signal prediction. Unconstrained ("floating") normalisation parameters $\mu_{b,l}$ can also be assigned to background processes. The POI and set of NPs $\alpha = (\mu, \theta)$ values are obtained from the fit to data through maximisation of the likelihood (or minimisation of the negative log-Likelihood) with respect to the set of parameters α. The resulting set of estimated parameters, $\hat{\alpha}$, are denoted as unconditional Maximum Likelihood Estimators (MLEs). The set of estimated parameters minimises the likelihood when fixing the value of the POI denoted as $\hat{\hat{\alpha}}$ and referred to as conditional MLEs. The estimated parameters $\hat{\alpha}$ and $\hat{\hat{\alpha}}$ depend on the underlying data. MLEs are asymptotically unbiased such that they reflect the true value for large data samples. The covariance matrix of all MLEs is given by:

$$V_{ij} = \text{cov}(\hat{\alpha}_i, \hat{\alpha}_j) \tag{12.13}$$

and provides information on all systematic uncertainties that are correlated with $\alpha_i \in \alpha$. The solution to the likelihood minimisation is numerically assessed with algorithms implemented in MINUIT. Following the redefinition of the NP range introduced in Equation 12.11, a fitted value close to 0 with a $\pm 1\sigma$ uncertainty implies that the data did not have sufficient power to *pull* the NP from its initial value and to reduce its initial uncertainty. A NP pull indicates that the data prefers a shifted NP value to improve the agreement to the prediction. If the fitted uncertainty is smaller than the initial $\pm 1\sigma$, it can be inferred that the data has the statistical power to *constrain* (reduce) the initial allowed systematic range within the region probed by the likelihood. Various orthogonal analysis regions are designed and considered with a large population of background events of a certain type but with a minimal signal contamination. Such CRs can be used to constrain the normalisation $\mu_{b,l}$ and associated uncertainties θ_b of that background type. The use of CRs allows for a reduction of the impact of systematic uncertainties on the search sensitivity.

Test statistic As previously mentioned, a test statistic is employed to compare the level of agreement between data and a hypothesis under consideration. The test statistic commonly employed at the LHC is defined by:

$$t_\mu = -2\ln(\lambda(\mu)) = -2\ln\left(\frac{L(\mu, \hat{\hat{\theta}}_\mu)}{L(\hat{\mu}, \hat{\theta})}\right), \tag{12.14}$$

with $\lambda(\mu)$ expressing the Log-Likelihood Ratio (LLR) with values close to one implying good agreement between the underlying data and hypothesis. The ensemble of all possible values of the defined test statistic is given by the sampling distribution. This is interpreted as the pdf of the test statistic, $f(t_\mu|\mu, \hat{\hat{\theta}}_\mu)$, which is obtained through drawing from a randomised data set corresponding to a given hypothesis fixed by the choice of μ and constructed at the pulled and constrained NPs under the data set. The previously discussed p-value for testing a particular value of μ is given by:

$$p_{\mu,\mathrm{obs}} = \int_{t_{\mu,\mathrm{obs}}}^{\infty} f(t_\mu|\mu, \hat{\hat{\theta}}_\mu)\,\mathrm{d}t_\mu \tag{12.15}$$

where $t_{\mu,\mathrm{obs}}$ corresponds to the value of the test statistic obtained from data. Note, that in order to test if the hypothesis with μ is compatible also with a generated data set corresponding to an alternative hypothesis μ', $f(t_\mu|\mu', \hat{\hat{\theta}}_{\mu'})$ is drawn from an alternative data set generated under the assumption of μ'. The set of profiled NPs can either be taken as obtained from the fit to data or to a toy data set. The obtained median of $f(t_\mu|\mu', \hat{\hat{\theta}}_{\mu'})$ can be used to extract the corresponding median expected p-value and is given by:

$$p_{\mu,\mathrm{median}} = \int_{t_{\mu',\mathrm{median}}}^{\infty} f(t_\mu|\mu', \hat{\hat{\theta}}_{\mu'})\,\mathrm{d}t_\mu. \tag{12.16}$$

Figure 12.4 shows the observed and median expected p-values and the sampling distributions obtained when drawing from two different data sets corresponding to the hypothesis with μ and μ'.

When performing experiments and optmising an analysis, it is important to know the expected median significance that is needed to reject different signal hypotheses $\{H_s\}$ with varying values of μ. In discovery mode, one is interested in the median expected significance when

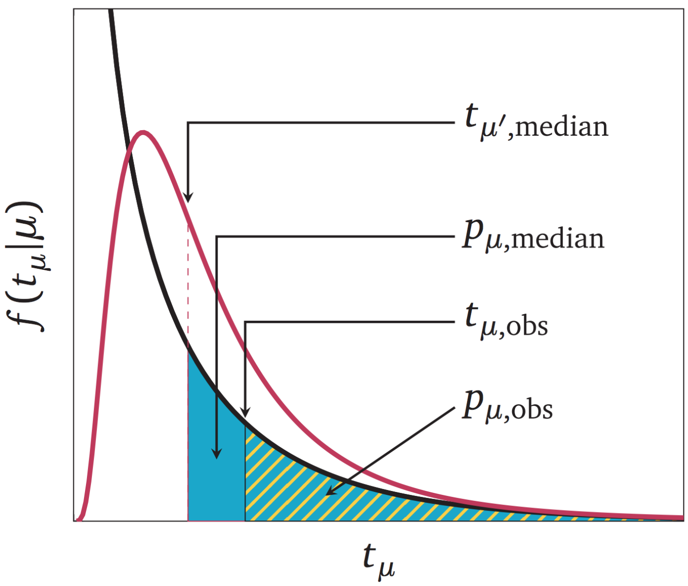

Figure 12.4: A schematic representation of the observed and median expected p-value for a signal hypothesis with a certain predicted value of μ and the sampling distributions drawn from a generated data set corresponding to μ and μ' [254].

data is drawn from a certain $S + B$ hypothesis ($\mu = 1$) with which one would reject the B hypothesis ($\mu = 0$). The corresponding pdf $f(t_0|\mu = 0, \hat{\hat{\theta}}_{\mu=0})$ is integrated above the median of $f(t_0|\mu = 1, \hat{\hat{\theta}}_{\mu=1})$ giving $p_{0,\text{median}}$. The compatibility of the data with the B only hypothesis is checked by integrating $p_{0,\text{obs}}$ (Equation 12.15 under the B only hypothesis corresponding to $\mu = 0$) above $t_{0,\text{obs}}$ which provides the p_0-value. In case no significant data excess above the B hypothesis prediction is observed, the analysis results are converted into an upper limit on the POI μ.

In limit setting mode, the 95% CL is derived from $f(t_1|\mu = 0, \hat{\hat{\theta}}_{\mu=0})$ for various signal hypothesis h_s with varying μ employing the above described CL_s method. For each hypothesis, μ is scanned until $\text{CL}_s \leq 0.05$. The corresponding pdf $f(t_1|\mu = 0, \hat{\hat{\theta}}_{\mu=0})$ is integrated above the median of $f(t_1|\mu = 1, \hat{\hat{\theta}}_{\mu=1})$ giving $p_{1,\text{median}}$. For the analyses in this dissertation, the limits directly translate into an upper limit on the associated production cross section as a function of the VLQ mass, which can thus be interpreted as a lower limit on the associated mass of the hypothetical new particle. The analysis cuts employed in the respective analysis were optimised on the basis of a maximisation of the expected sensitivity in limit setting mode.

Asymptotic formula The test statistic t_μ given in Equation 12.14 can be approximated in the limit of large statistics N. Wald [255] showed that the sampling distribution $f(t_\mu|\mu')$ of the test statistic t_μ with strength parameter μ and underlying data distributed according to μ' is given approximately by

$$t_\mu = -2\ln\lambda(\mu) \simeq \frac{(\mu-\hat{\mu})^2}{\sigma^2} + \mathcal{O}(1/\sqrt{N}). \tag{12.17}$$

for a single POI. $\hat{\mu}$ is a normal distribution with mean μ' and standard deviation σ:

$$f(\hat{\mu}|\mu') = \frac{1}{\sqrt{2\pi}\sigma}\exp-\left(\frac{\mu-\hat{\mu})^2}{\sigma^2}\right) \tag{12.18}$$

The standard deviation can be obtained through an *Asimov data set*. An Asimov data set is defined as the pseudo data generated from a given distribution that corresponds to the sum of background predictions. Equation 12.18 can be transformed into a non central χ^2 distribution. Wilk [256] showed that for the special case of $\mu = \mu'$ the sampling distribution of t_μ follows a χ^2 distribution with one degree of freedom:

$$f(t_\mu|\mu) = \frac{1}{\sqrt{2\pi}}e^{-t_\mu/2}\frac{1}{\sqrt{t_\mu}}. \tag{12.19}$$

The analyses results presented in Chapters 13 and 14 are derived based on the asymptotic approximation. For details the reader is referred to Ref. [257].

Nuisance parameter ranking When the fit to data is performed under the $S+B$ hypothesis ($\mu = 1$) for a given signal hypothesis h_s, the effect of each NP on the extracted signal strength parameter μ can be approximately assessed. In this thesis, the procedure to obtain the effect of each NP on μ consists on rerunning the fit fixing first each NP to the initial (fitted) $+1\hat{\sigma}_\theta$ and then to the initial (fitted) -1$\hat{\sigma}_\theta$ and performing the fit to all other NPs. The difference between the fitted value of μ under these constrained fits and when the NP is set to its nominal value is taken as the impact on μ of that NP, denoted as $\Delta\mu$. Each NP is then ranked according to the absolute pre- and post-fit effect on the uncertainty on μ. This ranking procedure helps in the identification of the leading systematic uncertainties that affect the sensitivity of the search.

12.6 Boosted Decision Trees

A Boosted Decision Tree (BDT) is used to discriminate background and signal in one of the SRs of the analysis presented in Chapter 14. This section provides a very brief description of BDTs. A particular Multivariate Analysis (MVA) method commonly employed in HEP is a Decision Tree (DT) [258]. A DT executes cuts sequentially in order to perform a classification task on a given input data set using a tree like structure. A set of discriminating variables $\{x\}$ between signal and background are fed into the initial node of a tree (*root node*). A binary decision is made through a cut on a single variable $x_i \in \{x\}$ that shows the best separation gain between signal and background at each node of the tree which successively reduces the number of previous events and forms two branches, one for signal like and one for background like events. The last nodes in the tree are referred to as the *leaf nodes* which are required to contain a minimum percentage of the total events used as input in the *root node*. Following the resulting tree structure from root to a certain leaf node that is classified as signal or background like, depending on the majority of events assigned to either class[11], represents a cut sequence separating between signal and background events. The separation criteria at each node that define a cut value for a discriminating variable x_i in a predefined range is defined by the Gini Index (GI):

$$\mathrm{GI} = p \cdot (1-p) = \frac{sb}{(s+b)^2}, \text{ with } p = \frac{s}{s+b}, \tag{12.20}$$

where p is the purity, and s and b the signal and background events, respectively. The separation criterion ensures to find cut values that equally select background and signal events. It has a maximum in case the sample is fully mixed which results in $p = 0.5$ and falls off for asymmetric event classes, converging to zero for a single event class. The best discriminating variable is obtained by evaluating the separation gain considering the separation at a parent node and the sum of the two daughter nodes weighted by the relative event fraction.

DT are commonly employed in the context of HEP since they allow an interpretation through visualisation by a two-dimensional tree like structure. They are insensitive to input variables with low separation power. A downside of DTs is that they are sensitive to statistical fluctuations of the input variables such that variables that show a similar separation power to other variables might be neglected for node splitting. The latter decision variable neglect might result in a different classifier response. In addition, they can not effectively deal with correlated input variables. Ensemble learning methods can be employed in order to overcome limitations occuring in DTs. The idea is to define different discriminating variable sets $\{x\}_1, \{x\}_2, \ldots$ to build a *forest* of individual DTs. The input variables of each *root node* are reweighted in a certain

[11] A leaf is labeled signal like if the purity $p > 0.5$, background like otherwise.

manner, resulting in a different input variable set for the respective trees. The reweighting procedure is denoted as *boosting* [259, 260]. The idea is to start off with a tree that is based on an input variable set that is unmodified. The next tree assigns a higher weight to previously misclassified events resulting in a modified input variable set. The assigned multiplicative weight is defined as $\alpha = {}^{(1-\epsilon)}/_{\epsilon}$ with ϵ denoting the misclassification error [261] of the previously misclassified event. The sum of weights of all events is restricted to stay constant which is achieved through renormalising individual event weights. The individual BDTs project a final score as a result of the individual classifier, $y_i(\{x\}_i)$, which ranges from $+1$ for signal-like to -1 for background-like. The resulting boosted event classifier is the weighted average of the N individual classifiers and is expressed as:

$$y^{\text{boost}} = \frac{1}{N}\sum_{i}^{N} \ln(\alpha_i) y_i(\{x\}_i). \tag{12.21}$$

A sequential ensemble boosting method that is commonly used due to not being very prone to overtraining is an algorithm called AdaBoost [261] and is implemented in the Toolkit for Multivariate Data Analysis (TMVA) v4.2.0 [262]. The AdaBoost algorithm shows good performance for small tree depths with small respective discrimination power. The boosting weight is modified to α^{β} with β controlling the number of allowed boost steps. The AdaBoost algorithm was initially used in HEP by the MiniBooNE [263] and DØ [264] at Fermilab, USA.

Variable importance ranking The BDT variables are ranked according to their frequency of consultation to split a tree node. Each split occurrence is weighted by the total number of events in a tree node and the squared separation gain [258].

Chapter 13

Search for Vector-like T Quarks Decaying to a High Momentum W Boson and Bottom-quarks

This chapter presents a search for pair production of VLQs, $T\bar{T}$, where both T quarks decay to Wb. The final state consists of a high-p_{T} charged lepton (either an electron or muon) and missing transverse momentum from the leptonically decaying W boson, a high-momentum large-R jet from hadronically decaying W bosons, and two b-jets. Figure 14.1 depicts an example for a leading order Feynman diagram for the targeted process. It shows other allowed decay modes of the VLT into Zt or Ht.

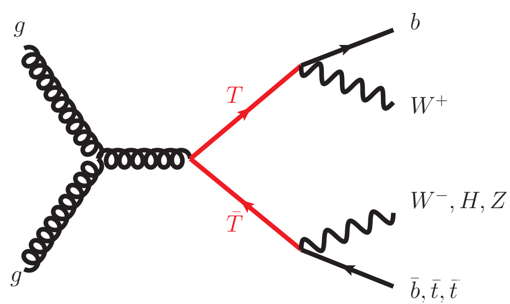

Figure 13.1: Example of a leading order Feynman diagram for $T\bar{T}$ production in the targeted Wb decay mode indicating the additional allowed decays into Ht and Zt.

13.1 Analysis Overview

The analysis presented supersedes a preliminary ATLAS result that was carried out for the ICHEP conference in 2016 based on an intermediate Run II data set combining the full 2015 and early 2016 data set that corresponded to a total integrated luminosity of 14.7 fb^{-1} [265]. The preliminary result set lower observed (expected) mass limits on VLTs at 1090 (980) GeV assuming $\mathscr{B}(T \to Wb) = 1$. For the $SU(2)$ singlet model a lower observed (expected) mass limit of 810 (870) GeV was set. Previous published ATLAS results based on 20 fb^{-1} at 8 TeV [266] and a preliminary CMS result based on 2.3 fb^{-1} at 13 TeV [267] were superseded. In contrast to the preliminary ATLAS result that targeted both resolved and boosted event topologies, the analysis presented solely focuses on a boosted topology. The addition of a resolved channel did not result in a sensitivity increase for the combined 2015 and 2016 data set. This search targets VLT masses above 1 TeV.

The VLTs in this mass range are reconstructed pre-dominantly as boosted objects. The decay products of objects that exceed a certain p_{T} threshold reduce the probability of resolving individual decay products reconstructed using standard narrow-radius jets such as the anti-k_t jets with $R = 0.4$. In order to recover sensitivity, large-R jets with an increased radius parameter $R = 1.0$ are used. The leptonic W boson decay results in a high-p_{T} lepton accompanied by moderate $E_{\mathrm{T}}^{\mathrm{miss}}$ and the hadronic W boson decays into a single large-R jet. The decay signature of the targeted VLT signal is identical to the main background which originates from $t\bar{t}$ events. The kinematics of the signal are thus exploited in order to discriminate signal from the dominant backgrounds. The angular separation between the lepton and the reconstructed neutrino, hadronically decaying large-R jets fulfilling W identification criteria [134, 268], and S_{T} are keys for the design of this search. After these tight selection criteria, the TT system is reconstructed resulting in good discrimination between signal and background. The results are found to be also applicable to the $SU(2)$ singlet and decays of the Y quarks. As a reminder, the latter exclusively decay to Wb.

13.2 Event Selection

The loose PRE-selection described in Chapter 12.3 imposes a standard set of cuts selecting lepton+$E_{\mathrm{T}}^{\mathrm{miss}}$ events. The following selection criteria were optimised for the $T \to Wb$ event topology and are applied on the physics objects defined in Part III.

13.2.1 BASE Selection

The targeted VLT signal comprises of a moderate jet multiplicity due to the hadronic W boson decay and two additional b-quarks. In addition to the PRE-selection requirement on the number of small-R jet's, at least one small-R jet is required to fulfil the b-tagging criterion at the 77% efficiency WP providing a good compromise between the identification of b-tagged jets while providing a sufficient c-tag and light jet rejection. The b-tag requirement suppress non-$t\bar{t}$ backgrounds such as W+jets. A moderate cut on $E_{\mathrm{T}}^{\mathrm{miss}} > 60$ GeV is imposed to suppress contributions from the multi-jet background, that typically contributes dominantly at low $E_{\mathrm{T}}^{\mathrm{miss}}$. One large-$R$ jet per event is required to fulfil the W tagging requirement defined in Section 7.5 as well as requiring the separation between the W-tagged large-R jet and b-jets to be $\Delta R > 1.0$. In case multiple large-R jets pass the W tagging criterion, the one with a mass closest to the world average W mass is chosen. The selected large-R jet is denoted as W_{had} candidate. In addition, an $S_{\mathrm{T}} > 1000$ GeV requirement is imposed. Both of the latter requirements reduce the background from $t\bar{t}$ events. An overlap-removal procedure is imposed to avoid double-counting of energy between an electron inside the large-R jets, by removing large-R jets if the separation with the electron is $\Delta R < 1.0$.

After this BASE selection, the main background originates from $t\bar{t}$ which represents an irreducible background due to the identical decay signature as the VLT signal. Other background components are efficiently suppressed. Moderate contributions originate from single-top and W+jets events. Single-top events stem primarily from the Wt channel and have a lower jet multiplicity at LO; thus they are only selected if a sufficiently hard jet is produced as additional radiation. The W+jets background contribution comes from W bosons with additional heavy flavour jets. $W + b\bar{b}$+jets is suppressed by its low production rate. $W + c\bar{c}$+jets can contribute as high-p_{T} c-jets have a relatively high probability of being mis-identified as a b-jet. Although background contributions from W+light jets are sufficiently suppressed by the b-tagging requirement due to a low b mis-tag efficiency, the relative contribution is still moderate due to the high production rate. Small background contributions including diboson, Z+jets, $t\bar{t}V$, and multi-jet production, make a smaller but non-negligible contribution. Diboson events pass the BASE selection when one of the bosons decays leptonically and the other decays into sufficiently hard jets. Z+jets background events contribute in case one of the two leptons from the Z boson is mis-identified or outside of the acceptance. The b-tagging requirement suppresses contributions from all small backgrounds except for $Z + b\bar{b}$+jets that has a low production rate. The $E_{\mathrm{T}}^{\mathrm{miss}}$ cut reduces background contributions from Z+jets and multi-jet.

13.3 The Definition of Analysis Regions

In addition to the cuts applied as part of the BASE selection, additional cuts on $\Delta R(\text{lep}, \nu)$, S_{T}, and $|\Delta m(T, \bar{T})|$ are imposed to define the two analysis regions.

Table 13.1: The table shows the expected yields for both the SM background and signal predictions in the CR and SR. The uncertainties include all systematics and MC statistics.

Sample	SR	CR
$t\bar{t}$	55 ± 26	720 ± 130
W+jets	9 ± 4	78 ± 41
Single top	15 ± 15	160 ± 110
Others	12 ± 10	82 ± 66
Total Background	91 ± 35	1040 ± 200
$m_T = 1$ TeV, $\mathcal{B}(T \to Wb) = 1$	45 ± 4	15 ± 2
$m_T = 1$ TeV, $SU(2)$ singlet	21 ± 2	8 ± 1
Data	58	972

The event selection in the two regions is optimised for the best expected limits for the VLT scenario assuming $\mathcal{B}(T \to Wb) = 1$. Both regions have an upper cut on $\Delta R(\text{lep}, \nu) < 0.7$ and $|\Delta m(T, \bar{T})| < 300$ GeV. The former cut selects events with a high momentum leptonically decaying W boson, whereas the latter cut was optimised to reject both the $t\bar{t}$ and Wt single-top background. The two regions are orthogonal by imposing a lower cut on S_{T} >1800 GeV for the SR which maximises the expected sensitivity for VLT masses above 1 TeV. The CR is defined by $1000 < S_{\text{T}} < 1800$ GeV.

The CR and SR are defined in the plane spanned by $\Delta R(\text{lep}, \nu)$ and S_{T}. Figure 13.2 shows the expected distribution of the simulation in this plane for the VLT signal assuming $\mathcal{B}(T \to Wb) = 1$ for $m_T = 1.2$ TeV and the $t\bar{t}$ background. The CR is used to constrain the production rate of $t\bar{t}$ events and the $t\bar{t}$ modelling uncertainties. The SR contains most of the expected VLT signal for masses above $m_T >$ 1 TeV. Table 13.1 shows the expected number of events in the two analysis regions for the SM background, signal prediction, and data. The main backgrounds originate from $t\bar{t}$, W+jets, and single top. The other SM processes diboson, Z+jets, $t\bar{t}V$, and multi-jet production, form a small contribution and are grouped together into "Oth-

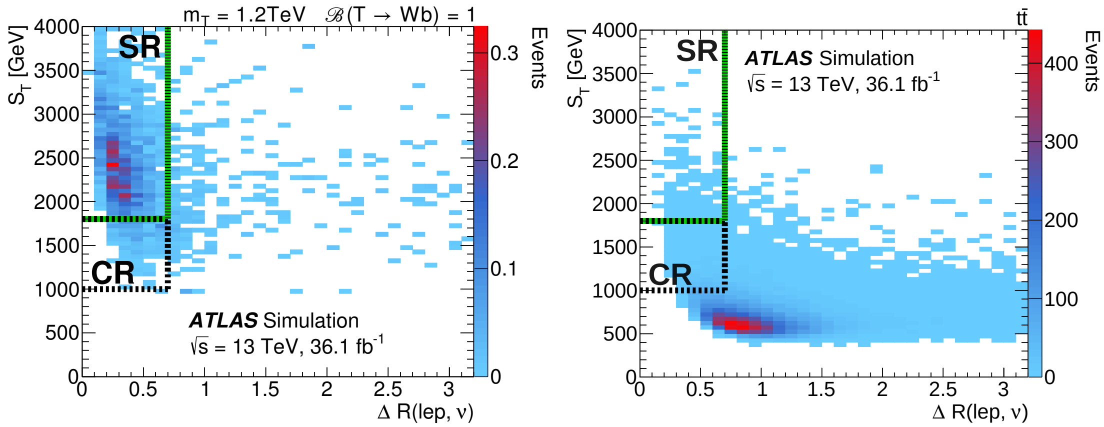

Figure 13.2: The CR and SR are indicated in a two-dimensional plane of S_{T} and $\Delta R(\text{lep}, \nu)$. The expected VLT signal distribution for $m_T = 1.2$ TeV assuming $\mathscr{B}(T \to Wb) = 1$ (left) and the distribution of the dominant $t\bar{t}$ background (right) is shown.

ers". Table 13.2 lists the signal contamination, quantified as S/B, within the two regions for different VLT masses assuming $\mathscr{B}(T \to Wb) = 1$. For low signal masses, $m_T \sim 800$ GeV, the signal contamination indicates that the CR acts as a second SR in the statistical analysis. For the targeted VLT signal mass range, the CR has a low signal contamination. This is underlined by Figure 13.3 that shows the signal acceptance times efficiency, $\mathscr{A}\epsilon$, for various signal masses under the two VLT decay mode assumptions, $\mathscr{B}(T \to Wb) = 1$ and $SU(2)$ singlet. The VLT signal $\mathscr{A}\epsilon$ in the CR for $m_T = 1$ TeV assuming $\mathscr{B}(T \to Wb) = 1$ is below 1%. Under the assumption of $\mathscr{B}(T \to Wb) = 1$, $\mathscr{A}\epsilon$ after full event selection ranges from 0.2% to 4% in the SR and 2% to 0.1% in the CR for VLT masses in the ranges from 500 to 1400 GeV. For the $SU(2)$ singlet, $\mathscr{A}\epsilon$ ranges from 0.1% to 2% (1% to 0.1%) for the CR (SR). Figure 13.4 shows the relative fraction of events in the SR for the different decay modes of a VLT signal, $m_T = 1000$ GeV starting with branching ratios of $\mathscr{B}(T \to Wb) = \mathscr{B}(T \to Ht) = \mathscr{B}(T \to Zt) = 1/3$.

Table 13.2: Summary of signal contamination S/B within the two analysis regions for different masses of m_T assuming $\mathscr{B}(T \to Wb) = 1$.

m_T in GeV	500	700	900	1000	1100	1300
SR S/B in %	275	163	84	57	34	11
CR S/B in %	143	34	5.5	1.5	0.5	0.1

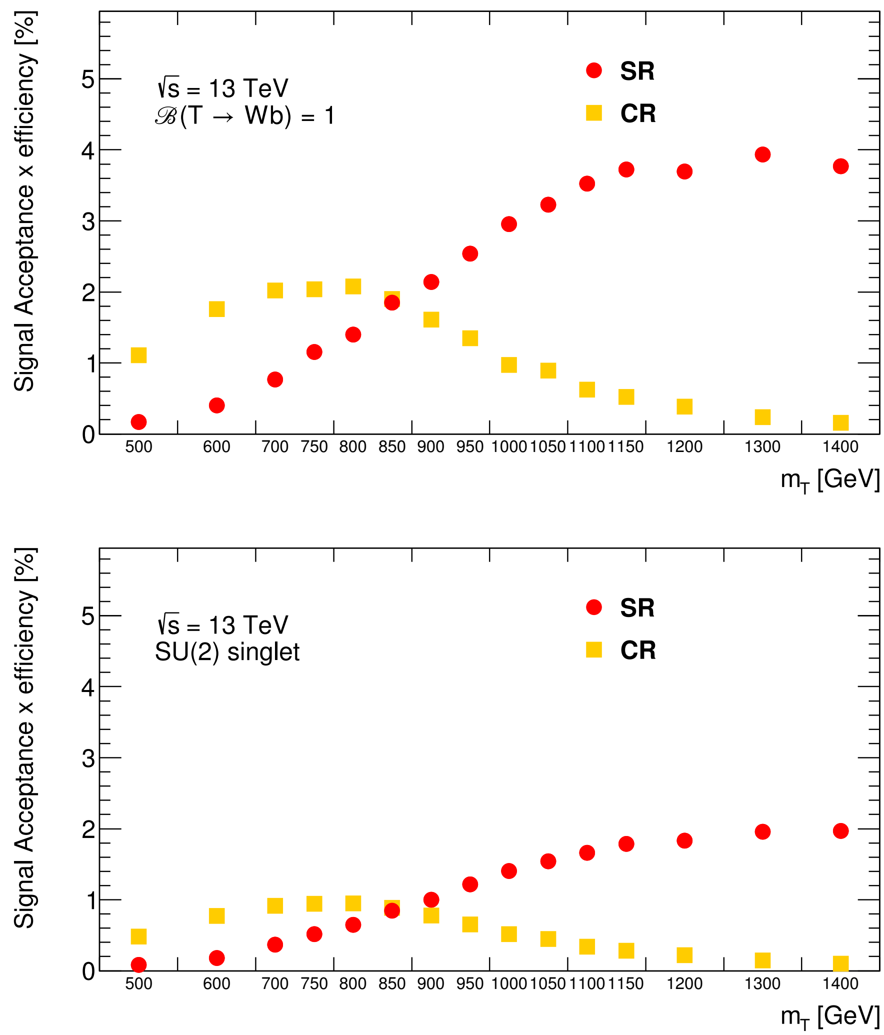

Figure 13.3: The signal acceptance times efficiency at various VLQ masses, assuming $\mathscr{B}(T \to Wb) = 1$ (top) and the $SU(2)$ singlet (bottom) for the CR and SR used in this analysis.

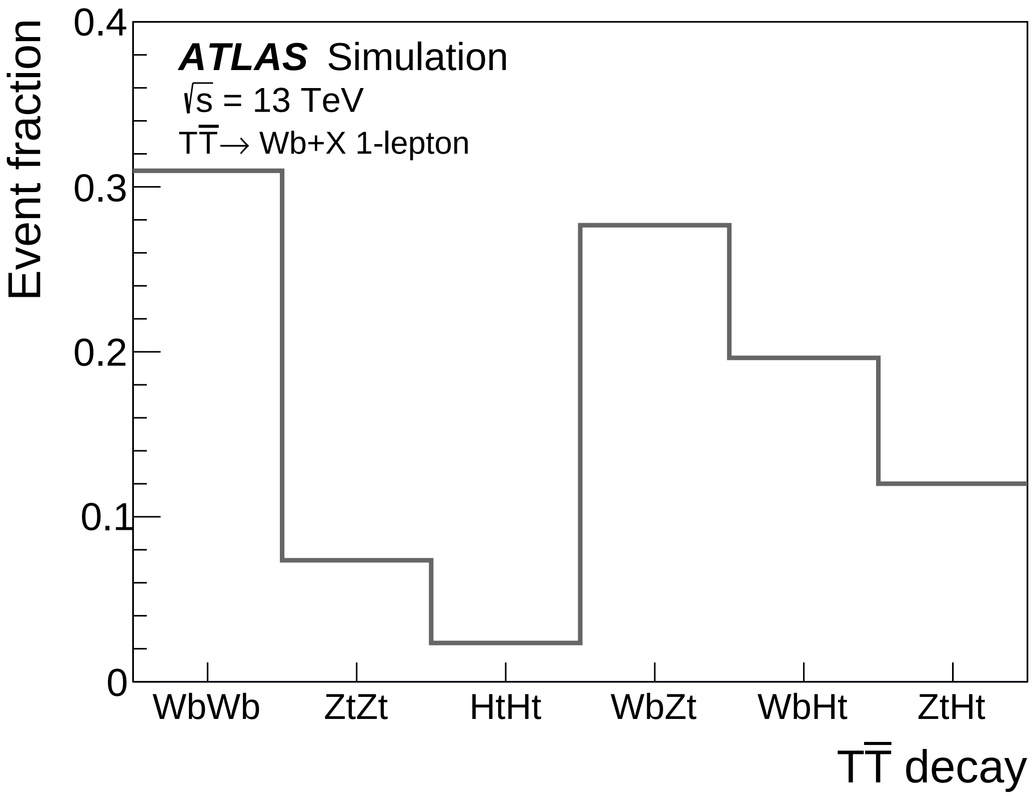

Figure 13.4: The relative fraction of events in the SR originating from the different decay modes of the VLT pair assuming $m_T = 1$ TeV and starting with branching ratios $\mathscr{B}(T \to Wb) = \mathscr{B}(T \to Ht) = \mathscr{B}(T \to Zt) = 1/3$ [218].

13.4 VLT System Reconstruction

The TT system is reconstructed using the reconstructed four momenta of the hadronic and leptonic VLT exploiting the leptons, the reconstructed neutrino (described in Section 12.4), and the W_{had}. The leptonic W, W_{lep}, is reconstructed from the four momenta of the lepton and neutrino in the event. In case an event contains two or more b-jets, the two leading[12] b-jets are taken as proxies for the b-jets for the combination with the W_{lep} and W_{had}. All possible permutations of associating a b-jet with one of the W's are tested and the combination that minimises the absolute mass difference between the hadronic and leptonic VLT candidate, $|\Delta m(T,\bar{T})| = |m_T^{\text{had}} - m_T^{\text{lep}}|$, is chosen. In case only one b-jet is present in the event, all permutations with the remaining small-R jets are tested to find the configuration that minimises $|\Delta m(T,\bar{T})|$. Figure 13.5 shows m_T^{lep} for six VLT signal masses and $t\bar{t}$ production in the SR after the reconstruction algorithm is applied. The reconstructed masses for the signal and $t\bar{t}$ background are shown to peak at the generated VLT and top-quark masses, respectively. The tails arise from misreconstructed VLT candidates.

13.5 Multi-jet Background Estimation in CR and SR

In Section 12.1.3 it was described that the tight event selection for the CR and SR significantly reduces the contribution of the multi-jet background, to the point where statistical uncertainties make MM predictions unreliable. A looser region is thus defined that encompasses both the CR and SR in order to estimate the contribution from the multi-jet background. The estimate derived in this looser region is extrapolated to the analysis regions. The loose region is defined after BASE selection with an additional cut on $\Delta R(\text{lep}, \nu) < 1.5$. The resulting statistics in this region provide a reliable multi-jet prediction for both the shape and normalisation. The shape is taken from the "Others" template. A shape comparison between the multi-jet estimate and the "Others" background is found to be stable under incremental small changes to the loose region lower requirement on S_{T} ($S_{\text{T}} >$ 800-1200 GeV). The fraction of multi-jet events is computed after $S_{\text{T}} >$1000 GeV and is found to be 20% larger than the expected total event yield of the "Others" background. The "Others" template is then scaled up by 20% in the CR and SR. The multi-jet background contribution relative to the total background is ∼6%.

[12]"Leading" in this context is defined with respect to an ordering in p_{T}.

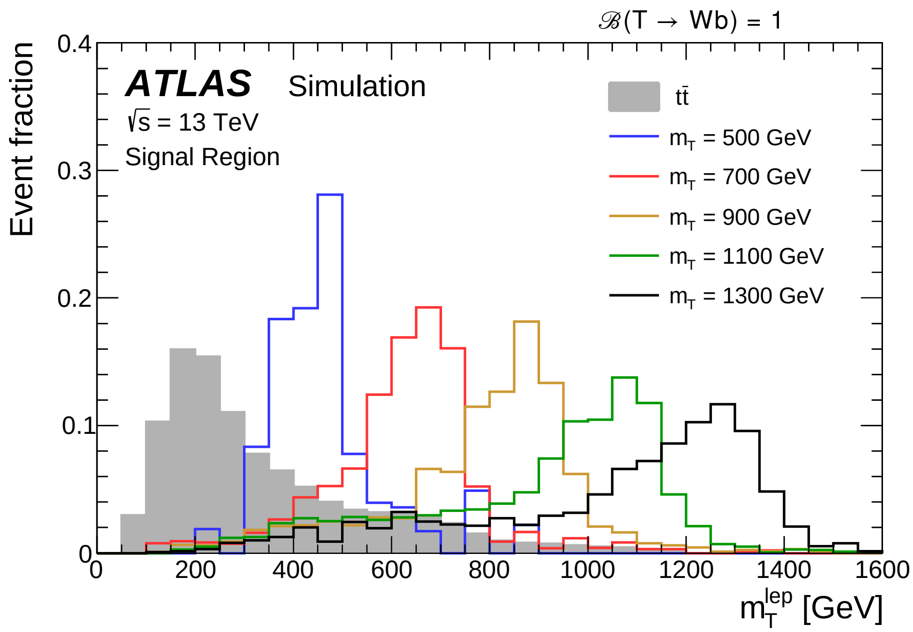

Figure 13.5: The reconstructed leptonic T quark mass in the SR is shown for the $t\bar{t}$ background and six signal masses varying from $m_T = 500 - 1300$ GeV in 200 GeV increments assuming $\mathscr{B}(T \rightarrow Wb) = 1$. In both figures, the distributions are normalised to unity for comparison of the relative shapes at each mass point. Due to the limited Monte Carlo sample size, the $t\bar{t}$ distribution has been smoothed [218].

13.6 Statistical Analysis

This section provides details about the setup of the statistical analysis, discusses results after unblinding of the analysis regions and the impact of the dominant uncertainties, as well as the results and interpretations of the findings.

13.6.1 The Fit Definition: Discriminant and Unblinded Results

The choice of the final discriminant is motivated by the maximal expected sensitivity. A set of variables showing good separation between the background and expected signal in the SR was identified and the statistical analysis performed. Variables considered were S_{T}, m_T^{had}, ${}^{m_T^{\mathrm{lep}}+m_T^{\mathrm{had}}}/_2$, and m_T^{lep}. The reconstructed leptonic VLT mass, m_T^{lep}(defined in Section 13.4), resulted in the best expected sensitivity for masses between 800 GeV and 1.2 TeV. m_T^{lep} is also chosen as discriminant in the CR. The final binning of the two discriminants was chosen to ensure sufficient MC statistics in all the bins for all backgrounds as well as for the alternative MC generators used to obtain for the top modelling systematic uncertainties. The fit is performed simultaneously in the two analysis regions, CR and SR with eight and five bins, respectively. The unblinded data compared to the total SM background prediction is shown in Figure 13.6 before the fit to data ("pre-fit"). The expected VLT signal at $m_T = 1$ TeV assuming $\mathscr{B}(T \to Wb) = 1$ is also shown. A good agreement between data and background prediction is observed in the CR whereas a

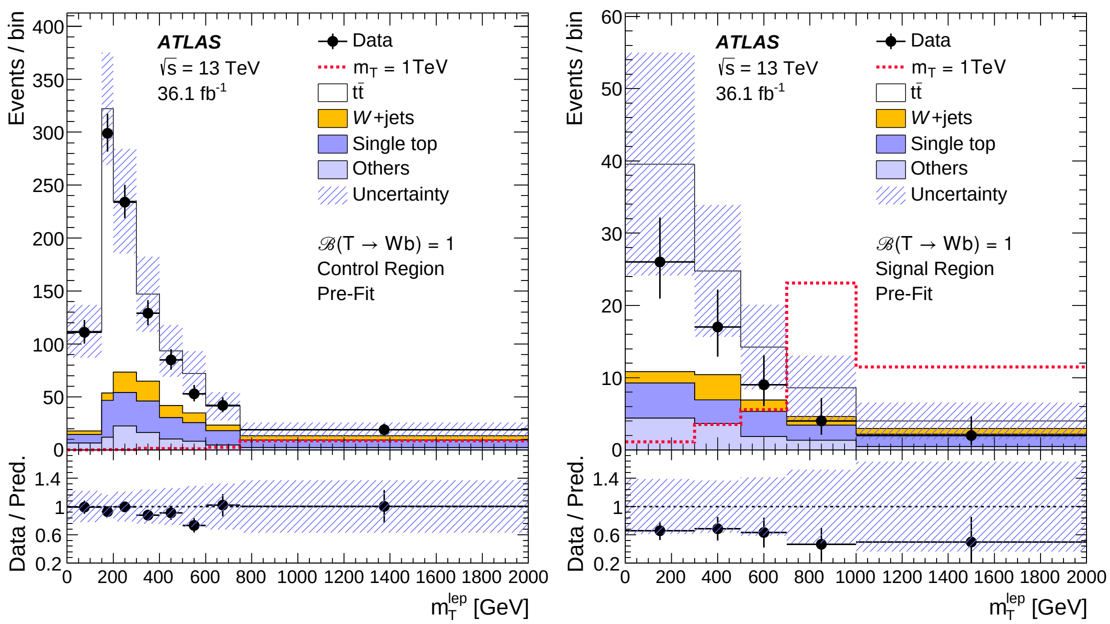

Figure 13.6: Comparison between data and total SM background predictions for the m_T^{lep} distribution in the CR (left) and SR (right) before the fit to data is shown. An expected VLT signal at $m_T = 1$ TeV assuming $\mathscr{B}(T \to Wb) = 1$ is overlaid. The lower panel shows the ratio of data to the background yields. The blue uncertainty band represents the total uncertainty in the background [218].

data deficit of ∼40% is observed in the SR. The observed data deficit is most likely driven by an increased $t\bar{t}$ mismodelling of the S_{T} variable at high S_{T}. The compatibility of the data is checked with the computed p-value assuming the background only hypothesis for all VLT signal mass hypothesis and varying assumption on the VLT decay branching ratio. The test statistic, q_0, approximated with the asymptotic formula is integrated out from above the observed value. The resulting p-value is found to be the lowest for $m_T = 700$ GeV and corresponds to ∼50%. Therefore, no significant excess above the SM expectation is observed.

13.6.2 Fit Results

The results after the data fit to the background-only hypothesis including all systematic uncertainties in the two analysis regions are shown in Figure 13.7 and Table 13.3. The impact of the 15 dominant uncertainties on the extracted signal strength parameter, μ, before and after the fit to the prediction under the signal-plus-background hypothesis as well as the pull of the associated NPs for the simultaneous fit are shown in Figure 13.8 (see Section 12.5.1). The signal hypothesis corresponds to $m_T = 1000$ GeV assuming $\mathcal{B}(T \to Wb) = 1$. The observed pre-fit

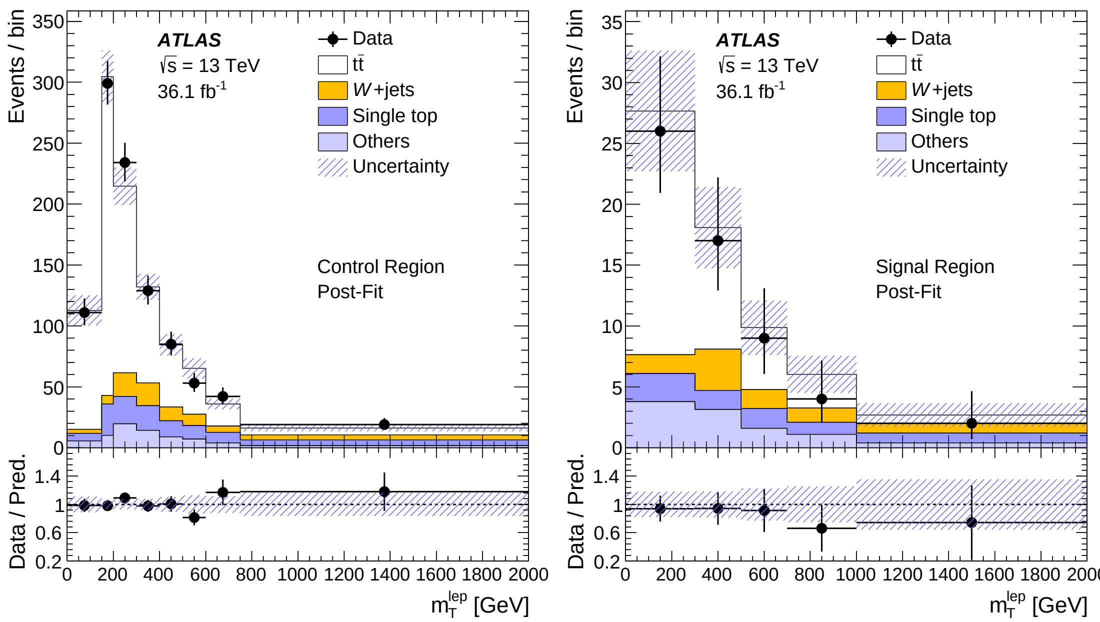

Figure 13.7: Comparison between data and SM prediction of m_T^{lep} in the CR (left) and SR (right) after the simultaneous fit in the two regions to data under the background-only hypothesis. The lower panel shows the ratio of data to the expected background yields. The band represents the systematic uncertainty after the maximum-likelihood fit [218].

data deficit in the SR is compensated for by the fit and as a result normalisation and shape uncertainties are pulled. An uncertainty reduction, limited by the precision of the data, results in constraints of the NPs and is pre-dominantly observed in the top-quark modelling uncertainties. This effect can be seen in the constraints shown in Figure 13.8 and the reduced systematic uncertainties on the respective background predictions in Table 13.3. The pre-fit agreement between data and background prediction in the CR fixes the NPs affecting the normalisation of the $t\bar{t}$ prediction close to the nominal values which results in the restriction for the fit to only

Table 13.3: Event yields in the SR and CR after the fit in the two regions under the background-only hypothesis. The uncertainties include statistical and systematic uncertainties. The uncertainties in the individual background components can be larger than the uncertainty in the sum of the backgrounds, which is strongly constrained by the data.

Sample	Signal region	Control region
$t\bar{t}$	39 ± 10	700 ± 70
W+jets	8 ± 4	78 ± 38
Single top	7 ± 4	110 ± 40
Others	10 ± 7	72 ± 48
Total background	64 ± 9	970 ± 50
Data	58	972

pull NPs that have a large impact on the normalisation in the SR but a small to negligible effect on normalisation and shape in the CR. A small data deficit is observed in the SR for $m_T^{\text{lep}} > 700$ GeV. The NPs that are pulled as a consequence of the fit are the $t\bar{t}$ normalisation and top-quark modelling systematics; in particular the hard scatter generation, additional radiation, and single top DS vs. DR uncertainty. The total uncertainty on the "Others" background is also pulled. The $t\bar{t}$ normalisation that is kept floating in the fit is fitted to 0.94 ± 0.16 times the nominal $t\bar{t}$ prediction.

13.6.3 Discussion of The Dominant Uncertainties

The largest impact on μ stems from the statistical uncertainty of the data. The dominant sources of **detector-related uncertainties** (see Section 12.2.2) in the signal and background distribution relate to the JER. The JER uncertainty has the largest pre-fit impact on μ with $\sim$2%. Other detector-related uncertainties ranking amongst the ones showing the largest impact on μ stem from the efficiency of tagging c jets. The one with the highest pre-fit impact on μ which is $\sim$1% has a 3% pre-fit impact on the normalisation on the VLT signal and background yields. The pile-up modelling uncertainty has a pre-fit impact of $\sim$1.5% with the highest pre-fit normalisation impact being on the single top background ($\sim$12%).

Many of the largest systematic uncertainties on the extraction of the signal strength parameter stem from the top-quark **modelling systematics**. The single top DR vs. DS uncertainty has a 90% normalisation impact in the SR, resulting in a pre-fit impact on μ of $\sim$5%. The $t\bar{t}$ modelling uncertainty accounting for different fragmentation and hadronisation models and hard scatter generation shows a pre-fit impact on μ of $\sim$3% and $\sim$4%, respectively, and have a normalisation impact of 18% and 38% in the SR, respectively. The $t\bar{t}$ modelling uncertainty accounting for additional radiation has a pre-fit impact of $\sim$1% with a pre-fit normalisation impact of 12%.

13.7 Results

Since no significant excesses above the SM expectations were observed, expected and observed lower VLT signal production cross section limits are derived for different benchmark models as a function of the VLT mass as shown in Figure 13.9. These limits are compared to the theoretical prediction of the VLT production. The limits are obtained via linear interpolation between the calculated CL_s value and the different mass points. The lower mass limit on m_T is obtained by comparing the excluded limits to the central value of the theoretical prediction. The observed (expected) lower m_T limit is 1350 GeV (1310 GeV) assuming $\mathcal{B}(T \to Wb) = 1$. For the $SU(2)$ singlet scenario the observed (expected) lower m_T limit is 1170 GeV (1080 GeV). These limits are summarised in Table 13.4. The limits are also found to be applicable for the $SU(2)$ doublet

Table 13.4: Comparison of the expected and observed lower mass limits for the two VLT branching ratio assumptions, $\mathcal{B}(T \to Wb) = 1$ and $SU(2)$ singlet. The results are obtained from running the statistical analysis with the full set of systematics for 36.1 fb^{-1}.

Lower Mass Limits [GeV]	$\mathcal{B}(T \to Wb) = 1$	$SU(2)$ singlet
expected	1310	1080
observed	1350	1170

VLT and the VLY quark, that has $\mathcal{B}(Y \to Wb) = 1$, to which this analysis is sensitive. The observed limits are slightly stronger ($\mathcal{O}(1\sigma)$) than the expected limits at high mass due to the slight data deficit observed in the SR. The sensitivity of the VLT search is limited by the data statistics. Performing the statistical analysis ignoring all systematic uncertainties results in an expected mass limit improvement of only $\sim$20 GeV for a VLT signal of $m_T = 1$ TeV assuming

$\mathscr{B}(T \to Wb) = 1$.

The analysis is used for reinterpretation of a varying number of signal hypotheses defined by their respective scaling of relative branching ratios to Wb, Zt, and Ht assuming $\mathscr{B}(T \to Wb) + \mathscr{B}(T \to Ht) + \mathscr{B}(T \to Zt) = 1$. Expected and observed mass limits are set in the full branching ratio plane in steps of 0.05. The statistical analysis is repeated for each point in the plane. The corresponding expected and observed VLT mass limits are shown in Figure 13.10.

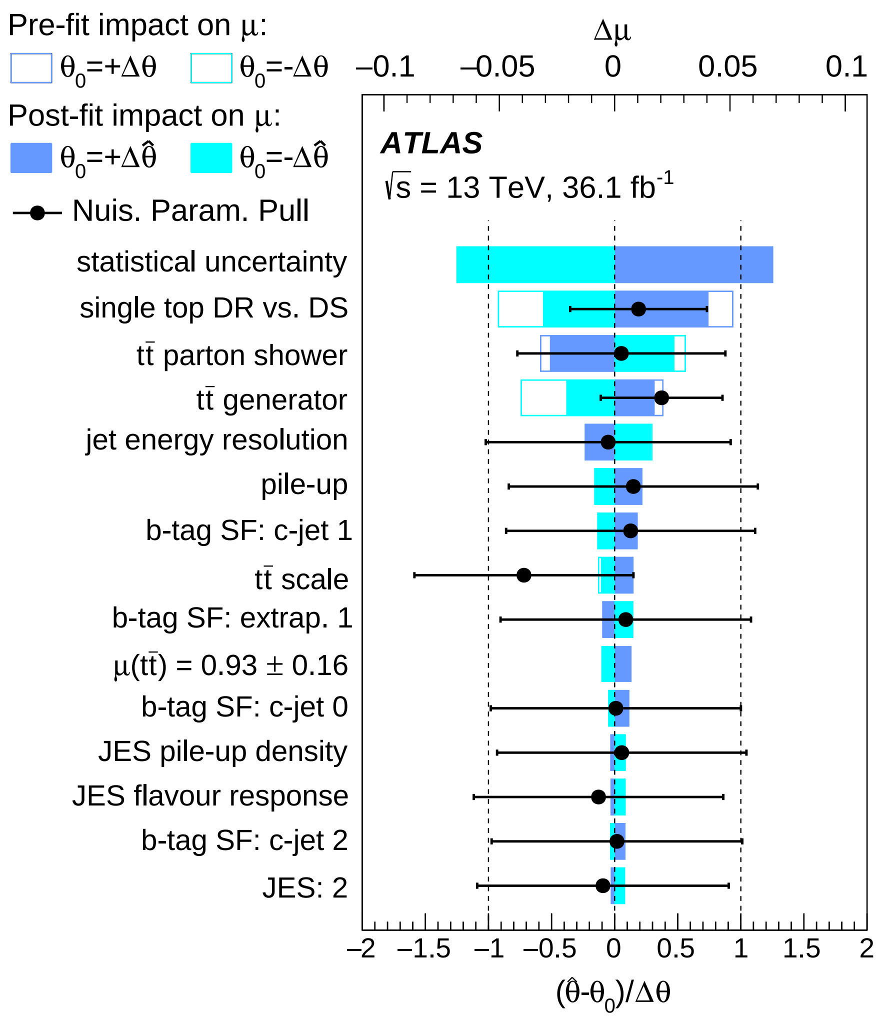

Figure 13.8: Ranking of NPs based on the fit to data in the signal-plus background hypothesis according to their effect on the uncertainty on μ ($\Delta\mu$). The TT signal hypothesis considered corresponds to $m_T = 1000$ GeV assuming $\mathscr{B}(T \to Wb) = 1$. The open boxes show the initial impact of that source of uncertainty in the precision of μ. The filled blue area shows the impact on the measurement of that source of uncertainty, after the profile likelihood fit at the $+1\sigma$ level. The filled cyan region illustrates the same for the -1σ impact. Both of those types of areas refer to the top axis. The ranking from top to bottom is done according to the effect on μ after the fit. The black points and associated error bars show the fitted value of the nuisance parameters and their errors and refer to the bottom axis; a mean of zero and a width of 1 would imply no constraint due to the profile likelihood fit. Only the 15 highest ranked uncertainties on μ are shown. No NP pull is shown for the statistical uncertainty and the unconstrained $t\bar{t}$ normalisation ($\mu(t\bar{t})$) parameter. The MC stat components as well as the $t\bar{t}$ normalisation uncertainty have priors at unity, all other nuisance parameters have priors at 0 [218].

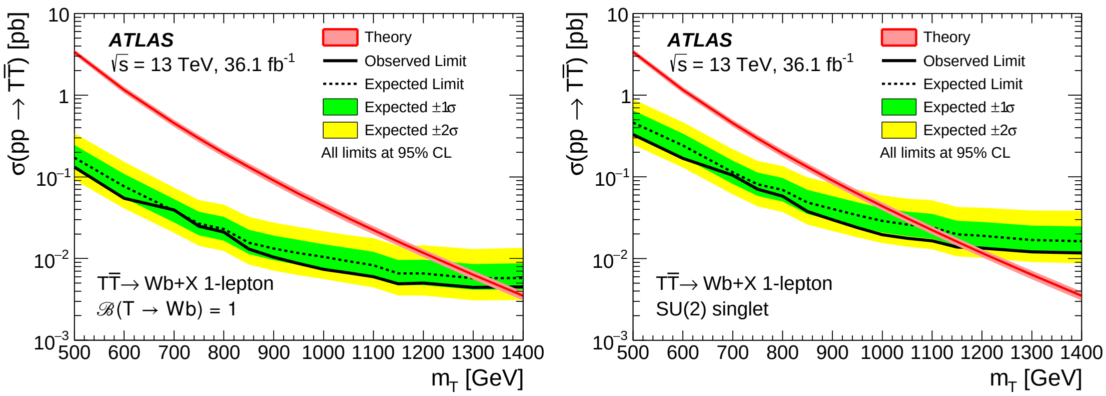

Figure 13.9: Expected (dashed black line) and observed (solid black line) upper limits at the 95% CL on the $T\bar{T}$ cross section as a function of T quark mass assuming $\mathcal{B}(T \to Wb) = 1$ (top) and in the SU(2) singlet T scenario (bottom). The green and yellow bands correspond to ±1 and ±2 standard deviations around the expected limit. The thin red line and band show the theoretical prediction and its ±1 standard deviation uncertainty [218].

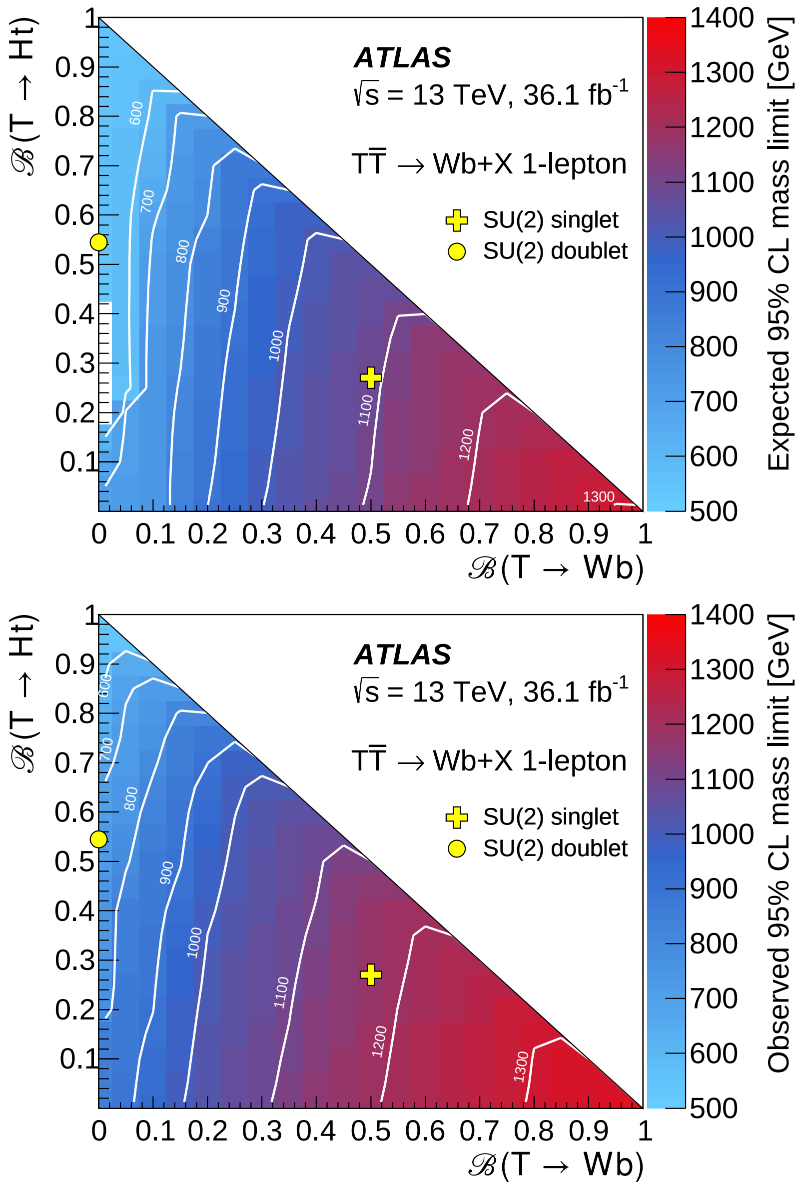

Figure 13.10: Expected (top) and observed (bottom) 95% CL lower limits on the mass of the T quark in the branching-ratio plane of $\mathscr{B}(T \to Wb)$ versus $\mathscr{B}(T \to Ht)$. Contour lines are provided to guide the eye. The markers indicate the branching ratios for the SU(2) singlet and doublet scenarios with masses above ∼0.8 TeV, where they are approximately independent of the VLQ T mass. The white region is due to the limit falling below 500 GeV, the lowest simulated signal mass [218].

Chapter 14

Search for Vector-like B Quarks Decaying to High Momentum W Bosons and Top-quarks

This chapter presents a search for pair production of VLQs, BB, where one B-quark decays to Wt and the other decays to Wt, Zb, or Hb. The final state consists of a high-p_{T} charged lepton (either an electron or muon) and missing transverse momentum from the decay of one of the W bosons, high-momentum large-R jets from hadronically decaying W bosons, and multiple b-jets. Figure 14.1 depicts an example of a leading order Feynman diagram for the targeted process.

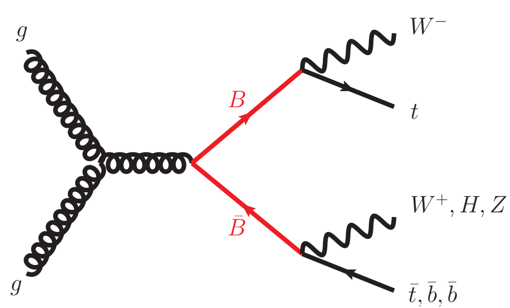

Figure 14.1: Example of a leading order production diagram for BB production in the targeted Wt decay mode indicating the additional allowed decays into "X" ($X = Wt, Hb, Zb$).

14.1 Analysis Overview

The analysis presented in Chapter 13 was found to be also sensitive to a B-quark decaying to Wt. The results were thus reinterpreted to provide a lower observed (expected) limit on the B-quark mass at 1250 (1150) GeV assuming $\mathscr{B}(B \to Wt) = 1$. For the VLB predicted by the

$SU(2)$ singlet, the observed (expected) limit was 1080 (980) GeV. As a result, the analysis presented here is optimised for VLB masses above 1 TeV with subsequent decay to two high-p_{T} W bosons and two top-quarks. A W boson directly originating from the B will be denoted as W_1 while the ones originating from the top-quark are dubbed W_2. Parton level truth studies suggest that in this mass regime the decay products of the VLBs have significant boost and get reconstructed in a single large-R jet. The studies also suggest that the number of leptonically decaying W_1 bosons is higher than the number of leptonically decaying W_2 bosons, most likely due to the lepton isolation requirement that suppresses boosted semi-leptonic top-quark decays at reconstruction level.

14.1.1 Truth Level Studies

This section gives a summary of truth studies performed to understand the hadronic decay products of the BB system at high VLB masses above 1 TeV. The truth level corresponds to the prediction of MC generators at parton level.

Parton level studies In order to further the understanding of the signal acceptance after the PRE-selection at reconstruction level (defined in Section 12.3), the multiplicities of parton level particles were studied. The BB pair production and decay into the single lepton final state is

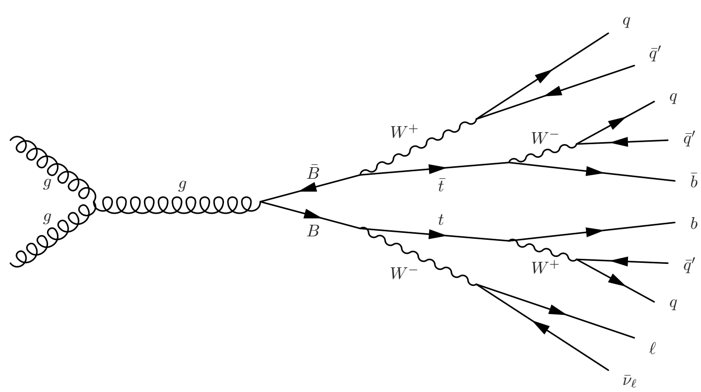

Figure 14.2: One example of a leading order diagram for the and gg- initiated BB pair production and decay into the single lepton final state.

shown in the Feynman diagram in Figure 14.2. The number of leptons and quarks of the final state partons after the top-quark and W boson decays show that the imposed event selection at reconstruction level does not exclusively select parton level ℓ+quark events. Signal events

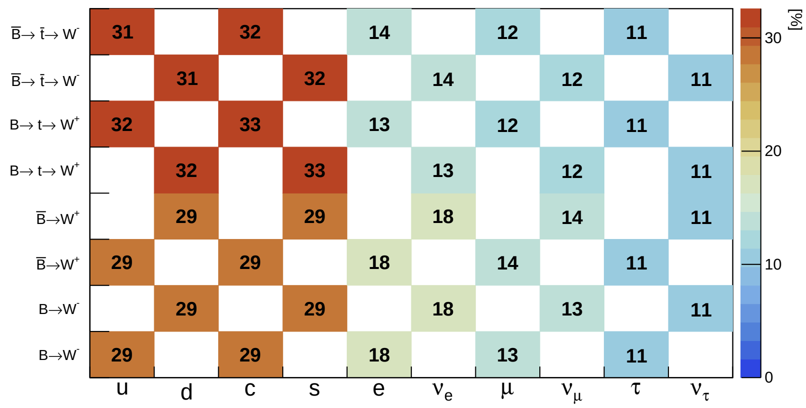

Figure 14.3: This figure shows the branching ratio in percent for the various decays of all W bosons originating from the BB production for $m_B = 1.15$ TeV assuming $\mathscr{B}(B \to Wt) = 1$. Each row shows the fractional number of the decay products of the various W bosons at parton level. A distinction is made between the respective up- and down type quark and lepton which are shown on the x-axis, e.g. $B \to t \to W$ would be a W_2 whereas $B \to W$ would be a W_1 as previously defined.

in which all W bosons decay into quarks do not contribute after PRE-selection, whereas events with one, two, or three parton level leptons represent ∼54%, ∼37% and ∼8% of acceptance, respectively.

Moreover, it is observed that the PRE-selection selects parton level W_1 bosons with a decay branching of ∼58% to hadrons and ∼42% to leptons, whereas the W_2 bosons decay in ∼63% of the cases hadronically and to ∼37% leptonically which is shown in Figure 14.3. This observation suggests that the applied reconstruction level PRE-selection biases slightly in favour of picking up leptons from W_1 most likely due to the imposed lepton isolation and identification criteria.

Figure 14.4 shows the p_{T} distributions at parton level of the VLBs and their decay products: the top-quarks, W_1 and W_2 bosons for signal masses corresponding to $m_B = 1.15,\ 1.4,\ 1.6,\ 1.8$ and 2 TeV assuming $\mathscr{B}(B \to Wt) = 1$ after PRE selection. The higher the signal mass, the harder the expected p_{T} spectrum of all components with a decreasing number of events due to the decreasing production cross section. Figure 14.5(a) shows the angular separation between the W_1 and top-quark originating from the VLB. It can be seen that they pre-dominantly decay back-to-back for a VLB produced at rest while the angular separation decreases for VLBs produced with increasing p_{T}. The p_{T} distribution for a hypothetical VLB with a mass of $m_B = 1.15$ TeV

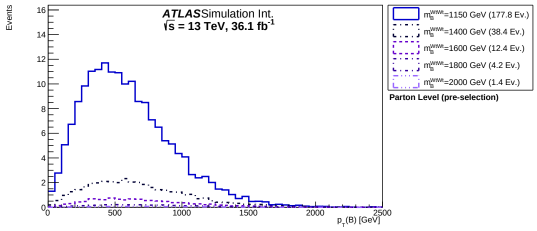

(a)

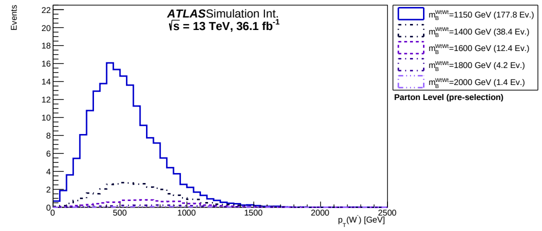

(b)

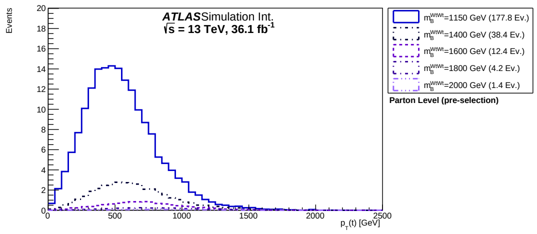

(c)

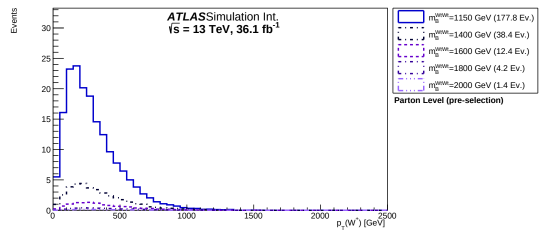

(d)

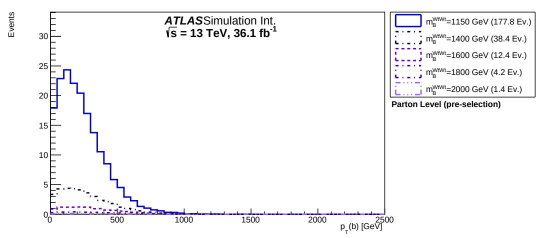

(e)

Figure 14.4: The p_{T} distributions of the VLB (a), W_1 (b), top-quark (c), W_2 (d), and b-quark (e) at parton level for signal mass points corresponding to $m_B = 1.15,\ 1.4,\ 1.8$ and 2 TeV. All plots are normalised to the expected event yield.

peaks at ∼500 GeV as shown in Figure 14.4(a). A VLB produced with that p_{T} shows an angular separation to the top-quark of $\Delta R(\mathrm{W, t}) \sim 2.5$. Looking at the next step in their decay chain, the W_1 and top-quark from the VLB decay are boosted and their respective decay products show an angular separation $\Delta R \lesssim 1$ as shown in Figures 14.5(b) and 14.5(c). The angular separation of the decay products of particle X can be approximated by [269]:

$$\Delta R_{\mathrm{yz}} \simeq \frac{\rho_0}{p_{\mathrm{T}}^X}, \tag{14.1}$$

with $\rho_0 \sim 2m_X$ for decay products y and z produced centrally. That behaviour can indeed be seen from a fit of equation 14.1 to the median $\Delta R(q, \bar{q})$ vs. $p_{\mathrm{T}}(W^-_{1,\mathrm{had}})$ distribution in Fig-

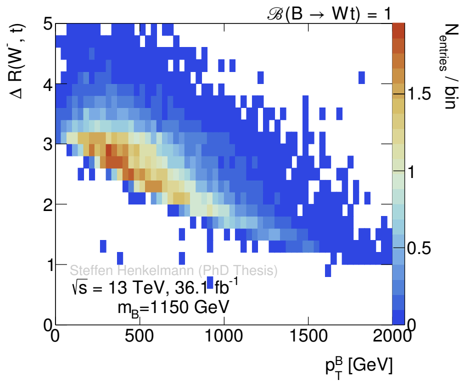

(a) $\Delta R\left(W_1^-, \text{top-quark}\right)$ vs. p_{T}^{B}

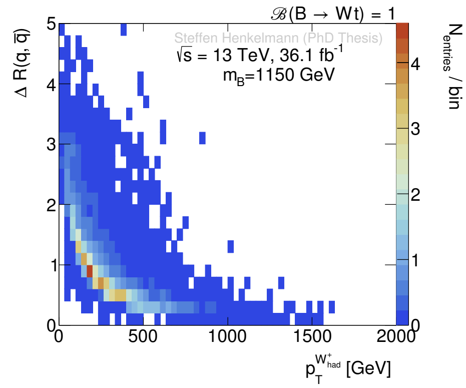

(b) $\Delta R\left(q, \bar{q}\right)$ vs. $p_{\mathrm{T}}\ (W_{2,\mathrm{had}}^-)$

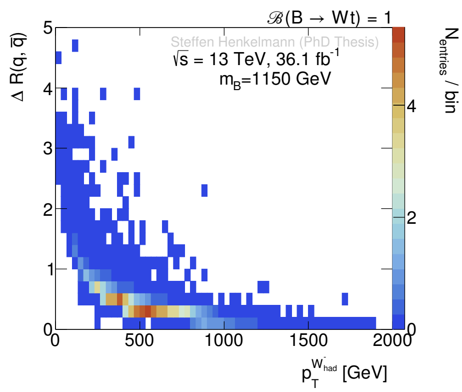

(c) $\Delta R\left(q, \bar{q}\right)$ vs. $p_{\mathrm{T}}\ (W_{1,\mathrm{had}}^-)$

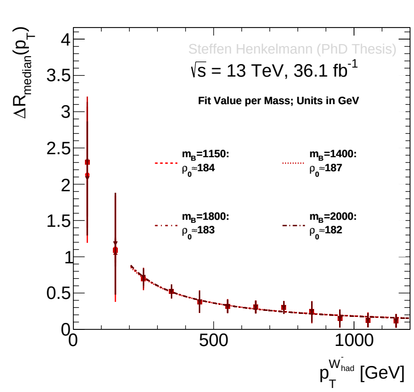

(d) $\Delta R\left(q, \bar{q}\right)$ vs. $p_{\mathrm{T}}\ (W_{1,\mathrm{had}}^-)$

Figure 14.5: The angular separation of the decay products of the VLB (a), $W_{2,\mathrm{had}}^-$ (b), and $W_{1,\mathrm{had}}^-$ (c) as a function of their p_{T} spectra for $m_B = 1.15$ TeV at parton level. The median angular separation vs. p_{T} for the W_1 boson for VLB masses corresponding to $m_B = 1.15, 1.6, 1.8$ and 2 TeV is shown alongside with values for ρ_0 is shown in (d) with uncertainties corresponding to the FWHM in each fitted p_{T} slice.

ure 14.5(d). As expected, the extracted value corresponds to $\rho_0 \sim 2m_W$, independently of the VLB mass assumed.

Parton to reconstruction level matching The substructure properties of a large-R jet depend not only on the p_{T} but also the number of parton decay products that are contained within the large-R jet, i.e. a large-R jet that contains two quarks and a b-quark is likely to have originated from the decay of a top-quark. A study of the respective *containment states* based on simulation thus provides a good handle to study characteristics of the signal composition. As example, Figure 14.5(c) suggests that at low p_{T} the angular separation between the W_1 decay products is larger compared to higher values which is expected to lead to a lower fraction of fully contained W large-R jets. Thus, the number of parton decay products contained within the large-R jet is studied as function of its kinematics. The containment states are studied as a function of the mass and p_{T} of the large-R jet selected after PRE-selection. This furthers the understanding of the VLB signal composition of the large-R jets at reconstruction level. Therefore, a parton to reconstruction level matching is performed. The parton level W_1 bosons and top-quarks are matched to the reconstruction level large-R jets by imposing the matching criteria:

- ΔR(reconstruction level large-R jet, parton level top-quark) < 0.75,
- $\Delta R\left(\text{reconstruction level large-}R\text{ jet, parton level }W_1\text{ boson}\right) < 0.75$,

following the truth-matching procedure described in Ref. [270]. Large-R jets fulfilling these criteria are either referred to parton matched W_1 or top-quark large-R jet. In order to define the containment states an additional matching requirement is applied to the parton matched W_1 and top-quark large-R jet:

- $\Delta R\left(\text{parton matched }W_1\text{ large-}R\text{ jet, parton}_{\mathrm{i}}\right) < 0.75$,
- $\Delta R\left(\text{parton matched top-quark large-}R\text{ jet, parton}_{\mathrm{j}}\right) < 0.75$,

with parton$_{\mathrm{i}}$ representing the hadronic decay products of W_1 and parton$_{\mathrm{j}}$ is the hadronic decay products of the top-quark (qqb). Figure 14.6 shows the number of expected events and the break down of parton W_1 bosons or top-quarks categories of contained light and b-quarks. These are shown as a function of the W_1 boson and top-quark transverse momentum. For example, $2q$ in the W_1 plots are cases in which both quarks are matched to the large-R jet. It is seen that only a small fraction of parton matched W_1 large-R jets are fully contained for $p_{\mathrm{T}} \lesssim 200$ GeV, whereas the vast majority of them are for higher p_{T}. For parton matched top-quark large-R jets, all three decay partons are contained for $p_{\mathrm{T}} \gtrsim 600$ GeV. At lower transverse momentum, the majority of events have only at least two quarks contained with the largest fraction stemming from one quark and one b-quark. It is found that most of the selected large-R jets at reconstruction level are fully contained W_1 bosons and fully or partially contained top-quarks.

The large-R jet composition is studied as a function of the number of large-R jets for the VLB signal mass template corresponding to $m_B = 1.15$ TeV assuming $\mathcal{B}(B \to Wt) = 1$ after PRE-selection. Figure 14.7(a) shows the large-R jet multiplicity overlaid with the relative

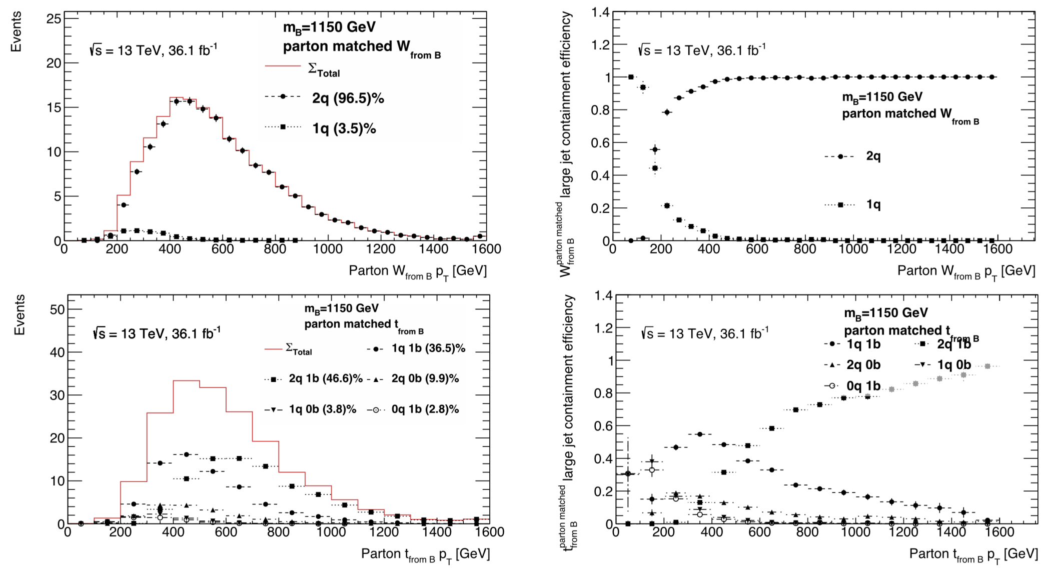

Figure 14.6: The number of expected events and containment states of the parton W_1 (top) and top-quark (bottom) matched large-R jets as function of their p_T (left). The containment state fraction as a function of the respective parton p_T is also shown (right). A VLB mass of $m_B = 1.15$ TeV assuming $\mathscr{B}(B \to Wt) = 1$ is shown. The bottom plots suffer from large MC statistical uncertainties in the low p_T region.

contributions from parton matched W_1 bosons and top-quarks. For that signal mass point, the majority of events are expected to contain one, two, or three large-R jets. The expected background contribution falls as a function of the large-R jet multiplicity. Therefore, Figure 14.7(b) details the fractional contribution in the two large-R jet and at least three large-R jet categories. Those two categories are promising with regard to both the expected S$/\sqrt{B}$ and allowing a BB system reconstruction.

It can be seen that in the three large-R jet category ∼70% of the reconstructed large-R jets are either matched to two top-quarks and one W_1-boson (∼40%) or to two W_1-bosons and one top-quark (∼30%). In the exclusive two large-R jet category, large-R jets are matched uniquely to two decay products of the VLB signal in ∼71% of the cases. In ∼14% of the cases the large-R jet is matched to three decay products implying overlapping objects within the same large-R jet. This study suggests that in most of the cases the selected large-R jets are the large-R jets of interest even before any jet flavour tagging criteria are applied. This motivates the BB system reconstruction described in Section 14.3.2.

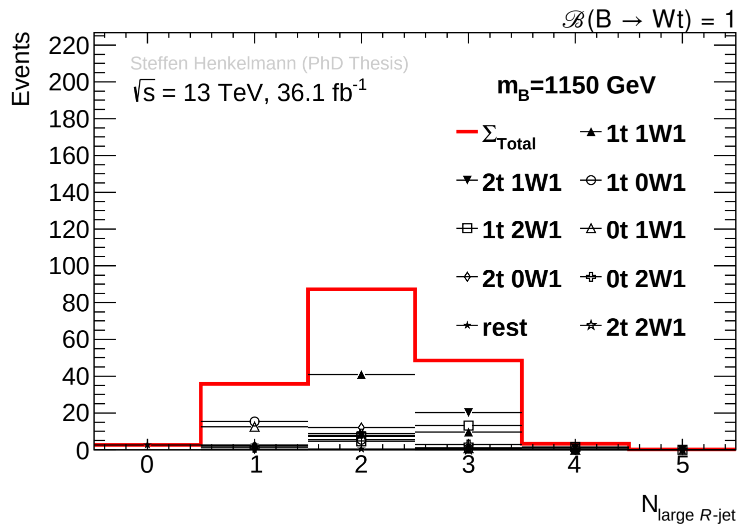

(a)

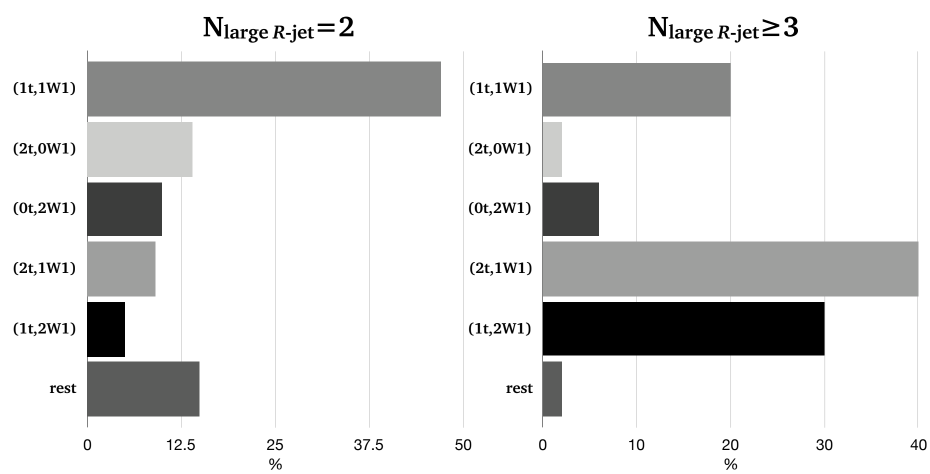

(b)

Figure 14.7: The number of large-R jets including the fraction of parton level matched W_1-bosons and top-quarks as well as a chart with a break down of the respective fractions in the two large-R jet exclusive and three large-R jet inclusive bins.

14.1.2 General Analysis Strategy

Based on the truth studies, the approach followed in this analysis is to require one of the four W bosons to decay leptonically and the others hadronically. This results in two classes of signatures.

- If it is one of the W_1 bosons that decays leptonically, 3 large-R jets (2 containing top-quarks, 1 containing a W), one lepton, and missing energy is expected.

- If it is one of the W_2 bosons that decays leptonically, 3 large-R jets (1 containing a top-quark, 2 containing a W), one additional small-R jet (from the b-quark from the leptonically decaying top), one lepton, and missing energy is expected.

Both of these topologies are treated together in the analysis (i.e. no attempt is made to separate these two cases). Due most likely to the lepton isolation requirement which rejects highly boosted semi-leptonic top decays, there are slightly more events in the first category than the second as previously shown. The observation that the two W bosons and two top-quarks are boosted, allows for the reconstruction of the BB system. This is in contrast to previous searches [271], targeting lower B masses, for which the combinatorics for small-R jets was too large to attempt a mass reconstruction.

To suppress the SM background, boosted jet reconstruction techniques [134, 268] are used to improve the identification of hadronically decaying high-p_{T} W bosons. This analysis, although targeting the $\mathscr{B}(B \to Wt) = 1$ decay mode, is sensitive to additional VLB decays which results in a wide sensitivity across the full branching ratio plane. In addition, the results are found to be equally applicable to B-quarks corresponding to either $SU(2)$ singlet or doublet models as well as applicable to the decays of X quarks. As a reminder, the latter exclusively decay to Wt.

14.2 Event Selection

The loose PRE-selection described in Chapter 12.3 imposes a standard set of cuts selecting lepton+$E_{\mathrm{T}}^{\mathrm{miss}}$ events. The following additional selection criteria were optimised for the VLB event topology and are applied to the physics objects defined in Part III.

14.2.1 BASE Selection

The VLB signal event topology consists of a high jet multiplicity driven by two b-jets and additional small-R jets from the hadronic decay of the three W bosons. As a result, at least four small-R jets out of which at least one is required to be a b-jet satisfying the 77% efficiency WP are required. After this selection, the expected signal yield when requiring exactly zero large-R jets for a VLB signal with $m_B = 1.15$ TeV assuming $\mathscr{B}(B \to Wt) = 1$ is $\sim$1% of the expected total signal yield. Therefore, an additional requirement of at least one large-R jet is applied. The leptonic decay of one of the W bosons results in moderate to high $E_{\mathrm{T}}^{\mathrm{miss}}$ for the targeted signal events. In order to suppress contributions from multi-jet background, a selection of $E_{\mathrm{T}}^{\mathrm{miss}} > 60$ GeV is applied. The contribution from $t\bar{t}$ events, constituting the main background, is suppressed by a lower requirement on $S_{\mathrm{T}} > 1200$ GeV. A collection of plots showing the agreement of the SM background predictions to data are shown in Figures 14.8 and 14.9. Backgrounds with large contributions include $t\bar{t}$, W+jets, and single-top events. Other SM processes, including diboson, Z+jets, $t\bar{t}V$, and multi-jet production, make a smaller but non-negligible contribution. Table 14.1 shows the resulting event yields for data and the SM background and signal predictions including the impact from all systematic uncertainties.

The observed data deficit is due to an over-prediction mostly stemming from the updated $t\bar{t}$ baseline model. A harder S_{T} spectrum for the updated relative to the initial $t\bar{t}$ baseline is observed.

Table 14.1: The table shows the expected yields for both the SM background and signal predictions after BASE selection. The uncertainties include all systematics.

Sample	Yield (BASE selection)
$t\bar{t}$	21 200 ± 7310
W+jets	4480 ± 2530
Single-top	2150 ± 1700
Diboson	359 ± 202
$t\bar{t}V$	353 ± 57.2
Z+jets	308 ± 176
Multi-jet	2480 ± 1250
Total Background	31 300 ± 8140
$m_B^{\mathrm{WtWt}} = 1.15$ TeV	146 ± 3.91
Data	25889

14.3 Classification of Event Topologies

This analysis defines two orthogonal SRs. The first SR denoted as RECOSR exploits the presence of multiple large-R jets in order to reconstruct the BB system. In addition, tighter selection criteria are applied to improve the signal sensitivity. A reconstruction algorithm for the BB system

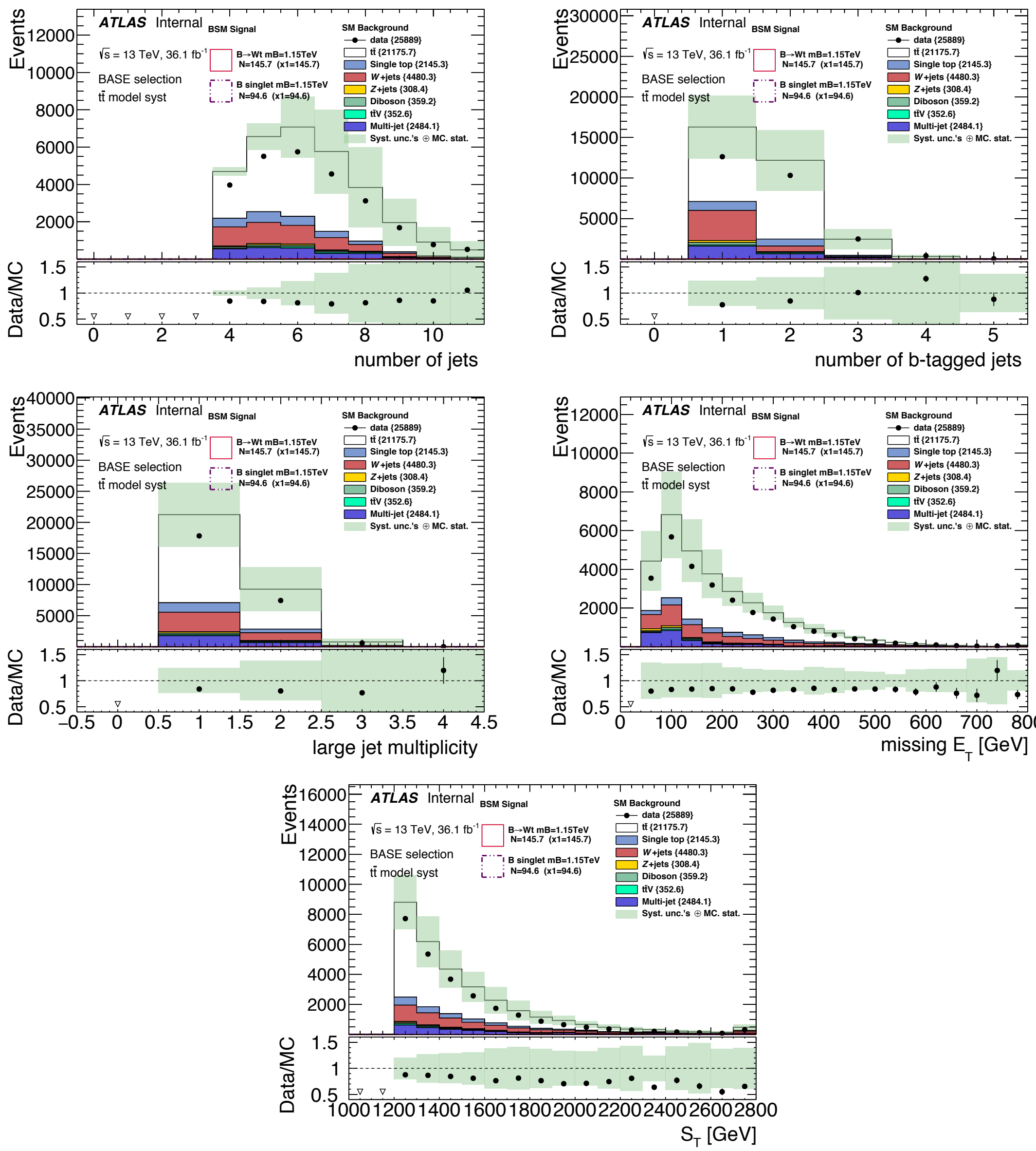

Figure 14.8: Kinematic distributions after BASE selection. Shown are the small-R jet, b-jet, large-R jet multiplicity, $E_{\mathrm{T}}^{\mathrm{miss}}$, and S_{T}. Uncertainties include MC statistics and $t\bar{t}$ modelling systematic uncertainties.

was designed on the basis of maximising the separation between the signal and dominant backgrounds. The mass of the hadronically decaying B candidate serves as the final discriminant.

The second SR dubbed BDTSR uses a BDT to separate the remaining high number of signal events from the background in a more inclusive region vetoing RECOSR.

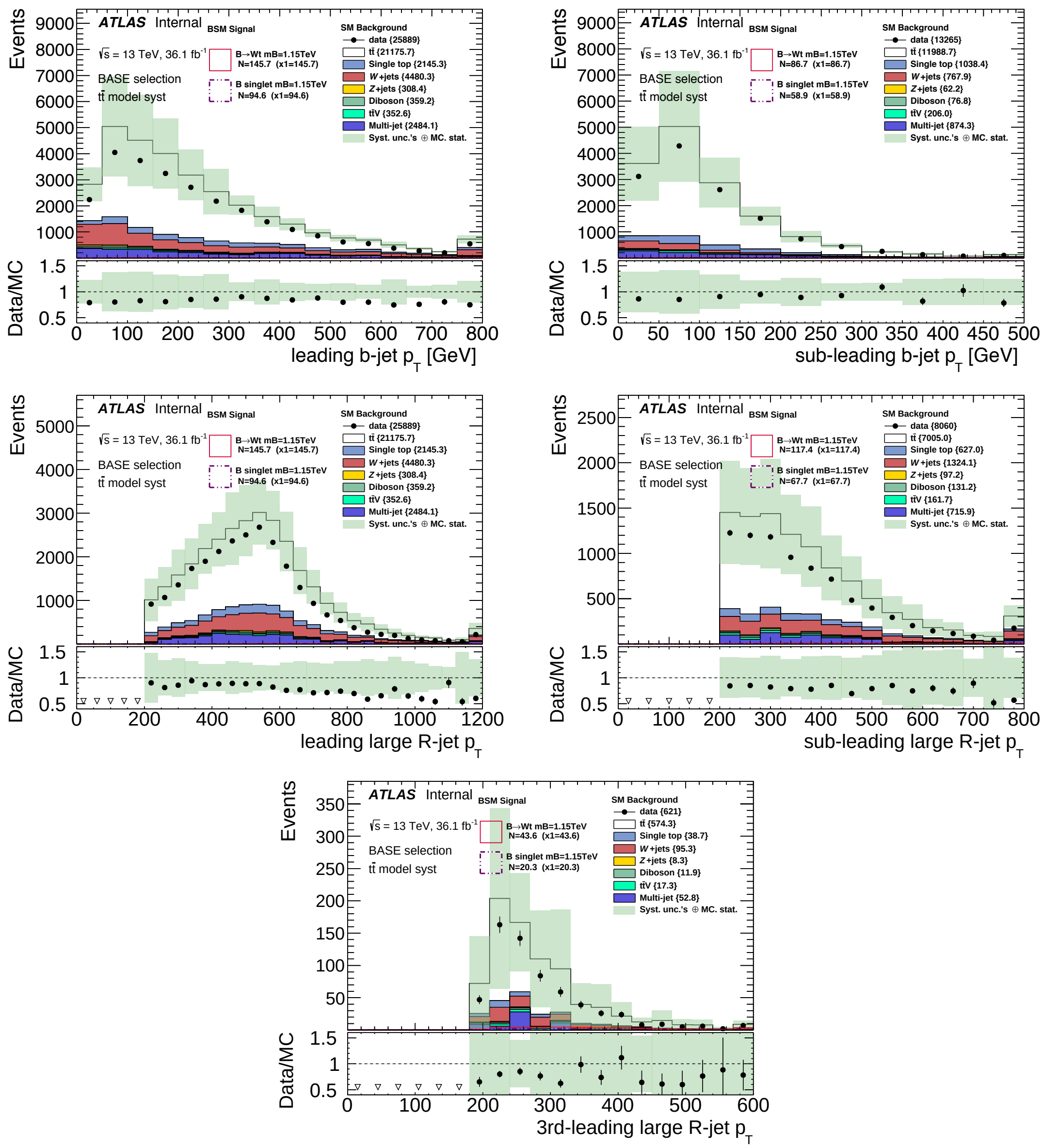

Figure 14.9: Kinematic distributions after BASE selection. Shown are the transverse momentum of the two (three) leading b-jets (large-R jets). Uncertainties include MC statistics and $t\bar{t}$ modelling systematic uncertainties.

14.3.1 RECOSR - Reconstructed Signal Region Definition

After the BASE selection an additional set of selection criteria are imposed. At least three large-R jets are required to further reduce the contamination from SM backgrounds and to provide inputs for a dedicated BB system reconstruction algorithm described in Section 14.3.2. Truth level studies summarized in Section 14.1 show that large-R jets are correctly matched to three VLB decay products in ∼70% of the cases when requiring at least three large-R jets. At least one of the large-R jets is required to be passing both the W tagging criteria (defined in Section 7.5), and is required to not overlap with an electron (b-jet) within $\Delta R < 1.0$ (0.75). The latter choice was found to be the optimal performer, among a various number of flavour tagging options tried, with regard to maximising the search sensitivity. After this selection a set of discriminant variables was identified. A two-dimensional profile likelihood scan was performed on individual sub sets of two kinematic variables with varying cut values. For each set of cut values, the search sensitivity was assessed with the final discriminant of the BB system reconstruction, m_B^{had}. Two final kinematic variables with optimised cut values are the result out of that optimisation procedure. Thus, two additional kinematic cuts are applied on top of the former selection criteria. Events fulfilling $S_\mathrm{T} \geq 1500$ GeV and $\Delta R(\ell$, leading b-jet$) \geq 1$ are selected. The leading b-jet populates both the same and opposite hemisphere relative to the lepton in the background events, whereas in the VLB signal events, the leading b-jet is usually opposite to the lepton.

Table 14.2 displays the expected number of events in the RecoSR for the SM background and signal prediction, and data including all systematic uncertainties. The main backgrounds originate from $t\bar{t}$, W+jets, and single-top. SM processes such as diboson, Z+jets, $t\bar{t}V$, and multi-jet production, form a small contribution. The latter backgrounds are grouped and referred to as "Others" background. Figure 14.10 illustrates $\mathcal{A}\epsilon$ for various signal masses under the two VLB decay mode assumptions, $\mathcal{B}(B \to Wt) = 1$ and $SU(2)$ singlet. Under the former assumption, $\mathcal{A}\epsilon$ after full event selection ranges from 0.1% to 4% for VLB masses from m_B = 500 to 2000 GeV. For the $SU(2)$ singlet, $\mathcal{A}\epsilon$ ranges from 0.04% to 1.5%. Figure 14.17 shows the relative fraction of events in the SRs for the different decay modes of a VLB signal $m_B = 1.15$ TeV and $m_B = 1.3$ TeV with $\mathcal{B}(B \to Wt) = 1$ and equal decay branching ratios of $\mathcal{B}(B \to Wt) = \mathcal{B}(B \to Hb) = \mathcal{B}(B \to Zb) = 1/3$. It shows that the RecoSR mainly selects VLB signal events that decay purely into $WtWt$ with additional acceptance for $WtHb$ and $WtZb$. This SR does not show significant acceptance to other decay modes that do not include the decay into Wt. The BdtSR shows most of its acceptance to the decay modes $WtHb$, $WtZb$, and $WtWt$ (in that order). Additional acceptance to the decay modes not including the decay into Wt are also present.

Table 14.2: The table shows the expected yields for both the SM background and signal predictions in the SRs RECOSR and BDTSR. The uncertainties include all systematics and MC statistics.

Sample	Yield (RECOSR selection)	Yield (BDTSR selection)
$t\bar{t}$	20.2 ± 15.7	21 200 ± 7310
W+jets	4.51 ± 2.68	4480 ± 2520
single top	2.36 ± 2.35	2140 ± 1700
Others	2.77 ± 1.26	0 ± 0
Diboson	0 ± 0	358 ± 202
$t\bar{t}V$	0 ± 0	351 ± 57.3
Z+jets	0 ± 0	308 ± 176
Multi-jet	0 ± 0	2490 ± 1260
Total Background	29.9 ± 16.4	31 300 ± 8150
$m_B = 1.15$ TeV, $\mathscr{B}(B \to Wt) = 1$	15.5 ± 1.29	130 ± 3.30
$m_B = 1.3$ TeV, $\mathscr{B}(B \to Wt) = 1$	7.41 ± 0.533	50.6 ± 1.51
$m_B = 1.15$ TeV, $SU(2)$ singlet	5.65 ± 0.421	89.0 ± 2.15
$m_B = 1.3$ TeV, $SU(2)$ singlet	2.67 ± 0.183	35.1 ± 0.921
Data	26	25863

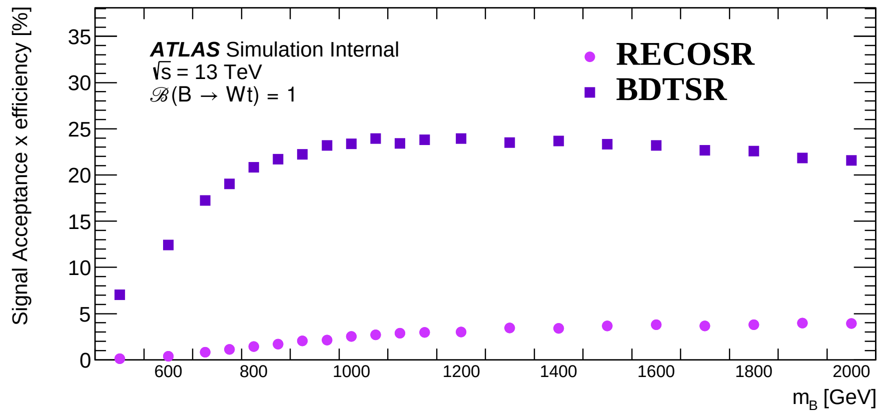

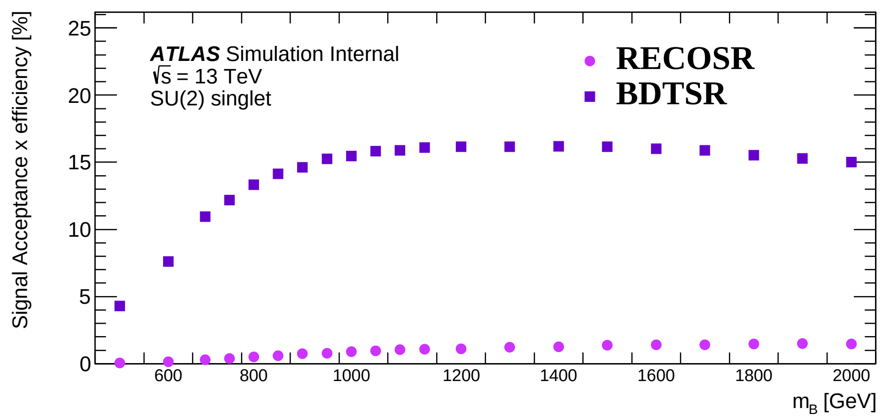

Figure 14.10: The signal acceptance times efficiency at each VLQ mass assuming 100% decay into Wt (top) and the $SU(2)$ singlet (bottom) for the two SRs used in this analysis.

14.3.2 VLB System Reconstruction

The event reconstruction in the RecoSr region requires the presence of at least three large-R jets in the event. The large-R jets are proxies for the hadronically decaying W bosons and top-quarks in the event. The algorithmic sequence is as follows. First the leptonic W candidate is reconstructed from the four-vector of the reconstructed neutrino and the electron or muon. As a next step, the leptonic W candidate is paired with a large-R jet as a proxy for the leptonic B candidate. Two additional large-R jets are combined as a proxy for the hadronic B candidate. All possible large-R jet permutations are tried; the combination for which $|\Delta m| = |m_B^{\text{had}} - m_B^{\text{lep}}|$ is minimal is chosen.

Multiple reconstruction algorithms were studied and this reconstruction algorithm was found to provide the best signal mass peak while still maintaining good separation from the dominant

$t\bar{t}$ background. The final discriminant is shown in Figure 14.11. The reconstructed mass peaks at the predicted VLB mass. It should be noted that in the cases in which the lepton originates

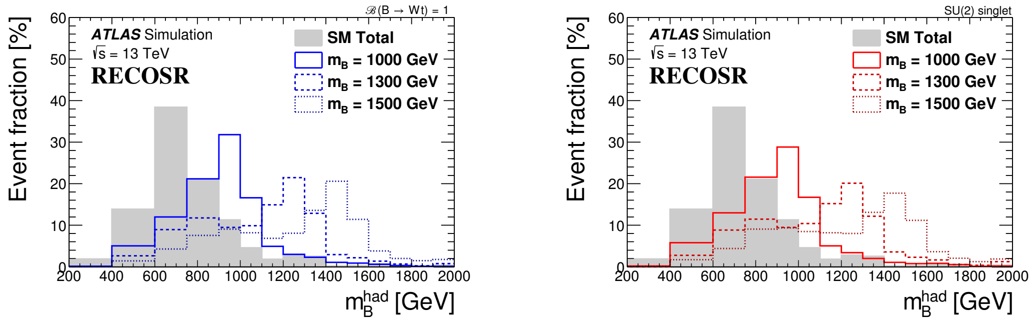

Figure 14.11: The reconstructed hadronic B mass is shown for signal samples with a mass of 1000, 1300, and 1500 GeV with the $\mathscr{B}(B \to Wt) = 1$ (left) and $SU(2)$ singlet (right) with the total SM background in the RecoSR region. The distributions are normalised to their relative event fraction for shape comparison.

from the top-quark, the above reconstruction neglects the presence of the additional b-jet. This was found to nonetheless, on average, provide the best separation between signal and background. Figure 14.12 illustrates the reconstructed hadronic VLB mass for the cases in which the leptonic W originated from the VLB and the top-quark, respectively. It can be seen that ∼65% (∼35%) of the time the leptonically decaying W boson originates from the VLB (from the top-quark) consistent with previous described observations. In addition, the tails stemming from misreconstructed VLBs originate mostly from cases in which the lepton originates from the top-quark.

14.4 BDTSR - BDT Signal Region Definition

The BdtSR encompasses all events passing the Base selection but vetoing the events passing RecoSR. This SR is thus more inclusive than the RecoSR. A BDT is trained in order to optimally discriminate between signal and background like events. Table 14.2 displays the expected number of events in the BdtSR. The main backgrounds originate from $t\bar{t}$, W+jets, multi-jet, and single-top events. SM processes such as diboson, Z+jets, and $t\bar{t}V$ show a comparably small event yield.

Table 14.3 lists the signal fraction, quantified as S/B, for the two SRs for different VLB masses assuming $\mathscr{B}(B \to Wt) = 1$. It can be inferred that the overall signal fraction is smaller

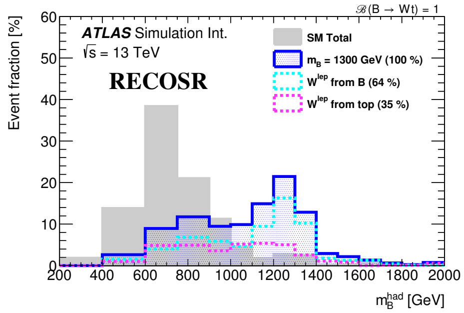

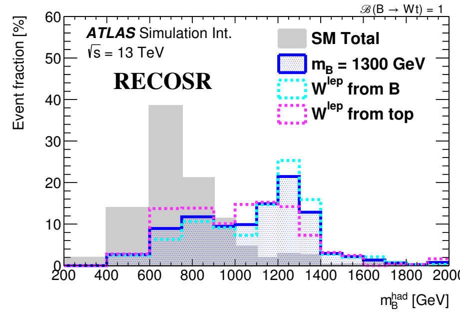

Figure 14.12: The reconstructed hadronic B mass is shown for a signal sample with a mass of 1300 GeV with $\mathscr{B}(B \to Wt) = 1$ and for the total SM background in the RECOSR region. The left plot shows the relative fraction of signal events in which the leptonic W originated from the VLB or the top-quark. The right plot shows the same distribution but scaled to the same area.

Table 14.3: Summary of signal contamination S/B within RECOSR and BDTSR for different masses of VLB assuming $\mathscr{B}(B \to Wt) = 1$.

m_B ($\mathscr{B}(B \to Wt) = 1$) [GeV]	500	800	1000	1200	1400	1800
RECOSR S/B in %	411	304	124	38	13	1
BDTSR S/B in %	26	4.4	1.1	0.3	0.1	0.01

in the BDTSR compared to the RECOSR which decreases in both regions with increasing signal masses. The signal acceptance times efficiency (as shown in Figure 14.10) for a signal model with $\mathscr{B}(B \to Wt) = 1$ ranges from 7% to 24% for VLB masses from $m_B = 500$ to 2000 GeV. For the $SU(2)$ singlet, $\mathscr{A}\epsilon$ ranges from 4% to 16%.

14.4.1 BDT Strategy

The BDT algorithm used for training and classification is an adaptive boosting algorithm referred to as AdaBoost as described in Chapter 12.6. Table 14.4 summarises the settings used for the BDT architecture. For training and testing of the BDT classifier, a set of combined signal simulation samples assuming $\mathscr{B}(B \to Wt) = 1$ with signal masses ranging from 1.05 to 1.6 TeV are combined together to take advantage of different kinematic characteristics at different masses. $t\bar{t}$ events which forms the main background component in the BDTSR are used in the training. The training and testing set is divided equally by randomly assigning events into

Table 14.4: Settings used for the BDT architecture. See Ref. [262] for further details on these parameters.

Parameter	Setting
Number of trees in the forest	850
Maximum depth of the decision tree allowed	3
Minimum percentage of training events required in a leaf node	2.5%
Number of grid points in variable range used in finding optimal cut in node splitting	20
Boosting type for the trees in the forest	AdaBoost
Learning rate for AdaBoost algorithm	0.5
Use only a random (bagged) subsample of all events for growing the trees in each iteration	true
Relative size of bagged event sample to original size of the data sample	0.5
Separation criterion for node splitting	GiniIndex

each set. Good agreement is observed for the BDT discriminant between training and testing. An initial set of 75 discriminating variables was identified. Individual variables were removed through an iterative process. The performance of the BDT was evaluated and variables removed on the basis of:

- a variable showing a poor separation power,
- a variable shows a high correlation with a variable with higher separation power, particularly if the correlation was similar between signal and background,
- a variable showing poor agreement between data and prediction.

Different BDTs with a varying number of variables were studied to assess the impact on the analysis sensitivity. The one presented resulted in the best sensitivity and was chosen. The selected variables describe both global event characteristics as well as the kinematics and angular separation of the reconstructed objects. Table 14.5 lists the final set of 20 variables selected for training. The five highest ranked variables are: S_{T}, the invariant mass of the highest p_{T} large-R jet, the sphericity of the event[13], ΔR between the lepton and the sub-leading small-R jet, and ΔR between the leading b-jet and the leading large-R jet. The five highest ranked BDT vari-

[13]Sphericity ($\mathscr{S} = \frac{2}{3}(\lambda_2 + \lambda_3)$) is a measure of the total transverse momentum with respect to the sphericity axis defined by the four-momenta used for the event shape measurement; $\lambda_{2,3}$ are the two smallest eigenvalues of the normalised momentum tensor of the small-R jet jets [272].

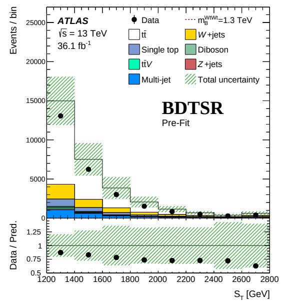

(a) S_{T}

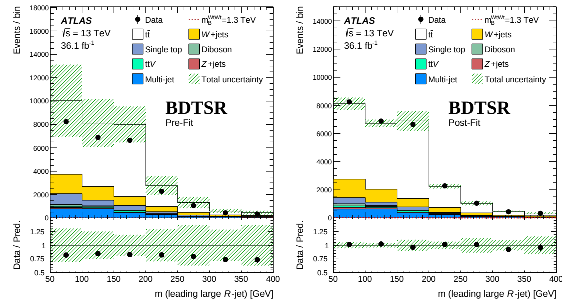

(b) m (leading large-R jet)

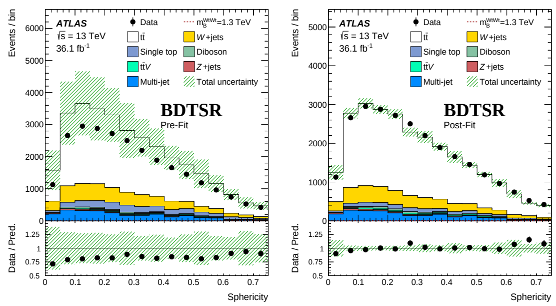

(c) Sphericity

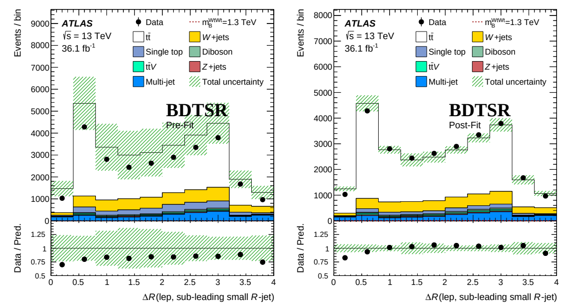

(d) ΔR (lep, sub-leading small-R jet)

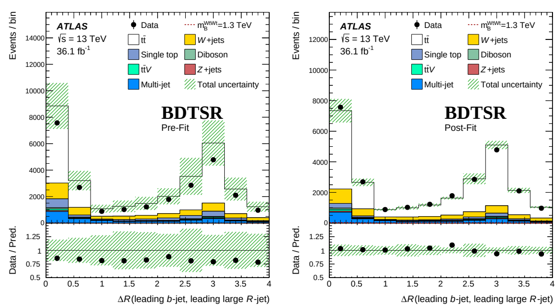

(e) ΔR (leading b-jet, leading large-R jet)

Figure 14.13: Pre-fit and post-fit distributions for the five highest ranked variables used in the BDT training. From top to bottom S_T, m (leading large-R jet), sphericity, ΔR(lep, sub-leading small-R jet) and ΔR(leading b-jet, leading large-R jet) are shown. The lower panel shows the ratio of data to the fitted background yields. The band represents the systematic uncertainty before the maximum-likelihood fit. Events in the overflow and underflow bins are included in the last and first bin of the histograms, respectively. The expected pre-fit $B\bar{B}$ signal corresponding to $m_B = 1300$ GeV assuming $\mathcal{B}(B \to Wt) = 1$ is also shown overlaid.

ables are shown for pre- and post-fit in Figure 14.13. A good agreement is observed between data and simulation with the MC over-prediction that was previously discussed. Figure 14.14

Table 14.5: List of the 20 BDT input variables used in the training of the BDTSR signal region, ordered by their respective TMVA ranking.

Variable	Description
S_{T}	Scalar sum of $E_{\mathrm{T}}^{\mathrm{miss}}$, the p_{T} of the lepton and the p_{T} of all small-R jets
m (leading large-R jet)	Mass of the leading large-R jet
Sphericity	Sphericity [272] ($\mathscr{S} = \frac{2}{3}(\lambda_2 + \lambda_3)$)
ΔR(lep, sub-leading small-R jet)	Angular separation between the lepton and the sub-leading small-R jet
ΔR(leading b-jet, leading large-R jet)	Angular separation between the leading b-tagged jet and the leading large-R jet
min[ΔR(lep, b-jet)]	Minimum angular separation between the lepton and all b-tagged jets
Aplanarity ($\mathscr{A} = \frac{3}{2}\lambda_3$)	Aplanarity [272], where λ_3 is the smallest eigenvalue of the norm. momentum tensor of small-R jets
min[M(W_{lep}, b-jet)]	Minimum invariant mass of W_{lep} and all b-tagged jets
ΔR(lep, third-leading small-R jet)	Angular separation between the lepton and the third-leading small-R jet
ΔR(W_{lep}, large-R jet closest to leading b-jet)	Angular separation between the W_{lep} and the large-R jet closest to the leading b-tagged jet
p_{T} (sub-leading large-R jet)	Transverse momentum of the sub-leading large-R jet
M_T^W	Transverse mass of the W_{lep}
Sphericity (large-R jets)	Sphericity, using normalised momentum tensor of the large-R jets
ΔR(lep, leading small-R jet)	Angular separation between the lepton and the leading small-R jet
ΔR(W_{lep}, leading large-R jet)	Angular separation between the W_{lep} and the leading large-R jet
ΔR(lep, sub-leading b-jet)	Angular separation between the lepton and the sub-leading b-tagged jet
$E_{\mathrm{T}}^{\mathrm{miss}}$	Missing transverse energy
p_{T} (W_{had})	Transverse momenta of the leading W_{had} candidate
$\mathrm{N}_{\mathrm{jets}}$	Small-R jet multiplicity
p_{T} (sub-leading small-R jet)	Transverse momentum of the sub-leading small-R jet

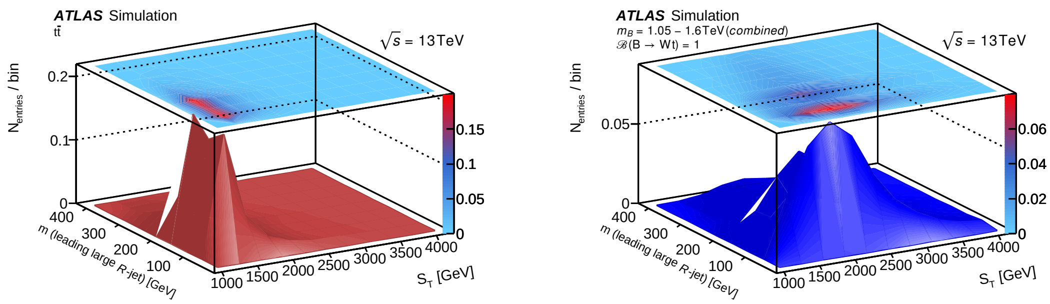

Figure 14.14: Example correlation plot of the two highest ranked BDT input variables: S_T and m (leading large-R jet). The left (right) plot shows the expected correlation for $t\bar{t}$ background (BB signal). Signal is shown combining six mass templates $m_B = 1.05 - 1.6$ TeV assuming $\mathscr{B}(B \to Wt) = 1$, as used for BDT training input.

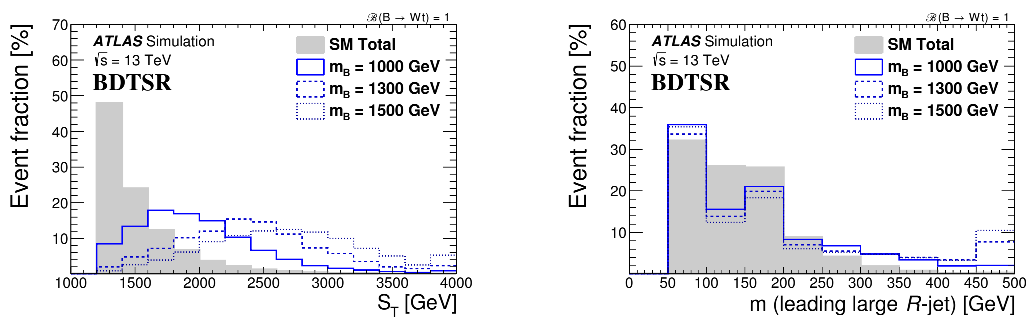

Figure 14.15: The S_{T} and mass of the leading large-R jet normalised to unity, after the BDTSR selection comparing the SM background and the VLB signal samples corresponding to masses of 1.0 TeV, 1.3 TeV, and 1.5 TeV for $\mathscr{B}(B \to Wt) = 1$.

shows the correlation between the two highest ranked BDT input variables S_{T} and the mass of the leading large-R jet. Figure 14.15 provides a shape comparison between the total SM background and three VLB masses assuming $\mathscr{B}(B \to Wt) = 1$. From the four figures, it can be seen that the VLB signal mainly contributes at higher S_{T} values, whereas the background expectation decreases. The leading mass of the large-R jet shows two peaks consistent with the W boson and top-quark mass. The latter two peaks are more distinct for the VLB signal compared to the background. This shows that the selected leading large-R jet more frequently fully reconstructs either particle for signal compared to background. The two variables show a signal and background correlation of ∼25% and ∼20%, respectively.

The BDT is evaluated on the full training and testing set as AdaBoost is not very prone to overtraining due to a relatively small number of trees and respective depth. Nonetheless, in order to check for potential occurrence of over-training, two signal samples with masses close to the mass exclusion limit of the presented analysis were split according to event mapping employed for training and testing of the BDT classifier. A shape comparison between the two resulting sets showed no sign of significant overtraining on the high mass sub-set of this signal training sample.

Figure 14.16 shows the BDT output in the BDTSR region for the $\mathscr{B}(B \to Wt) = 1$ and the $SU(2)$ singlet case using signal samples corresponding to a mass of 1, 1.3 and 1.5 TeV and the total SM background. The BDT output is used as final discriminant in the statistical analysis.

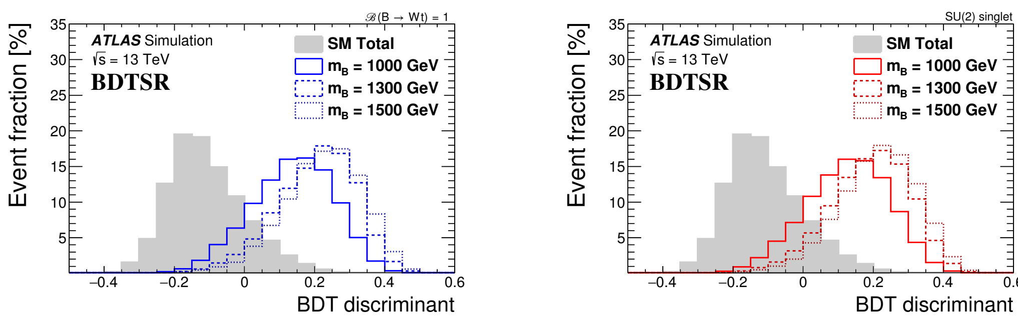

Figure 14.16: The BDT output is shown for signal samples with a mass of 1000, 1300, and 1500 GeV with the $\mathscr{B}(B \to Wt) = 1$ (left) and SU(2) singlet (right) with the total SM background in the BDTSR region. The distributions are normalised to their relative event fraction for comparison of the relative shapes.

14.5 Multi-jet Background Estimation in RECOSR

As outlined in Section 12.1.3, the tight event selection for the RECOSR significantly reduces the contribution of the multi-jet background, to the point where statistical uncertainties make MM predictions unreliable. After removing the requirement on the W-tagged large-R jet, the multi-jet shape is compared to the combined "Others" template comprised of the diboson, Z+jets, and $t\bar{t}V$ small background. The multi-jet shape is taken as the "Others" template. The fraction of multi-jet events in the looser region is 0.14 of the expected event yield of "Others". The "Others" template is thus scaled accordingly in RECOSR. The multi-jet background contribution compared to the total background is 1.3% in this region.

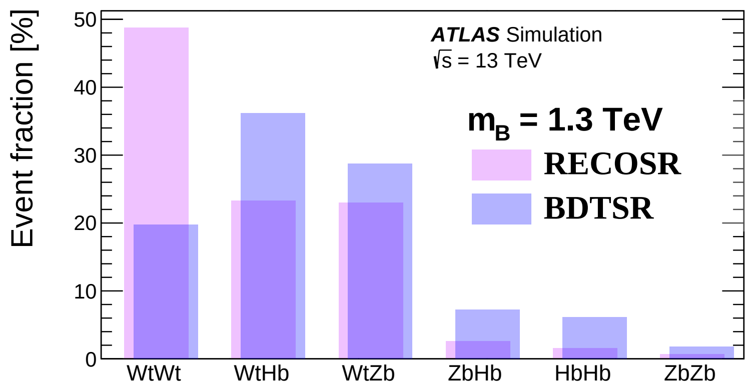

Figure 14.17: The relative event fraction in the SRs for the different decay modes of the VLB pair for $m_B = 1.3$ TeV starting from equal branching ratios $\mathscr{B}(B \to Wt) = \mathscr{B}(B \to Hb) = \mathscr{B}(B \to Zb) = 1/3$.

14.6 Statistical Analysis

This section provides details about the setup of the statistical analysis, discusses results after unblinding of the analysis regions and the impact of the dominant uncertainties, as well as gives the results and interpretations of the findings.

14.6.1 The Fit Definition: Discriminant and Unblinded Results

The two identified final discriminants described in the previous Sections resulted in the best search sensitivity for VLB masses above $\mathcal{O}(1$ TeV$)$. Other kinematic distributions showing significant discrimination between background and the VLB signal were tested for sensitivity in the RECOSR. Those variables were S_T, m_T^{lep}, $\Delta R(\ell$, leading b-jet$)$, and min[M(W_{lep}, b-jet)] (as defined in Table 14.5). The binning in the two SRs was optimised such that a consistent MC statistical uncertainty of less than 30% is achieved across the bins while also ensuring sufficient statistics for the top-quark modelling systematic samples. The fit is performed in the two SRs simultaneously with a total number of seven bins, three and four in the RECOSR and BDTSR respectively. The pre-fit distributions in the two SRs after unblinding the analysis is shown in Figure 14.18 with a VLB signal overlaid corresponding to $m_B = 1.3$ TeV assuming $\mathscr{B}(B \to Wt) = 1$. Good agreement between data and the total SM prediction is observed in the RECOSR, while a data deficit is seen in the more inclusive BDTSR. The latter observation is discussed in Section 14.2.1. The p-value of the largest excess is 50% and corresponds to

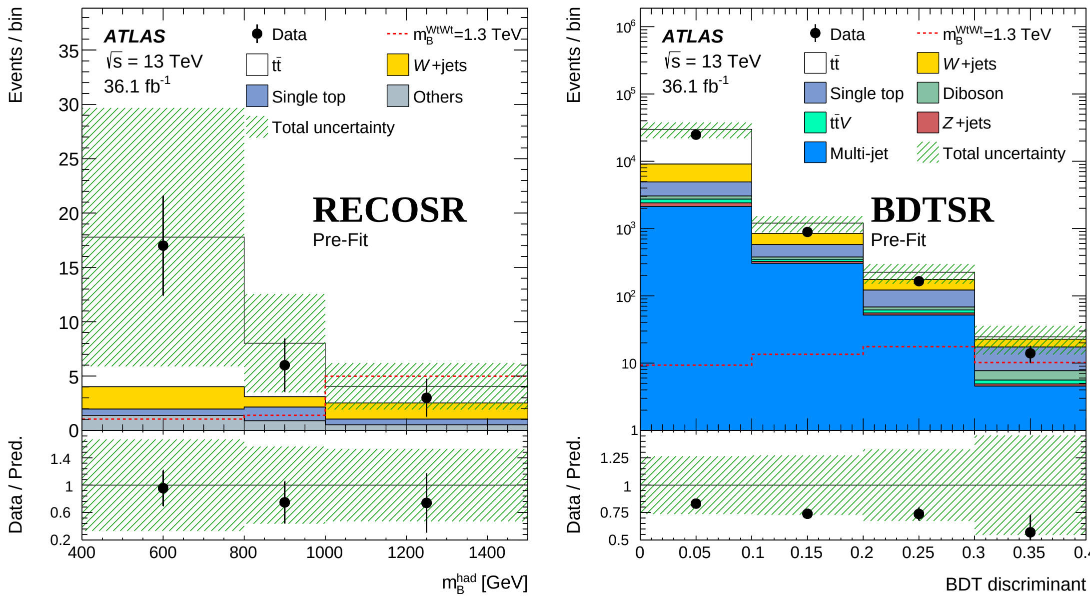

Figure 14.18: Pre-fit distributions for m_B^{had} (left) and the BDT output score (right) in the respective SRs. The lower panel shows the ratio of data to the background yields. The band represents the systematic uncertainty in the background. Events in the overflow and underflow bins are included in the last and first bin of the histograms, respectively. The expected BB signal corresponding to $m_B = 1300$ GeV assuming $\mathscr{B}(B \to Wt) = 1$ is overlaid.

$m_B = 800$ GeV. No significant excess above the SM background expectation is thus observed.

14.6.2 Fit Results

The agreement between data and SM prediction after the fit under the background-only hypothesis is shown in Figure 14.19. The post-fit event yields including all systematic uncertainties are summarised in Table 14.6. The respective pre- and post-fit impact of the 20 leading NPs is shown in Figure 14.20. In order to compensate for the observed data deficit, several NPs are pulled from their initial value with the maximum pull of $\mathscr{O}(+1/2\sigma)$ for the single top DR vs. DS uncertainty. As expected from the pre-fit SM over-prediction in Figure 14.18, the pulls are mainly resulting from the BDTSR. Additional NPs that are pulled are the W+jets, multi-jet normalisation in the BDTSR and the $t\bar{t}$ hard scatter uncertainty with pulls of $\mathscr{O}(-0.3\sigma)$, $\mathscr{O}(-0.4\sigma)$, and $\mathscr{O}(+0.2\sigma)$, respectively. The free floating $t\bar{t}$ normalisation is fitted to 0.92 ± 0.3 times the nominal $t\bar{t}$ prediction, mainly driven by the first bin of the BDT output score in the BDTSR

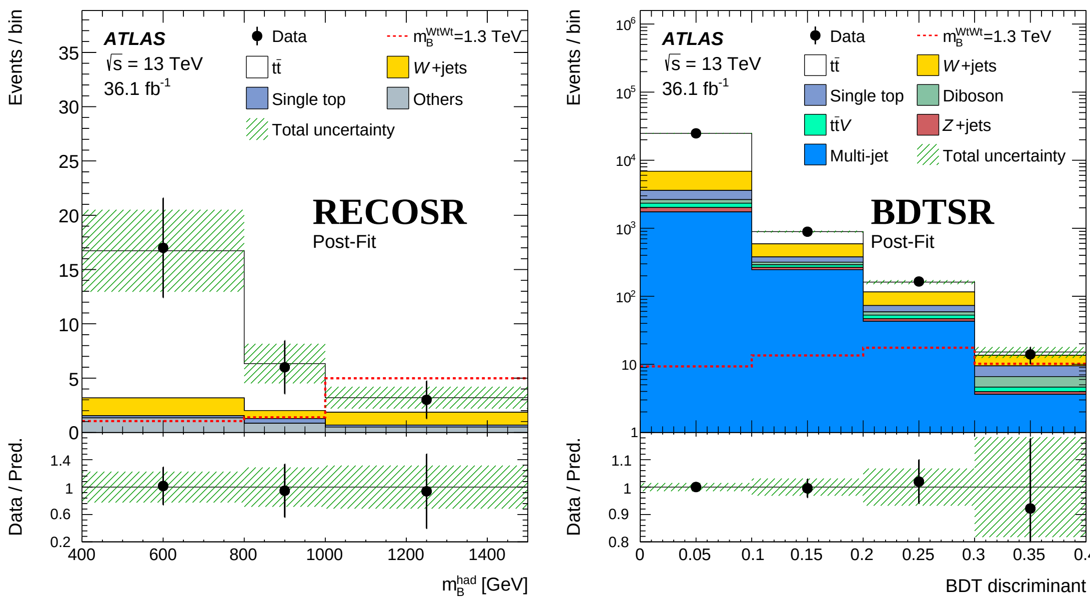

Figure 14.19: Comparison between data and SM prediction of m_T^{had} and the BDT output score in the RecoSr (left) and BdtSr (right) after the simultaneous fit in the two regions to data under the background-only hypothesis. The lower panel shows the ratio of data to the expected background yields. The band represents the systematic uncertainty after the maximum-likelihood fit. The expected pre-fit BB signal corresponding to $m_B = 1300$GeV assuming $\mathscr{B}(B \to Wt) = 1$ is overlaid.

which has the highest number of events. The largest pull from the RecoSr originates from the single top DR vs. DS, pile-up uncertainty, and the large-R jet scale uncertainty assessed by correlating the p_{T} and m^{comb} comparisons between data and simulation with pulls of $\mathscr{O}(+0.1\sigma)$, $\mathscr{O}(-0.05\sigma)$, and $\mathscr{O}(-0.01\sigma)$, respectively. The main constraints originate from the top modelling systematics associated to the $t\bar{t}$ and single top prediction as well as the normalisation uncertainty imposed on the W+jets and multi-jet background which can be seen by comparing the uncertainties summarized in Table 14.2 and Table 14.6. Those constraints are mostly driven by the BdtSr. Due to a conservative systematic uncertainty estimate for those two sources, the total variation of the assigned NPs is larger than the precision of the data. In addition to the constraints observed, several systematics have a similar effect and can not be disentangled which results in the creation of (anti-) correlations between the assigned NPs such that the combined effect is on the order of the data statistics. The correlations are measured by their impact on the best fit result (see Section 12.5.1). A correlation of NPs in the fit are observed between the $t\bar{t}$

Table 14.6: Event yields in both SRs after the background-only fit. The uncertainties include statistical and systematic uncertainties. The uncertainties in the individual background components can be larger than the uncertainty in the sum of the backgrounds, which is constrained by data. The contributions from dibosons, Z+jets, $t\bar{t}V$, and multi-jet production are included in the Others category for the RecoSr, whereas they are counted separately within the BdtSr.

Sample	RecoSr	BdtSr
$t\bar{t}$	19.2 ± 5.17	18 300 ± 1490
W+jets	3.56 ± 2.00	3550 ± 1920
single top	0.815 ± 1.02	1040 ± 812
Others	2.66 ± 1.11	0 ± 0
Diboson	0 ± 0	335 ± 191
$t\bar{t}V$	0 ± 0	352 ± 56.1
Z+jets	0 ± 0	303 ± 171
Multi-jet	0 ± 0	2030 ± 851
Total	26.3 ± 4.71	25 900 ± 384
Data	26	25863

normalisation parameter (free floating in the fit) and the hard scatter $t\bar{t}$ modelling uncertainty (∼80%). The BdtSr multi-jet normalisation uncertainty shows a correlation with the W+jets background uncertainty (∼-53%). The latter shows a correlation with the single top DR vs. DS uncertainty (∼42%). The correlation between the $t\bar{t}$ normalisation and the $t\bar{t}$ hard scatter uncertainty is largely reduced when excluding the first bin of the BdtSr in the fit. This shows that both systematic uncertainties have a similar effect on the first bin. Overall the fit is well behaved and excellent post-fit agreement between data and the total SM prediction is obtained as shown in Figure 14.19. No significant constraints of the dominant uncertainties with the highest impact on μ are observed as shown in Figure 14.20. The largest constraint is observed for the single top DR vs. DS uncertainty which is constrained by 50% to its initial size.

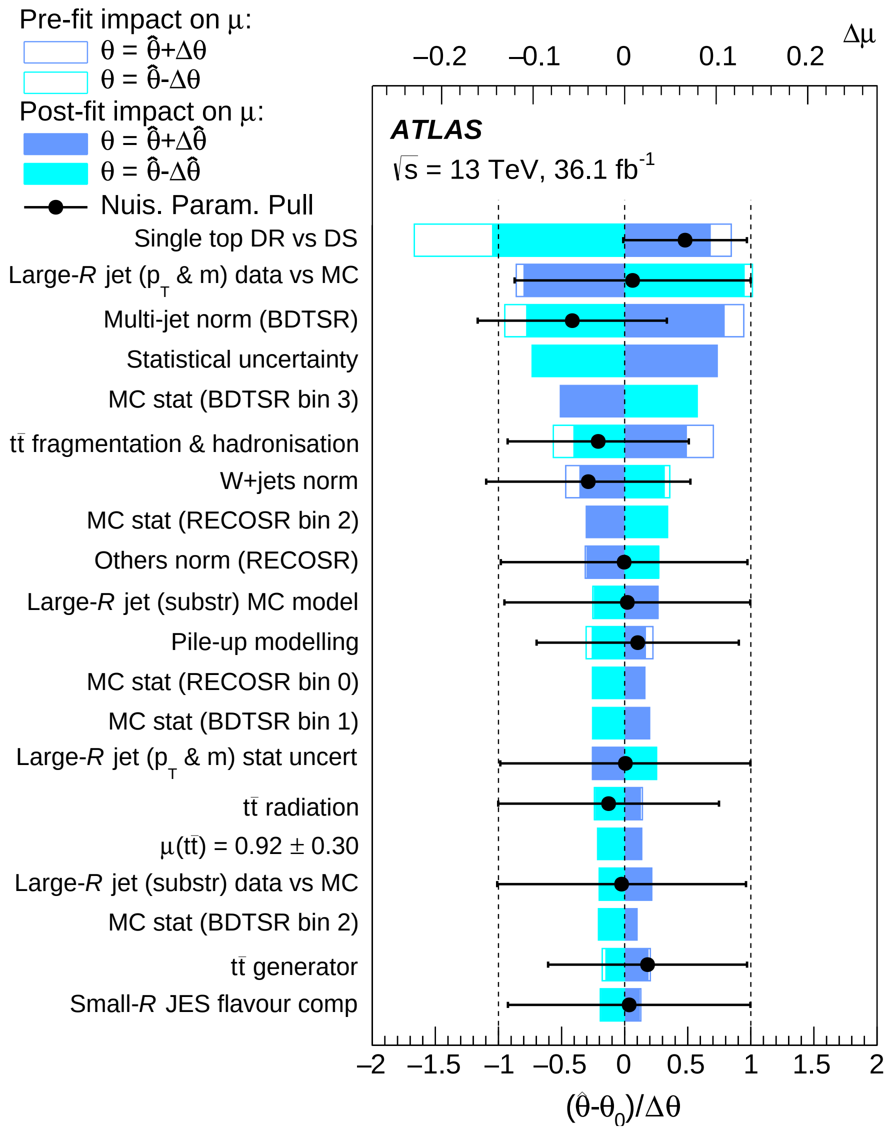

Figure 14.20: Ranking of nuisance parameters based on the fit to data under the signal-plus background hypothesis according to their effect on the uncertainty on μ ($\Delta\mu$). The $B\bar{B}$ signal hypothesis corresponds to $m_B = 1300$ GeV assuming $\mathscr{B}(B \to Wt) = 1$. Only the 20 highest ranked uncertainties on μ are shown. No nuisance parameter pull is shown for the statistical uncertainty, the MC statistical component per bin and the unconstrained $t\bar{t}$ normalisation ($\mu(t\bar{t})$) parameter. The MC stat components as well as the $t\bar{t}$ normalisation uncertainty have priors at unity, all other nuisance parameters have priors at 0. For additional details on this Figure, the reader is referred to Section 12.5.1 and Figure 13.8 in Chapter 13.

14.7 Discussion of the Impact of the Dominant Uncertainties

The dominant uncertainties, with the highest impact on μ, originate from the top-quark modelling uncertainties, normalisation uncertainties of the dominant SM backgrounds, data and MC statistics as well as those falling into the category of detector-related uncertainties. The uncertainties with the largest impact from the latter group are related to the large-R jet scale and substructure uncertainty components. The large-R jet scale uncertainty with the largest pre-fit impact on the signal strength of ∼12% is assessed by comparison of the large-R jet calibration between data and simulation impacting p_{T} and m^{comb}. The pre-fit normalisation impact on $t\bar{t}$ is 10%. The associated shape helps to compensate the data deficit in the RecoSr. The top-quark modelling uncertainties with the highest impact are the single top DR vs. DS uncertainty with a 90% and 80% normalisation impact on the single top prediction in the RecoSr and BdtSr, respectively, with a pre-fit impact on μ of ∼16%. Other top-quark modelling uncertainties such as the $t\bar{t}$ fragmentation and hadronisation uncertainty has a pre-fit normalisation impact of 55% and 5% in the RecoSr and BdtSr, respectively. The normalisation impact in the BdtSr on the nominal $t\bar{t}$ prediction for the last two bins that have the highest signal sensitivity are ∼20%. The resulting pre-fit impact on μ is ∼9%. The normalisation impact of the $t\bar{t}$ additional radiation uncertainty is 30% and 20% which results in a pre-fit impact on the extracted signal strength of ∼3%. The $t\bar{t}$ hard scatter generation uncertainty shows a ∼4% pre-fit impact on the signal strength with a normalisation impact on $t\bar{t}$ in both of the SRs of 27%. The impact from the data statistics is the fourth highest ranked uncertainty.

14.8 Results

As no significant excess above the SM background expectation is observed, upper limits (lower limits) on the VLB production cross section (VLB mass) are derived for a number of benchmark models. Figure 14.21 shows upper limits on the VLB signal production cross section as a function of m_B assuming $\mathscr{B}(B \to Wt) = 1$ and the $SU(2)$ singlet scenario that are compared to the theoretical VLB production prediction. The limits are obtained via linear interpolation between the calculated CL_s and the different mass points. The observed (expected) lower m_B mass limit is 1350 (1330) for the $\mathscr{B}(B \to Wt) = 1$ scenario and 1170 (1140) for the $SU(2)$ singlet case and are summarised in Table 14.7. The limits are also applicable to the $SU(2)$ doublet VLB and the VLX, that has $\mathscr{B}(X \to Wt) = 1$ and an exotic charge of $5/3e$. The inclusion of all the systematics

Table 14.7: Comparison of the expected and observed lower mass limits for the two VLB branching ratio assumptions, $\mathcal{B}(B \to Wt) = 1$ and $SU(2)$ singlet. The results are obtained from running the statistical analysis with the full set of systematics for 36.1 fb^{-1}.

Lower Mass Limits [GeV]	$\mathcal{B}(B \to Wt) = 1$	$SU(2)$ singlet
expected	1330	1140
observed	1350	1170

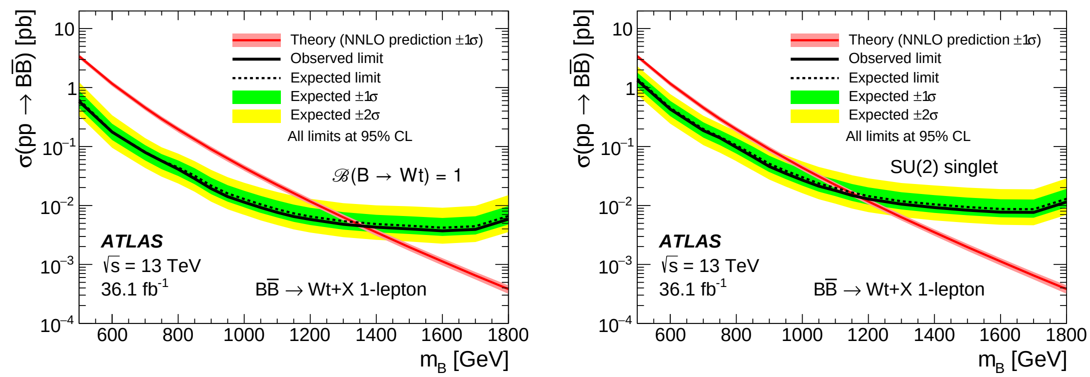

Figure 14.21: Expected (dashed black line) and observed (solid black line) upper limits at the 95% CL on the BB cross section as a function of B-quark mass assuming $\mathcal{B}(B \to Wt) = 1$ (top) and in the $SU(2)$ singlet B scenario (bottom). The green and yellow bands correspond to ± 1 and ± 2 standard deviations around the expected limit. The thin red line and band show the theoretical prediction and its ± 1 standard deviation uncertainty.

degrades the expected mass limit by ~40 GeV (~70GeV) for the VLB with $\mathcal{B}(T \to Wb) = 1$ ($SU(2)$ singlet case). Figure 14.22 shows a comparison of the extracted signal strength obtained through the combined fit of the two SRs and each SR individually for the $\mathcal{B}(B \to Wt) = 1$ and $SU(2)$ singlet scenario. For the $SU(2)$ singlet case the BDTSR dominates since this region has a significant acceptance to Wt decay modes as previously discussed and shown in Figure 14.17. For the $\mathcal{B}(B \to Wt) = 1$ signal model the two SRs contribute about the same. Those masses are chosen as they are close to the expected maximum excluded masses for each scenario. In addition to the derived limits on the two benchmark models, exclusion limits are derived as a function of the branching ratio assuming $\mathcal{B}(B \to Wt) + \mathcal{B}(B \to Hb) + \mathcal{B}(B \to Zb) = 1$. To probe the complete branching ratio plane spanned by $\mathcal{B}(B \to Wt)$ and $\mathcal{B}(B \to Hb)$, the VLB signal masses are weighted according to the respective decay modes. The statistical analysis

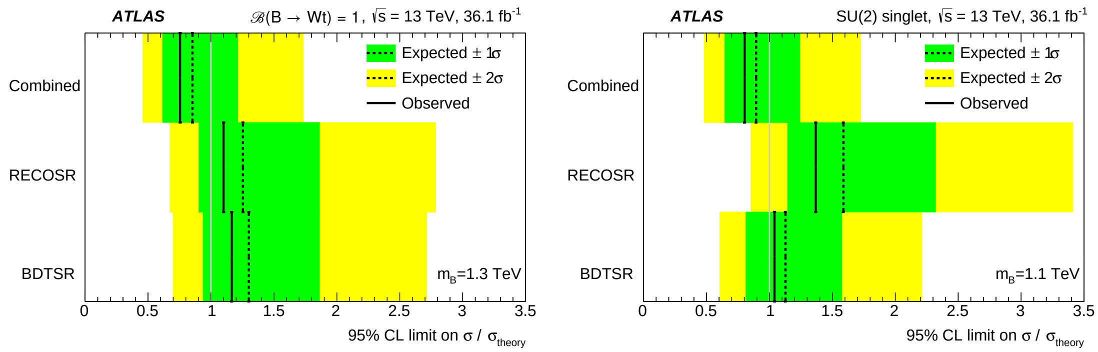

Figure 14.22: Comparison of the extracted signal strength obtained from the combined fit to the two SRs, and the fit to each signal region separately. Two signal model cases are shown; a signal model with $\mathscr{B}(B \to Wt) = 1$ and a B mass of 1.3 TeV (top) and the $SU(2)$ singlet for a B mass of 1.1 TeV (bottom).

is repeated for each point in the plane in step sizes of 0.05. The corresponding expected and observed VLB mass limits are shown in Figure 14.23.

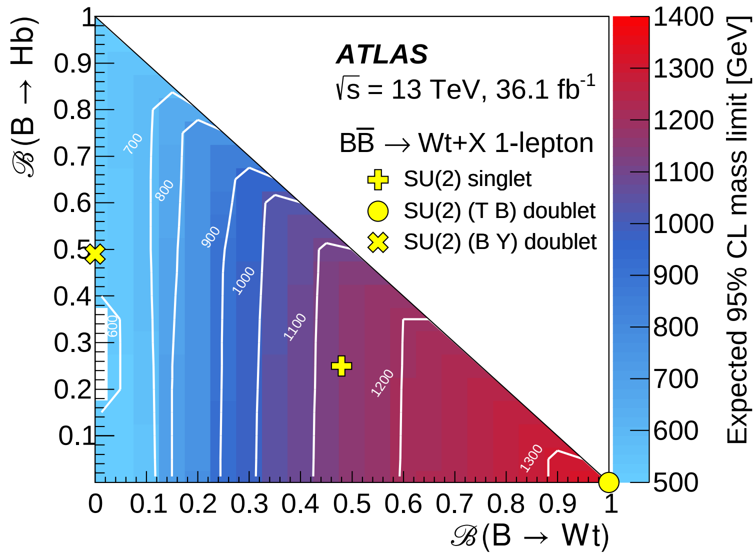

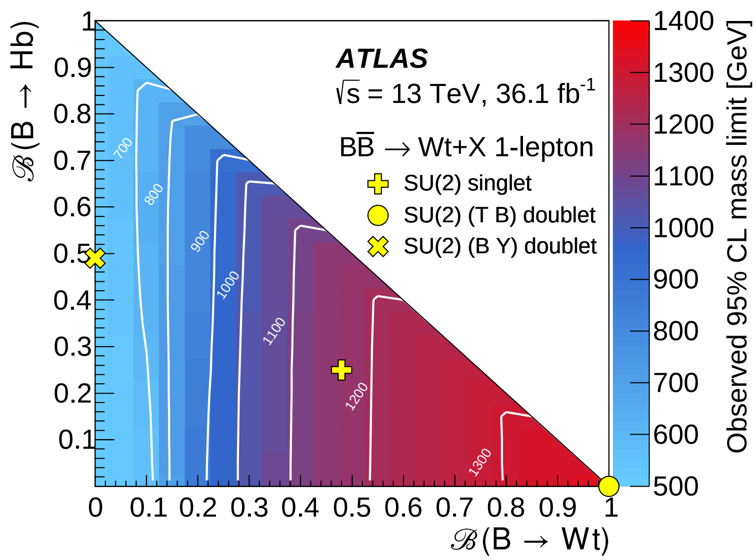

Figure 14.23: Expected (top) and observed (bottom) 95% CL lower limits on the mass of the B quark as a function of the decay branching ratios $\mathscr{B}(B \to Wt)$ and $\mathscr{B}(B \to Hb)$. The white contour lines represent constant mass limits. The markers indicate the branching ratios for the $SU(2)$ singlet and both $SU(2)$ doublet scenarios with masses above ∼800 GeV, where they are approximately independent of the VLB mass. The small white region in the upper plot is due to the limit falling below 500 GeV which corresponds to the lowest simulated signal mass.

Chapter 15

Conclusions and Outlook

Two searches for pair-produced VLTs and VLBs based on the combined data set recorded in 2015 and 2016 corresponding to 36.1fb^{-1} at $\sqrt{s} = 13$ TeV were presented in Chapter 13 and Chapter 14, respectively. The results are based on the VLQ signal assumptions discussed in Section 4.2. The analyses targeted the one lepton final state with moderate to high small-R jet multiplicity and moderate to high S_{T}. The two analyses targeted were designed to maximise the sensitivity to the VLQ decay into $\mathcal{B}(T \to Wb) = 1$ or $\mathcal{B}(B \to Wt) = 1$. Both of the searches resulted in no significant excess above the SM expectation. VLT (VLB) production cross section limits and m_T (m_B) mass limits were set for two benchmark models, $\mathcal{B}(T \to Wb) = 1$ ($\mathcal{B}(B \to Wt) = 1$) and the $SU(2)$ singlet. These limits are found to be equally applicable to the $SU(2)$ doublet VLTs (VLBs) and VLY (VLX) pair production. The limits on the VLT mass represent a significant improvement compared to Run I searches [273, 274] for which the observed mass limit were 780 GeV when assuming $\mathcal{B}(T \to Wb) = 1$ and 700 GeV for the $SU(2)$ singlet. The limits on the VLB mass also represent a significant improvement compared to Run I searches [271, 275, 276] for which the strongest observed mass limits assuming $\mathcal{B}(B \to Wt) = 1$ ($SU(2)$ singlet) were 810 GeV (640 GeV).

In addition to the mass limits on the benchmark scenarios, mass limits were also set as a function of the decay branching ratios assuming $\mathcal{B}(T(B) \to Wb(t)) + \mathcal{B}(T(B) \to Ht(b)) + \mathcal{B}(T(B) \to Zt(b)) = 1$. Both of the analyses constitute the strongest lower mass limits on the VLQ pair production for respective decays into $\mathcal{B}(T \to Wb) = 1$ and $\mathcal{B}(B \to Wt) = 1$ to the date of writing the dissertation. Other ATLAS analyses target the other corners of the $\mathcal{B}$ plane. Figure 15.2 and Figure 15.3 show the observed and expected exclusion limits in the $\mathcal{B}$ plane incorporating all public analysis results. These figures visualise the respective $\mathcal{B}$ plane coverage without combining the results which reflects a conservative scenario. A combination of the different analyses ensuring orthogonality is given in Ref. [277]. Figure 15.1 shows expected lower mass limits for the current luminosity projections of the LHC by the end of Run II. These

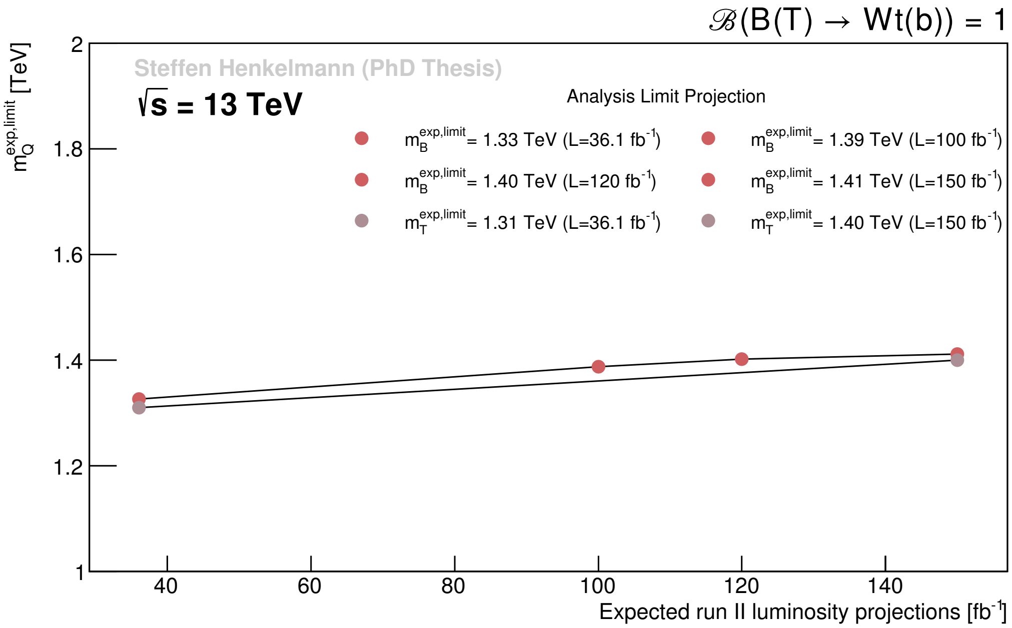

Figure 15.1: Projected exclusion limits for the VLQ pair production assuming $\mathscr{B}(B \to Wt) = 1$ ($\mathscr{B}(T \to Wb) = 1$) for different LHC luminosity projections expected for the end of Run II neglecting possible analysis improvements.

numbers were obtained with the same analyses setup presented but with scaling to higher luminosity scenarios.

Without any significant analysis improvements through increase of discrimination between background and expected VLQ signal and systematic uncertainty reductions, the expected lower VLT (VLB) mass limit for the scenario of $\mathscr{L} = 150$ fb^{-1} can only be increased by 90 GeV (80 GeV). The main challenges for the analyses improvements will stem from the reduction of the uncertainty covering interference effects between NLO Wt and LO $t\bar{t}$ production, the understanding of the high $t\bar{t}$ prediction at high S_{T}, as well as the available MC statistics in the even more extreme regions of phase space that need to be populated and probed for VLQ masses above $\mathscr{O}(1.4$ GeV).

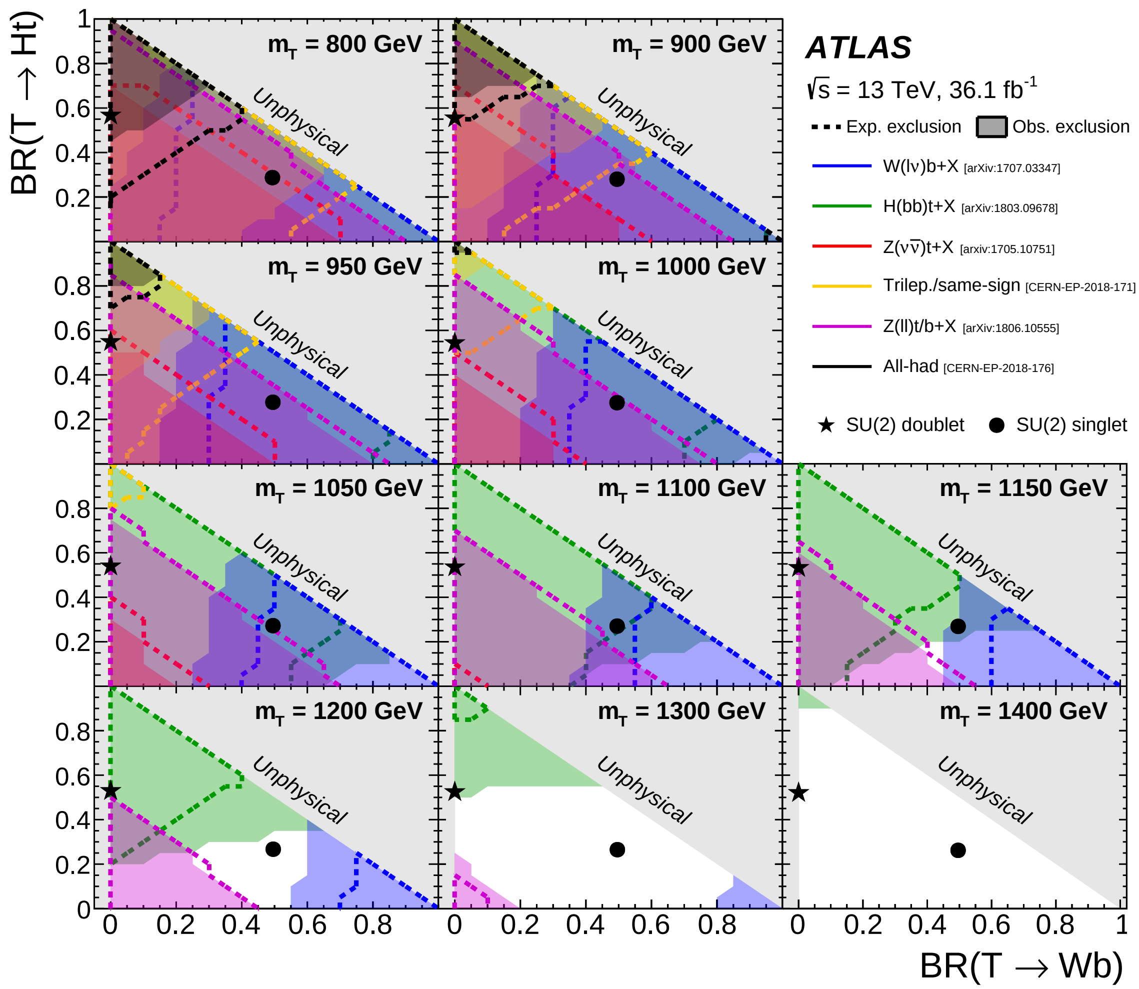

Figure 15.2: Observed (filled area) and expected (dashed line) 95% CL exclusion limit in the $\mathscr{B}$ plane spanned by $\mathscr{B}(T \to Ht)$ versus $\mathscr{B}(T \to Wb)$, for different VLT values for the $Wb + X$ (blue), $Ht + X$ (green), $Z(\nu\bar{\nu})t + X$ (red), tri-lepton/same-sign lepton (yellow), $Z(\ell\ell)t/b + X$ (pink) and all hadronic (black) analyses. The grey (light shaded) area corresponds to the unphysical region where $\mathscr{B}(T \to Wb) + \mathscr{B}(T \to Ht) + \mathscr{B}(T \to Zt) > 1$. The default $\mathscr{B}$ values for the $SU(2)$ singlet and doublet scenarios are depicted by the markers [277].

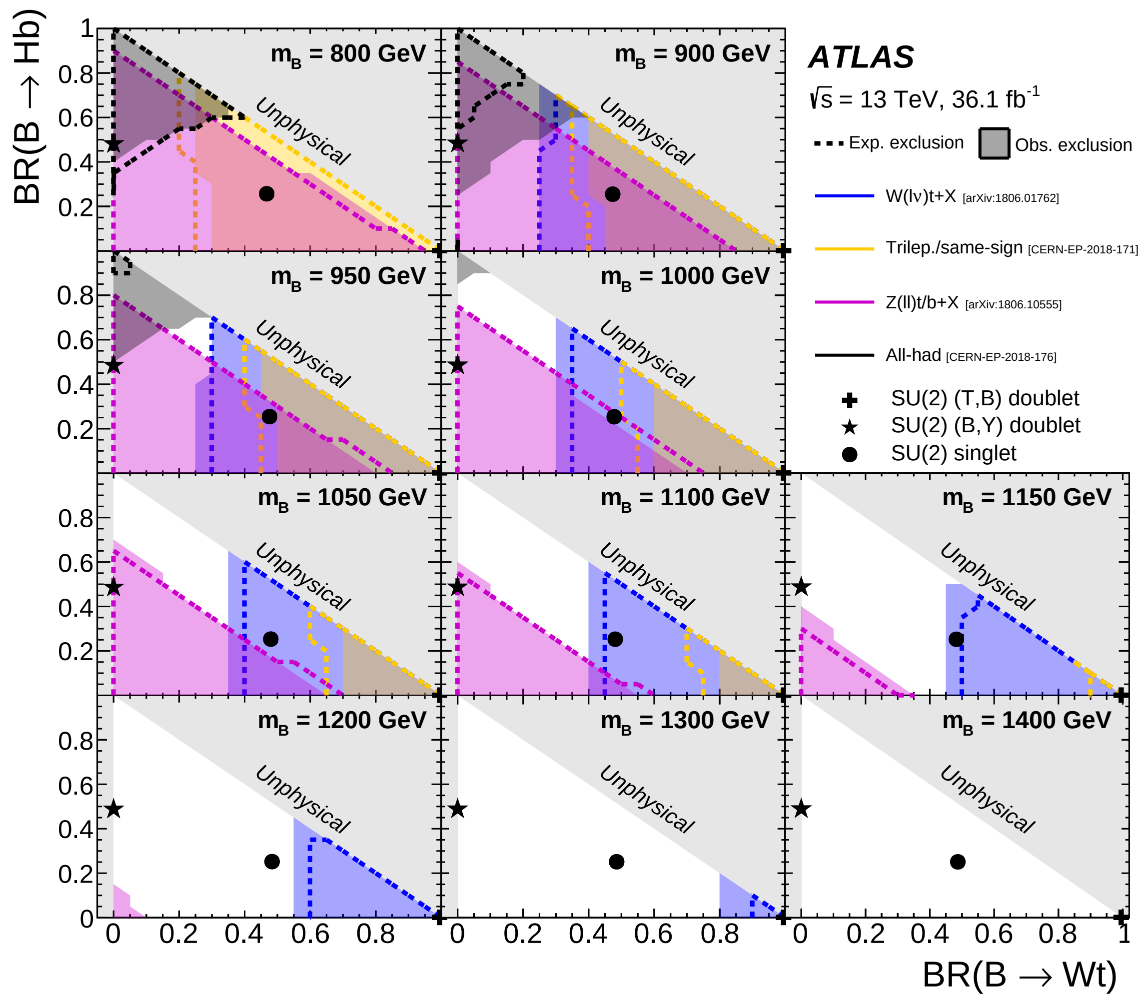

Figure 15.3: Observed (filled area) and expected (dashed line) 95% CL exclusion limit in the $\mathscr{B}$ plane spanned by $\mathscr{B}(B \to Hb)$ versus $\mathscr{B}(B \to Wt)$, for different VLB values for the $Wt + X$ (blue), tri-lepton/same-sign lepton (yellow), $Z(\ell\ell)t/b + X$ (pink) and all hadronic (black) analyses. The grey (light shaded) area corresponds to the unphysical region where $\mathscr{B}(B \to Wt) + \mathscr{B}(B \to Hb) + \mathscr{B}(B \to Zb) > 1$. The default $\mathscr{B}$ values for the $SU(2)$ singlet, $(T\ B)$, and $(B\ Y)$ doublet scenario are depicted by the markers [277].

Bibliography

[1] ATLAS Collaboration, *ATLAS Computing Acknowledgements*, ATL-GEN-PUB-2016-002.
Cited on p. ix.

[2] S. L. Glashow, *Partial Symmetries of Weak Interactions*, Nucl. Phys. **22** (1961) 579–588.
Cited on p. 4 and 8.

[3] S. Weinberg, *A Model of Leptons*, Phys. Rev. Lett. **19** (1967) 1264–1266.

[4] A. Salam, *Weak and Electromagnetic Interactions*, ed. Nobel Symposium No. 8 Almqvist & Wiksell, Stockholm (2008). Cited on p. 8.

[5] D. Griffiths, *Introduction to Elementary Particles*, Wiley-VCH, Weinheim (2008).

[6] A. Quadt, *Top quark physics at hadron colliders*, Eur. Phys. J. **C48** (2006) 835–1000.

[7] P. Langacker, *Introduction to the Standard Model and Electroweak Physics*, in *Proceedings of Theoretical Advanced Study Institute in Elementary Particle Physics on The dawn of the LHC era (TASI 2008): Boulder, USA, June 2-27, 2008*, pp. 3–48. (2010).
Cited on p. 4 and 7.

[8] S. Henkelmann, *Signal modelling and corresponding uncertainty studies for the search of the Higgs boson produced in association with a top-quark pair at the ATLAS experiment*, Master's thesis, University of Göttingen, (2013). Cited on p. 5.

[9] D. J. Gross and F. Wilczek, *Ultraviolet behavior of non-Abelian gauge theories*, Phys. Rev. Lett. **30** (1973) 1343–1346. Cited on p. 8.

[10] H. D. Politzer, *Reliable Perturbative Results for Strong Interactions?*, Phys. Rev. Lett. **30** (1973) 1346–1349. Cited on p. 8.

[11] The Particle Data Group, K. Nakamura, et al., *Review of Particle Physics*, J. Phys. G **37** (2010) 075021. Cited on p. xviii, xxi, 8, 11, 12, 23, and 91.

[12] C. S. Wu et al., *Experimental test of parity conservation in beta decay*, Phys. Rev. **105** (1957) 1413–1414. Cited on p. 9.

[13] MuLan Collaboration, *Improved measurement of the positive muon lifetime and determination of the Fermi constant*, Phys. Rev. Lett. **99** (2007) 032001. Cited on p. 11.

[14] N. Cabbibo, *Unitary Symmetry and Leptonic Decays*, Phys. Rev. Lett. **10** (1963) 531–532. Cited on p. 12.

[15] M. Kobayashi and T. Maskawa, *CP Violation in the Renormalizable Theory of Weak Interaction*, Prog. Theor. Phys. **49** (1973) 652–657. Cited on p. 12 and 13.

[16] Z. Maki, M. Nakagawa, and S. Sakata, *Remarks on the unified model of elementary particles*, Prog. Theor. Phys. **28** (1962) 870–880. Cited on p. 12.

[17] J. Carvalho et al., *Study of ATLAS sensitivity to FCNC top decays*, ATL-PHYS-PUB-2005-009 (2005). Cited on p. 13.

[18] ATLAS Collaboration, *Summary plots from the ATLAS Standard Model physics group: Standard Model Production Cross Section Measurements*, `https://atlas.web.cern.ch/Atlas/GROUPS/PHYSICS/CombinedSummaryPlots/SM/`. [Online; accessed 26-February-2018]. Cited on p. 15.

[19] J. E. Augustin et al., *Discovery of a Narrow Resonance in e^+e^- Annihilation*, Phys. Rev. Lett. **33** (1974) 1406–1408. Cited on p. 14.

[20] J. J. Aubert et al., *Experimental Observation of a Heavy Particle J*, Phys. Rev. Lett. **33** (1974) 1404–1406. Cited on p. 14.

[21] S. W. Herb et al., *Observation of a Dimuon Resonance at 9.5 GeV in 400 GeV Proton-Nucleus Collisions*, Phys. Rev. Lett. **39** (1977) 252–255. Cited on p. 14.

[22] CDF Collaboration, *Observation of top quark production in $\bar{p}p$ collisions*, Phys. Rev. Lett. **74** (1995) 2626–2631. Cited on p. 14.

[23] DØ Collaboration, *Observation of the top quark*, Phys. Rev. Lett. **74** (1995) 2632–2637. Cited on p. 14.

[24] M. L. Perl et al., *Evidence for Anomalous Lepton Production in e^+- e^- Annihilation*, Phys. Rev. Lett. **35** (1975) 1489–1492. Cited on p. 14.

[25] DONUT Collaboration, *Observation of tau neutrino interactions*, Phys. Lett. **B504** (2001) 218–224. Cited on p. 14.

[26] M. Kobayashi and T. Maskawa, *CP Violation in the Renormalizable Theory of Weak Interaction*, Prog. Theor. Phys. **49** (1973) 652–657. Cited on p. 14.

[27] UA1 Collaboration, *Experimental Observation of Isolated Large Transverse Energy Electrons with Associated Missing Energy at $\sqrt{s} = 540$ GeV*, Phys. Lett. **B122** (1983) 103–116. Cited on p. 14.

[28] UA1 Collaboration, *Experimental Observation of Lepton Pairs of Invariant Mass Around 95 GeV/c^2 at the CERN SPS Collider*, Phys. Lett. **B126** (1983) 398–410. Cited on p. 14.

[29] M. Baak et al., *Updated Status of the Global Electroweak Fit and Constraints on New Physics*, Eur. Phys. J. **C72** (2012) 2003. Cited on p. 14.

[30] ATLAS Collaboration, *Observation of a new particle in the search for the Standard Model Higgs boson with the ATLAS detector at the LHC*, Phys. Lett. B **716** (2012) 1. Cited on p. 14.

[31] CMS Collaboration, *Observation of a new boson at a mass of 125 GeV with the CMS experiment at the LHC*, Phys. Lett. B **716** (2012) 30. Cited on p. 14.

[32] A. G. Cohen, D. B. Kaplan, and A. E. Nelson, *Progress in electroweak baryogenesis*, Annu. Rev. Nucl. Sci. **43** (1993) 27–70. Cited on p. 15.

[33] K. G. Begeman, A. H. Broeils, and R. H. Sanders, *Extended rotation curves of spiral galaxies: Dark haloes and modified dynamics*, Mon. Not. R. Astron. Soc. **249** (1991) 523. Cited on p. 15.

[34] R. Massey, T. Kitching, and J. Richard, *The dark matter of gravitational lensing*, Rep. Prog. Phys. **73** (2010) 086901. Cited on p. 15.

[35] D. Larson et al., *Seven-Year Wilkinson Microwave Anisotropy Probe (WMAP) Observations: Power Spectra and WMAP-Derived Parameters*, Astrophys. J. Suppl. **192** (2011) 16. Cited on p. 15.

[36] Planck Collaboration, *Planck 2013 results. XVI. Cosmological parameters*, Astron. Astrophys. **571** (2014) A16. Cited on p. 15.

[37] Planck Collaboration, *Planck 2015 results. I. Overview of products and scientific results*, Astron. Astrophys. **594** (2016) A1. Cited on p. 16.

[38] Planck Collaboration, *Planck 2015 results. XIII. Cosmological parameters*, Astron. Astrophys. **594** (2016) A13. Cited on p. 16.

[39] Super-Kamiokande Collaboration, *Evidence for oscillation of atmospheric neutrinos*, Phys. Rev. Lett. **81** (1998) 1562–1567. Cited on p. 16.

[40] ATLAS, CDF, CMS, DØ Collaboration, *First combination of Tevatron and LHC measurements of the top-quark mass*, ATLAS-CONF-2014-008, CDF-NOTE-11071, CMS-PAS-TOP-13-014, D0-NOTE-6416, FERMILAB-TM-2582-E (2014). Cited on p. 17.

[41] M. Schmaltz and D. Tucker-Smith, *Little Higgs review*, Annu. Rev. Nucl. Sci. **55** (2005) 229–270. Cited on p. 18 and 20.

[42] S. P. Martin, *A Supersymmetry primer*, FERMILAB-PUB-97-425-T, (1997). Adv. Ser. Direct. High Energy Phys. 18, 1 (1998). Cited on p. 19.

[43] B. A. Dobrescu and C. T. Hill, *Electroweak symmetry breaking via top condensation seesaw*, Phys. Rev. Lett. **81** (1998) 2634–2637. Cited on p. 20.

[44] R. Chivukula et al., *Top Quark Seesaw Theory of Electroweak Symmetry Breaking*, Phys. Rev. **D59** (1999) 075003.

[45] H. Collins, A. K. Grant, and H. Georgi, *The Phenomenology of a top quark seesaw model*, Phys. Rev. **D61** (2000) 055002.

[46] H.-J. He, C. T. Hill, and T. M. P. Tait, *Top quark seesaw, vacuum structure and electroweak precision constraints*, Phys. Rev. **D65** (2002) 055006.

[47] C. T. Hill and E. H. Simmons, *Strong dynamics and electroweak symmetry breaking*, Phys. Rep. **381** (2003) 235–402. [Erratum: Phys. Rept.390,553(2004)].

[48] R. Contino, L. Da Rold, and A. Pomarol, *Light custodians in natural composite Higgs models*, Phys. Rev. **D75** (2007) 055014.

[49] C. Anastasiou, E. Furlan, and J. Santiago, *Realistic Composite Higgs Models*, Phys. Rev. **D79** (2009) 075003.

[50] K. Kong, M. McCaskey, and G. W. Wilson, *Multi-lepton signals from the top-prime quark at the LHC*, J. High Energy Phys. **04** (2012) 079.

[51] A. Carmona, M. Chala, and J. Santiago, *New Higgs Production Mechanism in Composite Higgs Models*, J. High Energy Phys. **07** (2012) 049.

[52] M. Gillioz et al., *Higgs Low-Energy Theorem (and its corrections) in Composite Models*, J. High Energy Phys. **10** (2012) 004. Cited on p. 20.

[53] N. Arkani-Hamed et al., *The Littlest Higgs*, J. High Energy Phys. **07** (2002) 034. Cited on p. 20.

[54] T. Han et al., *Phenomenology of the little Higgs model*, Phys. Rev. **D67** (2003) 095004.

[55] M. Perelstein, M. E. Peskin, and A. Pierce, *Top quarks and electroweak symmetry breaking in little Higgs models*, Phys. Rev. **D69** (2004) 075002. Cited on p. 20.

[56] N. Arkani-Hamed et al., *The Hierarchy problem and new dimensions at a millimeter*, Phys. Lett. **B429** (1998) 263–272. Cited on p. 20.

[57] L. Randall and R. Sundrum, *A Large mass hierarchy from a small extra dimension*, Phys. Rev. Lett. **83** (1999) 3370–3373.

[58] K. Agashe et al., *RS1, custodial isospin and precision tests*, J. High Energy Phys. **08** (2003) 050. Cited on p. 20.

[59] M. B. Einhorn and G. J. Goldberg, *Is There an Upper Limit to Fermion Masses?*, Phys. Rev. Lett. **57** (1986) 2115–2118. Cited on p. 21.

[60] O. Eberhardt et al., *Impact of a Higgs boson at a mass of 126 GeV on the standard model with three and four fermion generations*, Phys. Rev. Lett. **109** (2012) 241802. Cited on p. 21.

[61] K. Kumar, R. Vega-Morales, and F. Yu, *Effects from New Colored States and the Higgs Portal on Gluon Fusion and Higgs Decays*, Phys. Rev. **D86** (2012) 113002. [Erratum: Phys. Rev. D87, no.11, 119903 (2013)]. Cited on p. 21 and 24.

[62] G. D. Kribs et al., *Four generations and Higgs physics*, Phys. Rev. **D76** (2007) 075016. Cited on p. 21.

[63] ATLAS, CMS Collaboration, *Measurements of the Higgs boson production and decay rates and constraints on its couplings from a combined ATLAS and CMS analysis of the LHC pp collision data at $\sqrt{s} = 7$ and 8 TeV*, J. High Energy Phys. **08** (2016) 045. Cited on p. 21.

[64] J. A. Aguilar-Saavedra et al., *Handbook of vectorlike quarks: Mixing and single production*, Phys. Rev. D **88** (2013) no. 9, 094010. Cited on p. xviii, 21, 22, 24, 25, and 26.

[65] Y. Okada and L. Panizzi, *LHC signatures of vector-like quarks*, Adv. High Energy Phys. **2013** (2013) 364936. Cited on p. xviii, xxi, 22, and 26.

[66] F. del Aguila and M. J. Bowick, *The Possibility of New Fermions With $\Delta I = 0$ Mass*, Nucl. Phys. B **224** (1983) 107. Cited on p. 22.

[67] G. C. Branco and L. Lavoura, *On the Addition of Vector Like Quarks to the Standard Model*, Nucl. Phys. **B278** (1986) 738–754. Cited on p. 22.

[68] A. Atre et al., *Model-Independent Searches for New Quarks at the LHC*, J. High Energy Phys. **08** (2011) 080. Cited on p. 22.

[69] A. Atre et al., *Heavy Quarks Above the Top at the Tevatron*, Phys. Rev. **D79** (2009) 054018. Cited on p. 22.

[70] J. A. Aguilar-Saavedra, *Effects of mixing with quark singlets*, Phys. Rev. **D67** (2003) 035003. [Erratum: Phys. Rev.D69, 099901 (2004)]. Cited on p. 22.

[71] F. del Aguila, M. Perez-Victoria, and J. Santiago, *Observable contributions of new exotic quarks to quark mixing*, J. High Energy Phys. **09** (2000) 011. Cited on p. 23.

[72] B. A. Dobrescu and F. Yu, *Exotic Signals of Vectorlike Quarks*, FERMILAB-PUB-16-558-T, MITP-16-133 (2016). Cited on p. 23 and 24.

[73] F. del Aguila, J. A. Aguilar-Saavedra, and G. C. Branco, *CP violation from new quarks in the chiral limit*, Nucl. Phys. **B510** (1998) 39–60. Cited on p. 23.

[74] J. L. Hewett and T. G. Rizzo, *Low-Energy Phenomenology of Superstring Inspired E(6) Models*, Phys. Rept. **183** (1989) 193. Cited on p. 23.

[75] K. Kumar, W. Shepherd, T. M. P. Tait, et al., *Beautiful Mirrors at the LHC*, J. High Energy Phys. **08** (2010) 052. Cited on p. 24.

[76] M. E. Peskin and T. Takeuchi, *A New constraint on a strongly interacting Higgs sector*, Phys. Rev. Lett. **65** (1990) 964–967. Cited on p. 24.

[77] J. Bernabeu, A. Pich, and A. Santamaria, *$\Gamma(Z \to b\bar{B})$: A Signature of Hard Mass Terms for a Heavy Top*, Phys. Lett. **B200** (1988) 569–574. Cited on p. 24.

[78] S. Dawson and E. Furlan, *A Higgs conundrum with vector fermions*, Phys. Rev. D **86** (2012) 015021. Cited on p. 25.

[79] J. A. Aguilar-Saavedra, *Identifying top partners at LHC*, J. High Energy Phys. **11** (2009) 030. Cited on p. 25 and 28.

[80] O. Matsedonskyi, G. Panico, and A. Wulzer, *On the Interpretation of Top Partners Searches*, JHEP **12** (2014) 097. Cited on p. 25.

[81] ATLAS Collaboration, *Measurement of the Inelastic Proton-Proton Cross Section at $\sqrt{s}$ =13 TeV with the ATLAS Detector at the LHC*, Phys. Rev. Lett. **117** (2016) no. 18, 182002. Cited on p. 33.

[82] ATLAS Collaboration, *The ATLAS Experiment at the CERN Large Hadron Collider*, J. Instrum. **3** (2008) S08003. Cited on p. xxii, 35, and 43.

[83] ATLAS Collaboration, *ATLAS detector and physics performance: Technical Design Report, 1*, Technical Design Report ATLAS. CERN, Geneva (1999). Cited on p. 35.

[84] ATLAS Collaboration, *ATLAS Detector and Physics Performance TDR, Volume I+II*, CERN/LHCC/99-14/15 (unpublished) (1999) . Cited on p. 35.

[85] J. Pequenao, *Computer generated image of the whole ATLAS detector*, CERN-GE-0803012, (2008). Cited on p. xxi, 35, and 38.

[86] ATLAS Collaboration, *The ATLAS Experiment at the CERN Large Hadron Collider*, J. Instrum. **3** (2008) S08003. Cited on p. xviii and 37.

[87] N. Wermes and G. Hallewel, *ATLAS pixel detector: Technical Design Report*, Technical Design Report ATLAS. CERN, Geneva (1998). Cited on p. 37.

[88] ATLAS Collaboration, *ATLAS inner detector: Technical Design Report, 1*, Technical Design Report ATLAS. CERN, Geneva (1997).

[89] ATLAS Collaboration, *The ATLAS Inner Detector commissioning and calibration*, Eur. Phys. J. **C70** (2010) 787–821. Cited on p. 37.

[90] ATLAS Collaboration, *ATLAS magnet system: Technical Design Report, 1*, Technical Design Report ATLAS. CERN, Geneva (1997). Cited on p. 37 and 44.

[91] ATLAS Collaboration, *ATLAS central solenoid: Technical Design Report*, Technical Design Report ATLAS. CERN, Geneva (1997).

[92] ATLAS Collaboration, *ATLAS central solenoid: Technical Design Report*, Technical Design Report ATLAS. CERN, Geneva (1997). Cited on p. 37.

[93] ATLAS Collaboration, *ATLAS Insertable B-Layer Technical Design Report*, CERN-LHCC-2010-013. ATLAS-TDR-19 (2010). Cited on p. 38.

[94] P. Butti et al., *ATLAS Inner Detector Alignment Performance with February 2015 Cosmic Rays Data*, ATL-COM-PHYS-2015-198, CERN, Geneva (2015). Cited on p. xxii and 40.

[95] ATLAS Collaboration, *ATLAS tile calorimeter: Technical Design Report*, Technical Design Report ATLAS. CERN, Geneva (1996). Cited on p. 42.

[96] ATLAS Collaboration, *ATLAS liquid-argon calorimeter: Technical Design Report*, Technical Design Report ATLAS. CERN, Geneva (1996). Cited on p. 42.

[97] ATLAS Collaboration, *The muon spectrometer of the ATLAS experiment*, Nucl. Phys. B - Proc. Suppl. **125** (2003) . Cited on p. 44.

[98] ATLAS Collaboration, *ATLAS barrel toroid: Technical Design Report*, Technical Design Report ATLAS. CERN, Geneva (1997). Cited on p. 44.

[99] ATLAS Collaboration, *ATLAS end-cap toroids: Technical Design Report*, Technical Design Report ATLAS. CERN, Geneva (1997). Cited on p. 44.

[100] ATLAS Collaboration, *Performance of the ATLAS Trigger System in 2010*, Eur. Phys. J. **C72** (2012) 1849. Cited on p. 46.

[101] J. Pequenao and P. Schaffner, *An computer generated image representing how ATLAS detects particles*, (2013). Cited on p. xxii and 49.

[102] T. Cornelissen et al., *The new ATLAS track reconstruction (NEWT)*, J. Phys. Conf. Ser. **119** (2008) no. 3, 032014. Cited on p. 51.

[103] T. Cornelissen et al., *Concepts, Design and Implementation of the ATLAS New Tracking (NEWT)*, ATL-SOFT-PUB-2007-007. ATL-COM-SOFT-2007-002, CERN, Geneva (2007). Cited on p. 51 and 53.

[104] P. F. Åkesson, *ATLAS Tracking Event Data Model*, ATL-SOFT-PUB-2006-004. ATL-COM-SOFT-2006-005. CERN-ATL-COM-SOFT-2006-005, CERN, Geneva (2006). Cited on p. 51 and 72.

[105] R. Frühwirth, *Application of Kalman filtering to track and vertex fitting*, Nucl. Instrum. Methods **A262** (1987) 444–450. Cited on p. 52.

[106] T. Cornelissen, *Track Fitting in the ATLAS Experiment*, PhD thesis, U. Amsterdam, Amsterdam, (2006). Cited on p. 53.

[107] Wicke, D., *A new algorithm for solving track ambiguities*, PROG 236 TRACK 92 (1998). Cited on p. 53.

[108] ATLAS Collaboration, *Performance of the ATLAS Inner Detector Track and Vertex Reconstruction in the High Pile-Up LHC Environment*, ATLAS-CONF-2012-042, CERN, Geneva (2012). Cited on p. 53.

[109] ATLAS Collaboration, *Track Reconstruction Performance of the ATLAS Inner Detector at $\sqrt{s} = 13$ TeV*, ATL-PHYS-PUB-2015-018, CERN, Geneva (2015). Cited on p. 54.

[110] ATLAS Collaboration, *Early Inner Detector Tracking Performance in the 2015 data at $\sqrt{s} = 13$ TeV*, ATL-PHYS-PUB-2015-051, CERN, Geneva (2015). Cited on p. 53 and 54.

[111] ATLAS Collaboration, *Reconstruction of primary vertices at the ATLAS experiment in Run 1 proton-proton collisions at the LHC*, Eur. Phys. J. **C77** (2017) no. 5, 332. Cited on p. 54.

[112] G. Borissov et al., *ATLAS strategy for primary vertex reconstruction during Run 2 of the LHC*, J. Phys. Conf. Ser. **664** (2015) no. 7, 072041. Cited on p. 54.

[113] R. Frühwirth, W. Waltenberger, and P. Vanlaer, *Adaptive Vertex Fitting*, CMS-NOTE-2007-008, CERN, Geneva (2007). Cited on p. 55.

[114] ATLAS Collaboration, *Vertex Reconstruction Performance of the ATLAS Detector at $\sqrt{s} = 13$ TeV*, ATL-PHYS-PUB-2015-026, CERN, Geneva (2015). Cited on p. 55.

[115] W. Lampl et al., *Calorimeter Clustering Algorithms: Description and Performance*, ATL-LARG-PUB-2008-002. ATL-COM-LARG-2008-003, CERN, Geneva (2008). Cited on p. 55.

[116] M. Aharrouche et al., *Measurement of the response of the ATLAS liquid argon barrel calorimeter to electrons at the 2004 combined test-beam*, Nucl. Instrum. Methods **A614** (2010) 400–432. Cited on p. 55 and 57.

[117] ATLAS Collaboration, *Electron performance measurements with the ATLAS detector using the 2010 LHC proton-proton collision data*, Eur. Phys. J. **C72** (2012) 1909. Cited on p. 56 and 57.

[118] ATLAS Collaboration, *Electron and photon energy calibration with the ATLAS detector using LHC Run 1 data*, Eur. Phys. J. **C74** (2014) no. 10, 3071. Cited on p. 57.

[119] ATLAS Collaboration, *Electron efficiency measurements with the ATLAS detector using the 2015 LHC proton-proton collision data*, ATLAS-CONF-2016-024, CERN, Geneva (2016). Cited on p. 57 and 58.

[120] ATLAS Collaboration, *Muon reconstruction performance of the ATLAS detector in proton–proton collision data at $\sqrt{s}$=13 TeV*, Eur. Phys. J. C **76** (2016) no. 5, 292. Cited on p. 60.

[121] M. Cacciari, G. P. Salam, and G. Soyez, *The Anti-k(t) jet clustering algorithm*, J. High Energy Phys. **04** (2008) 063. Cited on p. 61.

[122] M. Cacciari and G. P. Salam, *Dispelling the N^3 myth for the k_t jet-finder*, Phys. Lett. **B641** (2006) 57–61. Cited on p. 61.

[123] ATLAS Collaboration, *Jet energy measurement with the ATLAS detector in proton-proton collisions at $\sqrt{s} = 7$ TeV*, Eur. Phys. J. **73** (2013) 2304. Cited on p. 62.

[124] D. Krohn, J. Thaler, and L.-T. Wang, *Jet Trimming*, J. High Energy Phys. **02** (2010) 084. Cited on p. 62.

[125] ATLAS Collaboration, *Jet mass reconstruction with the ATLAS Detector in early Run 2 data*, ATLAS-CONF-2016-035, CERN, Geneva (2016). Cited on p. 62.

[126] ATLAS Collaboration, *Performance of Top Quark and W Boson Tagging in Run 2 with ATLAS*, ATLAS-CONF-2017-064, CERN, Geneva (2017). Cited on p. 62.

[127] ATLAS Collaboration, *Jet energy resolution in proton-proton collisions at $\sqrt{s} = 7$ TeV recorded in 2010 with the ATLAS detector*, Eur. Phys. J. **C73** (2013) no. 3, 2306. Cited on p. 63.

[128] ATLAS Collaboration, *Pile-up subtraction and suppression for jets in ATLAS*, ATLAS-CONF-2013-083, CERN, Geneva (2013). Cited on p. 63.

[129] ATLAS Collaboration, *Performance of b -jet identification in the ATLAS experiment*, Journal of Instrumentation **11** (2016) no. 04, P04008. Cited on p. 64.

[130] ATLAS Collaboration, *Optimisation of the ATLAS b-tagging performance for the 2016 LHC Run*, ATL-PHYS-PUB-2016-012, CERN, Geneva (2016). Cited on p. 64.

[131] A. J. Larkoski, I. Moult, and D. Neill, *Power Counting to Better Jet Observables*, J. High Energy Phys. **12** (2014) 009. Cited on p. 64.

[132] A. J. Larkoski, I. Moult, and D. Neill, *Analytic Boosted Boson Discrimination*, J. High Energy Phys. **05** (2016) 117. Cited on p. 64.

[133] ATLAS Collaboration, *Jet mass reconstruction with the ATLAS Detector in early Run 2 data*, (2016). Cited on p. 64.

[134] ATLAS Collaboration, *Identification of boosted, hadronically-decaying W and Z bosons in $\sqrt{s} = 13$ TeV Monte Carlo Simulations for ATLAS*, ATL-PHYS-PUB-2015-033 (2015). Cited on p. 65, 136, and 160.

[135] ATLAS Collaboration, *Performance of missing transverse momentum reconstruction for the ATLAS detector in the first proton-proton collisions at $\sqrt{s}$= 13 TeV*, ATL-PHYS-PUB-2015-027, CERN, Geneva (2015). Cited on p. 65.

[136] B. Brunt et al., *Expected performance of missing transverse momentum reconstruction for the ATLAS detector at $\sqrt{s} = 13$ TeV*, ATL-COM-PHYS-2015-347, CERN, Geneva (2015). Cited on p. 66.

[137] ATLAS Collaboration, *Selection of jets produced in 13 TeV proton-proton collisions with the ATLAS detector*, ATLAS-CONF-2015-029, CERN, Geneva (2015). Cited on p. 66.

[138] T. Golling, *Alignment of the Silicon Tracking Detector using Survey Constraints*, ATL-INDET-PUB-2006-001. ATL-COM-INDET-2006-002. CERN-ATL-INDET-PUB-2006-001, CERN, Geneva (2006). Cited on p. 67.

[139] ATLAS Collaboration, *The ATLAS Inner Detector commissioning and calibration*, Eur. Phys. J. **C70** (2010) 787–821. Cited on p. 69.

[140] ATLAS Collaboration, *Alignment of the ATLAS Inner Detector Tracking System with 2010 LHC proton-proton collisions at $\sqrt{s} = 7$ TeV*, ATLAS-CONF-2011-012, CERN, Geneva (2011). Cited on p. 70.

[141] ATLAS Collaboration, *Common Framework Implementation for the Track-Based Alignment of the ATLAS Detector*, ATL-SOFT-PUB-2014-003, CERN, Geneva (2014). Cited on p. 70.

[142] P. Brückman, A. Hicheur, and S. J. Haywood, *Global χ^2 approach to the Alignment of the ATLAS Silicon Tracking Detectors*, ATL-INDET-PUB-2005-002, ATL-COM-INDET-2005-004, CERN-ATL-INDET-PUB-2005-002 (2005). Cited on p. 71.

[143] P. Brückman de Renstrom, *Alignment of the ATLAS inner detector tracking system: Solving the problem*, Nucl. Phys. Proc. Suppl. **197** (2009) 158–162. Cited on p. 71.

[144] ATLAS Collaboration, *Study of alignment-related systematic effects on the ATLAS Inner Detector tracking*, ATLAS-CONF-2012-141, CERN, Geneva (2012). Cited on p. 72 and 77.

[145] J. Boudreau and V. Tsulaia, *The GeoModel toolkit for detector description*, in *Computing in high energy physics and nuclear physics. Proceedings, Conference, CHEP'04, Interlaken, Switzerland, September 27-October 1, 2004*, pp. 353–356. (2005). Cited on p. 78.

[146] ATLAS Collaboration, *Study of the mechanical stability of the ATLAS Insertable B-Layer*, ATL-INDET-PUB-2015-001, CERN, Geneva (2015). Cited on p. 78.

[147] ATLAS Collaboration, *Alignment of the ATLAS Inner Detector and its Performance in 2012*, ATLAS-CONF-2014-047, CERN, Geneva (2014). Cited on p. 82.

[148] ATLAS Collaboration, *Study of the material of the ATLAS inner detector for Run 2 of the LHC*, JINST **12** (2017) no. 12, P12009. Cited on p. 82.

[149] ATLAS Collaboration, *The ATLAS Simulation Infrastructure*, Eur. Phys. J. **C70** (2010) 823–874. Cited on p. 85 and 111.

[150] J. C. Collins and D. E. Soper, *The Theorems of Perturbative QCD*, Annu. Rev. Nucl. Sci. **37** (1987) 383. Cited on p. 86.

[151] Y. L. Dokshitzer, *Calculation of the Structure Functions for Deep Inelastic Scattering and e+ e- Annihilation by Perturbation Theory in Quantum Chromodynamics.*, Sov. Phys. JETP **46** (1977) 641–653. [Zh. Eksp. Teor. Fiz.73,1216(1977)]. Cited on p. 87.

[152] V. N. Gribov and L. N. Lipatov, *Deep inelastic e p scattering in perturbation theory*, Sov. J. Nucl. Phys. **15** (1972) 438–450. [Yad. Fiz.15,781(1972)].

[153] G. Altarelli and G. Parisi, *Asymptotic Freedom in Parton Language*, Nucl. Phys. **B126** (1977) 298–318. Cited on p. 87.

[154] A. M. Cooper-Sarkar, R. C. E. Devenish, and A. De Roeck, *Structure Functions of the Nucleon and their Interpretation*, Int. J. Mod. Phys. A **13** (1998) 3385–3586. Cited on p. 87.

[155] J. Pumplin et al., *New Generation of Parton Distributions with Uncertainties from Global QCD Analysis*, J. High Energy Phys. **0207** (2002) 012.

[156] A. Martin et al., *Physical Gluons and High E_T Jets*, Phys. Lett. B **604** (2004) 61.

[157] A. Martin et al., *Uncertainties of predictions from parton distributions, I. Experimental errors*, Eur. Phys. J. C **28** (2003) 455. Cited on p. 87.

[158] F. Siegert, *Monte-Carlo event generation for the LHC*, PhD thesis, Durham U., Durham, (2010). Cited on p. 88.

[159] T. Kinoshita, *Mass singularities of Feynman amplitudes*, J. Math. Phys. **3** (1962) 650–677. Cited on p. 88.

[160] T. Lee and M. Nauenberg, *Degenerate Systems and Mass Singularities*, Phys. Rev. **133** (1964) B1549–B1562. Cited on p. 88.

[161] S. Frixione, Z. Kunszt, and A. Signer, *Three jet cross-sections to next-to-leading order*, Nucl.Phys. **B467** (1996) 399–442. Cited on p. 88.

[162] B. Webber, *Parton shower Monte Carlo event generators*, Scholarpedia **6** (2011) no. 12, 10662. revision no. 128236. Cited on p. 89.

[163] B. Cooper et al., *Importance of a consistent choice of $\alpha(s)$ in the matching of ALPGEN and PYTHIA*, Eur. Phys. J. **C72** (2012) 2078. Cited on p. 90.

[164] S. Catani, F. Krauss, R. Kuhn, et al., *QCD Matrix Elements + Parton Showers*, J. High Energy Phys. **0111** (2001) 063. Cited on p. 90.

[165] F. Krauss, *Matrix Elements and Parton Showers in Hadronic Interactions*, J. High Energy Phys. **0208** (2002) 015. Cited on p. 90.

[166] M. L. Mangano, *A Review of MLM's Prescription for Removal of Double Counting*, `http://cepa.fnal.gov/patriot/mc4run2/MCTuning/061104/mlm.pdf` (2013). Cited on p. 90.

[167] S. Frixione and B. R. Webber, *Matching NLO QCD computations and parton shower simulations*, J. High Energy Phys. **0206** (2002) 029. Cited on p. 90.

[168] P. Nason, *A new method for combining NLO QCD with shower Monte Carlo algorithms*, J. High Energy Phys. **11** (2004) 040. Cited on p. 90.

[169] S. Frixione, P. Nason, and C. Oleari, *Matching NLO QCD computations with Parton Shower simulations: the POWHEG method*, J. High Energy Phys. **0711** (2007) 070. Cited on p. 90.

[170] A. Buckley et al., *General-purpose event generators for LHC physics*, Phys. Rept. **504** (2011) 145–233. Cited on p. 90.

[171] B. Andersson et al., *Parton Fragmentation and String Dynamics*, Phys. Rept. **97** (1983) 31–145. Cited on p. 90.

[172] T. Sjöstrand, *Jet Fragmentation of Nearby Partons*, Nucl. Phys. **B248** (1984) 469–502. Cited on p. 90.

[173] B. R. Webber, *A QCD Model for Jet Fragmentation Including Soft Gluon Interference*, Nucl. Phys. **B238** (1984) 492–528. Cited on p. 90.

[174] G. Marchesini and B. R. Webber, *Monte Carlo Simulation of General Hard Processes with Coherent QCD Radiation*, Nucl. Phys. **B310** (1988) 461–526. Cited on p. 90.

[175] ATLAS Collaboration, *Measurement of the underlying event in jet events from 7 TeV proton-proton collisions with the ATLAS detector*, Eur. Phys. J. **C74** (2014) no. 8, 2965. Cited on p. 91.

[176] ATLAS Collaboration, *Underlying event characteristics and their dependence on jet size of charged-particle jet events in pp collisions at $\sqrt{s} = 7$ TeV with the ATLAS detector*, Phys. Rev. **D86** (2012) 072004. Cited on p. 91.

[177] A. Buckley et al., *General-purpose event generators for LHC physics*, Phys. Rept. **504** (2011) 145–233. Cited on p. 91.

[178] J. M. Butterworth, J. R. Forshaw, and M. H. Seymour, *Multiparton interactions in photoproduction at HERA*, Z. Phys. **C72** (1996) 637–646. Cited on p. 91.

[179] ATLAS Collaboration, G. Aad et al., *The ATLAS Simulation Infrastructure*, Eur. Phys. J. **C70** (2010) 823–874. Cited on p. 92.

[180] GEANT4 Collaboration, *GEANT4: A Simulation toolkit*, Nucl. Instrum. Methods **A506** (2003) 250–303. Cited on p. 92.

[181] W. Lukas, *Fast Simulation for ATLAS: Atlfast-II and ISF*, ATL-SOFT-PROC-2012-065, CERN, Geneva (2012). Cited on p. 92 and 111.

[182] ATLAS Collaboration, *The simulation principle and performance of the ATLAS fast calorimeter simulation FastCaloSim*, ATL-PHYS-PUB-2010-013, CERN, Geneva (2010). Cited on p. 92.

[183] ATLAS Collaboration, *Charged-particle distributions in $\sqrt{s}$=13 TeV pp interactions measured with the ATLAS detector at the LHC*, ATLAS-COM-CONF-2015-046, CERN, Geneva (2015). Cited on p. 92.

[184] T. Sjöstrand et al., PYTHIA, Comput. Phys. Commun. **135** (2001) 238. Cited on p. 94.

[185] T. Sjöstrand et al., *A Brief Introduction to PYTHIA 8.1*, Comput. Phys. Commun. **178** (2008) 852–867. Cited on p. 94, 98, and 99.

[186] G. Corcella et al., *HERWIG 6: An Event generator for hadron emission reactions with interfering gluons (including supersymmetric processes)*, J. High Energy Phys. **01** (2001) 010. Cited on p. 94 and 98.

[187] J. Bellm et al., *Herwig 7.0/Herwig++ 3.0 release note*, Eur. Phys. J. **C76** (2016) no. 4, 196. Cited on p. 94 and 99.

[188] P. Nason, *A New method for combining NLO QCD with shower Monte Carlo algorithms*, J. High Energy Phys. **11** (2004) 040. Cited on p. 94 and 98.

[189] S. F. et al., *A positive-weight next-to-leading-order Monte Carlo for heavy flavour hadroproduction*, J. High Energy Phys. **2007** (2007) no. 09, 126.

[190] S. Alioli et al., *A general framework for implementing NLO calculations in shower Monte Carlo programs: the POWHEG BOX*, J. High Energy Phys. **06** (2010) 043. Cited on p. 94 and 98.

[191] S. Alioli et al., *A general framework for implementing NLO calculations in shower Monte Carlo programs: the POWHEG BOX*, J. High Energy Phys. **1006** (2010) 043. Cited on p. 94.

[192] V. Hirschi et al., *Automation of one-loop QCD corrections*, J. High Energy Phys. **1105** (2011) 044. Cited on p. 94.

[193] Frederix et al., *Scalar and pseudoscalar Higgs production in association with a top-antitop pair*, Phys.Lett. **B701** (2011) 427–433.

[194] R. Pittau, *Status of MADLOOP/aMCatNLO*, (2012). Cited on p. 94.

[195] T. Gleisberg et al., *Event generation with SHERPA 1.1*, J. High Energy Phys. **02** (2009) 007. Cited on p. 95 and 114.

[196] G. Cullen et al., *Automated One-Loop Calculations with GoSam*, arXiv:1111.2034 (2011). Cited on p. 95.

[197] F. Krauss, R. Kuhn, and G. Soff, *AMEGIC 1.0: A Matrix element generator in C++*, J. High Energy Phys. **0202** (2002) 044. Cited on p. 95.

[198] J. Aguilar-Saavedra, *Protos: PROgram for TOp Simulations*, `http://jaguilar.web.cern.ch/jaguilar/protos/`. Cited on p. 95 and 112.

[199] P. Z. Skands, *Tuning Monte Carlo Generators: The Perugia Tunes*, Phys. Rev. **D82** (2010) 074018. Cited on p. 95 and 98.

[200] ATLAS Collaboration, *ATLAS Run 1 PYTHIA 8 tunes*, ATL-PHYS-PUB-2014-021 (2014) . Cited on p. 95, 99, and 112.

[201] G. D'Agostini, *A Multidimensional unfolding method based on Bayes' theorem*, Nucl. Instrum. Methods **A362** (1995) 487–498. Cited on p. 98.

[202] T. Adye, *Unfolding algorithms and tests using RooUnfold*, in *Proceedings, PHYSTAT 2011 Workshop on Statistical Issues Related to Discovery Claims in Search Experiments and Unfolding, CERN,Geneva, Switzerland 17-20 January 2011*, pp. 313–318. CERN, Geneva, (2011). Cited on p. 98.

[203] S. Alioli et al., *A general framework for implementing NLO calculations in shower Monte Carlo programs: the POWHEG BOX*, J. High Energy Phys. **06** (2010) 043. Cited on p. 98.

[204] T. Sjöstrand et al., *High-energy physics event generation with PYTHIA 6.1*, Comput. Phys. Commun. **135** (2001) 238–259. Cited on p. 98.

[205] J. Pumplin et al., *New generation of parton distributions with uncertainties from global QCD analysis*, J. High Energy Phys. **0207** (2002) 012. Cited on p. 98.

[206] J. Alwall et al., *The automated computation of tree-level and next-to-leading order differential cross sections, and their matching to parton shower simulations*, J. High Energy Phys. **07** (2014) 079. Cited on p. 98, 99, and 114.

[207] ATLAS Collaboration, *Simulation of top quark production for the ATLAS experiment at* $\sqrt{s}$= *13 TeV*, ATL-PHYS-PUB-2016-004, CERN, Geneva (2016). Cited on p. 98, 99, and 102.

[208] NNPDF Collaboration, *Parton distributions for the LHC Run II*, J. High Energy Phys. **04** (2015) 040. Cited on p. 98.

[209] R. D. Ball et al., *Parton distributions with LHC data*, Nucl. Phys. **B867** (2013) 244–289. Cited on p. 98.

[210] I. Connelly et al., *Studies on top-quark Monte Carlo modelling for Top2016*, ATL-COM-PHYS-2016-1235, CERN, Geneva (2016). Cited on p. 99, 100, and 119.

[211] ATLAS Collaboration, *Comparison of Monte Carlo generator predictions to ATLAS measurements of top pair production at 7 TeV*, ATL-PHYS-PUB-2015-002, CERN, Geneva (2015). Cited on p. 99.

[212] ATLAS Collaboration, *Further studies on simulation of top-quark production for the ATLAS experiment at $\sqrt{s}$= 13 TeV*, ATL-PHYS-PUB-2016-016, CERN, Geneva (2016). Cited on p. 99.

[213] A. Buckley et al., *Rivet user manual*, Comput. Phys. Commun. **184** (2013) 2803–2819. Cited on p. 100.

[214] ATLAS Collaboration, *Measurements of top-quark pair differential cross-sections in the lepton+jets channel in pp collisions at $\sqrt{s} = 13$ TeV using the ATLAS detector*, J. High Energy Phys. **11** (2017) 191. Cited on p. xxiii, 100, 103, and 104.

[215] J. Thaler and K. Van Tilburg, *Identifying Boosted Objects with N-subjettiness*, J. High Energy Phys. **03** (2011) 015. Cited on p. 101.

[216] ATLAS Collaboration, *Differential top-antitop cross-section measurements as a function of observables constructed from final-state particles using pp collisions at $\sqrt{s} = 7$ TeV in the ATLAS detector*, J. High Energy Phys. **06** (2015) 100. Cited on p. 101.

[217] ATLAS Collaboration, *Search for pair production of heavy vector-like quarks decaying into high-p_T W bosons and top quarks in the lepton-plus-jets final state in pp collisions at $\sqrt{s} = 13$ TeV with the ATLAS detector*, JHEP **08** (2018) 048. Cited on p. 109.

[218] ATLAS Collaboration, *Search for pair production of heavy vector-like quarks decaying to high-p_{T} W bosons and b quarks in the lepton-plus-jets final state in pp collisions at $\sqrt{s}$=13 TeV with the ATLAS detector.*, J. High Energy Phys. **10** (2017) 141. 41 p. Cited on p. xxv, xxvi, 109, 141, 143, 144, 145, 149, 150, and 151.

[219] CMS Collaboration, *Search for top quark partners with charge 5/3 in the single-lepton final state at $\sqrt{s} = 13$ TeV*, CMS-PAS-B2G-17-008, CERN, Geneva (2017). Cited on p. 109.

[220] CMS Collaboration, *Search for vector-like quark pair production* $\mathrm{T\bar{T}(Y\bar{Y})} \rightarrow \mathrm{bWbW}$ *using kinematic reconstruction in lepton+jets final states at $\sqrt{s}$=13 TeV*, CMS-PAS-B2G-17-003, CERN, Geneva (2017). Cited on p. 109.

[221] ATLAS Collaboration, *Summary of ATLAS PYTHIA 8 tunes*, ATL-PHYS-PUB-2012-003 (2012). Cited on p. 111.

[222] D. J. Lange, *The EvtGen particle decay simulation package*, Nucl. Instrum. Methods **A462** (2001) 152–155. Cited on p. 111.

[223] T. Sjöstrand, S. Mrenna, and P. Z. Skands, *A Brief Introduction to PYTHIA 8.1*, Comput. Phys. Commun. **178** (2008) 852–867. Cited on p. 112.

[224] J. Ferrando and D. Wendland, *Reference $t\bar{t}$ production cross sections for use in ATLAS analyses*, ATL-COM-PHYS-2014-112, CERN, Geneva (2014). Cited on p. xxiv and 112.

[225] M. Czakon and A. Mitov, *Top++: A Program for the Calculation of the Top-Pair Cross-Section at Hadron Colliders*, Comput. Phys. Commun. **185** (2014) 2930. Cited on p. 113 and 117.

[226] A. D. Martin, W. J. Stirling, R. S. Thorne, and G. Watt, *Heavy-quark mass dependence in global PDF analyses and 3- and 4-flavour parton distributions*, Eur. Phys. J. **C70** (2010) 51–72. Cited on p. 113.

[227] M. Botje et al., *The PDF4LHC Working Group Interim Recommendations*, arXiv:1101.0538 (2011). Cited on p. 113.

[228] J. Gao et al., *CT10 next-to-next-to-leading order global analysis of QCD*, Phys. Rev. **D89** (2014) no. 3, 033009. Cited on p. 113.

[229] R. D. Ball et al., *Parton distributions with LHC data*, Nucl. Phys. **B867** (2013) 244–289. Cited on p. 113.

[230] N. Kidonakis, *Next-to-next-to-leading-order collinear and soft gluon corrections for t-channel single top quark production*, Phys. Rev. **D83** (2011) 091503. Cited on p. 113.

[231] C. Anastasiou et al., *High precision QCD at hadron colliders: Electroweak gauge boson rapidity distributions at NNLO*, Phys. Rev. **D69** (2004) 094008. Cited on p. 114.

[232] K. Melnikov and F. Petriello, *Electroweak gauge boson production at hadron colliders through $\mathcal{O}(\alpha_S^2)$*, Phys. Rev. **D74** (2006) 114017.

[233] R. Gavin, Y. Li, F. Petriello, and S. Quackenbush, *FEWZ 2.0: A code for hadronic Z production at next-to-next-to-leading order*, Comput. Phys. Commun. **182** (2011) 2388–2403. Cited on p. 114.

[234] ATLAS Collaboration, *Measurement of the top quark-pair production cross section with ATLAS in pp collisions at $\sqrt{s} = 7$ TeV*, Eur. Phys. J. **C71** (2011) 1577. Cited on p. 114.

[235] ATLAS Collaboration, *Search for heavy particles decaying into top-quark pairs using lepton-plus-jets events in proton-proton collisions at $\sqrt{s} = 13$ TeV with the ATLAS detector*, Eur. Phys. J. **C78** (2018) no. 7, 565. Cited on p. 115.

[236] ATLAS Collaboration, *Luminosity determination in pp collisions at $\sqrt{s} = 8$ TeV using the ATLAS detector at the LHC*, Eur. Phys. J. **C76** (2016) no. 12, 653. Cited on p. 116.

[237] J. Butterworth et al., *Single Boson and Diboson Production Cross Sections in pp Collisions at $\sqrt{s}$=7 TeV*, ATL-COM-PHYS-2010-695, CERN, Geneva (2010). Cited on p. 117.

[238] ATLAS Collaboration, *ATLAS simulation of boson plus jets processes in Run 2*, ATL-PHYS-PUB-2017-006, CERN, Geneva (2017). Cited on p. 117.

[239] J. M. Campbell and R. K. Ellis, *$t\bar{t}W^{\pm}$ production and decay at NLO*, J. High Energy Phys. **07** (2012) 052. Cited on p. 117.

[240] P. Kant et al., *HatHor for single top-quark production: Updated predictions and uncertainty estimates for single top-quark production in hadronic collisions*, Comput. Phys. Commun. **191** (2015) 74–89. Cited on p. 117.

[241] M. Aliev et al., *HATHOR: HAdronic Top and Heavy quarks crOss section calculatoR*, Comput. Phys. Commun. **182** (2011) 1034–1046. Cited on p. 117.

[242] M. Cacciari et al., *Top-pair production at hadron colliders with next-to-next-to-leading logarithmic soft-gluon resummation*, Phys. Lett. **B710** (2012) 612–622. Cited on p. 117.

[243] M. Beneke et al., *Hadronic top-quark pair production with NNLL threshold resummation*, Nucl. Phys. **B855** (2012) 695–741.

[244] P. Baernreuther, M. Czakon, and A. Mitov, *Percent Level Precision Physics at the Tevatron: First Genuine NNLO QCD Corrections to $q\bar{q} \to t\bar{t} + X$*, Phys. Rev. Lett. **109** (2012) 132001.

[245] M. Czakon and A. Mitov, *NNLO corrections to top-pair production at hadron colliders: the all-fermionic scattering channels*, J. High Energy Phys. **12** (2012) 054.

[246] M. Czakon and A. Mitov, *NNLO corrections to top pair production at hadron colliders: the quark-gluon reaction*, J. High Energy Phys. **01** (2013) 080.

[247] M. Czakon, P. Fiedler, and A. Mitov, *Total Top-Quark Pair-Production Cross Section at Hadron Colliders Through $\mathcal{O}(\alpha_S^4)$*, Phys. Rev. Lett. **110** (2013) 252004. Cited on p. 117.

[248] E. Re et al., *Single-top Wt-channel production matched with parton showers using the POWHEG method*, Eur. Phys. J. **C71** (2011) 1547. Cited on p. xxiv and 119.

[249] S. Frixione et al., *Single-top hadroproduction in association with a W boson*, J. High Energy Phys. **07** (2008) 029. Cited on p. 119.

[250] F. James, *MINUIT Function Minimization and Error Analysis: Reference Manual Version 94.1*, CERN-D-506, CERN-D506 (1994). Cited on p. 124 and 126.

[251] W. Verkerke and D. P. Kirkby, *The RooFit toolkit for data modeling*, CHEP-2003-MOLT007, (2003). Cited on p. 126.

[252] TRexFitter group, *TRexFitter TWiki Page*, `https://twiki.cern.ch/twiki/bin/viewauth/AtlasProtected/TtHFitter`. Cited on p. 126.

[253] T. Junk, *Confidence level computation for combining searches with small statistics*, NIM **434** (1999) 435. Cited on p. 127.

[254] Stefan Gadatsch, *The Higgs Boson*, PhD thesis, Amsterdam U., (2015). Cited on p. xxiv and 131.

[255] A. Wald, *Tests of statistical hypotheses concerning several parameters when the number of observations is large*, Transactions of the American Mathematical society **54** (1943) no. 3, 426–482. Cited on p. 132.

[256] S. Wilks, *The large-sample distribution of the likelihood ratio for testing composite hypotheses*, The Annals of Mathematical Statistics **9** (1938) no. 1, 60–62. Cited on p. 132.

[257] G. Cowan et al., *Asymptotic formulae for likelihood-based tests of new physics*, EPJC **71** (2011) 1554. Cited on p. 132.

[258] L. Breiman et al., *Classification and Regression Trees*. Wadsworth and Brooks, Monterey, CA, (1984). Cited on p. 133 and 134.

[259] R. E. Schapire, *The strength of weak learnability*, Machine Learning **5** (1990) 197–227. Cited on p. 134.

[260] Y. Freund and R. E. Schapire, *Experiments with a New Boosting Algorithm*, (1996). Cited on p. 134.

[261] Y. Freund and R. E. Schapire, *A desicion-theoretic generalization of on-line learning and an application to boosting*, in *Computational Learning Theory*, P. Vitányi, ed., pp. 23–37. Springer Berlin Heidelberg, Berlin, Heidelberg, (1995). Cited on p. 134.

[262] A. Hoecker et al., *TMVA - Toolkit for Multivariate Data Analysis*, PoS **ACAT** (2007) 040. Cited on p. xx, 134, and 169.

[263] B. Roe et al., *Boosted decision trees, an alternative to artificial neural networks*, Nucl. Instrum. Methods **A543** (2005) no. 2-3, 577–584. Cited on p. 134.

[264] DØ Collaboration, *Evidence for production of single top quarks and first direct measurement of $|Vtb|$*, Phys. Rev. Lett. **98** (2007) 181802. Cited on p. 134.

[265] ATLAS Collaboration, *Search for pair production of heavy vector-like quarks decaying to high-p_T W bosons and b quarks in the lepton-plus-jets final state in pp collisions at $\sqrt{s}$=13 TeV with the ATLAS detector*, ATLAS-CONF-2016-102, CERN, Geneva (2016). Cited on p. 135.

[266] ATLAS Collaboration, *Search for production of vector-like quark pairs and of four top quarks in the lepton-plus-jets final state in pp collisions at $\sqrt{s} = 8$ TeV with the ATLAS detector*, J. High Energy Phys. **08** (2015) 105. Cited on p. 136.

[267] CMS Collaboration, *Search for pair production of vector-like T quarks in the lepton plus jets final state*, CMS-PAS-B2G-16-002, CERN, Geneva (2016). Cited on p. 136.

[268] ATLAS Collaboration, *Boosted hadronic top identification at ATLAS for early 13 TeV data*, ATL-PHYS-PUB-2015-053 (2015). Cited on p. 136 and 160.

[269] D. Krohn, J. Thaler, and L.-T. Wang, *Jets with Variable R*, J. High Energy Phys. **06** (2009) 059. Cited on p. 155.

[270] ATLAS Collaboration, *Optimisation procedure for two-variable top, W and Z substructure taggers for the ATLAS detector*, ATL-COM-PHYS-2017-033, CERN, Geneva (2017). Cited on p. 157.

[271] ATLAS Collaboration, *Search for vector-like B quarks in events with one isolated lepton, missing transverse momentum and jets at $\sqrt{s} = 8$ TeV with the ATLAS detector*, Phys. Rev. **D91** (2015) no. 11, 112011. Cited on p. 160 and 183.

[272] J. D. Bjorken and S. J. Brodsky, *Statistical Model for electron-positron Annihilation Into Hadrons*, Phys. Rev. **D1** (1970) 1416–1420. Cited on p. 169 and 171.

[273] ATLAS Collaboration, *Search for production of vector-like quark pairs and of four top quarks in the lepton-plus-jets final state in pp collisions at $\sqrt{s} = 8$ TeV with the ATLAS detector*, J. High Energy Phys. **08** (2015) 105. Cited on p. 183.

[274] CMS Collaboration, *Inclusive search for a vector-like T quark with charge $\frac{2}{3}$ in pp collisions at $\sqrt{s} = 8$ TeV*, Phys. Lett. **B729** (2014) 149–171. Cited on p. 183.

[275] CMS Collaboration, *Search for top-quark partners with charge 5/3 in the same-sign dilepton final state*, Phys. Rev. Lett. **112** (2014) no. 17, 171801. Cited on p. 183.

[276] CMS Collaboration, *Search for heavy quarks decaying into a top quark and a W or Z boson using lepton + jets events in pp collisions at $\sqrt{s} = 7$ TeV*, J. High Energy Phys. **01** (2013) 154. Cited on p. 183.

[277] ATLAS Collaboration, *Combination of the searches for pair-produced vector-like partners of the third-generation quarks at $\sqrt{s} = 13$ TeV with the ATLAS detector*, arXiv:1808.02343 (submitted to Phys. Rev. Lett.) (2018) . Cited on p. xxx, 183, 185, and 186.